MIT/WHOI

Massachusetts Institute of Technology
Woods Hole Oceanographic Institution

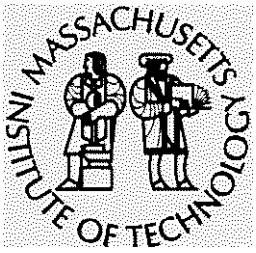

Joint Program in Oceanography/ Applied Ocean Science and Engineering

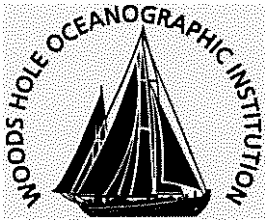

DOCTORAL DISSERTATION

New Insights into the Marine Oxygen Cycle Jrom Manganese Oxide Minerals and Reactive Oxygen Species

by

Kevin Michael Sutherland

February 2020

New Insights into the Marine Oxygen Cycle from Manganese Oxide Minerals and Reactive Oxygen Species

By

Kevin Michael Sutherland

B.S., California Institute of Technology (2013)
M.S., California Institute of Technology (2013)

Submitted in partial fulfillment of the requirements for the degree of

Doctor of Philosophy

at the

MASSACHUSETTS INSTITUTE OF TECHNOLOGY

and the

WOODS HOLE OCEANOGRAPHIC INSTITUTION

February 2020

Signature of Author

Joint Program in Oceanography/Applied Ocean Science and Engineering
Massachusetts Institute of Technology
And Woods Hole Oceanographic Institution
December 19, 2019

Certified by

Dr. Colleen M. Hansel
Thesis Supervisor
Woods Hole Oceanographic Institution

Certified by

Dr. Scott D. Wankel
Thesis Supervisor
Woods Hole Oceanographic Institution

Accepted by

Dr. Colleen M. Hansel
Chair, Joint Committee for Chemical Oceanography
Woods Hole Oceanographic Institution

New Insights into the Marine Oxygen Cycle from Manganese Oxide Minerals and Reactive Oxygen Species

by

Kevin Michael Sutherland

Submitted to the MIT-WHOI Joint Program in Oceanography and Applied Ocean Science and Engineering on December 19, 2019, in Partial Fulfilment of the Requirements for the Degree of Doctor of Philosophy

Abstract

The redox cycling of oxygen between O_2, water, and intermediate redox states including hydrogen peroxide and superoxide, has profound impact on the availability and distribution of dissolved O_2, the habitability of the marine biosphere, and cellular metabolic and physiological reactions that utilize O_2. The sum total of processes that produce, consume, and exchange atoms with O_2 in the atmosphere, oceans, and subsurface leave their isotopic fingerprints on the abundance of the three stable isotopes of O_2 in the environment. In this thesis, I explore two aspects of the oxygen cycle in the past and present. First, I investigate the ability of manganese (Mn) oxide minerals to capture and retain the oxygen isotopic signature of dissolved O_2 during the oxidation of aqueous Mn(II) to Mn-oxide minerals. I determine that approximately half of the oxygen atoms in Mn(III,IV) oxides are directly incorporated from dissolved oxygen, and use isotope labeling techniques to further constrain how the dissolved oxygen isotope signature may be determined from that of Mn oxides. I perform an in-depth characterization of a ferromanganese crust from the central Pacific and, using triple oxygen isotope measurements, demonstrate that Mn oxides in ferromanganese crusts from around the world retain signatures of dissolved oxygen for at least 30 million years. I next turn to a previously unconsidered aspect of the global oxygen cycle: dark, extracellular superoxide production by marine microbes. I measure extracellular superoxide production rates by some of the ocean's most abundant organisms. I use these rates along with previous measurements to estimate that extracellular superoxide production yields a net sink of 5-19% of marine dissolved oxygen. Ultimately, the degree to which superoxide production is a sink of oxygen lies in the fate of its primary decay product, hydrogen peroxide. I determine the range of oxidative and reductive decay of hydrogen peroxide across a range of environmental conditions in a meromictic pond, thus validating several assumptions from our global estimate. Altogether, this thesis illuminates a path toward investigating the oxygen cycle on million-year timescales in Earth's recent past and demonstrates the importance of microbial superoxide production in the biogeochemical cycling of O_2.

Thesis Supervisor: Dr. Colleen M. Hansel
Title: Associate Scientist, Woods Hole Oceanographic Institution

Thesis Supervisor: Dr. Scott D. Wankel
Title: Associate Scientist, Woods Hole Oceanographic Institution

Acknowledgements

I would like thank my committee, Colleen Hansel, Scott Wankel, and Kristin Bergmann for your academic guidance, feedback, and support in planning and executing my research. Thank you to Collin Ward for chairing my defense.

Thanks to WHOI academic programs office for the many ways you've supported my work at WHOI and facilitated classes, research, and living between MIT and WHOI. Thank you to the wonderful team of admins in MC&G who have provided incredible help and assistance the last five years.

Scott and Colleen, thank you for your mentorship, encouragement, and guidance in matters academic and otherwise over my time at WHOI. You have served as role models in and out of the lab, you gave me the freedom to pursue my own ideas, you have provided me with so many incredible research opportunities on land and at sea, and you have always been fierce advocates. Thank you for not giving up on me in year one when I almost destroyed both of your labs. Thank you for taking meetings at your dining room table and for blurring the lines between your lab children and your real children.

My lab family over the last five years: Emily, Carly, Julia, Tong, Gabi, Net, Jen, Vero, Kalina, and Lina, you've made our time in the office, in the lab, and in the field infinitely more enjoyable. Thank you for your humor, your sarcasm, your time, your help, your understanding, and your willingness to put up with me.

To my many teachers and professors, thank you helping me develop the tools to think and investigate interesting questions. Mr. Harris, thank you for making a time and a place to get excited about scientific concepts and explore my own interest during my high school years. Thank you to my undergraduate professors in GPS who framed so many interesting questions about the natural world and who helped me develop the toolbox to ponder them. Thank you to George Rossman for introducing me to the world of mineralogy, for solidifying my decision to study geology, and for giving me the opportunity to research in your lab. Thank you to Woody Fischer for introducing me to geobiology and for your helpful advice when I started considering graduate school.

To my friends around Boston, Woods Hole, back on the West Coast, and elsewhere, thank you for the board game nights, conversations over coffee, calls and texts, weekend visits, and friendship.

To my family, thank you for your love, support, and encouragement these past 29 years. Mom and Dad, thank you for giving me so many opportunities that have gotten me here today. Thank you for your guidance and wisdom on navigating many of life's big decisions. Thank you for not wishing you had been more specific when you first introduced me to the idea of being a doctor. Amy and Jon, thank you for so many laughs, weekend visits, and being our home base on the East Coast.

Lastly, to my wife, Danielle, thank you for 12+ years of unending support. You've been my partner and teammate through high school chemistry labs, college on opposite coasts, multiple cross-country moves, our first adult jobs, deciding to go back to school, a cancer diagnosis, the adoption of our dog-child Myrtle, and the highs and lows of graduate school. These words of thanks feel small in comparison to all you've been to me.

This work was funded by the following grants and organizations: NASA Earth and Space Science Fellowship (NNX15AR62H), MIT Praecis Presidential Graduate Fellowship, NASA Exobiology (NNX15AM046), NSF-OCE grant 1355720, WHOI Ocean Ventures Fund, MIT Student Assistance Fund, WHOI Academic Programs Office, and the Stanford Synchrotron Radiation Lightsource. Use of the Stanford Synchrotron Radiation Lightsource, SLAC National Accelerator Laboratory, is supported by the U.S. Department of Energy, Office of Science, Office of Basic Energy Sciences under Contract No. DE-AC02-76SF00515.

TABLE OF CONTENTS

1. Introduction

A brief history of life and oxygen

The evolution of oxygenic photosynthesis, and its subsequent rise to a major component of Earth's atmosphere over the past two and half billion years has had profound consequences on life and the geochemistry of surface and subsurface environments that support life. The presence (or lack thereof) and quantity of molecular oxygen in a given environment dictates the energetic limits of the life that inhabits it. Indeed, it is oxygen that has both enabled and directed life to its present complexity (Raymond and Segrè 2006). The evolution and rise of O_2, however, was not an unmitigated boon to life on Earth. The 16th century Swiss toxicologist Paracelsus captures this complexity well:

> "What is there that is not poison? All things are poison and nothing (is) without poison. Solely the dose determines that a thing is not a poison" (Deichmann et al. 1986).

Oxygen is a remedy and poison. It is the most thermodynamically favored electron acceptor under a wide range of environmental conditions. Life is able to harness this energy afforded by these unpaired electrons in aerobic respiration. It is the parallel spin of its two unpaired electrons that makes O_2 a "poison". This electron configuration favors one-electron transfers over concerted multi-electron transfers, producing reactive intermediates known as reactive oxygen species, or ROS (Taverne et al. 2018). Important examples of ROS in the environment are superoxide and hydrogen peroxide. High concentrations have the potential to be harmful to life in the form of oxidative damage to cells, primarily in the form of membrane peroxidation (Tyler 1975). While early adaptation to ROS was essential to survival, subsequent fine-tuning of ROS production and scavenging have been an ultimate evolutionary result of life in oxygen-rich environments. ROS are utilized by organisms for growth and proliferation, wound repair, cell signaling, cell defense, and gene activation (Carlioz and Touati 1986; Lamb and Dixon 1997; Saran 2003a; Buetler et al. 2004; Hansel et al. 2019). The benefits and challenges afforded by life in oxic environments have provided the evolutionary landscape on which microbial live has evolved a suite of cellular machinery for maximizing the benefits and mitigating the harm of oxygen and ROS.

The sum total of cellular reactions that produce and consume O_2, including many reactions that generate ROS, comprise the oxygen cycle. The cycling of oxygen between its oxidized (O_2) and reduced forms (H_2O) shape the climate and the extent of the surface Earth's oxygenation, which in turn shapes the evolutionary landscape on which oxygen consuming (and ROS-producing) cellular processes have evolved. These feedbacks may produce long periods of environmental stability, or, when perturbed or imbalanced, may drastically change surface Earth conditions.

In the thesis that follows, we explore aspects of the oxygen cycle of the modern and recent past with the mindset that a more thorough understanding of the marine oxygen cycle allows for a better understanding of the history and evolution of Earth as well as a better understanding of the underlying microbial processes involved. In the sections that follows, we outline the current understanding of the marine oxygen cycle and the techniques that have allowed this understanding, followed by a brief outline of the chapters to follow.

The Oxygen Cycle

The oxygen cycle consists of the series of biogeochemical sources and sinks of molecular oxygen. When sources and sinks are balanced, the atmospheric concentration of O_2 is unchanging. When small or large imbalances arise and persist in the oxygen cycle, atmospheric concentrations will rise or fall in proportion to the imbalance and the size of the major reservoirs of oxygen. The primary source of oxygen to the atmosphere is oxygenic photosynthesis (Knoll et al. 2012). Eukaryotic and prokaryotic phytoplankton in the global ocean, and higher plants on land produce O_2 as a byproduct of their photoautotrophic metabolism. Oxygen production is near evenly split between the land and sea (Field et al. 1998). UV photolysis of N_2O and water are also sources of O_2 to the atmosphere, but this contribution is several orders of magnitude lower than that of photosynthesis.

The major reductive sinks of O_2 include a suite biologically facilitated redox reactions that serve a wide range of roles. The preeminent sink of oxygen is aerobic respiration, in which cells couple oxygen reduction to substrate oxidation for the purpose of generating ATP to fuel other cellular processes. Photorespiration accounts for the second most significant oxygen loss term in the oxygen cycle. Photorespiration occurs when the enzyme RuBisCO (Ribulose-1,5-bisphosphate carboxylase/oxygenase) uses O_2 as a substrate instead of CO_2 in the reaction with ribulose 1,5-

bisphosphate (RuBP) as part of the normal functioning of the Calvin Cycle. Loss of O_2 through photorespiration may be as high as 30% of gross oxygen production (Guy et al. 1993; Bender et al. 1994). The Mehler reaction is still another significant oxygen sink term, accounting for ~10% of total oxygen sinks (Bender et al. 1994). In the Mehler reaction, O_2 is reduced to superoxide ($O_2^{\bullet-}$) by electrons evolved from reduced ferredoxin in photosystem I in the presence of light (Guy et al. 1993). These three reactions together are thought to comprise the vast majority of oxygen sinks, a notion that we will revisit in Chapter 6. We also acknowledge that the oxygen cycle also has several smaller sink terms including photochemical oxidation (Andrews et al. 2000), anthropogenic oxygen sinks, and the oxidation or atmospheric escape of reduced gases. While these are important on geologic timescales, they comprise a small fraction of the biological oxygen cycle, and we will not consider them in great detail in this thesis.

Much of what we know about the biological cycling of oxygen comes from the observations of minor isotopes, ^{17}O and ^{18}O, and the discrimination of many biological processes against oxygen's heavy isotopes in favor of ^{16}O. The different reaction rates of the three isotopes of oxygen in the oxygen cycle's source and sink reactions produce reactant and product pools that have a different proportion of the three isotopes. This fractionating behavior can be used to fingerprint individual reactions, and can be utilized to determine the relative influence of one or several reactions in a given environment. For decades, analytical limits confined these measurements to the biological fractionation of ^{18}O relative to ^{16}O. As early as the 1930s, Malcolm Dole observed that oxygen in the atmosphere contained more mass than the oxygen in the waters of Lake Michigan. Throughout the 20th century, several studies have quantified the extent to which globally consequential cellular processes discriminate against heavy isotopes (Feldman et al. 1959; Stevens et al. 1975; Guy et al. 1989, 1993; Farquhar et al. 1993). While photosynthesis produces very little isotope fractionation between the reactant water and product oxygen, the processes of respiration, photorespiration, and the Mehler reaction discriminate against ^{18}O by between 10 and 30‰ (Luz and Barkan 2011). The net expression of all these oxygen isotope fractionating processes, named the Dole Effect in recognition of Malcolm Dole's initial observation, were eventually summarized into descriptive models that describe the ~24‰ relative enrichment of ^{18}O in the atmosphere relative to seawater (Bender et al. 1994; Hoffmann et al. 2004).

In more recent decades, increased data collection efforts of oxygen in marine environments, isotope studies of organism isolates, and development of descriptive models have

greatly improved our understanding of oxygen cycling in the ocean (Kroopnick and Craig 1972, 1976; Kroopnick et al. 1972; Kroopnick 1980; Stolper et al. 2018). In the deep ocean, closed-system oxygen consumption by marine microbes produces a monotonic increase in the relative fraction of heavy isotopes of oxygen with decreasing oxygen concentration (Kroopnick and Craig 1976). Triple oxygen isotopes of O_2 (i.e. ^{17}O relative to both ^{18}O and ^{16}O) contains an even greater wealth of information about the state of the biosphere than the Dole effect alone. The triple oxygen isotope composition of tropospheric O_2 is controlled by mass-dependent processes and vertical mixing with the stratosphere where mass-independent exchange reactions occur (Thiemens and Heidenreich 1983; Luz et al. 1999; Blunier et al. 2002). The triple oxygen value of tropospheric O_2 is influenced by the partial pressures of CO_2 and O_2, their biogeochemical fluxes, and atmospheric vertical exchange. This isotope signature is used to determine gross primary productivity in the surface ocean from the mixture of isotopically distinct endmembers (i.e. new photosynthetic oxygen vs. equilibrated atmosphere) (Luz et al. 1999).

There are practical limits to investigating the oxygen isotope signature of tropospheric O_2 in the past. Direct measurements of atmospheric O_2 are largely limited to paleo-atmosphere trapped in ice on continental ice sheets. Records of oxygen isotopes trapped in ice cores have been used to reconstruct the Dole Effect and primary productivity (from triple oxygen) over the past ~100,000 years (Bender et al. 1994; Severinghaus et al. 2009). Measurements of the isotopes of atmospheric O_2 beyond the ice core record are limited to mineral proxies that directly incorporate some atmospheric oxygen into their mineral structure (Crockford et al. 2018). Insights into the history of oxygen afforded by ice core records and mineral proxies from shallow evaporite basins are also largely limited to signals from the bulk atmosphere, and contain no information about the marine environment. In chapters 2-4 of this thesis, we explore one candidate mineral system for its use as an isotope proxy of O_2 in the marine environment: manganese oxides (Mandernack et al. 1995). We explore the oxygen isotope systematics of manganese oxidation via different abiotic and biotic pathways. Additionally, we assess the role of ferromanganese crusts as potential isotopic recorders of dissolved O_2 in the global ocean.

Reactive Oxygen Species

Reactive oxygen species, as briefly mentioned above, are oxygen-containing radicals and intermediates present under a wide range of environmental conditions. These species have

lifetimes ranging from nanoseconds to hours in typical marine system. The most common forms of ROS in marine systems are hydrogen peroxide (H_2O_2), superoxide ($O_2^{\bullet-}/HO_2$), hydroxyl radical ($HO^{\bullet}$), singlet oxygen ($^1O_2$), and carbonate radical ($CO_3^{\bullet-}$). The formation of many ROS within aqueous systems occurs via sequential one-electron transfer reactions (Fridovich 1998). For instance, the ROS $O_2^{\bullet-}$, H_2O_2, and $HO^{\bullet}$ are the intermediates of the sequential one-electron reduction of molecular oxygen to water. ROS play a key role in the remineralization of carbon and the cycling of numerous metals within the ocean (Heller and Croot 2010; Rose 2012; Wuttig et al. 2013).

We focus here on superoxide, and, to a lesser extent, its primary decay product, hydrogen peroxide. Superoxide has a typical lifetime in the ocean on the order of one minute. Superoxide production is already known to play an important role in the oxygen cycle as it is a significant gross and net sink of O_2 in oxygenic phototrophs (Guy et al. 1993; Asada 2006). It is also produced in significant quantities as a byproduct of complexes I and III of the electron transport chain (Chen et al. 2003). The superoxide produced by Mehler and respiration reactions are largely confined within the cell, as cell membranes are highly impermeable to superoxide. In the last two decades, several studies have shown that the scope of superoxide production is not confined to intracellular processes (Kim et al. 2000; Kustka et al. 2005; Learman et al. 2011; Hansel et al. 2012; Diaz et al. 2013). Extracellular superoxide production, or superoxide production by trans-membrane, outer membrane, or extracellular enzymes, occurs across a wide diversity of phototrophs and heterotrophs (Hansel et al. 2012; Andeer et al. 2015; Diaz et al. 2019). There is an increasing recognition that superoxide is an essential molecule required for basic cellular physiology and growth of other plant, animal, and microbial cells (Saran 2003b; Buetler et al. 2004). For instance, extracellular superoxide has been shown to play an important role in cell signaling and growth stimulation in eukaryotes, and cell differentiation in fungi (Buetler et al. 2004; Dickinson and Chang 2011). In higher plants, oxidative bursts play a beneficial role in multiple physiological responses, including antimicrobial defense, oxidative cross-linking of cell walls preceding transcription-dependent defenses in wound repair, and gene activation of various stress responses (Lamb and Dixon 1997).

Despite the growing recognition that most organisms produce extracellular superoxide, and that superoxide plays an important set of roles in cell physiology, the impact of this process on the cycling of oxygen in marine environments has not been assessed. Broadly speaking, significant

superoxide production will influence carbon remineralization and the redox state of a wide range of biologically important redox-active metals. One mole of oxygen that is reduced to superoxide via extracellular superoxide production (as opposed to e.g. respiration) will produce a cascade of chemical reactions in marine waters, and the ultimate fate of superoxide (i.e. oxidize vs reduced) is poorly constrained. Chapters 5-7 aim to address the role extracellular superoxide production in the marine system and as a net sink of oxygen in the marine oxygen cycle.

Overview of this thesis

This thesis examines two major themes of the marine oxygen cycle. Chapters 2, 3, and 4, broadly speaking, examine manganese oxides as potential recorders of the isotopic signature of marine dissolved oxygen. Chapter 2 investigates the oxygen isotope systematics of biological and abiotic manganese oxidation. We perform a series of isotope labeling and closed-system Rayleigh distillation experiments to determine the fraction of oxygen in Mn oxides that is derived from dissolved O_2. We investigate different Mn-oxidizing mechanisms (direct enzymatic oxidation vs. oxidation by ROS production) and determine the extent to which oxygen isotope fractionation varies across these different reaction pathways.

Chapter 3 looks at one common Mn oxide deposit in marine environments: ferromanganese crusts. We use a variety of X-ray techniques to assess characteristics of this ferromanganese crust, including mineralogy, element distribution, metal oxidation state, and change in these properties with increasing depth (age) in the crust. With these measurements, we demonstrate many of the complexities that need to be considered to access the oxygen isotopic record within these crusts.

Guided by the insight of Chapters 2 and 3, Chapter 4 outlines our isotopic analysis of ferromanganese crusts from all major ocean basins. We use triple oxygen isotope measurements to assess the presence of an oxygen isotope signature of O_2 in crust tops and one crust interior to depths corresponding to 30 million years old. We use these findings to construct a model of the oxygen isotope signature in marine ferromanganese crusts and assess some of the challenges that remain in being able to access the oxygen record contained within these mineral deposits.

The second half of this thesis focuses on extracellular superoxide production by marine microbes. The recent identification of widespread extracellular superoxide production raises many questions about the amount of such production in the global ocean and its influence on the marine oxygen cycle. Chapter 5 examines the extracellular superoxide production of some of the ocean's

most abundant phototrophs and heterotrophs. We examine the population dynamics of many of these superoxide-producing organisms and determine the disparity between net and gross superoxide production in culture.

In Chapter 6, we extend the results from Chapter 5 into the context of the global oxygen cycle. We construct an estimate of global superoxide production, and place some constraints of the magnitude of the oxygen sink that results from this process. Finally, in Chapter 7, we address one of the most significant outstanding questions from Chapter 6, investigating the fate of hydrogen peroxide. We use isotopically labeled hydrogen peroxide to determine the proportion of hydrogen peroxide oxidation and reduction that occur across a range of light and oxygen conditions in a local stratified pond with sharp redoxcline. Altogether, Chapters 5-7 make the case that extracellular oxygen reduction is a globally significant oxygen sink with widespread implications on the biogeochemical cycling of oxygen, carbon, and other redox active elements.

References

Andeer, P. F., D. R. Learman, M. McIlvin, J. A. Dunn, and C. M. Hansel. 2015. Extracellular haem peroxidases mediate Mn(II) oxidation in a marine R oseobacter bacterium via superoxide production. Environ. Microbiol. **17**: 3925–3936. doi:10.1111/1462-2920.12893

Andrews, S. S., S. Caron, and O. C. Zafiriou. 2000. Photochemical oxygen consumption in marine waters : A major sink for colored dissolved organic matter? **45**: 267–277.

Asada, K. 2006. Production and scavenging of reactive oxygen species in chloroplasts and their functions. Plant Physiol. **141**: 391–396. doi:10.1104/pp.106.082040

Bender, M., T. Sowers, and L. Labeyrie. 1994. The Dole Effect and its Variations During the Last 130,000 Years as Measured in the Vostok Ice Core. Global Biogeochem. Cycles **8**: 363–376. doi:10.1029/94gb00724

Blunier, T., B. Barnett, M. L. Bender, and M. B. Hendricks. 2002. Biological oxygen productivity during the last 60 , 000 years from triple oxygen isotope measurements. **16**.

Buetler, T. M., A. Krauskopf, and U. T. Ruegg. 2004. Role of superoxide as a signaling molecule. Physiology **19**: 120–123.

Carlioz, A., and D. Touati. 1986. Isolation of superoxide dismutase mutants in Escherichia coli: is superoxide dismutase necessary for aerobic life? EMBO J. **5**: 623–630.

Chen, Q., E. J. Vazquez, S. Moghaddas, C. L. Hoppel, and E. J. Lesnefsky. 2003. Production of reactive oxygen species by mitochondria central role of complex III. J. Biol. Chem. **278**: 36027–36031.

Crockford, P. W., J. A. Hayles, H. Bao, and others. 2018. Triple oxygen isotope evidence for limited mid-Proterozoic primary productivity. Nature **559**: 613–616. doi:10.1038/s41586-018-0349-y

Deichmann, W. B., D. Henschler, B. Holmstedt, and G. Keil. 1986. What is there that is not poison? A study of the Third Defense by Paracelsus. Arch. Toxicol. **58**: 207–213.

Diaz, J. M., C. M. Hansel, B. M. Voelker, C. M. Mendes, P. F. Andeer, and T. Zhang. 2013. Widespread Production of Extracellular Superoxide by Heterotrophic Bacteria. Science (80-.). **340**: 1223–1226. doi:10.1126/science.1237331

Diaz, J. M., S. Plummer, C. M. Hansel, P. F. Andeer, M. A. Saito, and M. R. Mcilvin. 2019. NADPH-dependent extracellular superoxide production is vital to photophysiology in the marine diatom Thalassiosira oceanica. **116**. doi:10.1073/pnas.1821233116

Dickinson, B. C., and C. J. Chang. 2011. Chemistry and biology of reactive oxygen species in signaling or stress responses. Nat. Chem. Biol. **7**: 504.

Farquhar, G. D., J. Lloyd, J. A. Taylor, L. B. Flanagan, J. P. Syvertsen, K. T. Hubick, S. C. Wong, and J. R. Ehleringer. 1993. Vegetation effects on the isotope composition of oxygen in atmospheric CO2. Nature **363**: 439.

Feldman, D. E., H. T. Yost, and B. B. Benson. 1959. Oxygen isotope fractionation in reactions catalyzed by enzymes. Science (80-.). **129**: 146–147.

Field, C. B., M. J. Behrenfeld, J. T. Randerson, and P. Falkowski. 1998. Primary production of the biosphere: Integrating terrestrial and oceanic components. Science (80-.). **281**: 237–240. doi:10.1126/science.281.5374.237

Fridovich, I. 1998. Oxygen toxicity: a radical explanation. J. Exp. Biol. **201**: 1203–1209.

Guy, R. D., J. A. Berry, M. L. Fogel, and T. C. Hoering. 1989. Differential fractionation of oxygen isotopes by cyanide-resistant and cyanide-sensitive respiration in plants. Planta **177**: 483–491.

Guy, R. D., M. L. Fogel, and J. A. Berry. 1993. Photosynthetic Fractionation of the Stable Isotopes

of Oxygen and Carbon. Plant Physiol. **101**: 37–47. doi:10.1104/pp.101.1.37

Hansel, C. M., J. M. Diaz, and S. Plummer. 2019. Tight Regulation of Extracellular Superoxide Points to Its Vital Role in the Physiology of the Globally Relevant Roseobacter Clade. **10**: 1–13.

Hansel, C. M., C. A. Zeiner, C. M. Santelli, and S. M. Webb. 2012. Mn(II) oxidation by an ascomycete fungus is linked to superoxide production during asexual reproduction. Proc. Natl. Acad. Sci. U. S. A. **109**: 12621–12625. doi:10.1073/pnas.1203885109

Heller, M. I., and P. L. Croot. 2010. Kinetics of superoxide reactions with dissolved organic matter in tropical Atlantic surface waters near Cape Verde (TENATSO). J. Geophys. Res. **115**. doi:10.1029/2009jc006021

Hoffmann, G., M. Cuntz, C. Weber, and others. 2004. A model of the Earth ' s Dole effect. **18**: 1–15. doi:10.1029/2003GB002059

Kim, D., A. Nakamura, T. Okamoto, N. Komatsu, T. Oda, T. Iida, A. Ishimatsu, and T. Muramatsu. 2000. Mechanism of superoxide anion generation in the toxic red tide phytoplankton Chattonella marina: Possible involvement of NAD(P)H oxidase. Biochim. Biophys. Acta - Gen. Subj. **1524**: 220–227. doi:10.1016/S0304-4165(00)00161-6

Knoll, A. H., D. E. Canfield, and K. Konhauser. 2012. Fundamentals of geobiology, Wiley Online Library.

Kroopnick, P. 1980. Isotopic Fractionations During Oxygen Consumption and Carbonate Dissolution within the North-Atlantic Deep-Water. Earth Planet. Sci. Lett. **49**: 485–498. doi:10.1016/0012-821x(80)90089-8

Kroopnick, P., and H. Craig. 1972. Atmospheric oxygen: isotopic composition and solubility fractionation. Science (80-.). **175**: 54–55.

Kroopnick, P., and H. Craig. 1976. Oxygen isotope fractionation in dissolved oxygen in the deep sea. Earth Planet. Sci. Lett. **32**: 375–388.

Kroopnick, P., R. F. Weiss, and H. Craig. 1972. Total CO2, 13C, and dissolved oxygen-18O at Geosecs II in the North Atlantic. Earth Planet. Sci. Lett. **16**: 103–110.

Kustka, A. B., Y. Shaked, A. J. Milligan, D. W. King, and F. M. M. Morel. 2005. Extracellular production of superoxide by marine diatoms: Contrasting effects on iron redox chemistry and bioavailability. Limnol. Oceanogr. **50**: 1172–1180. doi:10.4319/lo.2005.50.4.1172

Lamb, C., and R. A. Dixon. 1997. The oxidative burst in plant disease resistance. Annu. Rev. Plant Biol. **48**: 251–275.

Learman, D. R., B. M. Voelker, A. I. Vazquez-Rodriguez, and C. M. Hansel. 2011. Formation of manganese oxides by bacterially generated superoxide. Nat. Geosci. **4**: 95–98. doi:10.1038/ngeo1055

Luz, B., and E. Barkan. 2011. Proper estimation of marine gross O2 production with 17O/16O and 18O/16O ratios of dissolved O2. Geophys. Res. Lett. **38**. doi:10.1029/2011GL049138

Luz, B., E. Barkan, M. L. Bender, M. H. Thiemens, and K. A. Boering. 1999. Triple-isotope composition of atmospheric oxygen as a tracer of biosphere productivity. Nature 547–550. doi:10.1038/22987

Mandernack, K. W., M. L. Fogel, B. M. Tebo, and A. Usui. 1995. Oxygen Isotope Analyses of Chemically and Microbially Produced Manganese Oxides and Manganates. Geochim. Cosmochim. Acta **59**: 4409–4425. doi:10.1016/0016-7037(95)00299-f

Raymond, J., and D. Segrè. 2006. The effect of oxygen on biochemical networks and the evolution of complex life. Science (80-.). **311**: 1764–1767.

Rose, A. L. 2012. The influence of extracellular superoxide on iron redox chemistry and

bioavailability to aquatic microorganisms. Front. Microbiol. **3**: 1–21. doi:10.3389/fmicb.2012.00124

Saran, M. 2003a. To what end does nature produce superoxide? NADPH oxidase as an autocrine modifier of membrane phospholipids generating paracrine lipid messengers. Free Radic. Res. **37**: 1045–1059.

Saran, M. 2003b. To what end does nature produce superoxide? NADPH oxidase as an autocrine modifier of membrane phospholipids generating paracrine lipid messengers. Free Radic. Res. **37**: 1045–1059. doi:10.1080/10715760310001594631

Severinghaus, J. P., R. Beaudette, M. A. Headly, K. Taylor, and E. J. Brook. 2009. Oxygen-18 of O2 records the impact of abrupt climate change on the terrestrial biosphere. Science (80-.). **324**: 1431–1434.

Stevens, C. L. R., D. Schultz, C. Van Baalen, and P. L. Parker. 1975. Oxygen isotope fractionation during photosynthesis in a blue-green and a green alga. Plant Physiol. **56**: 126–129.

Stolper, D. A., W. W. Fischer, and M. L. Bender. 2018. Effects of temperature and carbon source on the isotopic fractionations associated with O2 respiration for 17O/16O and 18O/16O ratios in E. coli. Geochim. Cosmochim. Acta **240**: 152–172. doi:10.1016/j.gca.2018.07.039

Taverne, Y. J., D. Merkus, A. J. Bogers, B. Halliwell, D. J. Duncker, and T. W. Lyons. 2018. Reactive Oxygen Species: Radical Factors in the Evolution of Animal Life: A molecular timescale from Earth's earliest history to the rise of complex life. BioEssays **40**: 1700158.

Thiemens, M. H., and J. E. Heidenreich. 1983. The Mass-Independent Fractionation of Oxygen : A Novel Isotope Effect and its Possible Cosmochemical Implications. **219**: 1073–1075.

Tyler, D. D. 1975. Role of superoxide radicals in the lipid peroxidation of intracellular membranes. FEBS Lett. **51**: 180–183.

Wuttig, K., M. I. Heller, and P. L. Croot. 2013. Reactivity of Inorganic Mn and Mn Desferrioxamine B with O-2, O-2(-), and H2O2 in Seawater. Environ. Sci. Technol. **47**: 10257–10265. doi:10.1021/es4016603

2. Oxygen Isotope Analysis of Bacterial and Fungal Manganese Oxides

This chapter was originally published as:

Sutherland, K. M., S. D. Wankel, and C. M. Hansel. "Oxygen isotope analysis of bacterial and fungal manganese oxidation." *Geobiology* 16.4 (2018): 399-411.

Abstract

The ability of microorganisms to oxidize manganese (Mn) from Mn(II) to Mn(III/IV) oxides transcends boundaries of biological clade or domain. Many bacteria and fungi oxidize Mn(II) to Mn(III/IV) oxides directly through enzymatic activity or indirectly through the production of reactive oxygen species (ROS). Here we determine the oxygen isotope fractionation factors associated with Mn(II) oxidation via various biotic (bacteria and fungi) and abiotic Mn(II) reaction pathways. Since oxygen in Mn(III/IV) oxides may be derived from precursor water and molecular oxygen, we use a two-fold approach to determine the isotope fractionation with respect to each oxygen source. Using both ^{18}O-labeled water and closed-system Rayleigh distillation approaches, we constrain the kinetic isotope fractionation factors associated with O atom incorporation during Mn(II) oxidation to -17.3‰ to -25.9‰ for O_2 and -1.9‰ to +1.8‰ for water. Results demonstrate that stable oxygen isotopes of Mn(III/IV) oxides have potential to distinguish between two main classes of biotic Mn(II) oxidation: direct enzymatic oxidation in which O_2 is the oxidant and indirect enzymatic oxidation in which superoxide is the oxidant. The fraction of Mn(III/IV) oxide-associated oxygen derived from water varies significantly (38 to 62%) among these bio-oxides with only weak relationship to Mn oxidation state, suggesting Mn(III) disproportionation may account for differences in the fraction of mineral-bound oxygen from water and O_2. Additionally, direct incorporation of molecular O_2 suggests that Mn(III/IV) oxides contain a yet untapped proxy of $\delta^{18}O_{O2}$ of environmental O_2, a parameter reflecting the integrated influence of global respiration, photorespiration, and several other biogeochemical reactions of global significance.

2.1 Introduction

The cycling of manganese (Mn) among its naturally occurring redox states is inextricably linked with the biogeochemical cycling of macro- and micro-nutrients on the surface and subsurface of Earth. For example, Mn in the oxygen-evolving complex of photosystem II provides the redox potential needed by photosynthetic organisms to oxidize water and produce O_2 (Iwata & Barber, 2004). Oxides of Mn(III) and/or Mn(IV) in anoxic environments are used as terminal electron acceptors by heterotrophic microbes, and are thus closely linked with the fate of organic matter in terrestrial and marine environments (Ehrlich et al., 2015). Mn(III/IV) oxides are also strong sorbents, serving to scavenge a wide range of materials including organic matter and metal cations, and as such host a great number of elemental proxies of geochemical interest (Ehrlich et al., 2015).

Mn(III/IV) oxide minerals are pervasive throughout a number of surface earth environments. These mineral occurrences include rock varnishes in arid- and aeolian-influenced regions such as deserts, ferromanganese nodules and crusts in pelagic environments, crusts around deep-sea vents, and cave deposits (Mandernack et al., 1995 ; Krinsley et al., 2009). Their precipitation may proceed via direct abiotic oxidation or through the indirect or direct activity of Mn(II)-oxidizing microorganisms, which to date include both bacteria and fungi (Mandernack et al., 1995 ; Learman et al., 2013 ; Learman et al., 2011b ; Learman et al., 2011a ; Andeer et al., 2015 ; Tang et al., 2013 ; Hansel et al., 2012 ; Zeiner, 2015 ; Santelli et al., 2011 ; Tebo et al., 2004 ; Tebo et al., 2005). Based on presumed reaction kinetics, Mn(II) oxidation on Earth is believed to be mediated primarily by microbial activity, but elucidating operative reaction pathways and the contribution of coupled and parallel biotic and abiotic reactions is complex and has remained elusive (Tebo et al., 2005). Additionally, there is no direct evidence that Mn(II) oxidation imparts any metabolic benefit, and the physiological basis for biological Mn(II) oxidation still remains unclear. Further, despite observations of Mn(II) oxidation in suboxic environments, all presently known Mn(II) oxidation pathways rely on the presence of oxygen or other strong oxidants (e.g., reactive oxygen species, ROS) (Clement et al., 2009).

While the mechanisms and consequences of Mn(II) oxidation in marine and terrestrial environments are still active areas of investigation, recent chemical data collected by NASA's Curiosity rover have broadened the implications of Mn oxidation. Several recent studies make a compelling case for the widespread occurrence of Mn oxides on the surface of Mars, suggesting

the Martian atmosphere and subsurface fluids contained significantly more molecular O_2 in the past (Maurice et al., 2016 ; Lanza et al., 2014 ; Lanza et al., 2016 ; Lanza et al., 2015). Given that the evolution of oxygenic photosynthesis preceded the rise of atmospheric oxygen and the widespread occurrence of Mn(III/IV) oxides in the rock record on Earth, the presence of oxidized Mn on the surface of Mars highlights a significant knowledge gap in our understanding of how such oxidizing conditions may arise (Johnson et al., 2016 ; Maurice et al., 2016 ; Lanza et al., 2014 ; Lanza et al., 2016 ; Lanza et al., 2015). Thus, a more nuanced understanding of the cycling of Mn in suboxic and anoxic environments on Earth may provide more perspective for understanding the nature of Mn oxidation on Mars.

While decades of studies have closely examined the oxygen isotope composition of mineral phases including carbonates, sulfates, phosphates, and other oxides, very few studies have investigated the systematics of oxygen isotope compositions in Mn(III/IV) oxides (Hoefs, 2008). Mandernack et al. (1995) showed that different Mn(II) oxidation pathways may impart a pathway-dependent oxygen isotope effect on the precursor oxygen atoms during incorporation into Mn(III/IV) oxide minerals (Mandernack et al., 1995). This study also revealed that biologically catalyzed formation of Mn oxides derive more than 50% of their oxygen atoms from dissolved oxygen (Mandernack et al., 1995). This is in contrast with other low temperature minerals such as iron oxides, carbonates, and phosphates that tend to readily achieve oxygen isotope equilibrium with the water in which they form (Bao & Koch, 1999 ; Bao et al., 2000). Additionally, evidence suggests that Mn(III/IV) oxides, unlike many other low temperature minerals, are resistant to oxygen exchange with water under Earth surface conditions, thereby preserving their fidelity as records of oxidation pathways, environmental conditions, and the isotopic composition of precursor molecules (Mandernack et al., 1995).

In the more than two decades since Mandernack et al. (1995) published their findings, significant strides have been made toward understanding the environmental and biological conditions that lead to Mn(II) oxidation. Unlike other redox active transition metals such as iron (Fe), Mn(II) oxidation via a one electron transfer with molecular oxygen is thermodynamically prohibited at circumneutral pH in the absence of (in)organic catalysts (Tebo et al., 2005 ; Luther, 2010). Three general pathways exist for the oxidation of soluble Mn(II) to insoluble Mn(III/IV)-oxide minerals at circumneutral pH. First, Mn(II) can be oxidized by molecular oxygen (O_2) when complexed to mineral surfaces or organic ligands (Madden & Hochella, 2005 ; Duckworth &

Sposito, 2005). Second, some bacteria and fungi directly catalyze oxidation with outer-membrane or secreted enzymes such as multi-copper oxidases (MCO) that produce extracellular Mn(III/IV) oxides (Zeiner, 2015). Third, the oxidation of Mn(II) to Mn(III/IV) oxides can also occur via reaction with the ROS superoxide ($O_2^{\bullet-}$) of abiotic or biotic origin (Learman et al., 2013 ; Learman et al., 2011a ; Tang et al., 2013 ; Hansel et al., 2012). Extracellular superoxide production, which is ubiquitous in multi-cellular organisms (including fungi), is also widespread throughout the bacterial domain (Aguirre et al., 2005). Superoxide is also formed abiotically through various (photo)reactions with metals, mineral particles, and dissolved organic matter and under anoxic conditions through photolysis of H_2O (Nico et al., 2002 ; Hoigné et al., 1989 ; Gournis et al., 2002).

The recent insights into the nature of Mn(II) oxidation under surface earth conditions give us a much more comprehensive framework to revisit the questions posed by Mandernack et al. (1995). In this study, we explore the oxygen isotope systematics of several direct and indirect biotic Mn(II) oxidation pathways and one abiotic pathway. Using a combination of open system and closed system Mn(II) oxidation experiments, we build on previous studies to determine the source oxygen atoms in Mn oxides and the fractionation factors expressed with respect to incorporation of each of these oxygen sources. We examine whether these fractionation factors may be diagnostic of each unique oxidation pathway or set of oxidation pathways that share similar rate-limiting steps. Additionally, if one or more Mn(II) oxidation reactions with similar fractionation factors is thought to be operative in a given environment, and the oxygen isotope signature is preserved in the mineral phase, variations in $\delta^{18}O_{MnOx}$ may be useful for determining isotopic variations in the $\delta^{18}O$ signature of environmental H_2O or O_2, which may be useful for fingerprinting a number of (bio)geochemical processes. This study of Mn(II) oxidizing reactions surveys a selection of representative Mn(II)-oxidizing organisms from both the bacterial and eukaryotic domains of life, meant to capture a wide breadth of oxygen isotope fractionation factors that might be observed in nature, and provide the necessary context for interpreting natural deposits of Mn(III/IV) oxides.

2.2 Materials and Methods

2.2.1 Approach

While many well characterized oxygen isotope systems in oxygen-bearing minerals focus on water oxygen equilibration, previous work tells us that Mn oxides derive oxygen atoms from multiple sources which include molecular oxygen (or oxygen derivatives including ROS) and water (Mandernack et al., 1995). This understanding of the potential sources of oxygen in Mn(III/IV) oxides gives us the following isotope mass balance:

$$\delta^{18}O_{MnOx} = X_{H_2O}\left(\delta^{18}O_{H_2O} + \varepsilon_{MnOx-H_2O}\right) + X_{O_2}\left(\delta^{18}O_{O_2} + \varepsilon_{MnOx-O_2}\right) \qquad (1)$$

where $\delta^{18}O$ represents the oxygen isotope signature of the Mn oxides, water, and molecular oxygen, X represents the fraction of oxygen from water or molecular oxygen, X_{H_2O} and X_{O_2} sum to 1, and ε represents the kinetic isotope effect with respect to incorporation from each corresponding precursor pool of oxygen atoms. Our approach aims to put multiple independent constraints on equation (1) such that all terms can be directly measured or calculated. Here we expand on previous work investigating the oxygen isotope systematics of Mn(II) oxidation by performing direct measurements of $\varepsilon_{MnOx\text{-}O2}$ in closed-system Rayleigh distillation experiments (Mandernack et al., 1995).

2.2.2 Preparation of biotic and abiotic oxide samples

We investigated the oxygen isotope systematics of Mn oxides from six Mn(II)-oxidizing microbes including three bacteria and three fungi. Bacterial strains include two marine *Alphaproteobacteria*, *Roseobacter* sp. AzwK-3b and *Erythrobacter* sp. SD-21, isolated from a coastal estuary (Hansel & Francis, 2006) and coastal sediment (Tebo et al., 2007), respectively, and dormant spores from a gram-positive bacillus, *Bacillus* sp. strain SG-1, isolated from coastal sediment (Murray & Tebo, 2007). Mn(II)-oxidizing fungi in this study include three filamentous Ascomycete fungi: *Pyrenochaeta* sp. DS3sAY3a, *Stagonospora* sp. SRC11sM3a (both of which were isolated from passive limestone beds treating coal mine drainage in the Appalachian

Mountains), and *Paraconiothyrium sporulosum* AP3s5-JAC2a (isolated from a freshwater pond) (Estes et al., 2016 ; Tang et al., 2013 ; Zeiner, 2015 ; Santelli et al., 2011).

All Mn(II)-oxidizing microbes were cultured using growth media shown to facilitate Mn(II) oxidation in previous studies (Estes et al., 2016 ; Murray & Tebo, 2007). All biogenic oxides produced in this study, save those from *Bacillus* sp. SG-1, were precipitated in cell-free media filtrate with starting Mn(II) concentrations ranging from 100 μM to 250 μM. Both *Alphaproteobacteria* (*Roseobacter and Erythrobacter)* were grown to mid-log phase (as determined by optical density at 600 nm) in 3-4 L cultures on a magnetic stir plate. Cultures were centrifuged at 6,000 *g* for 15 minutes and filtered through a 0.22 μm low protein binding membrane to remove cells. Cell-free filtrate was supplemented with 100 μM $MnCl_2$ and stirred with a magnetic stir plate (400-500 rpm) for 4 days. Cell-free filtrates from both *Alphaproteobacteria* turned semi-transparent yellowish-brown within hours, indicating the formation of colloidal oxides, which ripened to particulate oxides over several days.

Following oxide formation, the oxide particles were allowed to settle to the bottom of the vessel for several hours and the filtrate was decanted. The oxides were washed three times with ultrapure water, submerged in a sonication bath for one hour at 60°C, and washed three additional times with ultrapure water before freezing at -20°C until preparation for analysis. While a more extensive chemical workup has been used to eliminate the influences of organic matter on oxygen isotope analysis of Mn (III/IV) oxides in a previous study, we chose to avoid use of oxidizing agents that might further oxidize these mixed valence oxide minerals (Mandernack et al., 1995).

All three fungal strains were cultured in AY media as described in Estes et al. (2016) with 25-50 μM $MnCl_2$ to serve as a visual indicator of Mn(II) oxidation (Estes et al., 2016). Cultures were grown in 500 mL cultures (in 1L Erlenmeyer flasks) without agitation at room temperature (Santelli et al., 2011). Once each fungal colony secreted its Mn(II)-oxidizing enzyme(s), the culture flask formed a film of Mn oxide particles along the air-media interface. Unlike filtrate from *Roseobacter* and *Erythrobacter*, the fungal filtrates never produced a yellowish-brown hue indicating presence of colloidal particles, but instead produced visibly discernable particles that settled quickly.

Filtrate collection included a coarse filtration with nylon mesh to remove large fungal colonies, and a fine filtration through a 0.45 μm low protein binding membrane to remove remaining cells and pre-formed oxide particles used to indicate release of Mn(II)-oxidizing

enzyme. The cell-free filtrate was supplemented with 250 μM $MnCl_2$ and left on an orbital shaker to react for 4 days (120 rpm). Oxides formed by fungal filtrate were allowed to settle, the solution was decanted, and oxides were washed in the same manner as bacteria-derived oxides described above.

Bacillus cultures were grown at room temperature on an orbital shaker for 4 days in several 1L Erlenmeyer flasks filled with 500 mL of media. Light microscopy was used to confirm that sporulation was widespread in each flask before harvesting spores. During spore harvest and purification, we used an ultrasonic homogenizer (30-60 seconds) to break up spore aggregates between washes. The wet weight of the purified spore pellet was recorded before resuspending the pellet in 50 mL ultra-pure water. The spore slurry was added (90 mg wet weight spore isolate per liter) to HEPES-buffered artificial seawater (pH 7.5) containing 100 μM $MnCl_2$. This spore solution was left on an orbital shaker (120 rpm) for several days, during which Mn oxide particles formed.

Roseobacter and *Erythrobacter* produce Mn(III/IV) oxides via activity of extracellular animal heme peroxidase (AHP) (Andeer et al., 2015). AHP produced by *Roseobacter* has been well characterized and shown to oxidize Mn(II) through superoxide production (Andeer et al., 2015 ; Learman et al., 2011a). Oxides formed via AHP-derived $O_2^{\bullet-}$ using similar methods have been shown to yield hexagonal birnessite colloids, which over the course of several days undergo partial transformation to triclinic birnessite particles (Learman et al., 2011b). The AHP from *Erythrobacter* has been implicated in direct Mn(II) oxidation; however, addition of 50 μM SOD to protein extracts led to a 20% decrease in Mn oxidation activity (Learman et al., 2013 ; Learman et al., 2011a ; Learman et al., 2011b ; Andeer et al., 2015 ; Nakama et al., 2014). The mechanism of Mn(II) oxidation by *Erythrobacter* in cell-free filtrate containing the whole secretome (not concentrated protein extracts) has not been reported. Thus, to provide adequate mechanistic information to interpret our isotopic results, we performed a Mn(II) oxidation assay with superoxide dismutase (SOD, Sigma) to determine the role of superoxide in oxidation by the cell-free filtrate of *Erythrobacter*. This assay involved 100 mL aliquots of cell-free filtrate with 100 μM $MnCl_2$, and SOD additions ranging 0 kU to 50 kU performed in duplicate. Oxidized Mn was quantified using Leucoberbelin Blue colormetric dye (Sigma).

We also investigated oxides produced by three fungal strains, *Pyrenochaeta, Stagonospora,* and *Paraconiothyrium sporulosum*. While previous work is extremely helpful in

identifying the length of time from inoculation to the secretion of Mn(II)-oxidizing enzymes, we found that the timing of this enzyme secretion can vary by up to several days (Zeiner, 2015). In this study cultures of *Pyrenochaeta, Stagonospora,* and *Paraconiothyrium sporulosum* were grown for 25 days, 9 days, and 15 days, respectively. Each culture was harvested within 24 hours of observing widespread formation of oxide particles away from the fungal colonies. The mineral identity of oxides grown from *Pyrenochaeta* and *Stagonospora* using similar liquid media conditions have been shown to be poorly crystalline hexagonal birnessite (Santelli et al., 2011).

Manganese oxidation by *Bacillus* spores is one of two reactions included in this study meant to provide a common thread between this work and that of Mandernack et al. (1995) (Mandernack et al., 1995). *Bacillus* cells were grown and spores were collected and purified using similar methods presented in Rosson and Nealson (1987) with modifications made by Murray and Tebo (2007) to remove any preformed Mn oxides formed in culture (Rosson & Nealson, 1982 ; Murray & Tebo, 2007). Previous studies show that oxides formed using these methods are a poorly-crystalline hexagonal phyllomanganate (presumably birnessite) (Murray & Tebo, 2007). To minimize any O atom contribution from the more substantial organic matter content within the spore-precipitated Mn oxides we used a more involved chemical treatment. Oxides from *Bacillus* were washed in the same manner as described for other bacterial oxides, followed by a 12-hour treatment in 2.5% hypochlorite solution (at 4ºC), and three additional washes with ultrapure water before being frozen at -20ºC.

To provide a second common thread between our study and that presented in Mandernack et al. (1995), we synthesized abiotic Mn oxide under alkaline conditions using similar methods presented in their study. Equal volumes of 6M NaOH and 0.5M $MnCl_2$ were sparged for 30 mins with lab air and combined in a single vessel while being vigorously stirred. The mixture was sparged with lab air for several hours in an ice bath, at which point the oxides were collected and washed 10 times with 200mL of ultra-pure water. This oxide synthesis method has been shown to yield a 10Å birnessite-like structure that collapses irreversibly to 7Å spacing upon drying, typically referred to as buserite (Post, 1999 ; Mandernack et al., 1995).

2.2.3 Closed system Mn Oxidation

Closed-system Rayleigh oxidation experiments, for determination of kinetic isotope effects during incorporation of O atoms from dissolved oxygen (see below), were prepared using the same

media and solutions described in the synthesis section above with slight modification. Prior to the filtration step, each oxidizing solution was sparged with filtered room air through a glass frit for 30 minutes to ensure dissolved O_2 was at saturation. Following filtration, oxidizing solutions were aseptically transferred to 160mL serum vials and crimp-sealed (using gray butyl septa) with no headspace. Typical analyses included 8-10 individual vials. Addition of 1M $MnCl_2$ was conducted by syringe to achieve final concentrations between 0μM and 500μM Mn(II). Serum vials were incubated at room temperature on an orbital shaker at 120 rpm for 1-4 days before oxygen isotope analysis of the remaining dissolved O_2 pool.

2.2.4 Oxygen Isotope Analysis of Mn oxides

Oxide samples were lyophilized and weighed into silver boats with ~1mg of preconditioned carbon black to catalyze high-temperature conversion to CO. All $\delta^{18}O_{MnOx}$ measurements were collected with an IsoPrime100 continuous-flow isotope ratio mass spectrometer (IRMS) coupled to an Elementar pyro-CUBE elemental analyzer configured for pyrolysis at 1450°C. Typical precision achieved for Mn oxides is ±0.4‰. This method produced acceptable oxygen yields, which ranged from 31.9 to 38.5 weight percent (compare to 36.8% for MnO_2, see Table 3). The fractions of oxygen in Mn oxides derived from water and O_2, X_{H_2O} and X_{O_2}, were determined by performing each mineral synthesis under 2-3 $\delta^{18}O_{H_2O}$ values ranging from approximately -5‰ to +40‰ (oxygen isotope values in this study are reported relative to VSMOW). All $\delta^{18}O$ water measurements were made using a Picarro L1102-i Isotopic Water Liquid Analyzer at Brown University's Environmental Chemistry Facilities, with typical precision (1σ) of < 0.2‰.

2.2.5 Oxygen Isotope Analysis of Dissolved Oxygen

All O_2 samples from closed-system Rayleigh Distillation experiments were measured using an IsoPrime100 IRMS modified with a manual gas injection port upstream of a packed 2m molecular sieve (5Å) gas chromatography column (1/16" OD) for separation of O_2 and N_2 peaks prior to introduction into the IRMS. A 2m Nafion dryer with a dry helium purged jacket was used just after the injection port to remove water vapor in the sample. Prior to analysis, 5mL of ultra-high purity helium was introduced to each sample vial and equilibrated on its side for a minimum

of 30 minutes on an orbital shaker (120 rpm). All samples were run against a single point calibration of lab air and check standard consisting of ultra-pure water to verify equilibrium $\delta^{18}O$ values (~0.7‰) were achieved (Benson & Krause, 1984). This IsoPrime 100 uses multiple collectors for simultaneous collection of signal intensities at *m/z* 32, 33, 34 and 40 without peak jumping. O_2:Ar ratios were used to determine the relative O_2 consumption from Mn oxidation. After Scott and others (2004), we used a modified treatment of the traditional Rayleigh equation to solve for $\varepsilon_{MnOx\text{-}O_2}$ (Scott et al., 2004). The traditional Rayleigh equation is as follows:

$$\frac{^{18}R}{^{18}R_o} = \left(\frac{C}{C_o}\right)^{^{18}\alpha - 1} \qquad (2)$$

Where ^{18}R represents the initial or instantaneous oxygen isotope ratio, C represents the initial or instantaneous concentration of dissolved oxygen (or in this case O_2:Ar ratio), and $^{18}\alpha$ is the oxygen isotope effect associated with Mn oxidation. Solving for an isotope effect using this equation places significant weight on the starting isotope ratio and O_2:Ar value, and can compound measurement uncertainty when the starting measurement has approximately the same uncertainty as each subsequent measurement (Scott et al., 2004). To avoid additional error in our Rayleigh distillation experiments, we used a slightly modified form of the equation:

$$\ln\left(^{18}R\right) = \left(^{18}\alpha - 1\right)\ln(C) - \left(^{18}\alpha - 1\right)\ln(C_o) + \ln\left(^{18}R_o\right) \qquad (3)$$

The two constant terms in this modified Rayleigh equation, $(^{18}\alpha-1)\ln(C_o)$ and $\ln(^{18}R_o)$, can be ignored for the purpose of determining the slope of this linearized equation, $(^{18}\alpha-1)$; this eliminates the concern of weighing initial values more than any other data point. We solved for $^{18}\alpha$ (and its corresponding uncertainty) using the York method with the parameters $\ln(^{18}R)$ and $\ln(C)$ (York et al., 2004 ; Scott et al., 2004 ; Mandernack et al., 1995). Although we used this modified treatment to calculate $^{18}\alpha$, all Rayleigh distillation plots are shown using traditional axes ($\ln(R/R_o)$ vs. $\ln(C/C_o)$) to avoid confusion.

2.2.6 X-ray Absorption Spectroscopy

Mn oxides were analyzed by X-ray absorption near-edge structure (XANES) spectroscopy to determine oxidation state of Mn in each oxide sample. Spectra were collected at beamline 4-3 or 11-2 at the Stanford Synchrotron Radiation Lightsource (SSRL) with Si(111) monochromator (Φ = 90º) and Si(220) monochromator (Φ = 90º), respectively. Manganese K-edge fluorescence was measured with a Lytle, Germanium, or Passivated Implanted Planar Silicon (PIPS) detector. All XANES spectra collected as part of this study were averaged over 2-4 scans and background subtracted using the SIXPack software package (Webb, 2005). The average oxidation state was calculated using linear least-squares fitting of Mn reference spectra with each relevant whole-number oxidation state: $MnCl_2$, feitknechtite (β-MnOOH), and δ-MnO_2 for Mn(II), Mn(III), and Mn(IV), respectively (Learman et al., 2011b). We note that due to structural influences on the Mn XANES white line, linear combination fitting provides only an estimate of the average Mn oxidation state. Previous investigations have defined the 1σ error estimates to be 1.7%, 2.6%, and 2.9% for Mn(II), Mn(III), and Mn(IV), respectively (Bargar et al., 2005).

2.3 Results

2.3.1 Manganese Oxidation Assay for Erythrobacter sp. SD-21

The enzymes involved in each oxidation pathway as described above are provided in Table 1. While AHP have been attributed to direct Mn(II) oxidation pathway in protein extracts for *Erythrobacter*, oxidation mechanisms in the cell free filtrate as prepared here are unknown. We found a clear concentration dependent inhibition of Mn(II) oxidation by SOD within the *Erythrobacter* cell-free filtrate (Figure 1). Specifically, Mn(II) oxidation decreased by >95% with the addition of 50kU SOD to 100 mL *Erythrobacter* filtrate amended with 100 μM Mn(II) (Figure 1). This evidence indicates that Mn(II) oxidation by *Erythrobacter* cell-free filtrate is performed by AHP-derived superoxide and not direct enzymatic oxidation under these conditions.

2.3.2 XANES Analysis

The average oxidation state of these samples ranged from 3.5 to 3.9 (Table 2). Oxides derived from fungi *Paraconiothyrium sporulosum, Pyrenochaeta,* and *Stagonospora* produced oxides with average Mn oxidation states of 3.65, 3.75, and 3.53 respectively. Oxides derived from

AHP activity yielded average oxidation states of 3.86 and 3.68 for *Roseobacter* and *Erythrobacter,* respectively. *Bacillus* and alkaline oxidation yielded average oxidation states of 3.58 and 3.56, respectively.

2.3.3 Oxygen Isotope Analysis of Mn(III/IV) Oxides

Values for X_{H_2O}, $\varepsilon_{MnOx\text{-}H_2O}$, and $\varepsilon_{MnOx\text{-}O_2}$ for the seven Mn(III/IV) oxides of biotic and abiotic origin indicate a number of key features (Table 2). First, the isotope effect associated with O atom incorporation is very large with respect to O_2, while rather small, on the order of a few permil, with respect to water. Second, the fraction of Mn oxide associated oxygen that derived from water ranged from 38.4% to 61.6%, with lower values associating with oxides produced by AHP activity (Table 1).

These seven oxidation reactions appeared to reflect two distinct behaviors with respect to $\varepsilon_{MnOx\text{-}O_2}$ arising from either direct oxidation or indirect oxidation via ROS (Table 1). The first of these groups contains *Bacillus, Pyrenochaeta, Paraconiothyrium sporulosum, Stagonospora,* and Mn(II) oxidation in NaOH, all of which involve electron transfer to O_2 not $O_2^{\bullet-}$. Measured $\varepsilon_{MnOx\text{-}O_2}$ values for this group range from -20.9‰ to -25.9‰ (Table 1) and Rayleigh distillation experiment results are shown in Figure 3. Control samples without Mn(II) exhibited negligible O_2 consumption in these five synthesis pathways, indicating that any peripheral reactions involving O_2 and possible metabolites in the filtrate did not measurably contribute to the observed consumption of O_2.

Roseobacter and *Erythrobacter* produced oxygen isotope fractionation results that are similar to each other, but notably distinct from the other biotic and abiotic oxidation patterns (Table 1). In contrast to the abiotic, fungal, and *Bacillus* Mn(II) oxidation pathways, cell-free filtrate from *Roseobacter* and *Erythrobacter* bacterial cultures underwent a significant drawdown of dissolved O_2 in the absence of Mn(II). The pseudo-first order rates of O_2 consumption for both organisms in the absence of Mn(II) were -0.0124 hr^{-1} and -0.0098 hr^{-1} for *Roseobacter* (Figure 4) and *Erythrobacter,* respectively. This O_2 consumption yielded an $\varepsilon_{MnOx\text{-}O_2}$ of -19.6‰ and -19.8‰ for *Roseobacter* and *Erythrobacter,* respectively (Figure 5). In the presence of Mn(II), O_2 consumption is also notable, but the $\varepsilon_{MnOx\text{-}O_2}$ changed throughout the course of the reaction. Pseudo-first order rates for O_2 loss in the presence of 100 μM Mn(II) were -0.0047 hr^{-1} for

Roseobacter and -0.0402 hr^{-1} for *Erythrobacter*. The $\varepsilon_{MnOx\text{-}O_2}$ values for initial O_2 loss start at -17.7‰ and -17.3‰ for *Roseobacer* and *Erythrobacter,* respectively, and gradually decrease in magnitude with reaction progress.

2.4 Discussion

Our results reflect a range of oxygen isotope fractionation values that appear to be explained in large part by known or putative oxidation pathways. Here we explore the relationships and underlying mechanisms that result in the observed oxygen isotope systematics in these seven Mn(II)-oxidizing reactions, focusing on the behavior of dissolved oxygen, water oxygen, and Mn oxidation state as it relates to each system. Finally, we discuss the broader implications of these findings and its potential application to natural Mn(III/IV) oxide sample.

Foremost, the fractionation associated with O atom incorporation from O_2 during Mn(II) oxidation, $\varepsilon_{MnOx\text{-}O2}$, reveals an informative window into the nature of these various oxidation reactions. The four organisms (*Bacillus, Pyrenochaeta, Paraconiothyrium sporulosum,* and *Stagonospora*) that oxidize Mn(II) through direct enzymatic activity exhibit a fairly narrow range (-20.9‰ to -23.1‰) for values of $\varepsilon_{MnOx\text{-}O_2}$. The putative enzymes involved in fungal Mn(II) oxidation are bifunctional solanapyrone synthase and/or an unspecified FAD-binding protein for *Pyrenochaeta*, bilirubin oxidase for *Stagonospora*, and GMC oxidoreductase and/or bilirubin oxidase for *Paraconiothyrium sporulosum* (Zeiner et al., 2016 ; Zeiner, 2015). Mn(II) oxidation by *Bacillus* occurs via direct oxidation by a multicopper oxidase, mnxG, present in the exosporium of dormant *Bacillus* spores. Despite the apparent disparate functionality of these four enzymes, Mn(II) oxidation by these four organisms produces a narrow range of $\varepsilon_{MnOx\text{-}O_2}$ values, a finding that underscores likely mechanistic similarity. While the consistency of this $\varepsilon_{MnOx\text{-}O_2}$ value among disparate Mn(II)-oxidizing enzymes has not been directly observed previously, it is consistent with a model of Mn(II) oxidation that is kinetically controlled by O_2 (Luther, 2005). At circumneutral pH, Mn(II) exists as a hexaquo complex, with waters of hydration freely exchanged with a mean lifetime on the order of 10^{-8} seconds (Helm & Merbach, 1999). Because the highest occupied molecular orbital (HOMO) of Mn(II) and the lowest unoccupied molecular orbital (LUMO) of O_2 are a poor symmetry match, the coordination of dissolved O_2 is considered to be rate-limiting in Mn(II) oxidation (Luther, 2005). Complexation of Mn(II) with a Mn(II)-binding site of each of

these enzymes distorts the d-orbitals, allowing for a greater symmetry match between the interacting orbitals of Mn (II) and O_2, permitting oxidation to proceed (Luther, 2005).

The largest value for $\varepsilon_{MnOx\text{-}O_2}$ (-25.9‰) is produced by direct oxidation of Mn(II) by O_2 in NaOH. At high pH, water molecules in a Mn(II) hexaquo complex will freely interchange with hydroxyl ions. This exchange will produce molecular orbital geometry that is readily accessible to electron transfer with O_2, and oxidation of Mn(II) is rapid (Luther, 2005). While there are very few natural environments to which we might reasonably compare the extreme alkalinity of these reaction conditions, this reaction does serve as a likely kinetic end-member of the most extreme fractionation that might be expected. Another possible explanation for this elevated $\varepsilon_{MnOx\text{-}O_2}$ (and the high variability in Figure 3e) may be mixed-phase (solid and aqueous) oxidation. Mn(II), upon being added to a NaOH solution, quickly forms a precipitate of $Mn(OH)_2$ and Mn(II) oxidation occurs at the precipitate surface. If oxidation of $Mn(OH)_2$ is faster than O_2 diffusion in water, the expressed $\varepsilon_{MnOx\text{-}O_2}$ value may be slightly larger than the intrinsic isotope effect of Mn(II) oxidation as a result of Rayleigh distillation occurring in a poorly mixed system.

Under the conditions employed here, the cell-free filtrate of both *Alphaproteobacteria* oxidizes Mn(II) through indirect AHP activity. In the case of *Roseobacter*, it has been demonstrated that AHP activity produces $O_2^{\bullet-}$, which serves as the oxidant for Mn(II) (Learman et al., 2011b ; Andeer et al., 2015 ; Learman et al., 2011a). A previous study proposed that extracellular AHP from *Erythrobacter* may oxidize Mn(II) by a two-fold mechanism including direct enzymatic oxidation and $O_2^{\bullet-}$ production (Nakama et al., 2014). Under the conditions we used here, however, the sole oxidation mechanism in cell-free filtrate from *Erythrobacter* is via $O_2^{\bullet-}$ (Figure 1). Given the similarity to the Roseobacter filtrate and the fact that AHPs are abundant within the Erythrobacter exoproteome (Estes et al., 2016), $O_2^{\bullet-}$ is presumably derived from AHP activity.

A significant complication to performing Rayleigh distillation experiments on these two bacterial systems is that even in the absence of Mn(II), $O_2^{\bullet-}$ is still being produced by AHP and consumed from either $O_2^{\bullet-}$ dismutation or reaction of $O_2^{\bullet-}$ with components of the filtrate (i.e. carbon metabolites or metals). We can interpret $\varepsilon_{MnOx\text{-}O_2}$ of O_2 in the absence of Mn(II) in one of two ways: the intrinsic kinetic isotope effect of O_2 consumption by AHP or the net isotope effect of O_2 consumption and subsequent O_2 regeneration. The former would require that all generated

$O_2^{\bullet-}$ be irreversibly lost from the system without regeneration of O_2, while the latter requires some O_2 to be partially regenerated during dismutation of $O_2^{\bullet-}$. In either case, unamended media filtrate (no Mn(II)) from both organisms yielded a constant $\varepsilon_{MnOx\text{-}O_2}$ value (-19.6‰, -19.8‰) over the course of O_2 consumption. The close agreement between the ε values of O_2 consumption by enzymatic $O_2^{\bullet-}$ production of *Roseobacter* and *Erythrobacter* under different culture conditions (different salinity, media recipes) again underscores likely mechanistic similarity of ROS formation and cycling within the filtrate of these two organisms.

The consumption of O_2 that is not associated with Mn(II) oxidation makes it difficult to constrain $\varepsilon_{MnOx\text{-}O_2}$ with the same clarity with which we were able to measure $\varepsilon_{MnOx\text{-}O_2}$ from the direct enzymatic oxidation pathways. The presence of 100 μM Mn(II) produces notable changes in $\varepsilon_{MnOx\text{-}O_2}$ as observed from the residual oxygen pool (Figure 5). The first 10-20% of O_2 depletion occurs with $\varepsilon_{MnOx\text{-}O_2}$ of -17.7‰ and -17.3‰, for *Roseobacter* and *Erythrobacter*, respectively. Beyond 10-20% O_2 depletion, the slope of the Rayleigh plots shallows to produce lower net values for $\varepsilon_{MnOx\text{-}O_2}$. This bend in the slope of the Rayleigh distillation data (plotted as $\ln(O_2/Ar)$ vs $\ln(^{18}R)$) indicates that these systems violate the assumption of irreversibility of the Rayleigh distillation model and that some regeneration of O_2 must be involved. The addition of Mn(II) produced opposite effects on the two filtrates; 100 μM Mn(II) enhanced the loss of O_2 in *Erythrobacter* filtrate, but decreased the net O_2 loss rate in *Roseobacter* filtrate. This complex behavior is likely the result of a combination of biotic and abiotic factors that influence Mn(II) oxidation, including $O_2^{\bullet-}$ and H_2O_2 production rate, the presence of templating molecules, light, media chemistry, mineral colloid characteristics, and many others (Learman et al., 2011b ; Learman et al., 2011a ; Learman et al., 2013).

The question remains how to interpret $\varepsilon_{MnOx\text{-}O_2}$ in these systems that oxidize Mn(II) through production of $O_2^{\bullet-}$. Since we cannot simultaneously quantify the reaction rates and isotope composition of all ROS in solution, the most straightforward approach is to accept the $\varepsilon_{MnOx\text{-}O_2}$ value when O_2 levels are still relatively high, very little Mn(II) has been oxidized, and back reactions reforming O_2 are insignificant with respect to the dissolved O_2 pool. Using this framework, these values, -17.7‰ and -17.3‰ for *Roseobacter* and *Erythrobacter,* respectively, are our best estimates for the predicted open system behavior of the net isotope effect on O_2 during

Mn(II) oxidation. The close correspondence of $\varepsilon_{MnOx\text{-}O_2}$ values for *Roseobacter* and *Erythrobacter* reaffirm our findings that the cell-free filtrate of *Roseobacter* and *Erythrobacter* oxidize Mn(II) via superoxide production. The two systems, however, deviate in $\varepsilon_{MnOx\text{-}O_2}$ in the presence of Mn(II) as O_2 becomes depleted and Mn is oxidized (Figure 5). We suggest this behavior arises from the oxidation of ROS (coupled with the reduction of oxidized Mn), returning a fraction of the O_2 that was lost from AHP activity back to the O_2 pool.

In determining these $\varepsilon_{MnOx\text{-}O_2}$ values for *Roseobacter* and *Erythrobacter* (Table 1) we implicitly assume that Mn(II) is the only sink of $O_2^{\bullet-}$ until appreciable oxidized Mn initiates the back reaction of $O_2^{\bullet-}$ to O_2. Additionally, we suggest that oxygen atoms are assimilated into the Mn-O complex that will eventually precipitate as an oxide. Indeed, our finding that 61-62% of oxygen in Mn(III/IV) oxides formed via AHP-derived $O_2^{\bullet-}$ originates from sources that are not water requires direct incorporation of molecular O_2 or $O_2^{\bullet-}$. Dissolved $O_2^{\bullet-}$ oxidizes Mn(II) to Mn(III), with the first step in this reaction proceeding as the formation of MnO_2^+ (Wuttig et al., 2013). The fate of MnO_2^+, including subsequent redox reactions yielding Mn(III/IV) oxides, is not well characterized, and may be highly dependent on the availability of complexing ligands and other environmental factors (Wuttig et al., 2013). Once formed, Mn(III) and Mn(III) complexes may be oxidized or reduced by $O_2^{\bullet-}$ (Learman et al., 2013). Likewise, $O_2^{\bullet-}$ dismutation and other decay pathways can produce H_2O_2, which can reduce Mn(III) species, again yielding Mn(II) and O_2 (Learman et al., 2013). Mn(III) species may undergo further oxidation by O_2 (Learman et al., 2013). If Mn(III) oxidation by O_2 is operative after Mn(II) is oxidized by $O_2^{\bullet-}$, the isotope effect of this second step would not be readily extracted from the experiment setup we use here. Still another pathway of Mn(III) loss is disproportionation, which may yield dissolved Mn(II) and Mn oxides without requiring additional consumption of O_2 or $O_2^{\bullet-}$. In summary, these short-lived ROS and other reactive intermediates produce a rapid, cryptic oxygen cycle. While we are able to constrain the source and relative contributions of each source of the Mn-bound oxygen, more detailed concentration and rate information (especially of reactive intermediate species) will help improve kinetic models and corresponding prediction of oxygen isotope ratios.

While we originally hypothesized that average oxidation state, which ranged from 3.5 to 3.9, would scale with the fraction of oxygen derived from O_2, we found only a modest correlation ($R^2 = 0.4$) (Figure 6). The lack of a strong correlation between the average Mn oxidation state of Mn(III/IV) oxides and X_{O2} implicates multiple electron transfer mechanisms involved in each

individual oxidation pathway, including electron transfer between Mn(II) and the oxidant and Mn(III) disproportionation into Mn(II) and Mn(IV) (Figure 7). Additionally, surface catalyzed oxidation and comproportionation may also play a role in these systems (Hem, 1981). The oxidation of Mn(II) to Mn(III) is controlled by the interaction between complexed or aqueous Mn(II) and either O_2 or $O_2^{\bullet-}$, but the oxidation of Mn(III) to Mn(IV) may result from further interaction with O_2, $O_2^{\bullet-}$, or Mn(III) disproportionation into Mn(II) and Mn(IV) species. Previous work has shown that oxygen atoms in Mn(III/IV) oxides derived from Mn(III) disproportionation in the form of hausmannite (Mn_3O_4) originate entirely from water (Learman et al., 2013 ; Mandernack et al., 1995). Additionally, there may be intermediate species that undergo some oxygen isotope exchange with water. A higher proportion of Mn(III) disproportionation could explain why some samples (such as *Bacillus* or alkaline conditions) have higher percentages of oxygen derived from water.

The calculated oxygen isotope effect with respect to water, $\varepsilon_{MnOx\text{-}H_2O}$, is much lower than our empirically derived values of $\varepsilon_{MnOx\text{-}O_2}$, though does exhibit a range of ~±2‰. This variation might represent true fractionation with respect to water, propagated error from individual measurements, or an artifact of oxygen contributions from small amounts interlayer water or adsorbed organic matter. If the water incorporated into Mn(III/IV) oxides is derived directly from the hydration shell of the Mn(II) hexaquo complex, we might expect an equilibrium isotope effect between free water and waters of hydration to account for all or some of the magnitude of observed $\varepsilon_{MnOx\text{-}H_2O}$ values. While previous studies have attempted to calculate equilibrium isotope effects in the hydration shell of dissolved metals, no such studies have attempted to determine the oxygen isotope effect of Mn(II) water solvation (Driesner et al., 2000 ; Bopp et al., 1974). Our finding suggests that oxygen atoms incorporated into Mn(III/IV) oxides from water have a similar isotopic composition as the water in which it formed.

The previous report of 32% and 40% for the fraction of oxygen deriving from O_2 for chemical precipitation (high pH) and *Bacillus* spores, respectively (Mandernack et al., 1995), compare reasonably well with our 42% and 38% for the same two mechanisms, respectively. While results from *Bacillus* are remarkably similar, those from the high pH chemical precipitation vary by 10% and may result from slightly modified protocol (i.e. sparging with lab air vs. pure O_2). While the mass balance solutions for $\varepsilon_{MnOx\text{-}O_2}$ and $\varepsilon_{MnOx\text{-}H_2O}$ presented in Mandernack et al.

(1995) are non-unique since they did not independently constrain $\varepsilon_{MnOx\text{-}O_2}$, those measurements are nevertheless consistent with the overall direction and magnitude of $\varepsilon_{MnOx\text{-}O_2}$ and $\varepsilon_{MnOx\text{-}H_2O}$ values determined in this study.

2.4.1 Assessment of Oxygen Isotope Equilibrium

Oxygen-bearing mineral phases widely precipitate with isotopic compositions closely related to isotopic equilibrium with ambient water (e.g.,(Hoefs, 2009 ; Bao & Koch, 1999 ; Bao et al., 2000)). In contrast, our results confirm that this is not the case for Mn oxides. Specifically, the fact that X_{H_2O} does not equal 1 in any of the seven Mn(II)-oxidizing systems explored in this study confirms that Mn(III/IV) oxides do not precipitate in oxygen isotope equilibrium with water. The remaining oxygen must be derived from another source, which evidence suggests to be O_2. Nevertheless, we need to consider the extent to which the values measured and calculated in this study are influenced by isotope equilibrium exchange. Zheng used a semi-theoretical technique for calculating the reduced partition function of metal oxides and hydroxides by indexing mineral lattice parameters to those of a known mineral (Zheng, 1991 ; Zheng, 1998). Included in these calculations were the Mn (hydr)oxides pyrolusite (MnO_2) and pyrochroite ($Mn(OH)_2$). While these minerals cannot be considered substitutes for the phyllomanganates synthesized in our study, they can provide a close analogy to the Mn(IV)-O and Mn(II)-OH bonding environment in the biogenic and abiotic Mn(III/IV) oxide synthesis. The calculated values for $1000\ln\alpha_{mineral\text{-}water}$ (which is approximately equal to ε) for pyrolusite (MnO_2) and pyrochroite ($Mn(OH)_2$) at 298K are 9.5‰ and 7.9‰, respectively, with ^{18}O favoring the mineral phase in both cases (Zheng, 1991 ; Zheng, 1998). In other words, if the phyllomanganates we synthesized in this study formed in isotope equilibrium with water, we would expect $\varepsilon_{MnOx\text{-}H_2O}$ to be ~+8-9‰ and X_{H_2O} to be 1. Thus, considering our results, we see no evidence of such an equilibrium isotope enrichment in the oxygen derived from water in any synthetic Mn(III/IV) oxides – and therefore remain confident that the dynamics presented above arise from kinetic isotope effects. We note that further study and exploration of natural Mn(III/IV) oxide deposits are necessary to determine if authigenic Mn(III/IV) oxides undergo oxygen isotope exchange on geologically relevant time scales.

2.4.2 Extension to the Environment

The results of these combined open and closed system experiments provide a framework within which oxygen isotope measurements can be interpreted, given full consideration of the known complexity and limitations of $\delta^{18}O_{MnOx}$. First, in order to determine $\varepsilon_{MnOx\text{-}O_2}$ from a natural sample, some independent constraint must be placed on the $\delta^{18}O_{H_2O}$ in which the oxide formed. Second, the tendency of natural samples to co-precipitate with iron oxides and adsorb a wide range of dissolved and particulate species also means that purification or high spatial resolution of natural samples is essential. Third, the equilibration of oxygen atoms in Mn(III/IV) oxides with environmental water over geologic timescales requires further evaluation. Mandernack et al. (1995) addressed this question with one multi-year study in which oxides were placed in water of enriched ^{18}O for up to two years at 50°C. They reported no significant oxygen isotope exchange between the water and oxide, save a small enrichment in todorokite, possibly resulting from physical trapping in its tunnel structure as opposed to oxygen exchange with the Mn-O octahedral complex.

There is great potential within the $\delta^{18}O_{MnOx}$ record for shedding light on fluctuations in $\delta^{18}O_{O_2}$ on both a region and global scale. Identifying and exploring potential high-fidelity proxies of $\delta^{18}O_{O_2}$, such as Mn(III/IV) oxides, are essential to provide detailed perspectives on oxygen cycling in the past. We know that the current $\delta^{18}O_{O_2}$ value of our atmosphere, 23.88‰, has been dynamic in the limited history that is accessible to measurement (Barkan & Luz, 2005 ; Bender et al., 1994). This ^{18}O enrichment arises from a suite of biogeochemical reactions that preferentially consume light oxygen, and include respiration, photorespiration, and the Mehler reaction (Bender et al., 1994). Fluctuations of $\delta^{18}O_{O_2}$ can arise with major fluctuations in global biogeochemical cycling of oxygen including gross and net primary productivity, ocean circulation, and major climatic and tectonic events. Studies aimed at determining the extent to which this biogeochemical signal has fluctuated over time have turned to paleo-atmospheric gas bubbles trapped in ice cores. Bender et al. (1994) revealed a greater than 1‰ fluctuation in atmospheric $\delta^{18}O_{O_2}$, and demonstrated that these fluctuations had a structure that was not unlike modeled insolation changes resulting from Earth's precession. Ice cores, however, only allow us to look as far back as several hundred thousand years, and no such proxy for $\delta^{18}O_{O_2}$ exists to extend this record deeper into

Earth's history where fluctuations in global biogeochemical cycling of oxygen is almost certainly more dramatic.

Mn(III/IV) oxides in seafloor ferromanganese crusts present perhaps the most tractable path forward to measuring the natural $\delta^{18}O_{MnOx}$ record. Ferromanganese crusts in the Pacific offer a near 100 million year record of their formation environment, far exceeding that available in ice cores (Klemm et al., 2005). Marine environments offer some ability to independently constrain $\delta^{18}O_{H_2O}$ back in time. Seafloor oxygen levels can range from well-ventilated to anoxic, and Mn oxidation has been observed to proceed at oxygen levels as low as 5% saturation (Tebo, 1991). Using a respiration oxygen isotope effect of -20‰, we would expect a dynamic range in bottom water $\delta^{18}O_{O_2}$ of over 24‰ for oxygen levels ranging from 100% to 30% saturation (using Rayleigh model). This range far exceeds the ~6‰ range in observed oxygen isotope effect of Mn oxidation in this study. The effect of variability in $\varepsilon_{MnOx\text{-}O_2}$ may in fact be quite small if a single oxidation process dominates in marine environments. Variations in $\delta^{18}O_{MnOx}$ arising from changes in deep ocean oxygen saturation could be attributed to local or global biogeochemical events impacting marine production, respiration, and deep ocean ventilation. As such, future research will target the characterization and isotopic analysis of ferromanganese crusts.

2.5 Summary and Conclusion

We employed a two-pronged isotopic approach to constrain the oxygen source and fractionation factors associated with oxygen incorporation into Mn(III/IV) oxides. This approach combined measurements of the product oxide and the residual oxidant pool to fully constrain the oxygen isotope mass balance of Mn oxide production. With these techniques, we investigated the oxygen isotope behavior of six previously characterized microorganisms, including both bacteria and fungi that oxidize Mn(II) through either direct enzymatic activity or enzymatic production of ROS, and one abiotic oxidation pathway that has been previously characterized.

The fraction of oxygen derived from molecular O_2 varied from 38 to 62%, with the largest values associating with Mn oxides from *Roseobacter* and *Erythrobacter*, both of which produce Mn(III/IV) oxides via extracellular $O_2^{\bullet-}$ production. At the opposite end of this range sits the spore-forming *Bacillus*, which derives 38% of its oxygen from O_2. This set of findings suggests that oxidation by higher energy oxidants such as $O_2^{\bullet-}$ may lead to more direct incorporation of the

oxidant ($O_2^{\bullet-}$ or O_2), while enzymatically driven oxidation appears to result in higher levels of Mn(III) disproportionation during formation of Mn(III/IV) oxides. The magnitude of the fractionation factors with respect to dissolved O_2 in every case we observed was significantly larger (-17.3‰ to -25.9‰) than the calculated fractionation with respect to oxygen in water (-1.9‰ to +1.8‰), which is consistent with the rate-limiting nature of $O_2^{\bullet-}$ or O_2 in each of these cases.

The framework we present in this study is foundational to interpreting $\delta^{18}O_{MnOx}$ in natural environments. While this variation in fractionation factors and the fraction of oxygen derived from O_2 suggests that this technique may not be field-ready for implicating a specific oxidation pathway in natural environments where Mn(III/IV) oxides are common, there is a very clear opening for using this technique as a more uniformitarian approach. Specifically, in environments where Mn(II) oxidation is slow, continuous and presumably formed by the same oxidation process (i.e. abyssal regions of the world's oceans, Martian surface), it may be possible to use Mn(III/IV) oxides to extract a historical record of variations in $\delta^{18}O_{O_2}$.

Figures

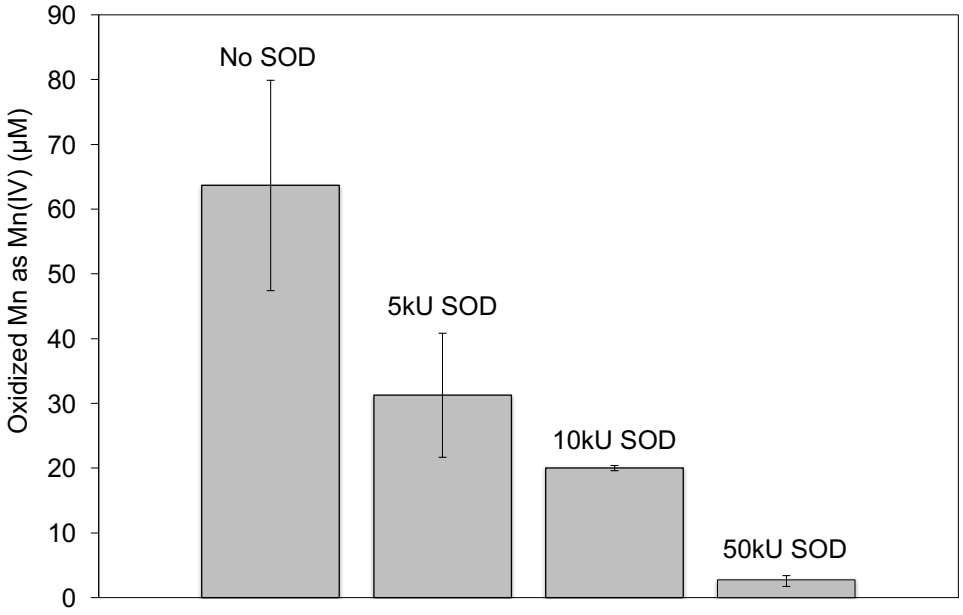

Figure 1- Mn(II) oxidized by *Erythrobacter* sp. SD-21 after 96 hours of incubation as determined using Leucoberbelin Blue (LBB) colormetric dye. Assay was performed with 100mL cell-free media filtrate amended with 100 µM Mn(II) and 0kU, 5kU, 10kU, or 50kU of superoxide dismutase (SOD).

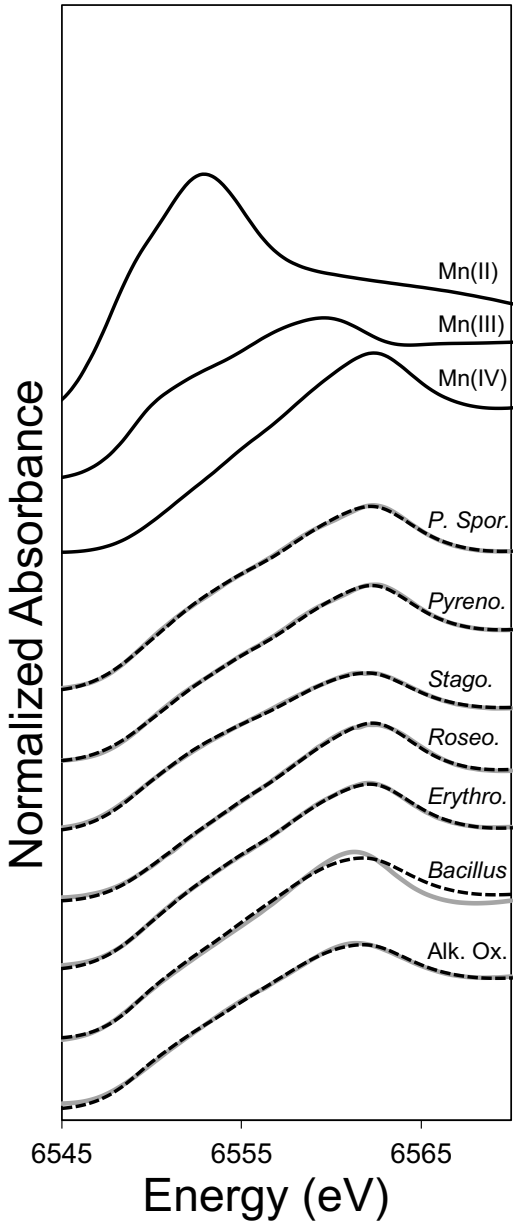

Figure 2- Results of linear least-squares fitting of XANES spectra of biogenic and abiotic oxides. Standard spectra in descending order (solid black line): $MnCl_2$, Feitnechtite (β-MnOOH), and δ-MnO_2. Sample spectra in descending order (solid gray line): *Paraconiothyrium sporulosum*, *Pyrenochaeta*, *Stagonospora*, *Roseobacter*, *Erythrobacter*, *Bacillus*, and Alkaline oxidation. The results of each least-squares fit (dashed black line) is plotted over each sample spectrum.

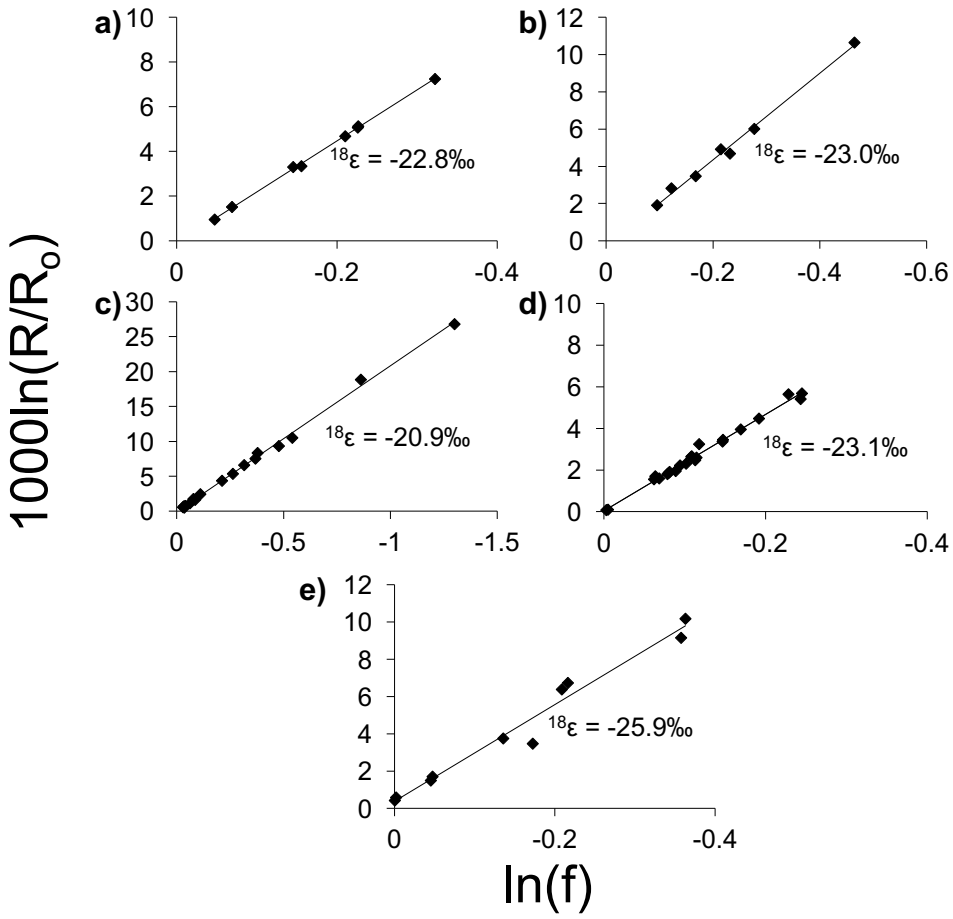

Figure 3- Rayleigh distillation plots for the determination of $^{18}\varepsilon_{MnOx\text{-}O_2}$ for a) *Paraconiothyrium sporulosum,* b) *Pyrenochaeta,* c) *Stagonospora*, d) *Bacillus*, and e) Alkaline oxidation. Slopes are calculated from $\ln(O_2/Ar)$ vs. $1000\ln(^{18}R)$, but plotted as ln(f) vs. $1000(^{18}R/^{18}R_o)$.

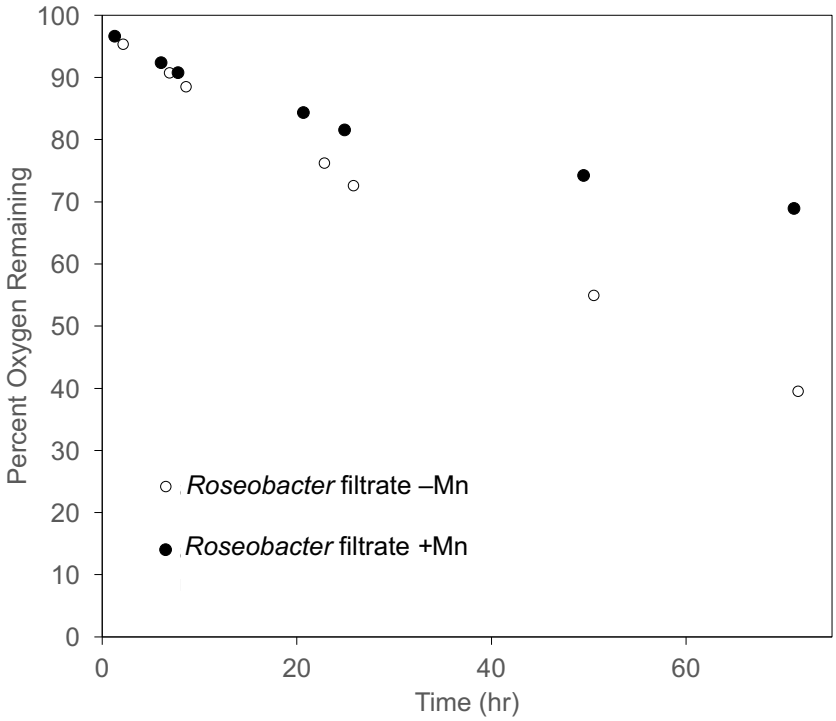

Figure 4- O_2 concentration (given as percent O_2 remaining) versus time (hours) for *Roseobacter* cell-free media filtrate in the presence and absence of 100 µM Mn(II). Pseudo-first order O_2 reactions rate constants are -0.0124 hr^{-1} without Mn(II) and -0.0047 hr^{-1} with 100 µM Mn(II).

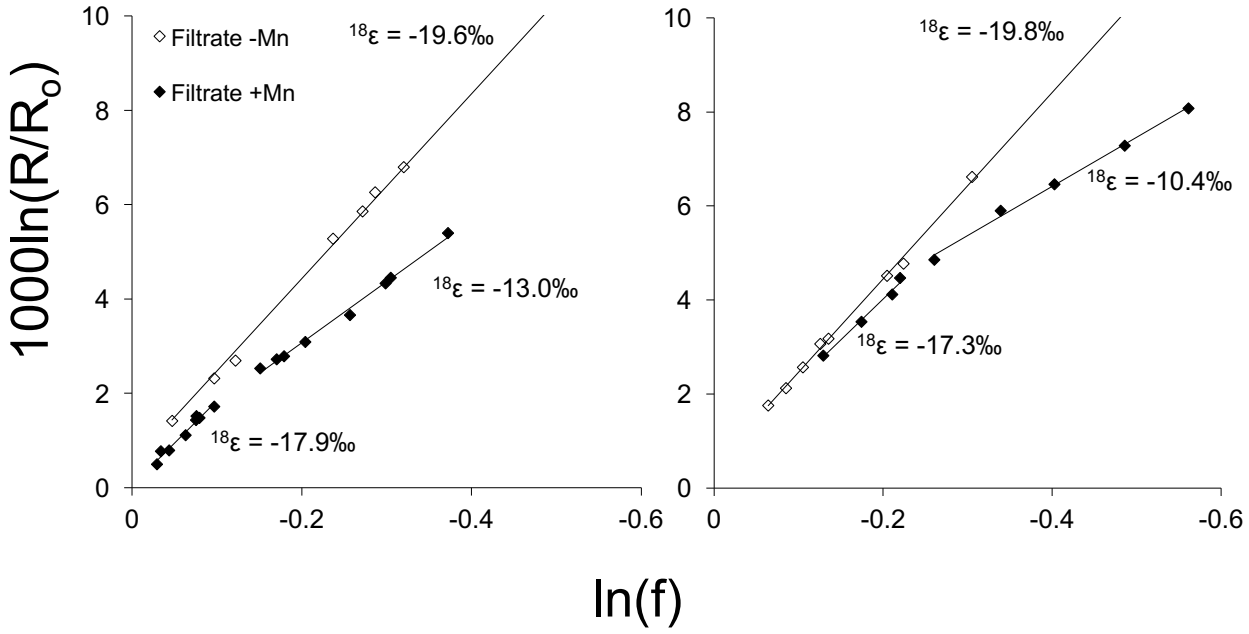

Figure 5- Rayleigh distillation plots for the determination of $^{18}\varepsilon_{MnOx\text{-}O_2}$ for *Roseobacter* (left) and *Erythrobacter* (right). Open diamonds indicate Rayleigh distillation behavior of cell-free filtrate in the absence of Mn(II), closed diamonds indicate the Rayleigh distillation behavior of cell-free filtrate in the presence of 100 μM Mn(II).

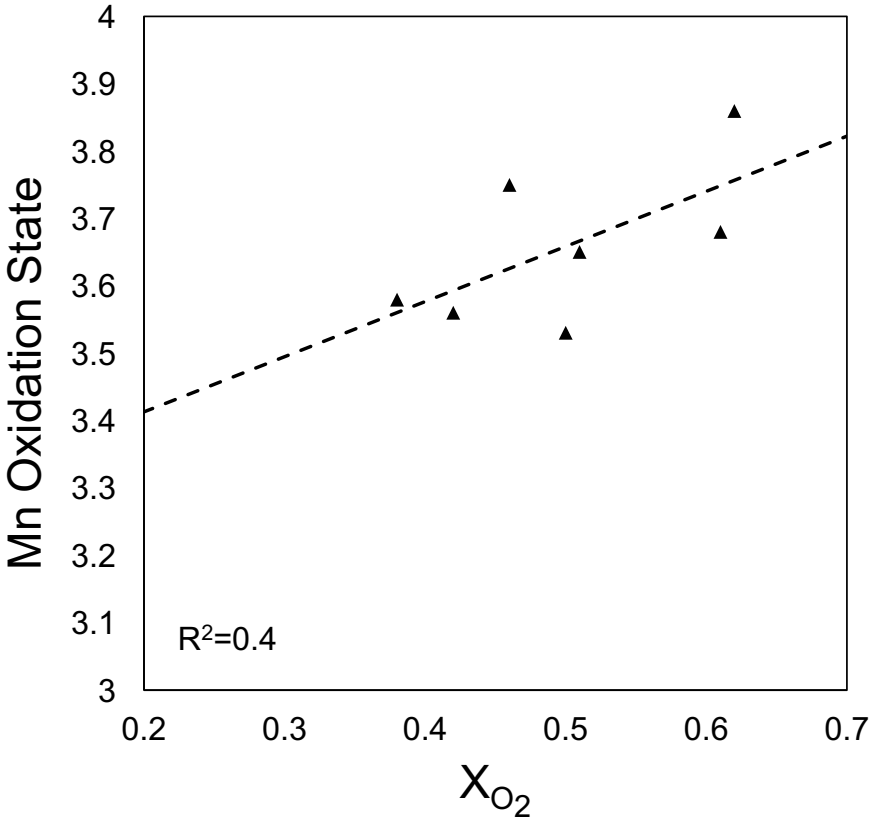

Figure 6- Average Mn oxidation states plotted as a function of the fraction of oxygen derived from O_2 (X_{O2}). Equation of best-fit line: $y = 0.82x + 3.2$.

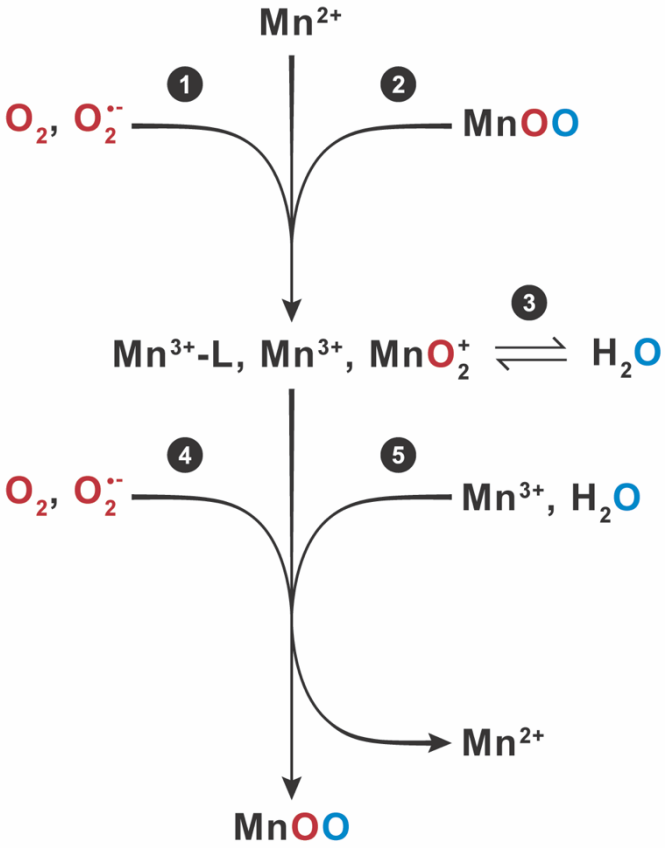

Figure 7- Schematic representation of possible oxygen atom incorporation steps that produce the observed values for X_{H_2O} and X_{O_2}. The oxidation from Mn(II) to Mn(III) requires the presence of an oxidant, O_2 or $O_2^{\bullet-}$ (Reaction 1), or may proceed through a comproportionation reaction if sufficient oxide is present (Reaction 2). The form(s) of aqueous Mn(III) are not well characterized, but may be present as a ligand-bound species, aqueous species, or oxygen-associated complex, which presents the possibility of oxygen atom exchange with water (Reaction 3). Mn(III) is oxidized to Mn(IV) via a second electron transfer with O_2 or $O_2^{\bullet-}$ (Reaction 4), or through Mn(III) disproportionation (Reaction 5). Since Mn(III) disproportionation produces Mn(IV) without interacting with O_2 or $O_2^{\bullet-}$, the Mn oxides formed from disproportionation will derive oxygen atoms from water.

Tables

Table 1-Summary of measured and calculated oxygen isotope parameters for Mn oxidation

Mn-oxidizing system	Organism type	Implicated Enzyme	$^{18}\varepsilon_{MnOx\text{-}O_2}$ (‰)	X_{H_2O}*	$^{18}\varepsilon_{MnOx\text{-}H_2O}$ (‰)	1σ of $^{18}\varepsilon_{MnOx\text{-}H_2O}$
Paraconiothyrium sporulosum	Fungus	GMC oxidoreductase, bilirubin oxidase	-22.8	0.49	+0.5	±0.6
Pyrenochaeta	Fungus	Bifunctional solanapyrone synthase, FAD-binding protein	-23.0	0.54	-1.3	±0.3
Stagonospora	Fungus	bilirubin oxidase	-20.9	0.50	-0.6	±1.2
Roseobacter	Bacterium	AHP ($O_2^{\bullet-}$)	-17.7	0.38	-1.9	±0.6
Erythrobacter	Bacterium	AHP ($O_2^{\bullet-}$)	-17.3	0.39	-0.7	±0.7
Bacillus	Bacterium	*mnxG*	-23.1	0.62	-1.1	±1.0
Alkaline Oxidation	N/A	N/A	-25.9	0.58	+1.8	±1.1

*$X_{O_2} = 1 - X_{H2O}$

Table 2-Summary of Mn XANES fits

Sample	Components			Statistics			Average Oxidation State of Fit
	δ-MnO_2	β-MnOOH	$MnCl_2$	Sum	R-factor	χ^2	
Paraconiothyrium sporulosum	0.776	0.148	0.104	1.028	0.0003	0.16	3.65
Pyrenochaeta	0.825	0.117	0.070	1.012	0.0004	0.17	3.75
Stagonospora	0.577	0.256	0.089	0.922	0.0003	0.11	3.53
Roseobacter	0.844	0.074	0.031	0.949	0.0005	0.23	3.86
Erythrobacter	0.747	0.200	0.060	1.007	0.00004	0.02	3.68
Bacillus	0.585	0.410	0.003	0.998	0.0111	3.97	3.58
Alkaline Oxidation	0.548	0.377	0.018	0.943	0.0008	0.32	3.56

Table 3-Summary of Mn oxide oxygen isotopes

Sample	$\delta^{18}O_{H2O}$ (VSMOW)	1σ of $\delta^{18}O_{H2O}$	$\delta^{18}O_{MnOx}$ (VSMOW)	1σ of $\delta^{18}O_{H2O}$	n	Average weight % Oxygen
Pyrenochaeta	-5.35	0.02	-3.08	0.43	6	
Pyrenochaeta	15.78	0.02	8.16	0.37	6	35.4
Pyrenochaeta	36.90	0.07	19.79	0.58	6	
P. sporulosum	-5.44	0.02	-1.81	0.18	6	38.5
P. sporulosum	37.00	0.09	19.11	0.52	6	
Stagonospora	-4.87	0.09	-0.96	0.84	5	
Stagonospora	16.16	0.09	9.22	0.50	6	32.9
Stagonospora	37.16	0.21	19.81	0.59	4	
Roseobacter	-4.93	0.07	1.32	0.25	5	
Roseobacter	13.03	0.06	8.53	0.60	5	35.7
Roseobacter	32.64	0.13	15.71	0.34	5	
Erythrobacter	-5.08	0.07	2.66	0.54	3	
Erythrobacter	16.88	0.02	10.35	0.17	6	31.9
Erythrobacter	39.35	0.07	19.57	0.26	6	
Alkaline	-5.10	0.22	-2.79	0.68	6	
Alkaline	23.85	0.24	14.06	0.37	6	35.7
Alkaline	45.17	2.28	25.89	0.23	6	
Bacillus SG-1	-6.53	0.06	-4.56	0.82	6	
Bacillus SG-1	13.76	0.05	9.49	1.48	6	37.8
Bacillus SG-1	33.94	0.11	20.53	0.36	6	

References

Aguirre, J., M. Rios-Momberg, D. Hewitt, and W. Hansberg. 2005. Reactive oxygen species and development in microbial eukaryotes. Trends Microbiol. **13**: 111–118. doi:10.1016/j.tim.2005.01.007

Andeer, P. F., D. R. Learman, M. McIlvin, J. A. Dunn, and C. M. Hansel. 2015. Extracellular haem peroxidases mediate Mn(II) oxidation in a marine R oseobacter bacterium via superoxide production. Environ. Microbiol. **17**: 3925–3936. doi:10.1111/1462-2920.12893

Bao, H. M., and P. L. Koch. 1999. Oxygen isotope fractionation in ferric oxide-water systems: Low temperature synthesis. Geochim. Cosmochim. Acta **63**: 599–613. doi:10.1016/s0016-7037(99)00005-8

Bao, H. M., P. L. Koch, and M. H. Thiemens. 2000. Oxygen isotopic composition of ferric oxides from recent soil, hydrologic, and marine environments. Geochim. Cosmochim. Acta **64**: 2221–2231. doi:10.1016/s0016-7037(00)00351-3

Bargar, J. R., S. M. Webb, and B. M. Tebo. 2005. EXAFS, XANES and in-situ SR-XRD characterization of biogenic manganese oxides produced in sea water. Phys. Scr. **T115**: 888–890.

Barkan, E., and B. Luz. 2005. High precision measurements of O-17/O-16 and O-18/O-16 ratios in H2O. Rapid Commun. Mass Spectrom. **19**: 3737–3742. doi:10.1002/rcm.2250

Bender, M., T. Sowers, and L. Labeyrie. 1994. The Dole Effect and its Variations During the Last 130,000 Years as Measured in the Vostok Ice Core. Global Biogeochem. Cycles **8**: 363–376. doi:10.1029/94gb00724

Benson, B. B., and D. Krause. 1984. The concentration and isotopic fractionation of oxygen dissolved in freshwater and seawater in equilibrium with the atmosphere. Limnol. Oceanogr. **29**: 620–632.

Bopp, P., K. Heinzinger, and P. C. Vogel. 1974. Calculations of the oxygen isotope fractionation between hydration water of cations and free water. Zeitschrift für Naturforsch. A **29**: 1608–1613.

Clement, B. G., G. W. Luther, and B. M. Tebo. 2009. Rapid, oxygen-dependent microbial Mn(II) oxidation kinetics at sub-micromolar oxygen concentrations in the Black Sea suboxic zone. Geochim. Cosmochim. Acta **73**: 1878–1889. doi:10.1016/j.gca.2008.12.023

Driesner, T., T.-K. Ha, and T. M. Seward. 2000. Oxygen and hydrogen isotope fractionation by hydration complexes of Li+, Na+, K+, Mg 2+, F−, Cl−, and Br−: a theoretical study. Geochim. Cosmochim. Acta **64**: 3007–3033.

Duckworth, O. W., and G. Sposito. 2005. Siderophore-manganese(III) interactions. I. Air-oxidation of manganese(II) promoted by desferrioxamine B. Environ. Sci. Technol. **39**: 6037–6044. doi:10.1021/es050275k

Ehrlich, H. L., D. K. Newman, and A. Kappler. 2015. Ehrlich's Geomicrobiology, CRC press.

Estes, E. R., P. F. Andeer, D. Nordlund, S. D. Wankel, and C. M. Hansel. 2016. Biogenic manganese oxides as reservoirs of organic carbon and proteins in terrestrial and marine environments. Geobiology.

Gournis, D., M. A. Karakassides, and D. Petridis. 2002. Formation of hydroxyl radicals catalyzed by clay surfaces. Phys. Chem. Miner. **29**: 155–158. doi:10.1007/s002690100215

Hansel, C. M., and C. A. Francis. 2006. Coupled photochemical and enzymatic Mn(II) oxidation pathways of a planktonic Roseobacter-like bacterium. Appl. Environ. Microbiol. **72**: 3543–3549. doi:10.1128/aem.72.5.3543-3549.2006

Hansel, C. M., C. A. Zeiner, C. M. Santelli, and S. M. Webb. 2012. Mn(II) oxidation by an ascomycete fungus is linked to superoxide production during asexual reproduction. Proc. Natl. Acad. Sci. U. S. A. **109**: 12621–12625. doi:10.1073/pnas.1203885109

Helm, L., and A. E. Merbach. 1999. Water exchange on metal ions: experiments and simulations. Coord. Chem. Rev. **187**: 151–181. doi:10.1016/s0010-8545(99)90232-1

Hem, J. D. 1981. Rates of Manganese Oxidation in Aqueous Systems. Geochim. Cosmochim. Acta **45**: 1369–1374. doi:10.1016/0016-7037(81)90229-5

Hoefs, J. 2009. Stable isotope geochemistry, Sixth Edit. Springer-Verlag.

Hoigné, J., B. C. Faust, W. R. Haag, F. E. Scully Jr, and R. G. Zepp. 1989. Aquatic humic substances as sources and sinks of photochemically produced transient reactants, *In* ACS Publications.

Iwata, S., and J. Barber. 2004. Structure of photosystem II and molecular architecture of the oxygen-evolving centre. Curr. Opin. Struct. Biol. **14**: 447–453. doi:10.1016/j.sbi.2004.07.002

Johnson, J. E., S. M. Webb, C. Ma, and W. W. Fischer. 2016. Manganese mineralogy and diagenesis in the sedimentary rock record. Geochim. Cosmochim. Acta **173**: 210–231. doi:10.1016/j.gca.2015.10.027

Klemm, V., S. Levasseur, M. Frank, J. R. Hein, and A. N. Halliday. 2005. Osmium isotope stratigraphy of a marine ferromanganese crust. Earth Planet. Sci. Lett. **238**: 42–48. doi:10.1016/j.epsl.2005.07.016

Krinsley, D., R. I. Dorn, and B. DiGregorio. 2009. Astrobiological Implications of Rock Varnish in Tibet. Astrobiology **9**: 551–562. doi:10.1089/ast.2008.0238

Lanza, N. L., W. W. Fischer, R. C. Wiens, and others. 2014. High manganese concentrations in rocks at Gale crater, Mars. Geophys. Res. Lett. **41**: 5755–5763. doi:10.1002/2014gl060329

Lanza, N. L., A. M. Ollila, A. Cousin, and others. 2015. Understanding the signature of rock coatings in laser-induced breakdown spectroscopy data. Icarus **249**: 62–73. doi:10.1016/j.icarus.2014.05.038

Lanza, N. L., R. C. Wiens, R. E. Arvidson, and others. 2016. Oxidation of manganese in an ancient aquifer, Kimberley formation, Gale crater, Mars. Geophys. Res. Lett. **43**: 7398–7407.

Learman, D. R., B. M. Voelker, A. S. Madden, and C. M. Hansel. 2013. Constraints on superoxide mediated formation of manganese oxides. Front. Microbiol. **4**: 11. doi:10.3389/fmicb.2013.00262

Learman, D. R., B. M. Voelker, A. I. Vazquez-Rodriguez, and C. M. Hansel. 2011a. Formation of manganese oxides by bacterially generated superoxide. Nat. Geosci. **4**: 95–98. doi:10.1038/ngeo1055

Learman, D. R., S. D. Wankel, S. M. Webb, N. Martinez, A. S. Madden, and C. M. Hansel. 2011b.

Coupled biotic-abiotic Mn(II) oxidation pathway mediates the formation and structural evolution of biogenic Mn oxides. Geochim. Cosmochim. Acta **75**: 6048–6063. doi:10.1016/j.gca.2011.07.026

Luther, G. W. 2005. Manganese(II) oxidation and Mn(IV) reduction in the environment - Two one-electron transfer steps versus a single two-electron step. Geomicrobiol. J. **22**: 195–203. doi:10.1080/01490450590946022

Madden, A. S., and M. F. Hochella. 2005. A test of geochemical reactivity as a function of mineral size: Manganese oxidation promoted by hematite nanoparticles. Geochim. Cosmochim. Acta **69**: 389–398. doi:10.1016/j.gca.2004.06.035

Mandernack, K. W., M. L. Fogel, B. M. Tebo, and A. Usui. 1995. Oxygen Isotope Analyses of Chemically and Microbially Produced Manganese Oxides and Manganates. Geochim. Cosmochim. Acta **59**: 4409–4425. doi:10.1016/0016-7037(95)00299-f

Maurice, S., S. M. Clegg, R. C. Wiens, and others. 2016. ChemCam activities and discoveries during the nominal mission of the Mars Science Laboratory in Gale crater, Mars. J. Anal. At. Spectrom. **31**: 863–889. doi:10.1039/c5ja00417a

Murray, K. J., and B. M. Tebo. 2007. Cr(III) is indirectly oxidized by the Mn(II)-Oxidizing bacterium Bacillus sp strain SG-1. Environ. Sci. Technol. **41**: 528–533. doi:10.1021/es0615167

Nakama, K., M. Medina, A. Lien, J. Ruggieri, K. Collins, and H. A. Johnson. 2014. Heterologous Expression and Characterization of the Manganese-Oxidizing Protein from Erythrobacter sp Strain SD21. Appl. Environ. Microbiol. **80**: 6837–6842. doi:10.1128/aem.01873-14

Nico, P. S., C. Anastasio, and R. J. Zasoski. 2002. Rapid photo-oxidation of Mn(II) mediated by humic substances. Geochim. Cosmochim. Acta **66**: 4047–4056. doi:10.1016/s0016-7037(02)01001-3

Post, J. E. 1999. Manganese oxide minerals: Crystal structures and economic and environmental significance. Proc. Natl. Acad. Sci. U. S. A. **96**: 3447–3454. doi:10.1073/pnas.96.7.3447

Rosson, R. A., and K. H. Nealson. 1982. Manganese Binding and Oxidation by Spores of a Marine Bacillus. J. Bacteriol. **151**: 1027–1034.

Santelli, C. M., S. M. Webb, A. C. Dohnalkova, and C. M. Hansel. 2011. Diversity of Mn oxides produced by Mn(II)-oxidizing fungi. Geochim. Cosmochim. Acta **75**: 2762–2776. doi:10.1016/j.gca.2011.02.022

Scott, K. M., X. Lu, C. M. Cavanaugh, and J. S. Liu. 2004. Optimal methods for estimating kinetic isotope effects from different forms of the Rayleigh distillation equation. Geochim. Cosmochim. Acta **68**: 433–442. doi:10.1016/s0016-7037(03)00459-9

Tang, Y. Z., C. A. Zeiner, C. M. Santelli, and C. M. Hansel. 2013. Fungal oxidative dissolution of the Mn(II)-bearing mineral rhodochrosite and the role of metabolites in manganese oxide formation. Environ. Microbiol. **15**: 1063–1077. doi:10.1111/1462-2920.12029

Tebo, B. M. 1991. Manganese(II) Oxidation in the Suboxic Zone of the Black-Sea. Deep. Res. Part a-Oceanographic Res. Pap. **38**: S883–S905. doi:10.1016/s0198-0149(10)80015-9

Tebo, B. M., J. R. Bargar, B. G. Clement, G. J. Dick, K. J. Murray, D. Parker, R. Verity, and S.

M. Webb. 2004. Biogenic manganese oxides: Properties and mechanisms of formation. Annu. Rev. Earth Planet. Sci. **32**: 287–328. doi:10.1146/annurev.earth.32.101802.120213

Tebo, B. M., B. G. Clement, and G. J. Dick. 2007. Biotransformations of manganese, p. 1223–1238. *In* Manual of Environmental Microbiology, Third Edition. American Society of Microbiology.

Tebo, B. M., H. A. Johnson, J. K. McCarthy, and A. S. Templeton. 2005. Geomicrobiology of manganese(II) oxidation. Trends Microbiol. **13**: 421–428. doi:10.1016/j.tim.2005.07.009

Webb, S. M. 2005. SIXpack: a graphical user interface for XAS analysis using IFEFFIT. Phys. Scr. **T115**: 1011–1014.

Wuttig, K., M. I. Heller, and P. L. Croot. 2013. Reactivity of Inorganic Mn and Mn Desferrioxamine B with O-2, O-2(-), and H2O2 in Seawater. Environ. Sci. Technol. **47**: 10257–10265. doi:10.1021/es4016603

York, D., N. M. Evensen, M. L. Martinez, and J. D. Delgado. 2004. Unified equations for the slope, intercept, and standard errors of the best straight line. Am. J. Phys. **72**: 367–375. doi:10.1119/1.1632486

Zeiner, C. 2015. Role of the secretome in manganese and carbon oxidation by filamentous ascomycete fungi. Harvard University.

Zeiner, C. A., S. O. Purvine, E. M. Zink, and others. 2016. Comparative Analysis of Secretome Profiles of Manganese(II)-Oxidizing Ascomycete Fungi. PLoS One **11**. doi:10.1371/journal.pone.0157844

Zheng, Y. F. 1991. Calculation of Oxygen Isotope Fractionation in Metal-Oxides. Geochim. Cosmochim. Acta **55**: 2299–2307.

Zheng, Y. F. 1998. Oxygen isotope fractionation between hydroxide minerals and water. Phys. Chem. Miner. **25**: 213–221. doi:10.1007/s002690050105

3. Spectroscopic Insights into Ferromanganese Crust Formation and Diagenesis

Abstract

Marine ferromanganese deposits, often called the scavengers of the sea, adsorb and coprecipitate with a wide range of metals of great interest for paleo-environmental reconstructions and economic geology. The long (up to ~75 Ma), near-continuous record of seawater chemistry afforded by ferromanganese deposits offers much historical information about the global ocean and surface earth including crustal processes, mantle processes, ocean circulation, and biogeochemical cycling of elements. The extent to which the ferromanganese deposits hosting these geochemical proxies undergo diagenesis on the seafloor, however, remains an important and challenging factor in assessing the fidelity of such records. In this study, we employ multiple X-ray techniques including micro-X-ray fluorescence, bulk X-ray absorption spectroscopy, micro-X-ray absorption spectroscopy, and X-ray powder diffraction to probe the structural, composition (including Mn, Fe, Si, Co, Ti, Ni, Cu, and Zn), redox, and mineral changes within a single ferromanganese crust, F7-86-HW CD29-2. These techniques illuminate a complex two-dimensional structure characterized by crust growth controlled by the availability of manganese, a manganese oxidation state range of +3.4 to +4.0, changes in manganese mineralogy over time, and recrystallization and exsolution banding in the lower phosphatized portions of the crust. Iron similarly demonstrates spatial complexity with respect to concentration and mineralogy, but lacks the dynamic range of oxidation state seen for manganese. Associations between trace metals and the two major oxide phases exhibits significant spatial variability. Taken all together, these findings provide evidence of post-depositional processes altering chemistry and mineralogy, and provide important geochemical context for the collection and interpretation of elemental and isotopic records in ferromanganese crusts.

3.1 Introduction

Marine ferromanganese deposits, including both crusts and nodules, form in all five global ocean basins at almost every ocean latitude (Cronan, 1977; Hein et al., 1997, 2000). Ferromanganese deposits have classically been categorized into one of three groups based on mode of formation and trace element associations: hydrogenetic deposits, diagenetic deposits, and hydrothermal deposits. Hydrogenetic ferromanganese deposits precipitate in direct contact with the water column on the surface of a substrate rock or existing crust or nodule (Hein et al., 1997, 2000). The direct exposure of hydrogenetic ferromanganese crusts to ambient seawater and the tendency of iron (Fe) and manganese (Mn) oxy(hydr)oxides to (ad)sorb various metal(oid)s makes them valuable recorders of past ocean chemistry (Hein et al., 2000; Klemm et al., 2005; H. F. Ling et al., 2002; Nielsen et al., 2009; Wang et al., 2016). Diagenetic Fe-Mn nodules are distinct from hydrogenetic Fe-Mn deposits in that they form from the reduction and reprecipitation of elements such as Mn, Cu, Ni, and Li in sedimentary porewaters (Crerar & Barnes, 1974). If the sediment redox boundary is close enough to the seafloor, then those released metals can migrate upward and contribute to the growth of Fe-Mn nodules on the seabed. Diagenetic nodules tend to grow at rates much faster than hydrogenetic Fe-Mn crusts (Jung & Lee, 1999; Von Stackelberg & Cronan, 2000). Hydrothermal Fe-Mn deposits occur near submarine hotspot volcanoes, volcanic arcs, and regions influenced by seafloor spreading. Deposits of hydrothermal origin tend to fall closer to pure Fe or Mn oxide endmembers and form as stratabound layers along the flow path of the hydrothermal fluid, giving them a distinct texture from hydrogenetic or diagenetic deposits (Hein et al., 1997, 2000). It is common to find nodules with compositions and/or morphologies reflecting two of these formation types, indicating the deposit formed in a transitioning environment (e.g. transition from purely hydrogenic to purely diagenetic nodules) or in an environment with intermediate character (i.e. mixed hydrothermal and hydrogenetic deposits where hydrothermal fluid enters the water column) (Bau et al., 2014).

While there are many compositional and morphological similarities between ferromanganese nodules and crusts, there are a few distinctions between their typical formation patterns and depositional environments. Nodules form by either hydrogenetic or diagenetic deposition on nucleation sites or as concentric layers on an existing nodule (Hein et al., 2000). Rock or mineral fragments, hard parts from animals such as bones or teeth, or even fragments from previous generations of nodules can serve as a nucleation site for a nodule (Hein et al., 2000). Fe-

Mn nodules are most commonly found in deep marine environments below 4000 meters depth where sedimentation rates are typically below 10 mm ky^{-1} (Hein & Koschinsky, 2014). Seafloor coverage by ferromanganese nodules within the abyssal Pacific and Indian Ocean basins is estimated to exceed 50% in places (Rona, 2008). The abundance of seafloor Fe-Mn nodules declines below depths of 6000 m. While the extent of coverage in the Atlantic and Artic Ocean basins is not fully characterized, documented occurrences of nodules in these two ocean basins appear to follow the same depth and sedimentation rate patterns observed for Pacific crusts (Hein et al., 2000; Hein & Koschinsky, 2014).

In contrast to nodules, Fe-Mn crusts form as layers coating hard-rock substrates. Fe-Mn crusts exhibit a much larger range of depositional depth and are typically observed between 400 m and 7,000 m ocean depth, with the thickest Fe-Mn crusts occurring between 800 m and 2500 m (Hein & Koschinsky, 2014). Crusts occur with greater frequency and tend to reach greater thicknesses in the Pacific Ocean basin. Crusts observed in the Atlantic and Indian Ocean basins tend to be closely associated with the spreading centers that dominant those basins, and therefore tend to have more hydrothermal character than their Pacific counterparts (Hein et al., 2000). In contrast with nodules, crusts exhibit formation patterns and elemental compositions most consistent with hydrogenetic formation (Hein & Koschinsky, 2014). Input of elements produced through redox cycling in sediments to crust formation has not as of yet been verified (Hein et al., 1997, 2000), but has been inferred to occur under unusual circumstances (Hein et al., 2012, 2017). Phosphatization is a common diagenetic feature of ferromanganese crusts. Phosphatization is observed in of older parts of thick crusts, typically dating to the middle Miocene or older. The apparent lack of significant diagenetic input to crusts makes them more viable candidates as hosts of basin-scale and global geochemical records as their chemistry is not influenced by sedimentary redox gradients and/or micro-environments.

Reliable age dating techniques are a central aspect of Fe-Mn crust geochemistry important for contextualizing historical records contained within Fe-Mn deposits. Uranium series isotope ratios and cosmogenic beryllium-10 abundance are among those successfully used to date such deposits, but the window of applicability, approximately 10 Ma for Be isotopes and 400 ka for U-series, is less than the typical age for crusts (typically <75 Ma) (Frank, 2002). Constant accumulation models of some elements have also been used to approximate Fe-Mn crust ages, but fall short in identifying periods of erosion or non-deposition and secular changes in seawater

chemistry (Conrad et al., 2017; Klemm et al., 2005). Stable osmium (Os) isotope ratios have been used for high-resolution age dating of samples up to 72 Ma, nearly 7 times what is achievable with Be-10 measurements (Klemm et al., 2005). Notably, however, some of the oldest observed Fe-Mn crusts exceed even this 70 Ma window (Klemm et al., 2005).

Beyond age dating, Fe-Mn crusts are passive recorders of changes in seawater chemistry on timescales of tens of millions of years to perhaps up to 100 million years and host a wide range of paleo-environmental proxies (Banakar & Hein, 2000; Christensen et al., 1997; Dausmann et al., 2015; Frank et al., 2006; Frank & O'Nions, 1998; Horner et al., 2015; Klemm et al., 2005; Nielsen et al., 2009). Analytical targets for paleo-records include proxies of Earth's crust and mantle processes, marine productivity, and other geochemical processes that produce variations in seawater chemistry. These studies, implicitly or explicitly, assume the Fe-Mn crust hosting these proxies are largely unaltered throughout their lifetime on the seafloor, with the exception of phosphatization by carbonate fluorapatite (CFA) in the older portions of many thick Pacific crusts. CFA precipitates in the pore spaces of older sections of Fe-Mn crusts, approaching 30 weight percent of the oldest sections of crusts from the Pacific, Atlantic, and Indian ocean basins (Hein et al., 2000). Clearly, Fe-Mn crusts offer an important window into modern and past seawater chemistry, yet little is known about the post-depositional changes in the redox state, structure, and mineralogy of the host Fe-Mn minerals. In this study, we use micro-X-ray fluorescence (μ-XRF) and bulk and micro-X-ray absorption spectroscopy (μ-XAS) as a novel way to obtain high-resolution maps of major and minor element distributions, Mn and Fe redox species, mineralogy, and primary and diagenetic textures within a well-studied hydrogenetic Fe-Mn crust from the Central Pacific Ocean (F7-86-HW CD29-2). These high-resolution analyses highlight the complex nature of the structure of Fe-Mn crusts not resolvable in bulk analyses. Additionally, these measurements capture post-depositional changes undergone by a Fe-Mn crust on the surface of the seafloor over approximately 75 Myr.

3.2 Materials and Methods

F7-86-HW CD29-2 (hereafter referred to as CD29) is a hydrogenetic Fe-Mn crust collected from the Karin Ridge in the Central Pacific Ocean (16° 42' N, 168° 14' W) (Hein et al., 1987). CD29 was collected from approximately 2000 meters depth. An age model correlating the Os isotope stratigraphy of CD29 with that of pelagic clays suggests that the first ferromanganese

layers of CD29 were deposited approximately 74 Ma atop basalt hyaloclastite (86 Ma) (Klemm et al., 2005; Nielsen et al., 2009). The oceanic crust underlying CD29 has undergone subsidence throughout the deposition of CD29. The deposition of CD29 began at about 1000 meters water depth, and its underlying oceanic crust has undergone approximately 1000 meters of thermal subsidence relative to sea-level (Horner et al., 2015). Over the same interval of time, the underlying crust of CD29 has drifted by approximately 25 degrees from 10°S latitude to the latitude at which it was collected. The particular section of CD29 used in this study has a thickness of 105 mm, which was prepared in thin section using low fluorescence EpoFix resin.

Bulk XAS, μ-XAS, and μ-XRF were conducted at Stanford Synchrotron Radiation Lightsource (SSRL) on beamlines 4-3, 2-3, 10-2, and 14-3. Bulk X-ray absorption near edge structure (XANES) and extended X-ray absorption fine structure (EXAFS) were collected for Mn and Fe on sub-samples of CD29 that were drilled from ten depths throughout the crust to capture the bulk redox and mineralogical trends within the crust (Figure 1). XANES and EXAFS spectra were fit using the SIXPACK Software package (Webb, 2005). Mn XANES spectra were fit with δ-MnO_2 (synthetic analog of vernadite), feitknechtite, and $MnCl_2$, and Fe XANES spectra were fit with synthetic ferrihydrite and siderite. Mn EXAFS spectra were fit over a *k* range of 1-12 with standard spectra including δ-MnO_2, acid-birnessite, sodium-birnessite, feitknechtite, groutite, hausmannite, todorokite, aqueous $MnSO_4$, pyrolusite, asbolane, and rhodochrosite (Bargar et al., 2005; Learman, Wankel, et al., 2011; Villalobos et al., 2003; Webb et al., 2005). Fe EXAFS were fit over a *k* range of 1-11 with two-line ferrihydrite, aluminum-doped ferrihydrite, feroxyhyte, goethite, hematite, siderite, Fe-rich biotite, Fe-smectite, green rust sulfate, lepidocrocite, and magnetite (Hansel et al., 2003, 2004). It is important to note that we recognize that the fits presented in this are only as good as the standards used to fit them, and that the mineralogy of ferromanganese crusts are exceedingly complex. Although we include a significant number of relevant phases for which endmember standards are available, we recognize that this may not be exhaustive, and therefore may not capture all of the mineralogical complexity in this sample.

Micro-XRF maps of several metals of interest within CD29 were collected at 11,000 eV (Mn, Fe, Co, Cu, Ni, Ti, and Zn) and 4,090 eV (Si) on beamlines 2-3 and 14-3, respectively. Mn and Fe redox maps were collected using beamline 2-3 using multiple-energy mapping. This technique involves collecting several 2-D maps of an area of interest at several different energies surrounding the absorption edge of the element of interest (Farfan et al., 2018; Mayhew et al.,

2011). For Mn, multiple-energy maps were collected at 6553, 6559, 6562, and 6570 eV (Hansel et al., 2012). For Fe, multiple-energy maps were collected at 7122, 7124, 7126, 7128, and 7130 eV (Mayhew et al., 2011). For each set of multiple energy maps, we performed a principal component analysis (PCA) using the SIXPACK Software Package to identify regions of greatest difference among the multiple-energy maps (Webb, 2005). Several reference (XANES) spectra were collected in each distinct region of the multiple-energy maps. We performed PCA on the XANES spectra (typically >20 distinct points for each region of interest) to determine the minimum number of XANES spectra required to describe the variation among each set of multiple energy maps. To avoid any influences of self-absorption on the fitting of each redox end-member and the multiple energy map, we used the self-absorption correction routine available in SIXPACK (Webb, 2005).

To further explore how Mn redox and mineral variability within the Fe-Mn crust related to individual growth features within the crust, we conducted Mn micro extended X-ray absorption fine structure (μ-EXAFS) spectroscopy. μ-EXAFS spectra were collected at SSRL on beamline 10-2 with a Si(220) monochrometer ($\Phi = 90°$) and a 30 micron beam size. For sample locations that required multiple scans, the beam position was slightly offset to avoid beam-induced photoreduction in the sample. Mn μ-EXAFS spectra were fit with the same suite of Mn mineral standards listed above. Any standard with a calculated contribution of 5% or less (the previously defined detection limit for this method (Bargar et al., 2000) to the EXAFS spectra was omitted from the fit and refit iteratively with the remaining components. While the EXAFS fits we present are quantitative, they are constrained by the model compounds within the spectral library. Thus, in order to further evaluate mineralogical heterogeneity, we also combined EXAFS with X-ray diffraction (XRD) analysis. We collected multiple X-ray powder diffraction patterns from discreet sections (Figure 8) throughout the crust for comparison with EXAFS measurements (Rigaku Rapid II, Mo source, 0.3 mm collimator, λ=0.70930Å). Samples were mounted on a Kapton tip with mineral oil and run for 20-30 minutes with omega fixed and phi rotating at 1 degree per second. Two-dimensional diffraction images were background corrected (manual setting of 5) and intensity integrated using the 2DP software package.

3.3 Results

3.3.1 Element Composition

Figure 2 shows the element distribution of the topmost section (0-10 mm) of crust for the three most abundant cations in CD29: Mn, Fe, and Si (Co, Ti, Ni, Cu, and Zn images of same region is provided in the supplement). These images clearly demonstrate that CD29 is composed of growth columns ranging in size from hundreds of microns to several millimeters within a ~10 mm thick section; the columnar sections alternate with 1 to 2 mm-thick mottled sections. The center of the columns is dominated by Mn, with the highest Fe and Si found between the columns, which is typical of hydrogenetic crusts—the columns are separated during growth by detrital silica and silicate grains cemented by predominantly Fe oxides. In Figure 3, we present a more detailed look at one set of Fe-Mn branched growth columns at 20 mm depth (just below Figure 2), including major and minor element concentrations of Mn, Fe, Co, Ti, Ni, Cu, and Zn (μ-XRF at 11 keV); this branched columnar section is underlain by a laminated section composed of acicular, massive, and mottled laminae. Further down in the crust (79 mm), where CFA fills in the pore space of CD29 (~10 wt% (Frank et al., 1999)), these columnar-laminated fabrics give way to a less porous fabric with distinct compositional banding parallel to the growth plane of the crust (Figure 4).

Correlation coefficient for the elements in Figures 3 and 4 are provided in Table 1 ($n >$ 400,000 pixels in both images). We note that values presented in Table 1 are not directly comparable to correlation matrices based on total element concentrations from bulk analysis presented elsewhere (Frank et al., 1999); the presence of cracks and metal poor regions in the crust mean that element correlations are not normalized to mass. Cu and Ni are predominately correlated with Mn (Cu: $r = 0.53, 0.45$; Ni: $r = 0.82, 0.57$, Figs. 3, 4, respectively), while Co is primarily associated with Fe (Co: $r= 0.86, 0.67$) (Figs. 3, 4; Table 1). Ti and Zn exhibit more complex behavior. Ti is positively correlated with both Fe ($r = 0.467$) and Mn ($r = 0.53$) in the topmost portion of the crust, but the Ti-Mn relationship becomes much weaker with depth ($r=0.18$). Zn has a weak positive correlation with both Mn ($r = 0.37,0.20$) and Fe ($r = 0.30,0.11$).

3.3.2 Bulk XAS

Bulk Mn and Fe XANES and EXAFS are shown in Figures 5 and 6, with quantitative fit results shown in Tables 2-5. Mn appears to have multiple trends in mineral character and redox state with depth (age) in the crust. The proportion of δ-MnO_2 within the EXAFS fits starts at 25.6%

near the surface, increasing with depth to >75% near the bottom of the crust (Table 3). Acid birnessite, todorokite, and asbolane spectra contribute 26.1, 47.4, and 26.4 at the first sampled interval, respectively. The fractional contribution of todorokite decreases with increasing depth in the crust, while birnessite and asbolane remain present throughout. XANES data reveal that these general trends in mineralogy occur in parallel with an overall increase in Mn oxidation state with increasing depth into the crust, with the shallowest section having an average Mn oxidation state of 3.46, and the deepest having an average Mn oxidation state of 3.91 (Table 2). Typical error for Mn redox states collected in this way is <3% (Bargar et al., 2005).

Iron EXAFS and XANES do not reveal similar trends in mineralogy and redox state. Feroxyhyte and ferrihydrite was the primary components at all depths (Table 5), with intermittent contributions from more crystalline oxides, goethite and hematite, and Fe-rich clay. Iron was near +3 valence at all sample depths (Table 4). Two samples demonstrated a small (~2%) Fe(II) component, but this is most likely within error and at the detection limit.

3.3.3 μ-EXAFS

Manganese μ-EXAFS spectra collected at several depths throughout the crust are shown in Figure 7. These spectra include representatives of the most recent growth, crust growth older than 50 Ma, specific growth structures, and space between growth structures. Several standards were used to fit these μ-EXAFS spectra, but only model compounds with >5% contribution to any sample are shown in Figure 7. Table 6 shows the component fits for each standard and a description of the location in which the spectrum was collected. Samples in the topmost portion of CD29 demonstrate Mn in bonding environments similar to a mixture of the spectral standards birnessite (include hexagonal and triclinic), todorokite, asbolane, and $MnSO_4$. At greater crust depths, δ-MnO_2, asbolane, and birnessite components represent the greatest fractional contributions to CD29 EXAFS spectra, with the exception in some instances of todorokite that appears on edges of individual growth structures.

3.3.4 XRD

XRD measurements were collected on four bulk samples (each representing approximately 2.5 mm of crust growth) from throughout the crust, including two samples in the upper, unphosphatized section of the crust (surface scrape and 17.5-20 mm), and two samples in the

lower, phosphatized section of the crust (48.5-51 mm and the bottom of the crust) (Figure 8). All sections of the crust exhibited broad XRD reflections at 2.46 Å and 1.45 Å d-spacing, characteristic of vernadite (Post, 1999). Reflections corresponding to CFA were observed in two samples in the lower phosphatized section of the crust. We did not observe 7 Å or 10 Å peaks in the diffraction pattern of CD29. No discernable Fe phases were seen in the diffraction pattern, and a small quartz peak was observed at 3.3 Å, both findings consistent with previous studies (Frank et al., 1999).

3.3.5 Mn and Fe Redox Maps

Maps of Mn and Fe oxidation states are shown in Figure 9. For Fe and Mn, two spectra were sufficient to describe >99% of the variation observed within the multiple energy maps. Using XANES fitting, we determined these two end-members to be the most oxidized and most reduced examples of each metal in the sample. Manganese oxidation state varies from +3.4 to +4.0 throughout the crust, and Fe varies from +2.8 to +3.0. Average Mn oxidation state tends to increase going outward from the center to the edge of columnar growth structures and going lower in ferromanganese crust stratigraphy. Average Fe oxidation state showed similar structural trends, with edges being the most oxidized. There was no significant Fe oxidation state trend with depth in the crust. These results largely agree with the redox trends determined via bulk XANES (Tables 2 and 4).

3.4 Discussion

3.4.1 Primary crust features

Fe-Mn crusts, by nature of their formation, have a defined start and end, with a clear sense of time between them. This application of Steno's principles guides us in our interpretation as to the primary and diagenetic features of the Fe-Mn crust investigated here. The most recent growth features of CD29 are laminated columnar growth structures that vary in scale from 100 μm to several mm (Figure 2). In general, individual growth features tend to have the highest Mn concentrations in their interior, with Mn concentrations decreasing towards the margin of growth columns. Fe concentration tends to vary inversely with Mn within these individual growth features. These findings demonstrate a strong relationship between composition and growth structure in the ferromanganese crust. The center of each growth column has Mn:Fe ratios greater than 1,

suggesting the nucleation of new crust growth is in large part controlled by the availability and/or the oxidation of Mn, which are reflected in the growth rates.

Columns contrast with the interstitial space between columns that have the highest concentrations of Fe, and correspondingly low Mn:Fe ratios. This distribution of Fe suggests that Fe minerals occur as both a co-precipitate with Mn oxides (high Mn:Fe) and as a cement for detritus-rich phases precipitated by fluid flow around primary growth columns (lower Mn:Fe). This interstitial space also hosts the majority of Si-bearing material. The texture of Si in CD29 is consistent with detrital silica (quartz) and silicate minerals (feldspar, clay minerals) and bio-opal. Phillipsite, a zeolite mineral, has been observed in a number of marine Fe-Mn deposits (Hein et al., 2004), but we could not positively identify such a phase in our measurements. A quartz peak at 3.3 Å (Figure 8) was the only discernable feature in XRD that allows for the positive identification of a silica, although previous work demonstrated plagioclase feldspar is also clearly present (Frank et al., 1999). The intermittent presence of Fe-smectite in bulk EXAFS fits points to detrital incorporation of authigenic clay.

A great deal of interest in Fe-Mn crusts, from the perspectives of reconstructing geochemical records, biological availability of metals, and identifying economically important minor constituents, aims to understand the association of minor and trace constituents with the main oxide phases (Bau et al., 2014; Koschinsky et al., 1997; Koschinsky & Hein, 2003). Several first-row transition metals, including those analyzed in this study (Co, Zn, Ni, Cu, Ti), exhibit complex behavior in how they partition among the various mineral phases present in these crusts (Bodei et al., 2007; Manceau et al., 1992a, 1992b, 2003; Manceau, Kersten, et al., 2007; Manceau, Lanson, et al., 2007; Peacock & Sherman, 2007; Takahashi et al., 2007). Surface sorption followed by incorporation into the mineral structure and diagenetic change mediate these relationships, and are in large part directed by the formation environment of a given deposit (e.g. hydrogenetic, diagenetic, or hydrothermal) (Bodei et al., 2007; Manceau et al., 2003; Manceau, Kersten, et al., 2007; Peacock & Sherman, 2007). Typically, elements exhibit bulk patterns of association with major phases in Fe-Mn crusts. Co, Zn, Ni are typically associated with the Mn-oxide phase, whereas Cu and Ti are typically associated with Fe oxide (Hein & Koschinsky, 2014; Manceau et al., 1992b, 1992a; Manceau, Lanson, et al., 2007). Our μ-XRF mapping allows for insights into these trace co-precipitation associations that bulk analyses do not. Indeed, findings demonstrate correlations of Ni and Cu with Mn, and Co with Fe. These methods also demonstrate the complex

nature of elements like Ti and Zn. For example, Ti has a moderate positive correlation with Mn in the topmost section of CD29 (r = 0.53), but this relationship gets much weaker with depth (r = 0.18). In the younger portions of the crust, the Zn distribution appears similar to that of Mn (Figure 3). In the older portions of the crust, however, Zn concentrations are highest in the regions with highest Mn and Fe (Figure 4). This is consistent with previous work demonstrating that Zn in soil Fe-Mn nodules partitions among several phases including goethite, birnessite, and phyllosilicates (Manceau et al., 2003), as it does with marine Fe-Mn crusts (Koschinsky & Hein, 2003). Such diverse metal associations within a single Fe-Mn crust should be considered, for example, when interpreting isotopic records contained within them (Little et al., 2014).

There has been much speculation about the role of microbes in the formation and growth of Fe-Mn deposits. Indeed, the surface of a Fe-Mn nodule was shown to host dense communities of bacteria and archaea (Shiraishi et al., 2016). The growth patterns of CD29 are reminiscent of stromatolites (Bosak et al., 2013), and microbial Mn oxidation has been demonstrated across disparate groups of eukaryotes and bacteria that produce Mn(II)-oxidizing enzymes and reactive oxygen species (Geszvain et al., 2012; Hansel, 2017; Hansel et al., 2012; Hansel & Learman, 2015; Learman, Voelker, et al., 2011; Sutherland et al., 2018; Tang et al., 2013; Tebo et al., 2004, 2005). Further, the dominant Mn oxide formed by microbes is a hexagonal birnessite phase similar in structure to δ-MnO_2, the dominant phase identified within the crusts (Bargar et al., 2005; Grangeon et al., 2010; Jürgensen et al., 2004; Learman, Wankel, et al., 2011; Santelli et al., 2011; Webb et al., 2005). These growth textures and oxide structures, however, are not necessarily microbial, and may result from abiotic, stochastic, and/or surface-normal growth processes (Grotzinger & Rothman, 1996). At most, Mn oxidation may control the nucleation and growth of Fe-Mn crusts, which in turn may be regulated by microbial activity, either directly or indirectly. We can only conclude that Mn-rich growth columns and crust texture are consistent with, but not necessarily indicative of, microbially mediated Mn oxidation.

The average Mn oxidation state in CD29 varies even within the primary growth features in the topmost section. The topmost layers of CD29 growth columns contain Mn in the lowest average redox state exhibited in the crust: +3.4. Similar mixed valance Mn-oxides have been observed on the outer rim of a ferromanganese nodule (Shiraishi et al., 2016). The Mn oxidation state in CD29 increases toward the edge of growth column structures, which shows a maximum of ~3.7 (Figure 9). This small-scale dynamic redox texture has implications for element associations and

geochemical records of redox-active elements and isotopes. Redox-active elements incorporate into the Fe-Mn crusts through oxidative sorption coupled with Mn reduction (Nielsen et al., 2013; Ohta & Kawabe, 2001; Peacock & Moon, 2012); the range of average Mn redox state demonstrates the ability for Mn to facilitate oxidative sorption that may vary spatially and temporally. Unlike Mn, Fe demonstrates very little redox structure throughout the crust. Bulk Fe EXAFS show the primary Fe-bearing phases are ferrihydrite and feroxyhyte. We also detected several occurrences of Fe-bearing clay and more crystalline Fe (hydr)oxide phases. The primary Mn phase(s) as determined by bulk EXAFS has mineral character consistent with a mixture of the disordered hexagonal birnessite phase vernadite (as identified via the synthetic analog δ-MnO_2), acid birnessite (hexagonal), asbolane, and todorokite (tunnel structure). The complexity in Mn mineralogy is further illuminated by the μ-EXAFS results, which identify a mixture of acid-birnessite (hexagonal), sodium birnessite (triclinic), todorokite (tunnel structure), asbolane, and a Mn(II) component (fit as $MnSO_4$). Deeper in the crust, this assemblage transitions to a similar mixture of components observed in the bulk EXAFS. We will discuss these mineralogical changes in more detail in the following section on diagenetic changes in the crust.

3.4.2 Diagenesis

High-resolution, two-dimensional analyses of Fe-Mn crust element distribution offer insight into changing element correlations with age. Some elements (e.g. Ni) show a strong preference for a given mineral phase, but many of these associations in the young crust become weaker with age. Secular variation in the bottom-water abundance of an element may explain some of these complex element associations. This explanation likely describes some of the behavior of Zn, which demonstrates growth bands (i.e. perpendicular to growth direction) of high concentration independent of Mn and Fe distributions (Figure 3). In addition to these observations, diagenetic changes within the crust may explain some of this compositional variability through time. A feature suggesting that diagenesis does play a role in such compositional changes is seen in Figure 4. This figure demonstrates columnar growth features giving way to a much less porous crust framework with compositional changes in laminae parallel to the plane of growth. This portion of crust in the lower, phosphatized region (>80 mm, >50 Ma) demonstrates a clear textural change and exsolution banding that is symptomatic of post-depositional processes. Similar observations have been previously reported, concluding that suboxic conditions facilitate a partial

dissolution and reprecipitation of more stable phases (Koschinsky et al., 1997; Puteanus & Halbach, 1988). This partial repartitioning of elements is apparent in chemical changes seen in Table 1 as well.

Bulk Mn XAS reveals post-depositional oxidation and mineralogical changes with increasing depth in CD29. The Mn oxidation state of the youngest crust (+3.4), is much less oxidized than the oldest crust (+4.0), a range easily resolved by Mn XANES (Bargar et al., 2000). Unlike new crust growth, the oldest crust does not show a relationship between Mn oxidation state and major growth features. Average Fe oxidation state is essentially unchanged between the topmost section of CD29 and the bottom most section, with a value of +3.0. While there are some slight Fe redox changes between the center and edge of growth structures, the dynamic range is less than 0.1 oxidation state, differences that are likely unresolvable using this method.

The changes in Mn redox state (Table 2, Figure 9) are consistent with primary precipitation of mixed-valance oxides, followed by post-depositional oxidation, or oxic diagenesis. Primary, mixed-valance Mn oxides are commonly seen in laboratory settings, including Mn oxides produced by bacteria and fungi (Grangeon et al., 2010; Jürgensen et al., 2004; Learman et al., 2013; Santelli et al., 2011; Sutherland et al., 2018; Webb et al., 2005), and in marine Fe-Mn oxide deposits (Manceau et al., 2014; Marcus et al., 2004). The changes in Mn redox state are not readily explained by secular changes in dissolved O_2 concentration of the ambient seawater. As previously mentioned, the deposition of CD29 began at ~1000 m water depth (Horner et al., 2015). In typical seawater, the dissolved O_2 concentration typically reaches a minimum near 1000 m from respiration of exported organic carbon from the surface ocean. The thermal subsidence that delivered CD29 to depths near 2000 m most likely carried CD29 toward more oxygen-ventilated deep water. This presumed history of dissolved O_2 concentration is at odds with more oxidized Mn down section in the crust. This indicates that whatever physical, chemical, or biological process that precedes the precipitation of individual growth columns in CD29 produces Mn oxides that contain substantial amounts of Mn(III). The more oxidized outer edges of growth columns also hint at oxidation resulting for greater exposure to oxygen-bearing poor waters (Figure 9).

A uniformitarian interpretation of EXAFS data collected from CD29 suggests Mn precipitates as a complex mixture of phases in ferromanganese crusts, which undergo transformations to a more stable manganate phase over several million years. Bulk EXAFS shows a trend of increasing vernadite (δ-MnO_2) with depth from a starting mixture of birnessite,

todorokite, and asbolane based on the model compounds used (Figure 6; Table 3). Birnessite, todorokite, and asbolane may contain stoichiometric Mn(II) and/or Mn(III) (Post, 1999). Consistent with this, there is a clear break in the Mn(III) content and mineralogy within the crust, wherein the uppermost crust has high Mn(III) and high asbolane and todorokite components, while the bottom 74.5-105 mm interval is primarily Mn(IV) (>90 mol%) and consists primarily of hexagonal birnessites (as δ-MnO_2 and acid birnessite). μ-EXAFS data demonstrate significant spatial heterogeneity within this overall trend. The first millimeter of new crust growth contains birnessite (hexagonal), sodium birnessite (triclinic), todorokite (tunnel structure), asbolane, and small contributions from a reduced Mn phase (nominally fit as $MnSO_4$). Over several millimeters of crust, these initial phases give way to mixture of vernadite (δ-MnO_2) (hexagonal), acid birnessite (hexagonal), and asbolane with instances of todorokite. This general agreement between the bulk and μ-EXAFS provides some validation for the general, down crust trends. These two measurements together suggest that the mixture of hexagonal phyllomanganates observed down crust may form from a recrystallization of primary disordered phases over several millimeters of ferromanganese crust.

The Mn mineralogy exhibits an increase in vernadite character with increasing diagenetic character in CD29. This is at odds with one previous set of observations of ferromanganese nodules. Dymond et al. (1984) identifies vernadite as a primary Mn-oxide phase, which may undergo oxic diagenesis in Fe-Mn nodules to form todorokite in the presence of abundant stabilizing cations such as Cu and Ni (Dymond et al., 1984). This model is based on traditional XRD techniques, which would not detect mineralogical changes on the scale we observe in this study. Todorokite is generally thought to be rare in hydrogenetic Fe-Mn crusts, and is found in less than 5% of crust samples (Hein, 2014). Previous XRD studies on this very same crust, CD29, have concluded that the only Mn oxide phase present is vernadite. Our XRD measurements of CD29 yielded peaks at ~2.5 Å and ~1.5 Å, which can be attributed to several Mn oxides, including vernadite and other birnessite minerals, but in the absence of a basal reflection is typically attributed exclusively to vernadite (Frank et al., 1999; Post, 1999). In addition to these peaks, our XRD data also show a broad XRD peak at 4.8 Å, which has been observed in nano-crystalline todorokite (Feng et al., 2010). Despite the persistent presence of todorokite and multiple birnessite-group minerals with bulk and μ-EXAFS, a basal reflection at 7 or 10 Å was not observed in our bulk XRD analysis. This lack of reflections at 7 and 10 Å does not necessarily preclude the

presence of these two minerals. Vernadite itself lacks a basal reflection (Post, 1999). Two explanations have been proposed to explain this lack of basal reflection. The first is that vernadite has a turbostratic layer configuration, meaning that sheets of MnO_6 octahedra are highly disordered in the layer stacking direction. While this would explain the lack of basal reflection in vernadite and birnessite, such an interpretation is not readily applied to todorokite, which has a 3 by 3 tunnel structure of MnO_6 octahedra (Post, 1999). The second explanation put forth to explain the lack of basal reflection in vernadite is exceedingly small domains of crystallinity. Post (1999) suggested that thin manganate plates less than 100 Å would be sufficient to preclude Bragg diffraction in the layer-stacking direction. Nano-crystalline todorokite has indeed been observed as a product of biogenic Mn oxides, and similarly lacks a ~10Å basal reflection due to thin layers along the c axis (Feng et al., 2010). Thus, our findings suggest that previous determinations of Mn-oxide mineralogy in marine Fe-Mn deposits may understate the abundance of other manganate (especially nano-crystalline) minerals like todorokite, buserite, asbolane, and other birnessite phases, including triclinic birnessite, when relying on traditional XRD techniques alone (e.g. Frank et al. 1999). Nevertheless, the birnessite group of minerals has a wide structural and compositional complexity such that there remains uncertainty as to the level of accuracy in modeling this group using mechanical mixtures of end members (F. T. Ling et al., 2018). We pose that combining bulk- and micro-scale analysis for linear combination EXAFS may alleviate some uncertainty and provide for confirmation of bulk modeling trends. Further, in systems such as Fe-Mn crusts that contain small domains of crystallinity and/or c-disordered crystals, μ-EXAFS tells a much more complex story of early and late mineralogical transformations occurring over the lifetime of the crust.

3.5 Summary and Conclusions

In this study, we demonstrate the use of μ-XRF, bulk XAS, and μ-XAS to measure major and minor element concentrations in the Fe-Mn crust CD29. These components include Mn, Fe, Si, and several transition metals that make up less than 1 weight percent of CD29. The distribution of these major elements suggests that nucleation and growth of this Fe-Mn crust is likely controlled by the availability of Mn and Fe, and detrital silicates and Fe oxides that form around these primary Fe-Mn growth columns. We used μ-XRF mapping at multiple energies to measure the two-dimensional redox structure of Mn and Fe in CD29. These maps show that Fe oxidation state has

very little spatial variation (all around +3), while Mn exhibits average oxidation states from +3.4 to +4.0. The most reduced Mn oxides are present toward the center of growth structures and toward the top of the crust, suggesting that primary Mn oxides in this environment form with an oxidation state of +3.4. Given that this crust has likely seen a monotonic increase in the dissolved oxygen of its surrounding seawater, we suggest that higher oxidation states deeper in the crust result from post-depositional oxidation. Using bulk and μ-EXAFS, we demonstrate that there are multiple distinct Mn bonding environments throughout the crust, including a primary depositional assemblage of hexagonal and triclinic birnessite, todorokite, asbolane, and a possibly more reduced Mn-phase. This primary assemblage transitions to a mixture of acid birnessite, vernadite and asbolane deeper in the crust. We characterized a region of significant post-depositional alteration, which demonstrates recrystallization and exsolution banding coincident with a Mn oxidation state of approximately +4.0.

Our findings highlight the need to consider post-depositional changes in oxidation state and mineralogy when considering element associations and geochemical proxies in ferromanganese crusts. The observed Mn redox changes in CD29 suggest that the ability to facilitate oxidative sorption, and potentially any associated isotopic fractionation, may be altered by post-depositional oxidation of Mn. The consequences of oxidative diagenesis of Mn in Fe-Mn crust on individual, redox-active metals, likely need to be considered on a case-by-case basis.

Figures

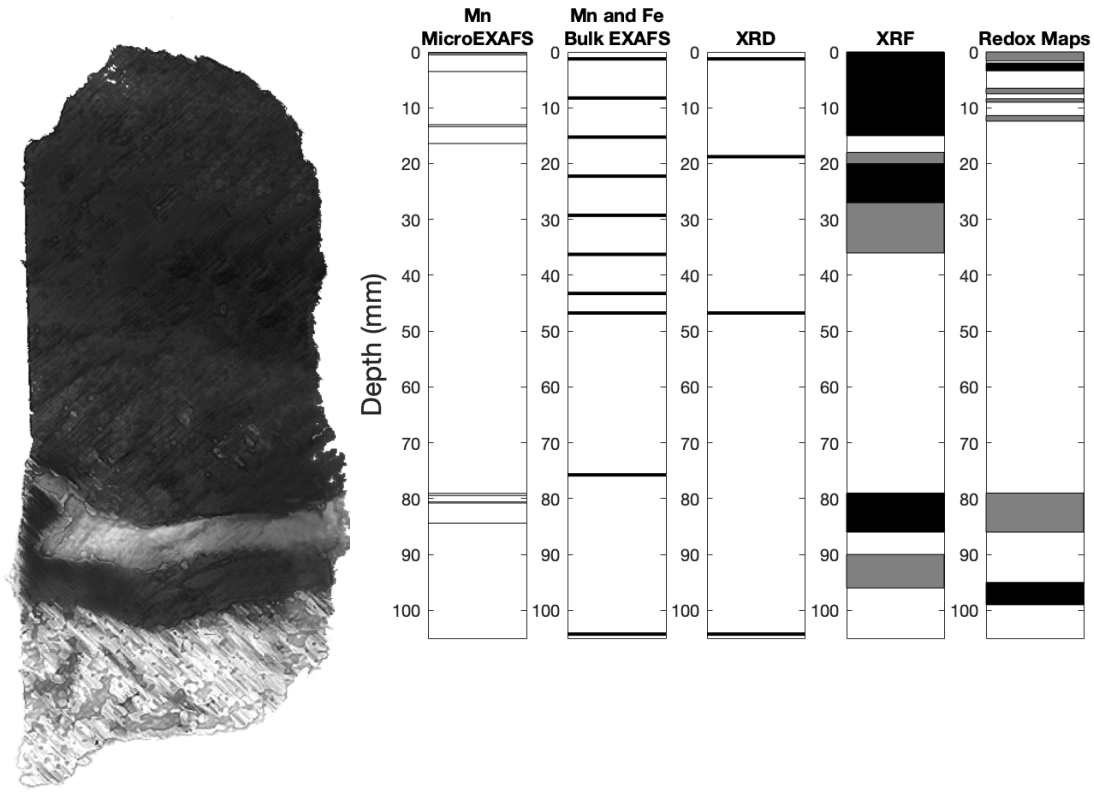

Figure 1- Schematic of the section of F7-86-HW CD29-2 used in this study. Black lines and boxes indicate the approximate depths of individual analyses conducted as part of this study. Gray boxes indicated data that are provided in the supplemental material.

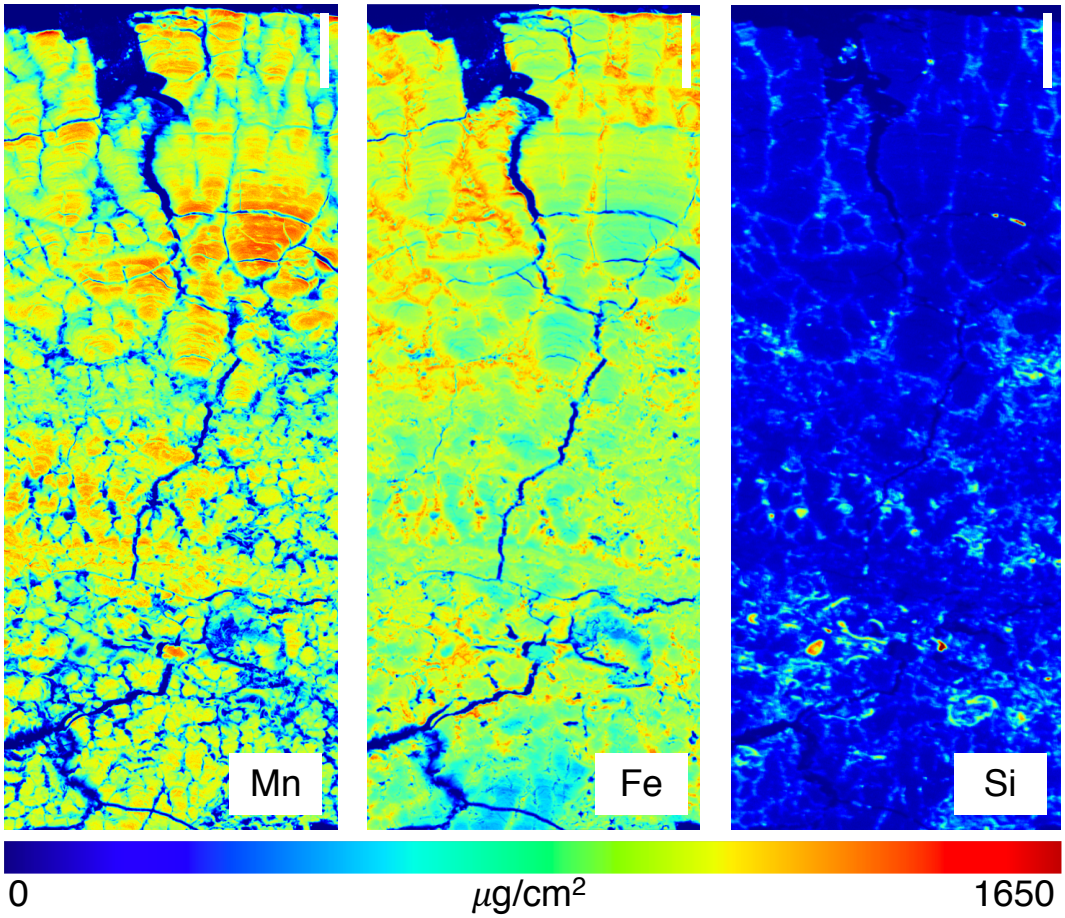

Figure 2- Micro- X-ray Fluorescence images of Mn, Fe, and Si of the topmost section of crust CD29. Mn concentrations are highest within individual growth columns, while Fe and Si concentrations are highest in the areas between columns and in material filling cracks. Scale bar (top right) represents 1 mm.

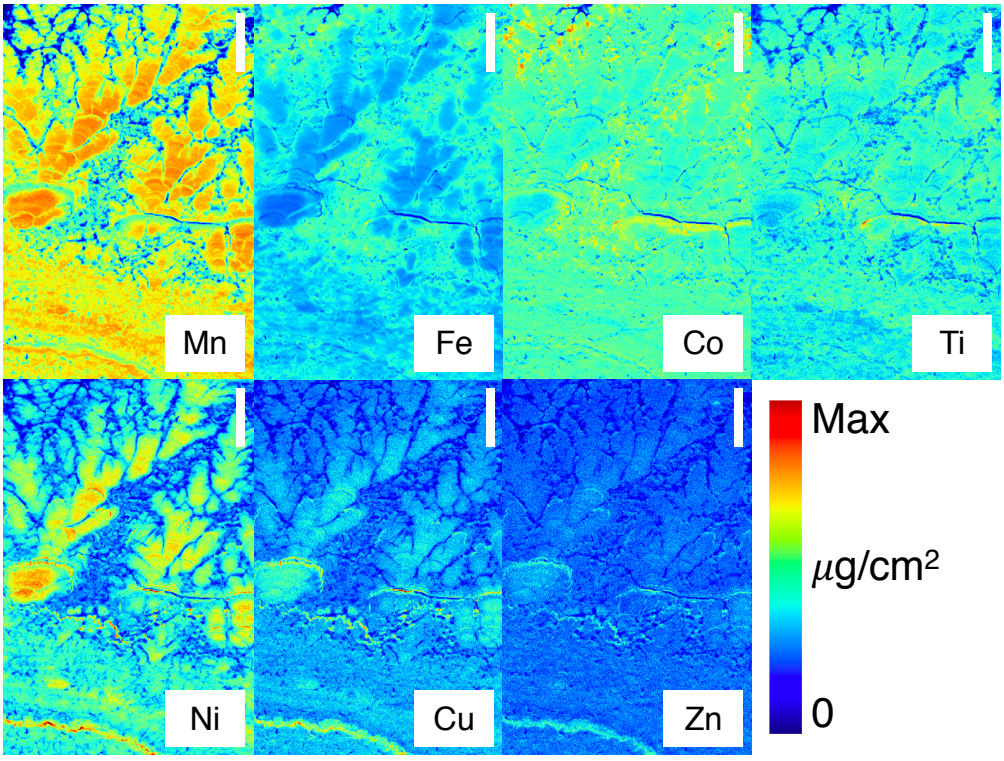

Figure 3- Micro- X-ray Fluorescence images of a representative section of ferromanganese growth structures (branching columns; laminations) in the upper section of the crust. Max concentrations are 1,350 μg/cm^2 (Mn, Fe), 100 μg/cm^2 (Co, Ti), 30 μg/cm^2 (Ni), and 10 μg/cm^2 (Cu, Zn). Scale bar (top right) represents 1 mm.

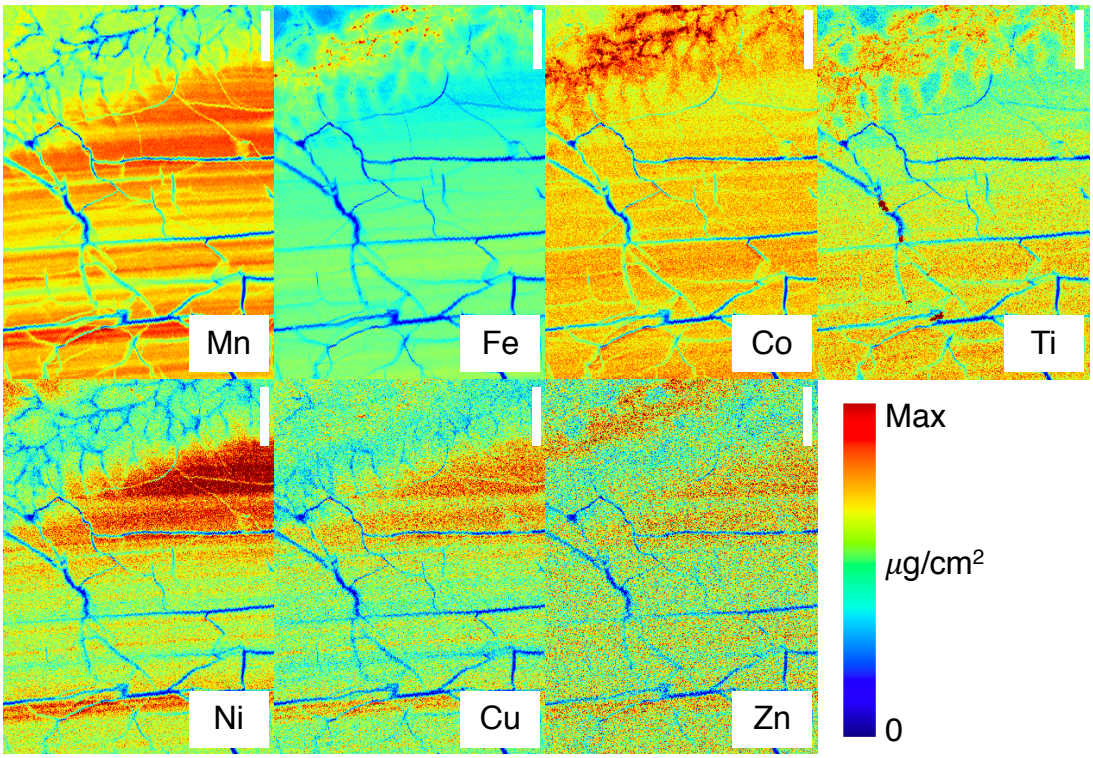

Figure 4- Micro- X-ray Fluorescence images of a representative parallel lamination section of the lower, phosphatized section of the crust. Max concentrations are 1,650 μg/cm^2 (Mn, Fe), 100 μg/cm^2 (Co, Ti), 30 μg/cm^2 (Ni), and 10 μg/cm^2 (Cu, Zn). Scale bar (top right) is 1 mm.

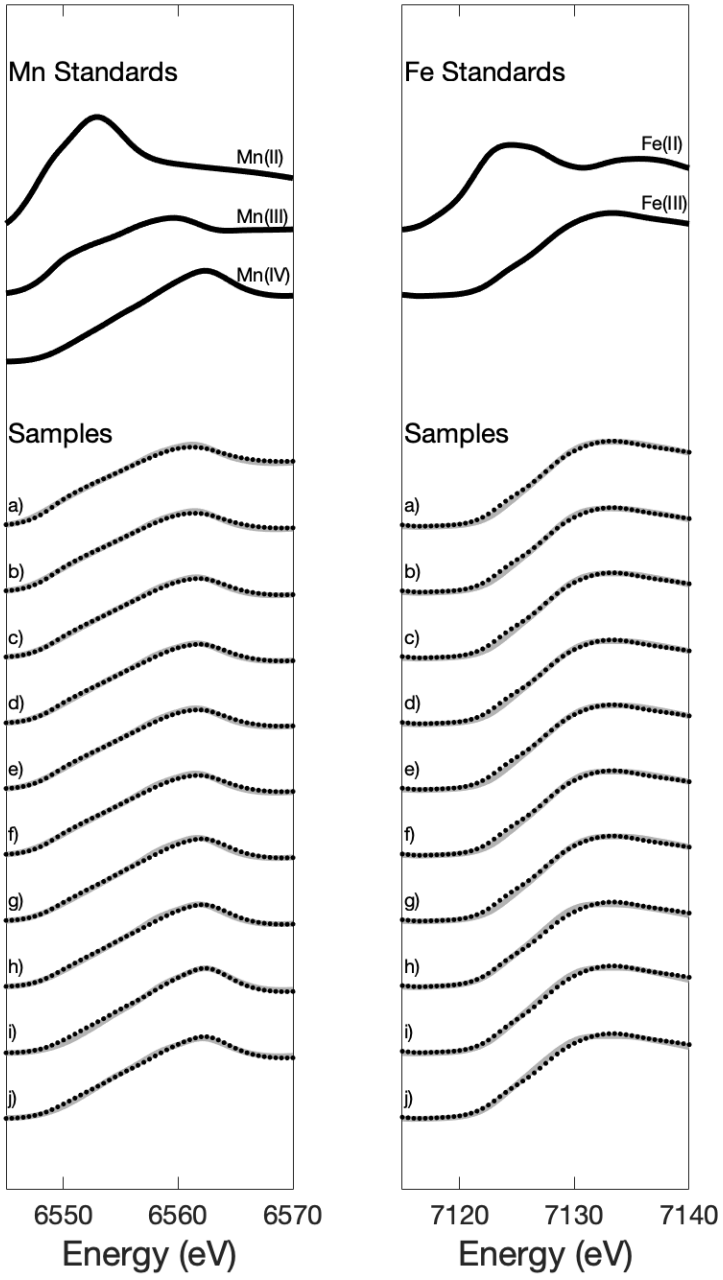

Figure 5- Mn and Fe XANES spectra and fits for bulk XANES analysis. δ-MnO_2, feitknechtite, and $MnCl_2$ were used for Mn redox standards, ferrihydrite and siderite were used for Fe redox standards. The raw data are plotted in gray, the least-squares fits of each spectrum is plotted on top of the data in black dotted line. Depths a) through j) correspond to the following: 0-2.5 mm, 7-9.5 mm, 14-16.5 mm, 21-23.5 mm, 28-30.5 mm, 35-37.5 mm, 42-44.5 mm, 45.5-48 mm, 74.5-77 mm, and 102.5-105 mm.

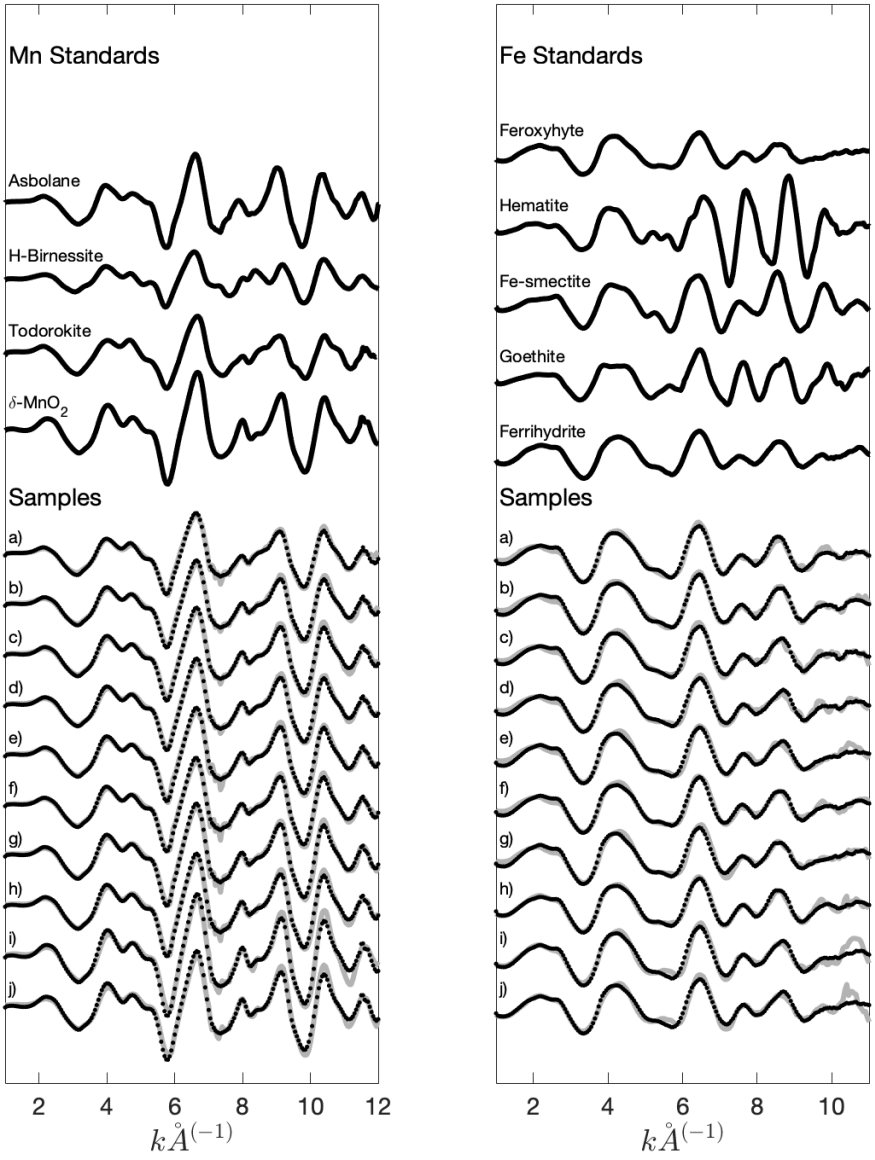

Figure 6- Mn and Fe EXAFS spectra and fits for bulk EXAFS analysis. Each included standard was determined to contribute >5% to the least squares fit of each EXAFS spectrum. The raw data are plotted in gray, the least-squares fits of each spectrum is plotted on top of the data in black dotted line. Depths a) through j) correspond to the following: 0-2.5 mm, 7-9.5 mm, 14-16.5 mm, 21-23.5 mm, 28-30.5 mm, 35-37.5 mm, 42-44.5 mm, 45.5-48 mm, 74.5-77 mm, and 102.5-105 mm.

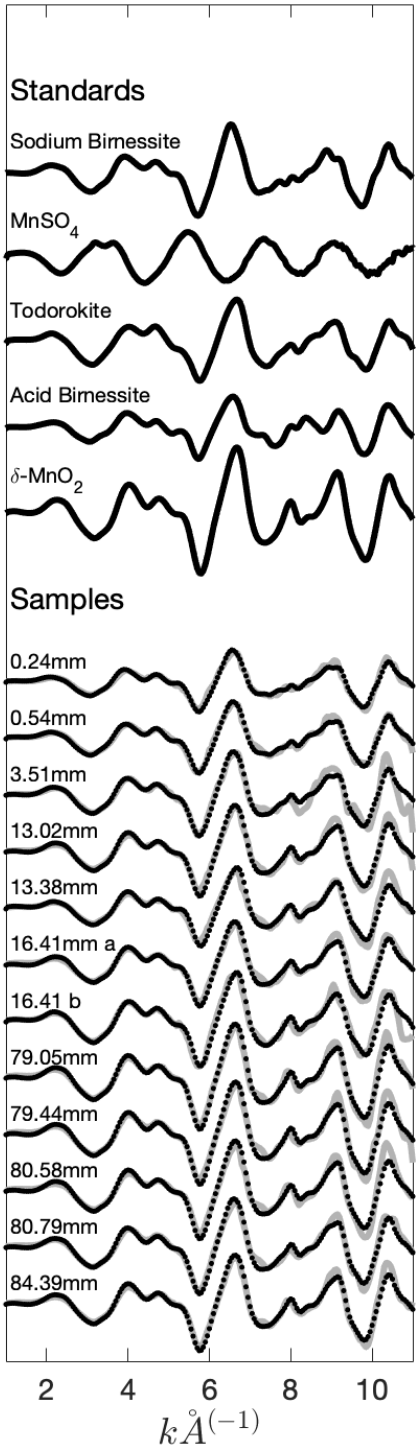

Figure 7- μ-EXAFS spectra of Mn in the ferromanganese crust CD29. Each included standards were determined to contribute >5% to the least squares fit of each EXAFS spectrum. The depth of each sample is listed. Description of each sample location is provided in Table 6.

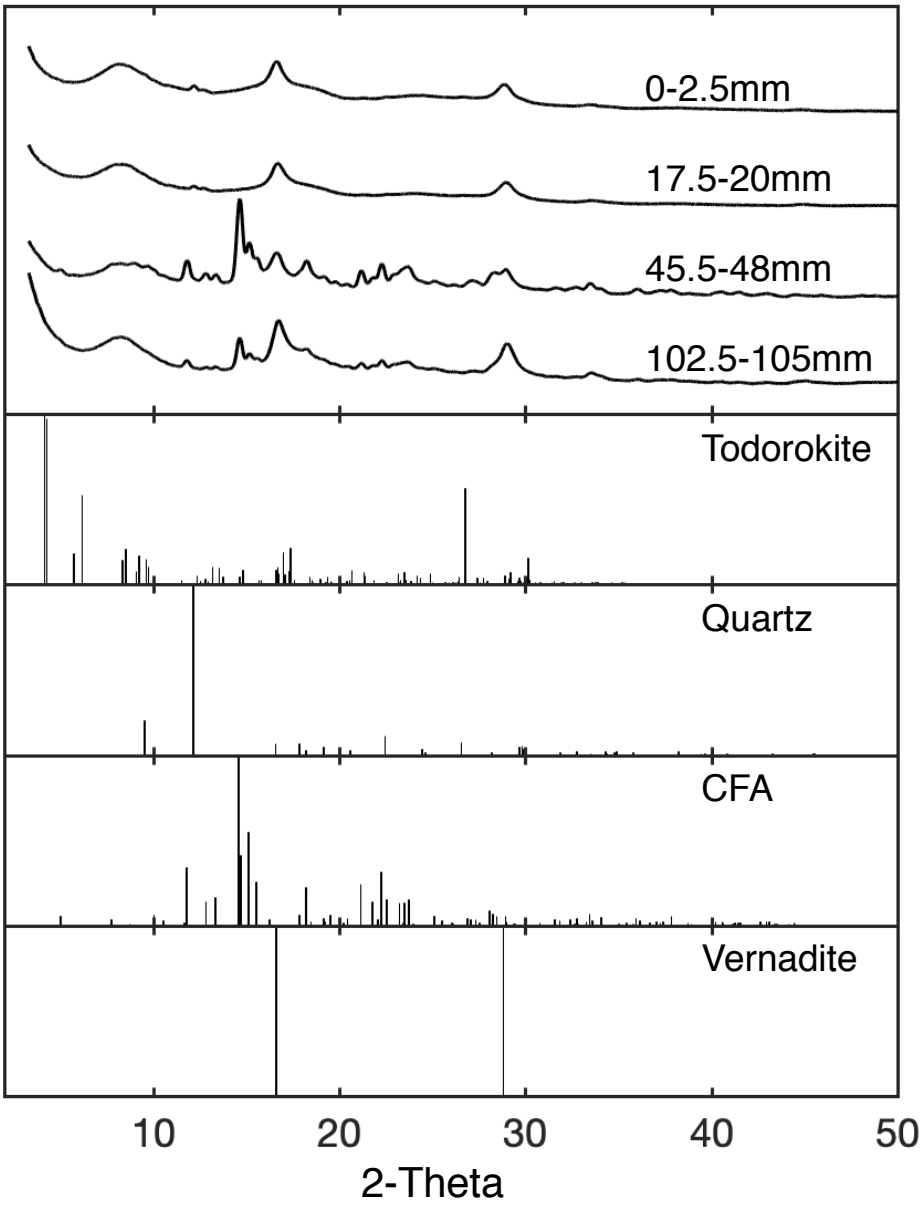

Figure 8- Bulk X-ray powder diffraction (Mo source, λ=0.70930Å) of samples from CD29 including the surface, 17.5-20 mm, 45.5-48 mm (first appearance of carbonate fluorapatite), and the bottom of the crust. Relevant XRD standards are included.

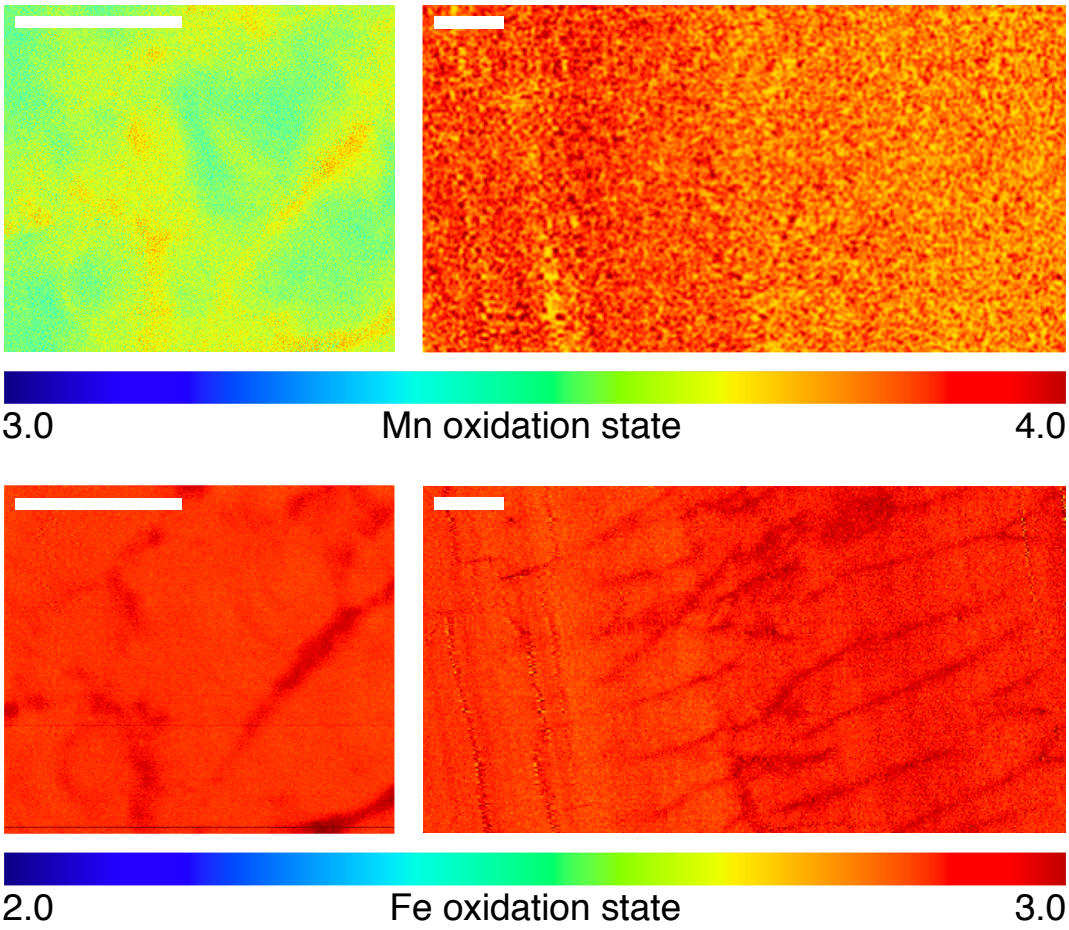

Figure 9- Mn (top) and Fe (bottom) oxidation state maps determined from multiple-energy mapping (see Materials and Methods) for representative sections from the top (left) and bottom (right) of crust CD29. Mn oxidation state is lower toward the top of the crust and the center of individual growth structures. Fe oxidation state changes little throughout CD29. Scale bar (top left) represents 500 μm.

Tables

Table 1- Correlation coefficient of elements in CD29 measured by μXRF for stratigraphic sections shown in figures 3 and 4

Figure 3	Mn	Fe	Zn	Cu	Ti	Co	Ni
Mn	1	0.182	0.368	0.534	0.528	0.255	0.822
Fe		1	0.298	0.161	0.467	0.857	0.108
Zn			1	0.355	0.374	0.317	0.324
Cu				1	0.365	0.216	0.542
Ti					1	0.528	0.402
Co						1	0.214
Ni							1
Figure 4							
Mn	1	0.248	0.201	0.452	0.181	0.271	0.575
Fe		1	0.11	0.054	0.468	0.667	0.011
Zn			1	0.139	0.063	0.130	0.149
Cu				1	0.040	0.117	0.425
Ti					1	0.303	0.017
Co						1	7.28E-02
Ni							1

Table 2- Bulk Mn XANES fitting results

Depth in CD-29 (mm)	Mn XANES Component Fits (fraction)			Average Oxidation State	X_υ^2
	Mn(IV) (δ-MnO_2)	Mn(III) (Feitknechtite)	Mn(II) ($MnCl_2$)		
0-2.5	0.462	0.538	—	3.46	0.0005
7-9.5	0.515	0.485	—	3.51	0.0003
14-16.5	0.615	0.385	—	3.62	0.0002
21-23.5	0.638	0.362	—	3.64	0.0002
28-30.5	0.608	0.392	—	3.61	0.0002
35-37.5	0.605	0.395	—	3.61	0.0003
42-44.5	0.753	0.247	—	3.75	0.0004
45.5-48	0.794	0.206	—	3.79	0.0003
74.5-77	1.000	0.000	—	4.00	0.0008
102.5-105	0.910	0.090	—	3.91	0.0005

Table 3- Bulk Mn EXAFS fitting results

Depth in CD-29 (mm)	Mn EXAFS Component Fits (fraction)						X_υ^2
	δ-MnO_2	Acid Birnessite	Sodium Birnessite	Todorokite	$MnSO_4$	Asbolane	
0-2.5	—	0.261	—	0.474	0.264	—	0.300
7-9.5	0.256	0.219	—	0.305	0.220	0.256	0.262
14-16.5	0.343	0.227	—	0.210	0.220	0.343	0.315
21-23.5	0.347	0.213	—	0.235	0.205	0.347	0.226
28-30.5	0.320	0.215	—	0.201	0.265	0.320	0.318
35-37.5	0.207	0.265	—	0.181	0.347	0.207	0.383
42-44.5	0.334	0.204	—	0.166	0.296	0.334	0.356
45.5-48	0.411	0.188	—	0.137	0.264	0.411	0.372
74.5-77	0.756	0.097	—	0.051	0.097	0.756	0.718
102.5-105	0.692	0.146	—	—	0.162	0.692	0.530

Table 4- Bulk Fe XANES fitting results

Depth in CD-29 (mm)	Fe XANES Component Fits		Average Oxidation State	X_υ^2
	Fe(III) Ferrihydrite	Fe(II) Siderite		
0-2.5	1.000	—	3.00	0.0007
7-9.5	1.000	—	3.00	0.0006
14-16.5	1.000	—	3.00	0.0007
21-23.5	1.000	—	3.00	0.0005
28-30.5	1.000	—	3.00	0.0008
35-37.5	1.000	—	3.00	0.0007
42-44.5	1.000	—	3.00	0.0008
45.5-48	0.981	0.019	2.98	0.0008
74.5-77	1.000	—	3.00	0.0006
102.5-105	0.982	0.018	2.98	0.0009

Table 5- Bulk Fe EXAFS fitting results

Depth in CD-29 (mm)	Fe EXAFS Component Fits					X_υ^2
	Fe-smectite	Goethite	Hematite	Ferrihydrite	Feroxyhyte	
0-2.5	0.189	—	—	0.287	0.524	0.251
7-9.5	—	0.118	—	0.704	0.179	0.224
14-16.5	0.102	—	0.064	0.404	0.430	0.308
21-23.5	—	—	0.080	0.584	0.336	0.334
28-30.5	—	—	0.067	0.394	0.539	0.393
35-37.5	—	0.118	—	0.503	0.378	0.240
42-44.5	—	—	—	0.294	0.706	0.321
45.5-48	0.150	0.095	—	0.237	0.519	0.167
74.5-77	—	—	0.070	0.485	0.445	0.639
102.5-105	—	—	0.087	0.493	0.420	0.616

Table 6- Mn Micro-EXAFS fitting results

Depth in CD-29 (mm)	Description	Mn EXAFS Component Fits (fraction)						X_υ^2
		δ-MnO_2	Acid Birnessite	Sodium Birnessite	Todorokite	$MnSO_4$	Asbolane	
0.24	Center of high-Mn growth column	—	0.178	0.262	0.116	0.074	0.193	0.164
0.54	High-Fe crack between new growth columns	—	0.202	0.269	0.300	0.060	0.123	0.174
3.51	High-Fe region on edge of growth column	—	0.113	0.066	0.238	—	0.476	0.959
13.02	Center of high-Mn growth column	0.338	0.256	—	—	—	0.307	0.289
13.38	High-Fe region on edge of growth column	0.193	0.406	—	—	—	0.284	0.358
16.41 a	Center of high-Mn growth column	0.267	0.294	—	—	—	0.309	0.208
16.41 b	High-Fe region on edge of growth column	0.111	0.310	—	0.144	—	0.458	0.495
79.05	Center of growth structure in phosphatized section of the crust	0.344	0.254	—	—	—	0.434	0.301
79.44	Transition between columnar growth and exsolution bands (high Mn)	0.377	0.321	—	—	—	0.334	0.444
80.58	Exsolution bands (high Mn)	0.283	0.277	—	—	—	0.425	0.503
80.79	Transition between columnar growth and exsolution bands (high Fe)	0.213	0.257	0.115	0.154	—	0.277	0.272
84.39	Exsolution bands (high Mn)	0.345	0.179	—	—	—	0.386	0.264

References

Banakar, V. K., and J. R. Hein. 2000. Growth response of a deep-water ferromanganese crust to evolution of the Neogene Indian Ocean. Mar. Geol. **162**: 529–540. doi:10.1016/s0025-3227(99)00077-8

Bargar, J. R., B. M. Tebo, and J. E. Villinski. 2000. In Situ Characterization of Mn (II) Oxidation by Spores of the Marine Bacillus sp . strain SG-1. 1–15.

Bargar, J. R., S. M. Webb, and B. M. Tebo. 2005. EXAFS, XANES and in-situ SR-XRD characterization of biogenic manganese oxides produced in sea water. Phys. Scr. **T115**: 888–890.

Bau, M., K. Schmidt, A. Koschinsky, J. Hein, T. Kuhn, and A. Usui. 2014. Discriminating between different genetic types of marine ferro-manganese crusts and nodules based on rare earth elements and yttrium. Chem. Geol. **381**: 1–9. doi:10.1016/j.chemgeo.2014.05.004

Bodei, S., A. Manceau, N. Geoffroy, A. Baronnet, and M. Buatier. 2007. Formation of todorokite from vernadite in Ni-rich hemipelagic sediments. Geochim. Cosmochim. Acta **71**: 5698–5716.

Bosak, T., A. H. Knoll, and A. P. Petroff. 2013. The Meaning of Stromatolites. Annu. Rev. Earth Planet. Sci. Vol 41 **41**: 21–44. doi:10.1146/annurev-earth-042711-105327

Christensen, J. N., A. N. Halliday, L. V Godfrey, J. R. Hein, and D. K. Rea. 1997. Climate and ocean dynamics and the lead isotopic records in Pacific ferromanganese crusts. Science (80-.). **277**: 913–918. doi:10.1126/science.277.5328.913

Conrad, T., J. R. Hein, A. Paytan, and D. A. Clague. 2017. Formation of Fe-Mn crusts within a continental margin environment. Ore Geol. Rev. **87**: 25–40. doi:10.1016/j.oregeorev.2016.09.010

Crerar, D. A., and H. L. Barnes. 1974. Deposition of deep-sea manganese nodules. Geochim. Cosmochim. Acta **38**: 279–300.

Cronan, D. S. 1977. Deep-sea nodules: distribution and geochemistry. Mar. manganese Depos. **15**: 11–44.

Dausmann, V., M. Frank, C. Siebert, M. Christl, and J. R. Hein. 2015. The evolution of climatically driven weathering inputs into the western Arctic Ocean since the late Miocene: Radiogenic isotope evidence. Earth Planet. Sci. Lett. **419**: 111–124. doi:10.1016/j.epsl.2015.03.007

Dymond, J., M. Lyle, B. Finney, D. Z. Piper, K. Murphy, R. Conard, and N. Pisias. 1984. Ferromanganese nodules from MANOP Sites H, S, and R-Control of mineralogical and chemical composition by multiple accretionary processes. Geochim. Cosmochim. Acta **48**: 931–949. doi:10.1016/0016-7037(84)90186-8

Farfan, G. A., A. Apprill, S. M. Webb, and C. M. Hansel. 2018. Coupled X-ray fluorescence and X-ray absorption spectroscopy for microscale imaging and identification of sulfur species within tissues and skeletons of scleractinian corals. Anal. Chem. **90**: 12559–12566.

Feng, X. H., M. Zhu, M. Ginder-vogel, C. Ni, S. J. Parikh, and D. L. Sparks. 2010. Formation of nano-crystalline todorokite from biogenic Mn oxides. Geochim. Cosmochim. Acta **74**: 3232–3245. doi:10.1016/j.gca.2010.03.005

Frank, M. 2002. Radiogenic isotopes: Tracers of past ocean circulation and erosional input. Rev. Geophys. **40**: 38. doi:10.1029/2000rg000094

Frank, M., and R. K. O'Nions. 1998. Sources of Pb for Indian ocean ferromanganese crusts: a record of Himalayan erosion? Earth Planet. Sci. Lett. **158**: 121–130. doi:10.1016/s0012-821x(98)00055-7

Frank, M., R. K. O'Nions, J. R. Hein, and V. K. Banakar. 1999. 60 Myr records of major elements and Pb-Nd isotopes from hydrogenous ferromanganese crusts: Reconstruction of seawater paleochemistry. Geochim. Cosmochim. Acta **63**: 1689–1708. doi:10.1016/s0016-7037(99)00079-4

Frank, M., N. Whiteley, T. van de Flierdt, B. C. Reynolds, and K. O'Nions. 2006. Nd and Pb isotope evolution of deep water masses in the eastern Indian Ocean during the past 33 Myr. Chem. Geol. **226**: 264–279. doi:10.1016/j.chemgeo.2005.09.024

Geszvain, K., C. Butterfield, R. E. Davis, and others. 2012. The molecular biogeochemistry of manganese(II) oxidation. Biochem. Soc. Trans. **40**: 1244–1248. doi:10.1042/bst20120229

Grangeon, S., B. Lanson, N. Miyata, Y. Tani, and A. Manceau. 2010. Structure of nanocrystalline phyllomanganates produced by freshwater fungi. Am. Mineral. **95**: 1608–1616. doi:10.2138/am.2010.3516

Grotzinger, J. P., and D. H. Rothman. 1996. An abiotic model for stromatolite morphogenesis. Nature **383**: 423–425. doi:10.1038/383423a0

Hansel, C. M. 2017. Manganese in Marine Microbiology, p. 37–83. *In* R.K. Poole [ed.], Advances in Microbial Physiology. Academic Press.

Hansel, C. M., S. G. Benner, J. Neiss, A. Dohnalkova, R. K. Kukkadapu, and S. Fendorf. 2003. Secondary mineralization pathways induced by dissimilatory iron reduction of ferrihydrite under advective flow. Geochim. Cosmochim. Acta **67**: 2977–2992. doi:10.1016/S0016-7037(03)00276-X

Hansel, C. M., S. G. Benner, P. Nico, and S. Fendorf. 2004. Structural constraints of ferric (hydr)oxides on dissimilatory iron reduction and the fate of Fe(II). Geochim. Cosmochim. Acta **68**: 3217–3229. doi:10.1016/j.gca.2003.10.041

Hansel, C. M., and D. R. Learman. 2015. The Geomicrobiology of Manganese, p. 403–452. *In* Ehrlich, Newman, and Kappler [eds.], Geomicrobiology.

Hansel, C. M., C. A. Zeiner, C. M. Santelli, and S. M. Webb. 2012. Mn(II) oxidation by an ascomycete fungus is linked to superoxide production during asexual reproduction. Proc. Natl. Acad. Sci. U. S. A. **109**: 12621–12625. doi:10.1073/pnas.1203885109

Hein, J. R. 2014. Cobalt-Rich Ferromanganese Crusts : Global Distribution , Composition , Origin and Research Activities,.

Hein, J. R., and A. Koschinsky. 2014. Deep-ocean ferromanganese crusts and nodules. The Treatise on Geochemistry 273–291.

Hein, J. R., A. Koschinsky, M. Bau, F. T. Manheim, J.-K. Kang, and L. Roberts. 2000. Cobalt-Rich Ferromanganese Crusts in the Pacific, p. 239–279. *In* D.S. Cronan [ed.], Handbook of Marine Mineral Deposits. CRC Press.

Hein, J. R., A. Koschinsky, P. Halbach, F. T. Manheim, M. Bau, J.-K. Kang, and N. Lubick. 1997. Iron and manganese oxide mineralization in the Pacific. Geol. Soc. London, Spec. Publ. **119**: 123–138.

Hein, J. R., W. C. Schwab, D. G. Foot, and others. 1987. Farnella cruise F7-86-HW, cobalt-rich ferromanganese crust data report for Karin Ridge and Johnston Island, central Pacific. US Geological Survey.

Hein, J. R., U. States, and G. Survey. 2004. Cobalt-Rich Ferromanganese Crusts : Global Distribution , Composition , Origin Workshop on Minerals Other than Polymetallic Nodules Of the International Seabed Area Prepared by :,.

Horner, T. J., H. M. Williams, J. R. Hein, M. A. Saito, K. W. Burton, A. N. Halliday, and S. G. Nielsen. 2015. Persistence of deeply sourced iron in the Pacific Ocean. Proc. Natl. Acad. Sci. U. S. A. **112**: 1292–1297. doi:10.1073/pnas.1420188112

Jung, H. S., and C. B. Lee. 1999. Growth of diagenetic ferromanganese nodules in an oxic deep-sea sedimentary environment, northeast equatorial Pacific. Mar. Geol. **157**: 127–144. doi:10.1016/S0025-3227(98)00154-6

Jürgensen, A., J. R. Widmeyer, R. A. Gordon, L. I. Bendell-Young, M. M. Moore, and E. D. Crozier. 2004. The structure of the manganese oxide on the sheath of the bacterium Leptothrix discophora: An XAFS study. Am. Mineral. **89**: 1110–1118.

Klemm, V., S. Levasseur, M. Frank, J. R. Hein, and A. N. Halliday. 2005. Osmium isotope stratigraphy of a marine ferromanganese crust. Earth Planet. Sci. Lett. **238**: 42–48. doi:10.1016/j.epsl.2005.07.016

Koschinsky, A., and J. R. Hein. 2003. Uptake of elements from seawater by ferromanganese crusts: solid-phase associations and seawater speciation. Mar. Geol. **198**: 331–351. doi:10.1016/s0025-3227(03)00122-1

Koschinsky, A., A. Stascheit, M. Bau, and P. Halbach. 1997. Effects of phosphatization on the geochemical and mineralogical composition of marine ferromanganese crusts. Geochim. Cosmochim. Acta **61**: 4079–4094. doi:10.1016/s0016-7037(97)00231-7

Learman, D. R., B. M. Voelker, A. S. Madden, and C. M. Hansel. 2013. Constraints on superoxide mediated formation of manganese oxides. Front. Microbiol. **4**: 11. doi:10.3389/fmicb.2013.00262

Learman, D. R., B. M. Voelker, A. I. Vazquez-Rodriguez, and C. M. Hansel. 2011a. Formation of manganese oxides by bacterially generated superoxide. Nat. Geosci. **4**: 95–98. doi:10.1038/ngeo1055

Learman, D. R., S. D. Wankel, S. M. Webb, N. Martinez, A. S. Madden, and C. M. Hansel. 2011b. Coupled biotic-abiotic Mn(II) oxidation pathway mediates the formation and structural evolution of biogenic Mn oxides. Geochim. Cosmochim. Acta **75**: 6048–6063. doi:10.1016/j.gca.2011.07.026

Ling, F. T., J. E. Post, P. J. Heaney, and E. S. Ilton. 2018. The relationship between Mn oxidation state and structure in triclinic and hexagonal birnessites. Chem. Geol. **479**: 216–227. doi:10.1016/j.chemgeo.2018.01.011

Ling, H. F., K. W. Burton, R. K. O'Nions, B. S. Kamber, F. von Blanckenburg, A. J. Gibb, and J.

R. Hein. 2002. Evolution of Nd and Pb isotopes in Central Pacific seawater from ferromanganese crusts. Earth Planet. Sci. Lett. **146**: 1–12. doi:10.1016/s0012-821x(96)00224-5

Little, S. H., D. Vance, C. Walker-Brown, and W. M. Landing. 2014. The oceanic mass balance of copper and zinc isotopes, investigated by analysis of their inputs, and outputs to ferromanganese oxide sediments. Geochim. Cosmochim. Acta **125**: 673–693.

Manceau, A., A. I. Gorshkov, and V. A. Drits. 1992a. Structural chemistry of Mn, Fe, Co, and Ni in manganese hydrous oxides: Part I. Information from XANES spectroscopy. Am. Mineral. **77**: 1133–1143.

Manceau, A., A. I. Gorshkov, and V. A. Drits. 1992b. Structural chemistry of Mn, Fe, Co, and Ni in manganese hydrous oxides: Part II. Information from EXAFS spectroscopy and electron and X-ray diffraction. Am. Mineral. **77**: 1144–1157.

Manceau, A., M. Kersten, M. A. Marcus, N. Geoffroy, and L. Granina. 2007a. Ba and Ni speciation in a nodule of binary Mn oxide phase composition from Lake Baikal. Geochim. Cosmochim. Acta **71**: 1967–1981.

Manceau, A., M. Lanson, and N. Geoffroy. 2007b. Natural speciation of Ni, Zn, Ba, and As in ferromanganese coatings on quartz using X-ray fluorescence, absorption, and diffraction. Geochim. Cosmochim. Acta **71**: 95–128.

Manceau, A., M. Lanson, and Y. Takahashi. 2014. Mineralogy and crystal chemistry of Mn, Fe, Co, Ni, and Cu in a deep-sea Pacific polymetallic nodule. Am. Mineral. **99**: 2068–2083.

Manceau, A., N. Tamura, R. S. Celestre, A. A. MacDowell, N. Geoffroy, G. Sposito, and H. A. Padmore. 2003. Molecular-scale speciation of Zn and Ni in soil ferromanganese nodules from loess soils of the Mississippi Basin. Environ. Sci. Technol. **37**: 75–80.

Marcus, M. A., A. Manceau, and M. Kersten. 2004. Mn, Fe, Zn and As speciation in a fast-growing ferromanganese marine nodule. Geochim. Cosmochim. Acta **68**: 3125–3136.

Mayhew, L. E., S. M. Webb, and A. S. Templeton. 2011. Microscale imaging and identification of fe speciation and distribution during fluid-mineral reactions under highly reducing conditions. Environ. Sci. Technol. **45**: 4468–4474. doi:10.1021/es104292n

Nielsen, S. G., S. Mar-Gerrison, A. Gannoun, D. LaRowe, V. Klemm, A. N. Halliday, K. W. Burton, and J. R. Hein. 2009. Thallium isotope evidence for a permanent increase in marine organic carbon export in the early Eocene. Earth Planet. Sci. Lett. **278**: 297–307. doi:10.1016/j.epsl.2008.12.010

Nielsen, S. G., L. E. Wasylenki, M. Rehkamper, C. L. Peacock, Z. C. Xue, and E. M. Moon. 2013. Towards an understanding of thallium isotope fractionation during adsorption to manganese oxides. Geochim. Cosmochim. Acta **117**: 252–265. doi:10.1016/j.gca.2013.05.004

Ohta, A., and I. Kawabe. 2001. REE(III) adsorption onto Mn dioxide (delta-MnO2) and Fe oxyhydroxide: Ce(III) oxidation by delta-MnO2. Geochim. Cosmochim. Acta **65**: 695–703. doi:10.1016/s0016-7037(00)00578-0

Peacock, C. L., and E. M. Moon. 2012. Oxidative scavenging of thallium by birnessite: Explanation for thallium enrichment and stable isotope fractionation in marine ferromanganese precipitates. Geochim. Cosmochim. Acta **84**: 297–313.

doi:10.1016/j.gca.2012.01.036

Peacock, C. L., and D. M. Sherman. 2007. Crystal-chemistry of Ni in marine ferromanganese crusts and nodules. Am. Mineral. **92**: 1087–1092.

Post, J. E. 1999. Manganese oxide minerals: Crystal structures and economic and environmental significance. Proc. Natl. Acad. Sci. U. S. A. **96**: 3447–3454. doi:10.1073/pnas.96.7.3447

Puteanus, D., and P. Halbach. 1988. Correlation of Co concentration and growth rate—A method for age determination of ferromanganese crusts. Chem. Geol. **69**: 73–85.

Rona, P. A. 2008. The changing vision of marine minerals. Ore Geol. Rev. **33**: 618–666. doi:10.1016/j.oregeorev.2007.03.006

Santelli, C. M., S. M. Webb, A. C. Dohnalkova, and C. M. Hansel. 2011. Diversity of Mn oxides produced by Mn(II)-oxidizing fungi. Geochim. Cosmochim. Acta **75**: 2762–2776. doi:10.1016/j.gca.2011.02.022

Shiraishi, F., S. Mitsunobu, K. Suzuki, T. Hoshino, Y. Morono, and F. Inagaki. 2016. Dense microbial community on a ferromanganese nodule from the ultra-oligotrophic South Pacific Gyre: Implications for biogeochemical cycles. Earth Planet. Sci. Lett. **447**: 10–20. doi:10.1016/j.epsl.2016.04.021

Von Stackelberg, U., and D. S. Cronan. 2000. Manganese nodules of the Peru Basin. Handb. Mar. Miner. Depos. 197–238.

Sutherland, K. M., S. D. Wankel, and C. M. Hansel. 2018. Oxygen isotope analysis of bacterial and fungal manganese oxidation. Geobiology. doi:10.1111/gbi.12288

Takahashi, Y., A. Manceau, N. Geoffroy, M. A. Marcus, and A. Usui. 2007. Chemical and structural control of the partitioning of Co, Ce, and Pb in marine ferromanganese oxides. Geochim. Cosmochim. Acta **71**: 984–1008.

Tang, Y. Z., C. A. Zeiner, C. M. Santelli, and C. M. Hansel. 2013. Fungal oxidative dissolution of the Mn(II)-bearing mineral rhodochrosite and the role of metabolites in manganese oxide formation. Environ. Microbiol. **15**: 1063–1077. doi:10.1111/1462-2920.12029

Tebo, B. M., J. R. Bargar, B. G. Clement, G. J. Dick, K. J. Murray, D. Parker, R. Verity, and S. M. Webb. 2004. Biogenic manganese oxides: Properties and mechanisms of formation. Annu. Rev. Earth Planet. Sci. **32**: 287–328. doi:10.1146/annurev.earth.32.101802.120213

Tebo, B. M., H. A. Johnson, J. K. McCarthy, and A. S. Templeton. 2005. Geomicrobiology of manganese(II) oxidation. Trends Microbiol. **13**: 421–428. doi:10.1016/j.tim.2005.07.009

Villalobos, M., B. Toner, J. Bargar, and G. Sposito. 2003. Characterization of the manganese oxide produced by Pseudomonas putida strain MnB1. Geochim. Cosmochim. Acta **67**: 2649–2662. doi:10.1016/s0016-7037(03)00217-5

Wang, X., N. J. Planavsky, C. T. Reinhard, J. R. Hein, and T. M. Johnson. 2016. A cenozoic seawater redox record derived from 238U/235U in ferromanganese crusts. Am. J. Sci. **315**: 64–83. doi:10.2475/01.2016.02

Webb, S. M. 2005. SIXpack: a graphical user interface for XAS analysis using IFEFFIT. Phys. Scr. **T115**: 1011–1014.

Webb, S. M., G. J. Dick, J. R. Bargar, and B. M. Tebo. 2005. Evidence for the presence of Mn(III)

intermediates in the bacterial oxidation of Mn(II). Proc. Natl. Acad. Sci. U. S. A. **102**: 5558–5563. doi:10.1073/pnas.0409119102

Supplemental Figures

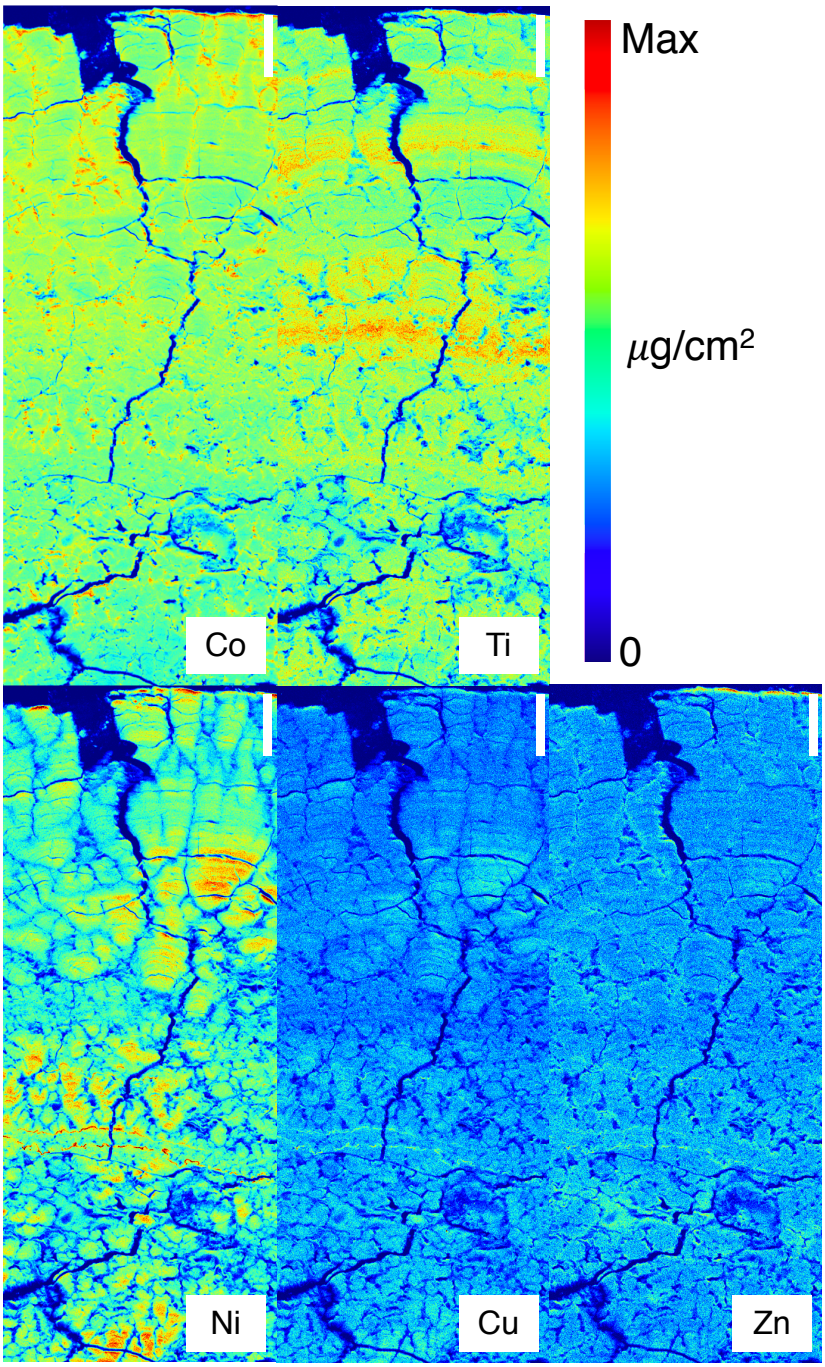

Figure S1- Micro- X-ray Fluorescence images of Co, Ti, Ni, Cu, and Zn of the topmost section (0-10 mm) of CD29 (corresponds to Figure 2 of the main text). Max concentrations are 1,350 μg/cm^2 (Mn, Fe), 200 μg/cm^2 (Co), 150 μg/cm^2 (Ti), 40 μg/cm^2 (Ni), and 10 μg/cm^2 (Cu, Zn). Scale bar (top right) is 1 mm.

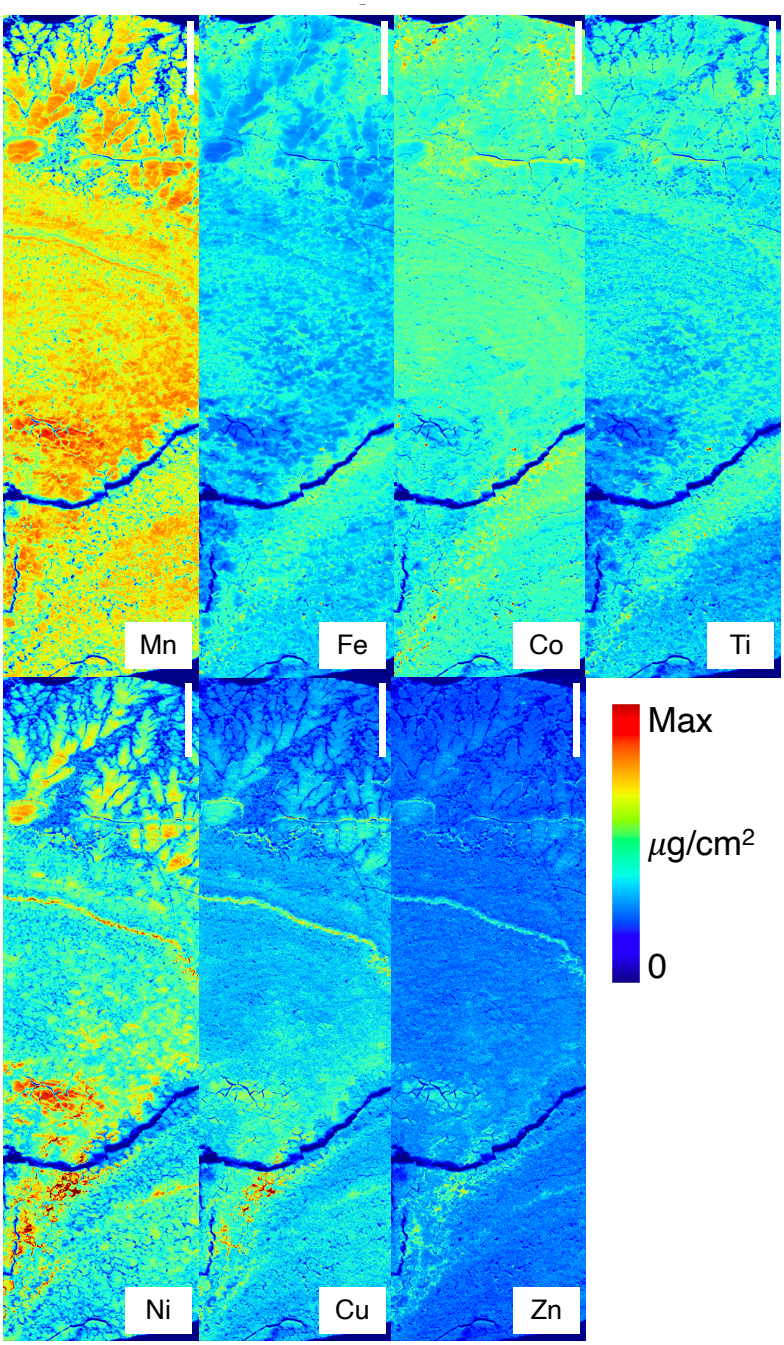

Figure S2- Micro- X-ray Fluorescence images of Mn, Fe, Co, Ti, Ni, Cu, and Zn of a central section of CD29 (corresponds to shallowest gray box in the XRF panel of Figure 1). Max concentrations are 1,350 μg/cm^2 (Mn, Fe), 100 μg/cm^2 (Co, Ti), 30 μg/cm^2 (Ni), and 10 μg/cm^2 (Cu, Zn). Scale bar (top right) is 2 mm.

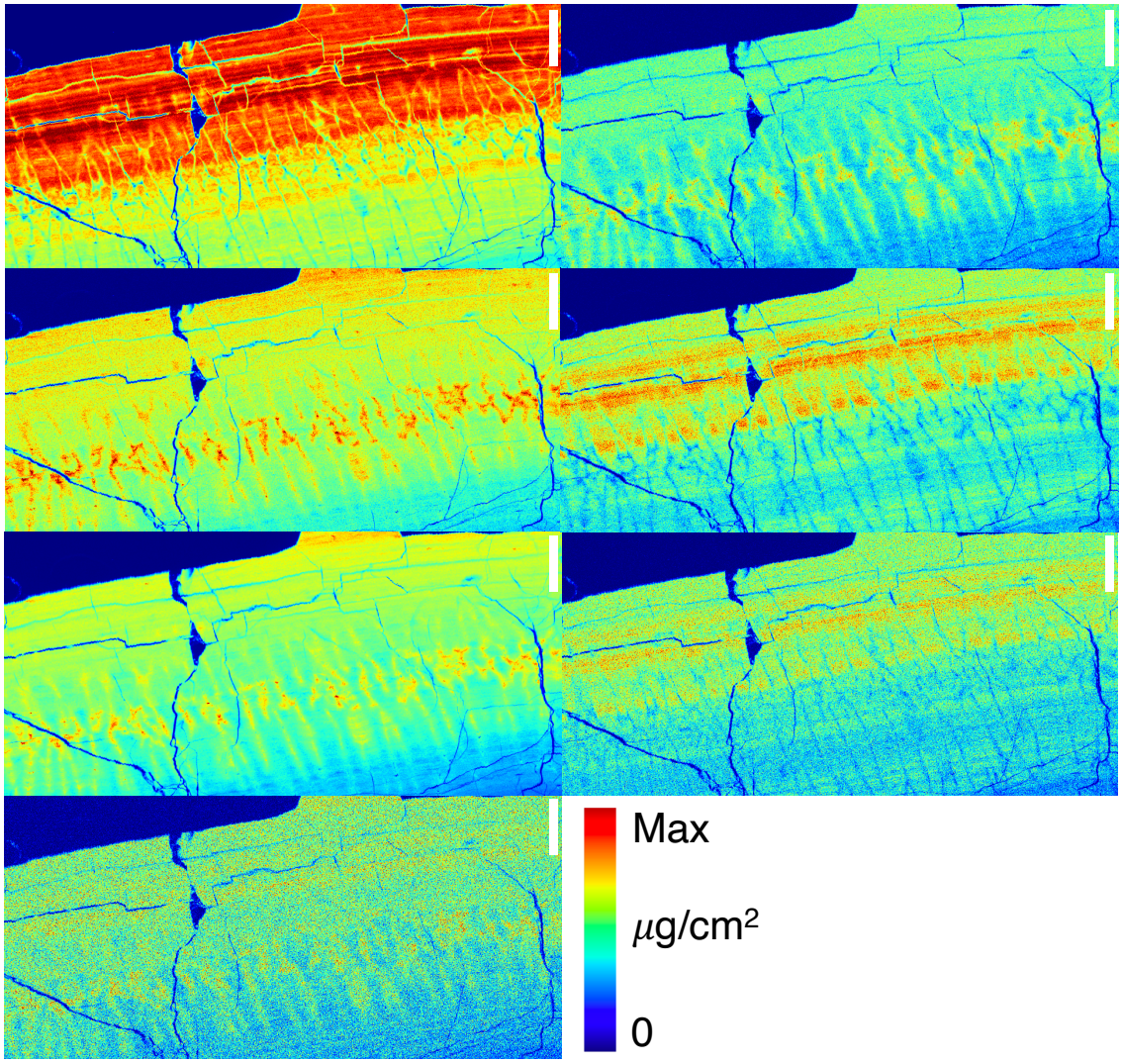

Figure S3- Micro- X-ray Fluorescence images of Mn, Fe, Co, Ti, Ni, Cu, and Zn of a central section of CD29 (corresponds to bottommost gray box in the XRF panel of Figure 1). Max concentrations are 1,350 μg/cm^2 (Mn, Fe), 100 μg/cm^2 (Co, Ti), 30 μg/cm^2 (Ni), and 10 μg/cm^2 (Cu, Zn). Scale bar (top right) is 1 mm.

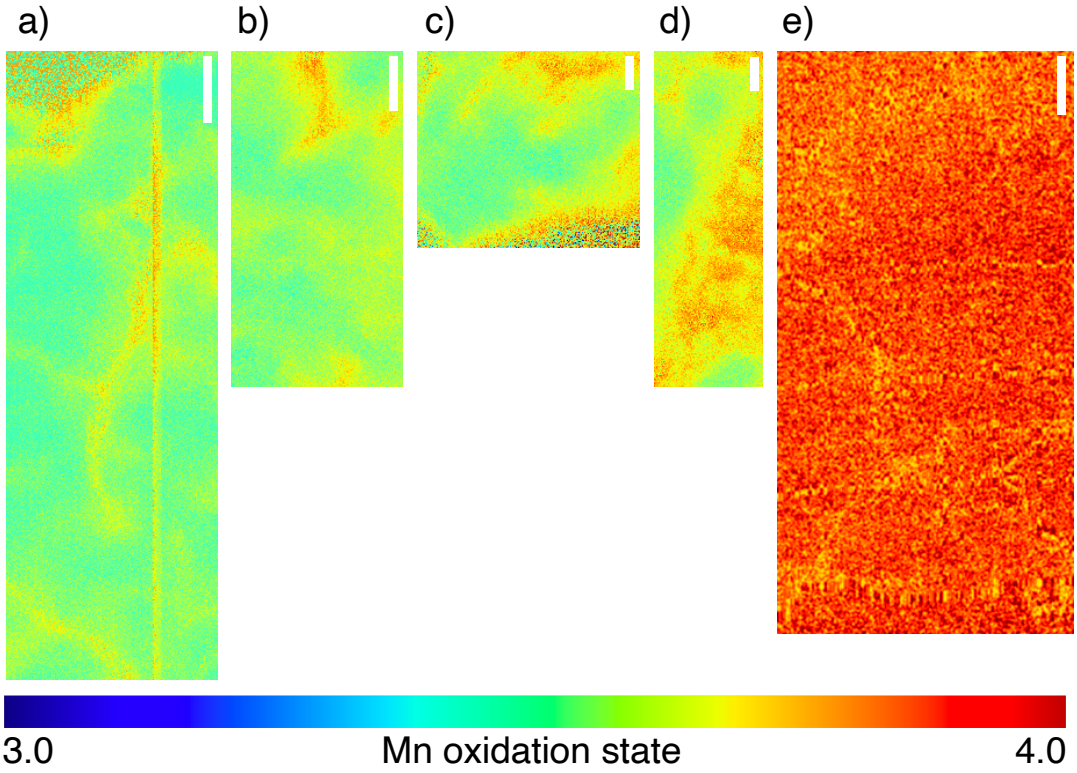

Figure S4- Manganese oxidation state maps from selected regions in the topmost (a,b,c, and d) and bottommost (e) sections of the crust. The five images shown correspond to the gray boxes in the "Redox Maps" panel of Figure 1. Scale bars are as follows: a) 200 μm, b) 200 μm, c) 100 μm, d) 100 μm, and e) 1 mm.

4. Ferromanganese Crusts as Recorders of Marine Dissolved Oxygen

This chapter is in review at *Earth and Planetary Science Letters*.

Abstract

The distinct triple oxygen isotope composition of tropospheric O_2 relative to seawater is the result of biogeochemical reactions (e.g. primary productivity, respiration), exchange with the stratosphere, and the relative size of different oxygen-containing reservoirs, namely O_2, O_3, and CO_2. This difference in isotopic composition gives tropospheric O_2 utility as a record of biogeochemical and atmospheric processes and may also be used for determining where in the rock record isotopic fingerprints of tropospheric oxygen may be preserved. The isotopic record of tropospheric oxygen in previous studies is largely limited to analyses of gas trapped in continental glaciers and a patchwork of other proxies, most notably the triple oxygen signature of sulfate. Here we show the uppermost layers of hydrogenetic, deep-ocean ferromanganese crusts from each of the major ocean basins have a triple oxygen isotope composition consistent with the direct incorporation of dissolved oxygen. The range of $\delta^{18}O$ and $\Delta'^{17}O$ in ferromanganese crusts suggests the Mn oxide endmember contains a near 50:50 mixture of oxygen from water and dissolved O_2. Our data indicate this signal also persists into older layers of the crusts, potentially preserving near 75 million years of the oxygen isotopic composition of the lower troposphere and subsequent deep-ocean respiration. Although some analytical challenges remain, these widespread, layered deposits of ferromanganese crust offer a tractable path for interrogating the history of the oxygen cycle of the troposphere and deep ocean millions of years into the past.

4.1 Introduction

The $^{18}O/^{16}O$ ratio of diatomic oxygen (expressed as $\delta^{18}O_{O2}$) in the troposphere integrates biogeochemical reactions and atmospheric exchange processes that produce, consume, and mix O_2 (Bender et al., 1994). The $\delta^{18}O_{O2}$ of the modern troposphere (~+24‰) (Barkan and Luz, 2005; Wostbrock et al., n.d.) is set primarily by mass-dependent processes that discriminate against the heavier isotopes during reduction of O_2 or evapotranspiration of leaf water (e.g., the 'Dole Effect') (Bender et al., 1994; Hoffmann et al., 2004). Ice core records indicate that the $\delta^{18}O_{O2}$ of the troposphere has fluctuated by >1‰ over the last hundred thousand years, primarily due to changes in the $\delta^{18}O$ of seawater from the periodic sequestration of isotopically light water in continental ice and changes in the magnitude of the Dole effect (Bender et al., 1994). In comparison, the $^{17}O/^{16}O$ composition of tropospheric O_2, typically expressed in linearized form as $\Delta'^{17}O$ ($\Delta'^{17}O = \delta'^{17}O - \lambda\delta'^{18}O$, with λ=0.528 used in this study), is controlled by mass-dependent processes and vertical mixing with the stratosphere where mass-independent exchange reactions occur (Blunier et al., 2002; Luz et al., 1999; Thiemens and Heidenreich, 1983). The $\Delta'^{17}O$ value of tropospheric O_2 is influenced by the partial pressures of CO_2 and O_2, their biogeochemical fluxes, and atmospheric vertical exchange (Cao and Bao, 2013; Thiemens, 2006). Importantly, modern tropospheric O_2 ($\Delta'^{17}O \approx -0.5$‰) has a triple oxygen isotope signature distinct from that of ocean water ($\Delta'^{17}O = 0$‰), which can be used as an independent tracer of O_2 cycling dynamics (Barkan and Luz, 2005; Luz et al., 1999; Pack et al., 2017; Wostbrock et al., n.d.).

The coarse and fine details of the oxygen cycle elucidated by direct measurements of $\delta^{18}O$ and $\Delta'^{17}O$ of atmospheric O_2 are largely limited to paleo-atmosphere trapped in continental ice (Bender et al., 1994; Blunier et al., 2002). These studies have used the oxygen isotope composition of ice-trapped atmosphere to estimate primary production in marine and terrestrial environments and identify the key influences on O_2 cycling dynamics on timescales up to ~100,000 years. As a high-potential oxidant of many reduced materials on the surface earth, the isotopic signature of O_2 can be retained by some oxygen-bearing minerals (e.g., sulfate (Crockford et al., 2018), phosphate (Gehler et al., 2011)), though oxygen isotope exchange of biotic or abiotic origin can confound interpretation and limit the timescales on which questions about past oxygen cycling can be addressed.

Manganese oxides are extremely common and geographically widespread in marine environments (Uramoto et al., 2019), exceeding 50% coverage of the seafloor in some abyssal

regions of the global ocean (Hein and Koschinsky, 2014). Manganese(II) oxidation by O_2 can be facilitated by biological or abiotic processes, including enzyme catalysis, surface and ligand complexation, or reactive oxygen species (ROS) of various origins (Learman et al., 2011; Sutherland et al., 2018; Tebo et al., 2005). Study of synthetic manganese (Mn) oxy(hydr)oxide minerals (hereafter referred to as Mn oxides) suggests they capture and retain oxygen atoms from dissolved O_2 during oxidation of aqueous Mn(II) to insoluble Mn(III/IV) (Mandernack et al., 1995; Sutherland et al., 2018). $\Delta'^{17}O$ values of one natural ferromanganese nodule suggests the same may be true in natural Mn oxides (Sharp et al., 2018), though comprehensive confirmation that this occurs in all natural low temperature Mn oxides has not yet been achieved (Luther, 2010; Mandernack et al., 1995; Sutherland et al., 2018). Thus, Mn oxides, if resistant to isotopic exchange with ambient water, could serve as a valuable isotopic proxy for O_2 over the lifetime of the oceanic crust on which these deposits form.

Let us consider what information may be gained from a detailed geochemical proxy for the triple oxygen isotope composition of dissolved oxygen. Gas exchange at the ocean surface leads to isotopic equilibrium between the atmosphere and dissolved gases. Following deep-water formation, the primary process influencing dissolved O_2 (DO) is the reduction of O_2 by biological processes, the most consequential being respiration. The biological reduction of O_2 roughly follows a closed-system Rayleigh fractionation curve (in addition to advection and diffusion), producing a monotonic increase in $\delta^{18}O$ with decreasing concentrations of DO (Kroopnick, 1980; Levine et al., 2009; Stolper et al., 2018). The $\delta^{18}O$ of dissolved oxygen in the marine water column typically ranges from ~+23‰ in productive surface waters to greater than +40‰ near the oxygen minimum (Levine et al., 2009). Assuming ~50% of oxygen atoms in the Mn-oxide endmember are from dissolved O_2, we would expect the oxygen isotope signature of Mn oxides to track that of O_2 with approximately half the magnitude and an offset accounting for any isotope fractionation.

Hydrogenetic, deep-ocean ferromanganese crusts have several characteristics that make them ideal hosts of such a geochemical proxy. Ferromanganese crusts are geographically widespread, form as layered deposits offering a clear sense of time, and age within a narrow temperature range. These deposits primarily constitute a co-precipitated mixture of Mn and Fe oxide phases, and often contain several weight percent of detrital or authigenic silicates and transition metals including cobalt, nickel, and copper. While the heterogeneity of ferromanganese deposits presents a challenge to isolating individual phases, here we demonstrate that bulk

ferromanganese-crust compositions contain clear indication of atmospheric O_2 in deposits over 30 Ma old and assess their fidelity as an isotopic record of DO. Below we first consider the $\delta^{18}O$ of natural ferromanganese deposits in both new and historical datasets (Section 3.1), followed by new insights offered by triple oxygen isotope results for the same sample set (Section 3.2).

4.2 Materials and Methods

4.2.1 Sample Location and Preparation

The top-most portion of each ferromanganese crust in this study served as the primary analytical target as it represents the youngest crust and has had the least amount of time to undergo possible post-depositional alteration. The top 0.5 mm to 3 mm was sampled from each crust using a ceramic blade. Sample locations and information are presented in Table 1 and shown in Figure 1. The geochemistry of ten major elements for the samples was determined by X-ray fluorescence (XRF) on borate-fused discs, which is included in the Supplemental Material along with sample ID, latitude and longitude, water depth, and the crust depth interval on which XRF was collected. Due to the difference in sampling intervals between XRF analysis and triple oxygen isotope analysis, the geochemical data presented in the Supplemental Material should be considered an approximation in relation to the triple oxygen isotope data. Sampling of CD29 below the stratigraphic intervals presented in Table 2 was not conducted due to significant phosphatization (formation of authigenic carbonate fluorapatite) in the crust (Frank et al., 1999). Ferromanganese crusts may also host extraterrestrial material (e.g. micrometeorites, cosmic spherules) in their matrix (Basu et al., 2006; Halbach et al., 1989). Meteorites typically exhibit anomalous $\Delta'^{17}O$ values, typically ranging from -1 to +1‰, with some exceptions (Clayton et al., 1983; Clayton and Mayeda, 1996). One study found such extraterrestrial material made up approximately 2 ppm of a ferromanganese crust by mass (Halbach et al., 1989). Given the low abundance of extraterrestrial material in ferromanganese crusts, we will not consider this minor contribution in subsequent oxygen isotope mass balance calculations.

4.2.2 Oxygen Isotope Measurements

Samples were analyzed using a ThermoFinnigan MAT 253 configured for O_2 analysis at the University of New Mexico Center for Stable Isotopes. All samples were analyzed as O_2 gas, which was extracted using conventional laser fluorination (Sharp, 1990). Each sample was placed

in a drying oven (110ºC) for a minimum of 12 hours prior to handling to drive off adsorbed water. We measured the effect of this drying procedure on the average Mn oxidation state of one sample (CD29 0-2.5mm, average oxidation state: +3.5) using X-ray absorption spectroscopy and found no significant change in the average Mn oxidation state before and after drying. The dried samples were weighed (2-4 mg) before introduction to the fluorination chamber. Samples were pre-fluorinated with 100 mbar BrF_5 gas for approximately 1-2 hours. Prior to the analyses presented in this study, we observed a steady decrease in sample O_2 yield and $\delta^{18}O$ value the longer a standard was exposed to BrF_5 in the sample chamber. Given the direction of the $\delta^{18}O$ shift, we concluded that one of the components in the ferromanganese material was undergoing passive reaction with BrF_5 due to incidental heating from the laser. Submerging the sample chamber in an ice bath during sample fluorination prevented this passive reaction; all analyses reported in this study were measured using this procedure. Following O_2 extraction, the sample was passed through multiple liquid nitrogen traps, a warm sodium chloride trap, and a gas chromatography column to remove contaminants. The effluent O_2 was condensed onto a 5Å molecular sieve and the carrier gas (ultra-high purity helium) was pumped away prior to introduction into the mass spectrometer. The reference gas used in this study is calibrated to VSMOW and SLAP, and all values are standardized to the VSMOW-SLAP scale. The delta values presented in this study ($\delta^xO = ({}^xR_{sample}/{}^xR_{standard} - 1) \times 1000$, ${}^xR_{sample} = {}^xO/{}^{16}O$) are converted to linearized delta notation ($\delta'^xO = 1000(\ln(1+\delta^xO/1000))$) (Hulston and Thode, 1965; Miller, 2002). The oxygen-17 compositions are reported using the $\Delta'^{17}O$ value, defined as $\Delta'^{17}O = \delta'^{17}O - \lambda\delta'^{18}O$, where λ is a reference slope. We use $\lambda=0.528$ to report values in this study's text, table, and figures, and include $\Delta'^{17}O$ values calculated using $\lambda=0.5305$ (theoretical high temperature limit) for ease of comparison to studies using this convention. We also discuss θ values of equilibrium and kinetic processes throughout the text, which are defined as $\theta = \ln^{17}\alpha/\ln^{18}\alpha$, ${}^x\alpha = {}^xR_A/{}^xR_B$, respectively, where A and B represent two oxygen-bearing compounds.

There has been only limited investigation on the triple oxygen isotopic analysis of ferromanganese materials. The $\delta^{18}O$ values of some Mn oxides and ferromanganese materials have been previously measured (Mandernack et al., 1995; Sutherland et al., 2018; Yeh et al., 1985). We performed an interlaboratory comparison of $\delta^{18}O$ of a widely available ferromanganese reference material (USGS Nod-A-1) to ensure that the oxygen isotope measurements are robust and sample conversions to O_2 were near complete. Bulk and trace metal chemistry for USGS Nod-A-1 have

been previously characterized (Flanagan and Gottfried, 1980). For inter-laboratory comparison, USGS Nod-A-1 was measured on the MAT 253 at UNM and also at the Woods Hole Oceanographic Institution (WHOI) using high temperature micro-fluorination on an Isoprime100 IRMS (analytical precision ±0.4‰ for Mn Oxides). In short, samples run with micro-fluorination method were packed with Teflon powder and pyrolyzed at 1450ºC. A more detailed treatment of the method is described elsewhere (Menicucci et al., 2013; Sutherland et al., 2018). The mean $\delta'^{18}O$ of USGS Nod-A-1 was +11.600 ± 1.544‰ (n=9) and +11.8 ± 0.7‰ (n=9) measured at UNM and WHOI, respectively. No statistically significant difference was observed between the two sets of measurements (two-sample t-test, p=0.73). $\Delta'^{17}O$ values could only be measured using the conventional fluorination method. The $\Delta'^{17}O$ value of Nod-A-1 is -0.112±0.014 (n=9).

4.2.3 Estimate of Marine Dissolved Oxygen

Measurements of marine dissolved O_2 are routinely collected as a part of oceanographic research, making a direct comparison between the oxygen isotope composition of ferromanganese crust and an estimate of local DO concentration possible. The World Ocean Atlas 2018 (WOA2018) offers sufficient spatial resolution to produce such an estimate for each of the sample locations in this study (Garcia et al., 2018). The WOA2018 dissolved oxygen data was queried for the dissolved oxygen concentration at the latitude, longitude, and depth closest to the sample location (data shown in Table S1). If the sample depth was not available at the closest latitude and longitude, the next closest cell for which the sample depth was available was used. We also manually inspected adjacent data points to ensure dissolved oxygen concentrations smoothly varied locally.

4.3 Results and Discussion

4.3.1 $\delta^{18}O$ of Manganese Oxides

We determined the $\delta^{18}O$ values of 13 ferromanganese crusts from 12 locations throughout the global ocean (Figure 1). The range of $\delta^{18}O$ values of these ferromanganese crusts spans from +5.1‰ to +11.9‰ (average: +9.0, standard deviation: 1.7‰), with top-layer samples occupying a slightly more limited range (+6.7‰ to +11.9‰, average: +9.7‰, standard deviation: 1.3‰, Table 2). The stratigraphically older subsamples of F7-86-HW CD29 ranged from +5.1‰ to +8.4‰ (average: +7.2‰, standard deviation: 1.1‰,). The range of $\delta^{18}O$ values in the sample set may

reflect a variety of factors, including different environmental conditions (e.g. O_2 concentration), bulk chemistry and/or mineralogy, or diagenesis. The $\delta^{18}O$ values alone cannot be used to distinguish these processes because the oxygen isotope mass balance is underconstrained when the isotopic composition of water or O_2 is unknown *a priori*. In addition to multiple oxygen sources, variability among isotope fractionation factors, the relative contribution of each oxygen source, Mn oxidation state, and the partial or complete isotopic equilibration with ambient water may confound the $\delta^{18}O$ values of natural manganates. To determine what information can be gathered from $\delta^{18}O$ values, we compiled every oxygen isotope measurement of Mn oxides and Mn oxide-rich material available in the literature (103 measurements; Figure 2) (Bar-Matthews and Matthews, 1990; Chyi et al., 1984; Dymond et al., 1973; Levin et al., 2014; Mandernack et al., 1995; Sharp et al., 2018; Yeh et al., 1985). We categorize previous samples as either non-marine, which range from -7.7‰ to +6.4‰, or marine samples, which range from -1.0‰ to +21.9‰. If we omit marine samples exhibiting clear evidence of hydrothermal alteration and those containing a significant portion of silicate material, the range of $\delta^{18}O$ of marine Mn oxides narrows to +5.5‰ to +15.8‰. This range is more than double that of deep ocean marine carbonates over the last 70 Myr (e.g. Zachos et al., 2001).

A bimodal separation is evident, where non-marine Mn oxides have a lower $\delta^{18}O$ value than marine Mn oxides ($p < 0.0001$, two-sample t-test) (Figure 2). Non-marine samples average -1.4‰, while marine samples average +10.8‰. The difference between the average marine and non-marine samples, ~12 per mil, bears the oxygen isotope fingerprints of ocean and meteoric water. However, such an interpretation is complicated by complex thermal histories, incomplete mineralogical information, unknown source oxygen, and compositional heterogeneity. In fact, an outlier among the marine samples, a hydrothermal Mn oxide lens from the Franciscan Assemblage, has a calculated $\delta^{18}O$ value of -1.0‰ for the Mn oxide and reflects a clear history of hydrothermal alteration in the presence of seawater (Chyi et al., 1984). The differences between terrestrial vs. marine Mn oxides and primary vs. hydrothermal marine Mn oxides could be reconciled by one or more of three likely scenarios. First, all Mn oxides could be in oxygen isotope equilibrium with its water of formation (marine or meteoric), with higher $\delta^{18}O$ values corresponding to lower water temperatures. Second, mineralogical differences (e.g. Mn oxide mineral phases) may produce different equilibrium oxygen fractionation factors between water and Mn oxide minerals. Lastly, low-temperature Mn oxides (which may or may not derive their

oxygen from O_2) may not typically exchange oxygen with the surrounding water except when exposed to high temperatures or certain recrystallization conditions, causing oxygen atoms to re-equilibrate with ambient water.

One anecdotal comparison between marine Mn oxides and a freshwater Mn oxide formed in water of known $\delta^{18}O$ composition provides a useful perspective for narrowing down the most parsimonious model for oxygen isotope systematics in our data compilation. A freshwater ferromanganese nodule from Lake Oneida ($\delta^{18}O_{H2O}$ = -8.9‰) has a calculated Mn-oxide $\delta^{18}O$ value of +7.5‰, 16.4‰ higher than the corresponding lake water (Mandernack et al., 1995). By comparison, the average marine Mn oxide has a $\delta^{18}O$ value of +10.8‰, corresponding to an offset of +10.8‰ from the $\delta^{18}O$ value of seawater (~0‰). Thus, the difference between the $\delta^{18}O$ values of marine and freshwater Mn oxides (3.3‰) is only ~40% the difference between the $\delta^{18}O$ values of their waters of formation (8.9‰). This difference is unlikely to be explained only by temperature since the approximate temperature difference is just a few degrees C (Mandernack et al., 1995). The lack of 1:1 correlation between the $\delta^{18}O$ values of Mn oxides and their environmental water is consistent with the incorporation of DO in hydrogenetic Mn oxides, and is explained by a ~60% contribution from dissolved O_2. The 40% incorporation of oxygen atoms from ambient water with the remainder coming from DO is supported by controlled laboratory experiments that found 38%–62% O_2 incorporation among several biotic and abiotic Mn oxidation reactions (Mandernack et al., 1995; Sutherland et al., 2018). Although this single freshwater oxide is consistent with the oxygen isotope framework presented in previous studies, we caution the reader that more measurements of freshwater systems are necessary for a robust comparison.

4.3.2 $\Delta'^{17}O$ of Manganese Oxides

Triple oxygen isotope measurements provide an additional dimension to explore the oxygen source to ferromanganese crusts. The $\Delta'^{17}O$ values of ferromanganese crusts in this global crust-top survey ranged from -0.088‰ to -0.200‰ (Table 2). Measured values in the stratigraphic study of CD29 ranged from -0.147‰ to -0.200‰. The only other reported values of $\Delta'^{17}O$ for marine ferromanganese deposits similarly range from -0.070‰ to -0.172‰ (Sharp et al., 2018). Intriguingly, these Mn oxides occupy a unique region in oxygen three-isotope space that is not shared by any commonly measured Earth materials (Figure 3) and are inferred to have incorporated low-$\Delta'^{17}O$ from dissolved diatomic oxygen (Mandernack et al., 1995; Sharp et al., 2018;

Sutherland et al., 2018). We can better contextualize the distribution of ferromanganese triple oxygen isotope compositions by considering their bulk chemistry. The primary oxygen-bearing phases in ferromanganese crusts include Mn and Fe oxides, with minor contributions from silicate phases (bulk ferromanganese crust chemistry data provided in the Supplemental Material). While other metal oxides are present, some of which may share oxygen bonds with the primary Mn, Fe, or Si phases, their contributions to the oxygen mass balance is minor and we do not consider them here. Of these three primary oxygen-bearing mineral groups, the systematic experimental or theoretical investigation of mineral-water triple oxygen isotope equilibria have only been conducted for a few iron (Fe) oxide and silicate minerals (Hayles et al., 2018; Sharp et al., 2016). Authigenic Fe oxides (hematite and magnetite) formed at bottom water temperatures are expected to have a $\Delta'^{17}O$ value no lower than -0.040‰ ($\delta'^{18}O$ = ~3‰ at 0ºC) (Hayles et al., 2018). Iron oxides in ferromanganese crusts are typically poorly crystalline Fe oxyhydroxides having a presumably similar $\Delta'^{17}O$ values to other Fe oxides and thus to that of seawater (Frank et al., 1999; Hein and Koschinsky, 2014). In comparison, silicates of detrital or authigenic origin may span a much wider range of $\Delta'^{17}O$ values (Sharp et al., 2016). The $\Delta'^{17}O$ values of detrital silicates from high temperature systems are approximately 0‰, while low-temperature silica deposits (e.g. chert or opal) formed in 0˚C seawater will have $\delta'^{18}O$ and $\Delta'^{17}O$ values of +44.5‰ and -0.190‰, respectively. The triple oxygen isotope values of other silicate minerals will likely vary from the pure SiO_2–water equilibrium isotope fractionation curve, though a systematic analysis of other relevant silicates has not been conducted. One anecdotal data point of a clay mineral, which are commonly present in ferromanganese crusts, falls very close to the SiO_2-H_2O equilibrium line (e.g. kaolinite $\delta'^{18}O$=24.536‰ and $\Delta'^{17}O$=-0.030‰) (Sengupta, 2016) (Figure 3). For simplicity, we assume any silicates present in the crust fall on this SiO_2-H_2O equilibrium line. The range of $\delta'^{18}O$ and $\Delta'^{17}O$ values from a mixture of silicate and low-temperature Fe oxides cannot produce a $\Delta'^{17}O$ low enough to describe the bulk ferromanganese crust values (Figure 3). In sum, the Mn-oxide endmember must have lower $\Delta'^{17}O$ values to explain the bulk crust values.

For completeness, we consider three plausible explanations for the distribution of $\delta'^{18}O$ and $\Delta'^{17}O$ in Mn-oxide minerals. First, ferromanganese crusts may reflect mineral-water oxygen isotope equilibrium between oxide and seawater. Second, DO may be kinetically incorporated with a small oxygen isotope fractionation ($^{18}\varepsilon_{MnOx\text{-}O2} \approx 0$‰) and preserved in ferromanganese crusts (Mandernack et al., 1995). Lastly, DO may be kinetically incorporated in Mn oxides with a large

isotope fractionation ($^{18}\varepsilon_{MnOx\text{-}O2} \approx$ -20‰) and preserved in ferromanganese crusts (Mandernack et al., 1995; Sutherland et al., 2018).

First, we consider whether it is possible for an equilibrium isotope fractionation regime to play a role in the oxygen isotope composition of the ferromanganese crusts. Temperature is the main driver of variation during equilibrium oxygen isotope processes (Sharp, 2017). The $\delta^{18}O$ values of the crusts used in this study range from 5.1-11.9‰. Bottom water temperature does not vary between sites by more than a few degrees C, and the $\delta^{18}O$ value of bottom water varies by ~0.5‰ (Adkins et al., 2002). Since temperature and water oxygen isotope composition are essentially constant, the 6.8‰ variation in our dataset cannot be explained using equilibrium fractionation processes alone. Although there is no direct evidence of Mn oxides forming in oxygen isotope equilibrium with water, we can also evaluate whether these $\Delta'^{17}O$ values could reasonably result from equilibrium processes by looking at the inferred $\delta^{17}O$-$\delta^{18}O$ fractionation relationship between samples, or $\theta_{EQ\text{-}inferred}$. Typically, θ is used to describe a fixed triple oxygen mass relationship intrinsic to a single process at a given temperature. In this thought experiment we use $\theta_{EQ\text{-}inferred}$ and the assumption that a sample is in equilibrium with seawater, to evaluate whether the observed triple oxygen values are more consistent with a composition reflecting oxygen isotope equilibrium with seawater or some mixture of water and dissolved O_2 (Sutherland et al., 2018). Typical values of θ_{EQ} in low-temperature (0-100ºC) mineral-water oxygen isotope equilibrium vary from 0.523 to 0.525 (Bao et al., 2016; Cao and Liu, 2011). Computational studies investigating the bounds of θ between two oxygen-bearing systems (not just mineral-water pairs) have shown that θ may deviate from canonical values when $^{18}\alpha$ is low, but even still, 90% of theoretical oxygen-bearing species pairs produce θ values falling in the range 0.5285±0.01 (Bao et al., 2015). In comparison, we calculate values of $\theta_{EQ\text{-}inferred}$ of 0.499 to 0.520 for the global ferromanganese crusts, with an average value of 0.513. The Mn-oxide endmember contained within these ferromanganese crusts must have a $\theta_{EQ\text{-}inferred}$ that is lower still if the other O-bearing components in the crust (e.g., Fe oxides and silicates) fall within the typical 0.523 to 0.525 range. Mn oxides with the lowest $\Delta'^{17}O$ have a $\theta_{EQ\text{-}inferred}$ of ~0.500, a value quite distinct from those typically observed in mineral-water equilibrium systems. Similarly low values of θ have been observed for some kinetic isotope effects related to reactive oxygen species production (derived from O_2) and some observations of respiration (Helman, 2005; Stolper et al., 2018). However,

given that $\theta_{EQ\text{-}inferred}$ deviates quite significantly from typical θ_{EQ} predictions and from observations of θ_{EQ} in mineral-water systems, mineral-water oxygen isotopic equilibrium can plausibly be ruled out for these natural marine Mn-oxide phases.

Next, we consider kinetic incorporation of DO and water with very little fractionation. There is evidence for a Mn-oxide endmember that derives its oxygen from a 50:50 mixture of O_2 and H_2O with little to no oxygen isotopic fractionation with respect to each source. This has been observed in one example of bacterial Mn(II) oxidation (*Aurantimonas manganoxydans* SI85-9A1 and inferred for freshwater ferromanganese nodules form Lake Oneida (Mandernack et al., 1995). This theoretical Mn-oxide endmember would fall on a mixing line between H_2O and O_2 (MnOx1 in Figure 3), and could adequately explain the observed distribution of $\delta'^{18}O$ and $\Delta'^{17}O$ in the global ferromanganese crust samples (given certain constraints on the silicate endmember). While this explanation is plausible, it raises questions as to why O_2 may be subject to such a wide range of fractionation regimes during Mn oxidation. We discuss this further below (Section 3.5).

Lastly, we consider kinetic incorporation of DO with a large fractionation factor. In laboratory precipitated oxides, the oxidation of aqueous Mn(II) to Mn(III/IV) mediated by bacterial, fungal, and abiotic processes results in a large mineral-DO oxygen isotope fractionation ($^{18}\varepsilon_{MnOx\text{-}O2}$= -17 to -23‰) and a small mineral-water oxygen isotope fractionation ($^{18}\varepsilon_{MnOx\text{-}H2O}\approx$0‰) (Mandernack et al., 1995; Sutherland et al., 2018). In these systems, approximately half of the oxygen atoms derive from each reservoir (DO and H_2O). If natural Mn oxides exhibit similar isotope fractionation factors during formation as laboratory precipitated oxides, we would expect the Mn-oxide endmember to have $\delta'^{18}O$ and $\Delta'^{17}O$ values of approximately 0–+4‰ and -0.080– -0.180‰, respectively (MnOx2 in Figure 3, assuming starting $\delta^{18}O_{O2}$ = +24.5‰, $\Delta'^{17}O_{O2}$ = -0.45‰ and $\delta^{18}O_{H2O}$ = 0‰, $\Delta'^{17}O_{H2O}$ = 0‰, ε_{O2} = -17– -23‰, ε_{O2} = 0‰, and θ_{KIE} = 0.515-0.520). This theoretical Mn-oxide endmember could explain $\delta'^{18}O$ and $\Delta'^{17}O$ values in bulk ferromanganese crusts, but would require that most silicate in the sample formed at low temperature or that θ_{KIE} be slightly higher than we assume (Figure 3). In either case, the large fractionation framework represents most lab-based observations and can explain the $\Delta'^{17}O$ of natural ferromanganese crusts, thereby offering the most parsimonious explanation for the Mn oxide system.

Indeed, the incorporation of DO into Mn-oxide minerals under both fractionation frameworks (MnOx1 and MnOx2, Figure 3) provides plausible explanations for the triple oxygen values and $\theta_{EQ\text{-}inferred}$ observed in the global ferromanganese crust dataset (Mandernack et al., 1995;

Sutherland et al., 2018). MnOx2 offers a particularly compelling explanation as it reconciles synthetic and natural oxides. Mineral-water equilibrium does not offer a satisfactory explanation of the ferromanganese crusts $\Delta'^{17}O$. Observationally, Mn-oxide minerals precipitated by biotic and abiotic reaction mechanisms at low temperatures in circumneutral pH waters do not exchange oxygen isotopes with water (Mandernack et al., 1995). Instead, these low-temperature Mn oxides retain oxygen derived from the surrounding dissolved O_2 and water. Such a mixture of O atom sources would in fact yield values for $\theta_{EQ\text{-}inferred}$ lower than what is typically observed in mineral-water equilibrium; in fact, θ would no longer be an appropriate variable to use since our calculated θ values represent the result of an isotopic mixture and isotopic fractionation – rather than a single fractionating process.

A significant question still remains: why do Mn oxides exhibit such a significant mineral-DO oxygen isotope fractionation range? Synthetic biotic and abiotic Mn oxides are typically precipitated in systems designed to quickly oxidize a significant quantity of Mn(II), typically involving >100 μM Mn(II) and unnaturally high abundances of Mn(II)-oxidizing microbes, and likely fail to capture the complexity of Mn speciation in nature. Mn oxidation rates in nature are typically much slower than in benchtop experiments. Further, Mn(III)-ligand complexes can comprise a significant fraction (>80%) of the dissolved Mn pool in oxic marine environments (Oldham et al., 2017), and thus natural Mn oxides may form in large part via the one-electron oxidation of Mn(III). To our knowledge, there has been no study on the oxygen isotope effects of Mn(III)-ligand complex oxidation. The range of fractionation factors may reflect the diversity of Mn-ligand complexes and their coordination with O_2 prior to oxidation. In any case, the inferred differences in oxygen isotope fractionation between the high-fractionation and low-fractionation cases require further study to determine the conditions under which each mechanism is operative. From here we explore the utility of triple oxygen isotopes of Mn-oxide minerals and associated challenges with its realization.

4.3.3 Comparison to Estimates of Marine Dissolved Oxygen

We performed a pairwise linear regression of the estimated local dissolved oxygen concentration (see methods) against the other five measured parameters (Fe wt%, Mn wt%, Si wt%, $\delta^{18}O$, and $\Delta'^{17}O$, full results available in the Supplemental Material). Only two of these five parameters (Mn wt% and $\delta^{18}O$) had an R^2 greater than 0.1 when plotted against DO: Mn wt% and

$\delta^{18}O$. Mn wt% and the dissolved oxygen concentration demonstrated a negative relationship with a fairly robust correlation (R^2 = 0.72), while bulk $\delta^{18}O$ demonstrated a rather weak positive relationship (R^2 = 0.25). These correlations reveal that significant compositional differences that are related to dissolved oxygen may be masking some of the effect of oxygen saturation on $\delta^{18}O$ of manganese oxides in ferromanganese crusts. To explore these correlations further and determine if our data could be further explained by relationships among the measured parameters, we performed a principal component analysis (PCA). The six principle components explain the following fraction of the total variance of the system: PC1: 43.5%, PC2: 26.0%, PC3: 13.6%, PC4: 10.6%, PC5: 5.3%, PC6: 1.0%. PC1 has high positive loading on Mn, and negative loading on all other parameters. PC2 has strong positive loadings on Si and Fe, strong negative loading on $\Delta'^{17}O$, and moderate loadings on the remaining three parameters. These two components (PC1 and PC2) account for 69.5% of the variance in the data. The long tail in the distribution of variance across the principal components highlights the complexity of this system. We hypothesize that some of this complexity arises from variability in the oxygen isotope composition of the Fe and Si endmembers, which we discuss below (Section 3.5). Additionally, variability in the oxygen isotope fractionation of Mn oxidation cannot be ruled out. Notably, the near-orthogonal nature of Mn versus Si and Fe suggests independence between Mn and the other major compositional parameters. Similarly, the strong loading of PC1 on Mn, $[O_2]$, and $\delta'^{18}O$ hint at an underlying relationship (e.g. high dissolved Mn concentrations in low oxygen settings). A full presentation of the results of this PCA are provided in the Supplemental Material.

4.3.4 Utility of Triple Oxygen Isotope Measurements of Manganese Oxides

The triple oxygen isotope signature of O_2 incorporated into ferromanganese crusts will be governed by the isotopic signature of bottom seawater and dissolved O_2, with the former having a much smaller potential dynamic range than the latter. The $\delta^{18}O$ of Mn oxides can constrain the $\delta^{18}O$ of dissolved O_2, which in turn constrains the oxygen saturation of bottom-water O_2. Assuming a 50:50 oxygen contribution from water and DO, the limit to which $\delta^{18}O$ and $\Delta'^{17}O$ may provide paleo-environmental data on dissolved O_2 is set by the fraction of the Mn-oxide endmember present in a sample. A pure Mn-oxide endmember will have ~50% of the isotopic dynamic range of the dissolved O_2 in which it formed, and this dynamic range will decrease proportionally with Mn content. The Mn oxides in this study ranged from 8.2 to 32.5 weight percent Mn, compared to

~63% for pure MnO_2. A typical ferromanganese crust from the Pacific Ocean contains approximately 19 weight percent Fe, 23 weight percent Mn, and 5 weight percent Si (Hein and Koschinsky, 2014). Approximating this assemblage as a water-free oxide mixture, approximately 50% of the oxygen in the crusts will be associated with Mn, meaning approximately 25% of mineral-bound oxygen will be from O_2.

To further illustrate the combination of factors that produce the $\delta^{18}O$ and $\Delta'^{17}O$ range observed in this study, we constructed a simple three endmember mixing ternary (Figure 4). This ternary includes one possible Mn-oxide endmember for oxygen saturated bottom water (from MnOx2, Figure 3), hematite in oxygen isotopic equilibrium with seawater at 0ºC (Hayles et al., 2018), and a mixture of SiO_2 endmembers that best fit the data in this study (20% authigenic, 80% detrital) (Sharp et al., 2016). The relatively low $\Delta'^{17}O$ of the Mn-oxide endmember produces a $\delta'^{18}O$ and $\Delta'^{17}O$ that is unique to each assemblage. In a system where the relative abundance of Mn, Fe, and Si and the isotopic composition of the Fe and Si endmembers is constrained, the Mn-oxide triple oxygen endmember, and therefore the O_2 saturation state at the time of formation, could be determined. Thus, the combination of $\delta'^{18}O$ and $\Delta'^{17}O$ of hydrogenetic ferromanganese crusts may theoretically provide a useful constraint on bottom-water dissolved oxygen over the last ~75 Ma, shedding light on patterns of ocean circulation, primary productivity, and respiration.

4.3.5 Challenges of the Manganese Oxide Triple Oxygen Isotope System

Several challenges need to be addressed in the collection and measurement of $\delta'^{18}O$ and $\Delta'^{17}O$ of Mn-oxide minerals. First, the fraction of Mn-oxide oxygen derived from DO and the presumed oxygen fractionation factors need further investigation. Some evidence suggests the O_2-derived oxygen may depend on Mn oxidation state in mixed valence oxides (Sutherland et al., 2018). While these fractionation factors agree with some previous observations of synthetic and natural Mn oxides, a comprehensive explanation for the range of oxygen isotope fractionation values remains elusive. Related to this, the operative oxidation mechanism(s) in naturally occurring low-temperature Mn-oxide deposits are still unknown. Measurements of ferromanganese crusts where the $\delta'^{18}O$ and $\Delta'^{17}O$ of modern DO and water are directly measured could provide greater insight. Phase isolation is another necessary step for triple oxygen isotope measurements of marine Mn oxides; further study of the triple oxygen isotope systematics in low-temperature Fe oxides and silicates would provide better endmember constraints. The three-

dimensional compositional heterogeneity in ferromanganese crusts is another element of complexity. Geochemical phase separation has been performed on ferromanganese crusts, but none of these commonly used techniques can satisfactorily isolate the Mn-oxide endmember (Koschinsky and Halbach, 1995; Koschinsky and Hein, 2003). Leveraging internal heterogeneity among regions of similar age to calculate the Mn-oxide endmember isotope composition may be a viable approach.

4.4 Summary and Conclusion

We investigated the bulk triple oxygen isotope signature of 13 ferromanganese crusts from throughout the global ocean for evidence of a DO signal. The range of $\delta'^{18}O$ values among deep-ocean samples collected in this study and those compiled here from previous studies suggests that the isotopic signature of water plays a significant role in determining the $\delta'^{18}O$ of Mn oxides, but water alone does not explain the full range of $\delta'^{18}O$ values in Mn oxides. Deep-ocean ferromanganese crust samples from all major ocean basins have a much lower $\Delta'^{17}O$ value than is typically observed in mineral-water equilibrium, and lower than can be explained as a mixture of Fe oxide and silicates present in the crust, providing evidence that DO is incorporated and preserved on million-year time scales in the Mn-oxide component of deep-ocean ferromanganese crusts. The combination of $\delta'^{18}O$ and $\Delta'^{17}O$ values in natural ferromanganese crusts makes it difficult to fully constrain the isotope fractionation factors associated with Mn oxidation, although lab studies suggest O_2 incorporation gives rise to a -17 to -23‰ oxygen isotope effect during Mn(II) oxidation, while water incorporation imparts very little oxygen isotope fractionation.

We constructed a three-component mixing model to explain the distribution of $\delta'^{18}O$ and $\Delta'^{17}O$ values in ferromanganese crusts. We propose that oxides of Mn, Fe, and Si, which make up the bulk of ferromanganese crusts, produce a bulk ferromanganese $\Delta'^{17}O$ that is the sum of their individual components. If the mineralogy and isotopic composition of the Fe and Si endmembers are well known, our model illustrates how the Mn-oxide endmember and its O_2-derived oxygen isotope composition may be calculated. While phase isolation and more thorough study of Mn(II) and Mn(III) oxidation mechanism(s) and isotope fractionation dynamics are necessary, the values we present provide a framework for future study. Despite these challenges, bulk ferromanganese crust triple oxygen isotope values provide strong evidence that hydrogenetic Mn oxides contain a previously unknown and untapped isotopic record of oceanic bottom water DO extending up to 75

Ma. Such a record promises greater insight on the saturation state of oxygen in the ocean, the balance of global productivity and respiration, and processes related to the composition of Earth's atmosphere.

Figures

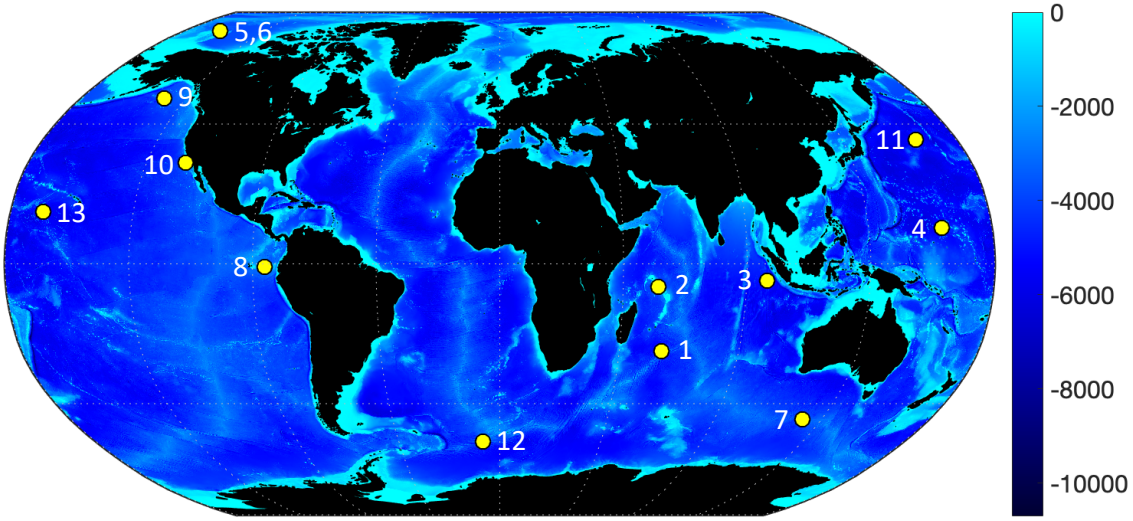

Figure 1- Distribution of ferromanganese crusts analyzed in this study with seafloor depth given in meters.

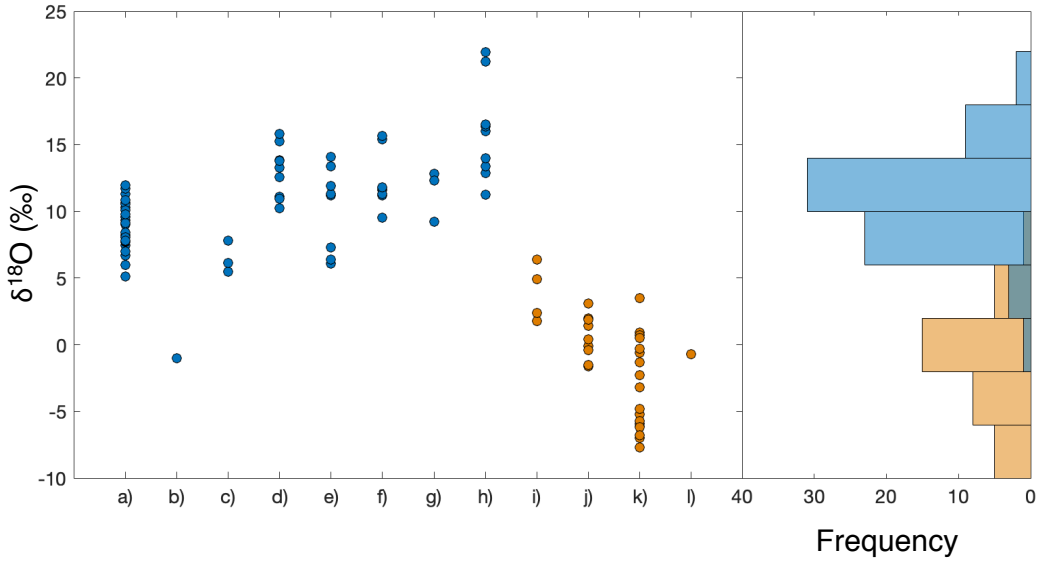

Figure 2- $\delta^{18}O$ of manganate samples (left) and frequency distribution of marine and non-marine manganate $\delta^{18}O$ values. Marine samples (blue) are separated by study and sample type. Marine samples from left to right are a) ferromanganese crusts in this study, b) hydrothermal manganate lens from Franciscan assemblage (Chyi et al., 1984), c) hydrothermal manganate from Kaikata seamount (Mandernack et al., 1995), d) Pacific ferromanganese nodules (Dymond et al., 1973), e) ferromanganese crusts and nodules (Yeh et al., 1985), f) ferromanganese nodule near Hawaii (Sharp et al., 2018), g) ferromanganese nodules from Blake Plateau (Bar-Matthews and Matthews, 1990), and h) Mn and Fe oxide-rich sediment (Dymond et al., 1973). Non-marine samples (orange) from left to right are i) a freshwater ferromanganese nodule (Mandernack et al., 1995), j) endmember sedimentary Mn oxides (Bar-Matthews and Matthews, 1990), k) volcanogenic and sedimentary Mn oxides (Yeh et al., 1985), and l) manganese oxide from Hotazel Formation (Levin et al., 2014).

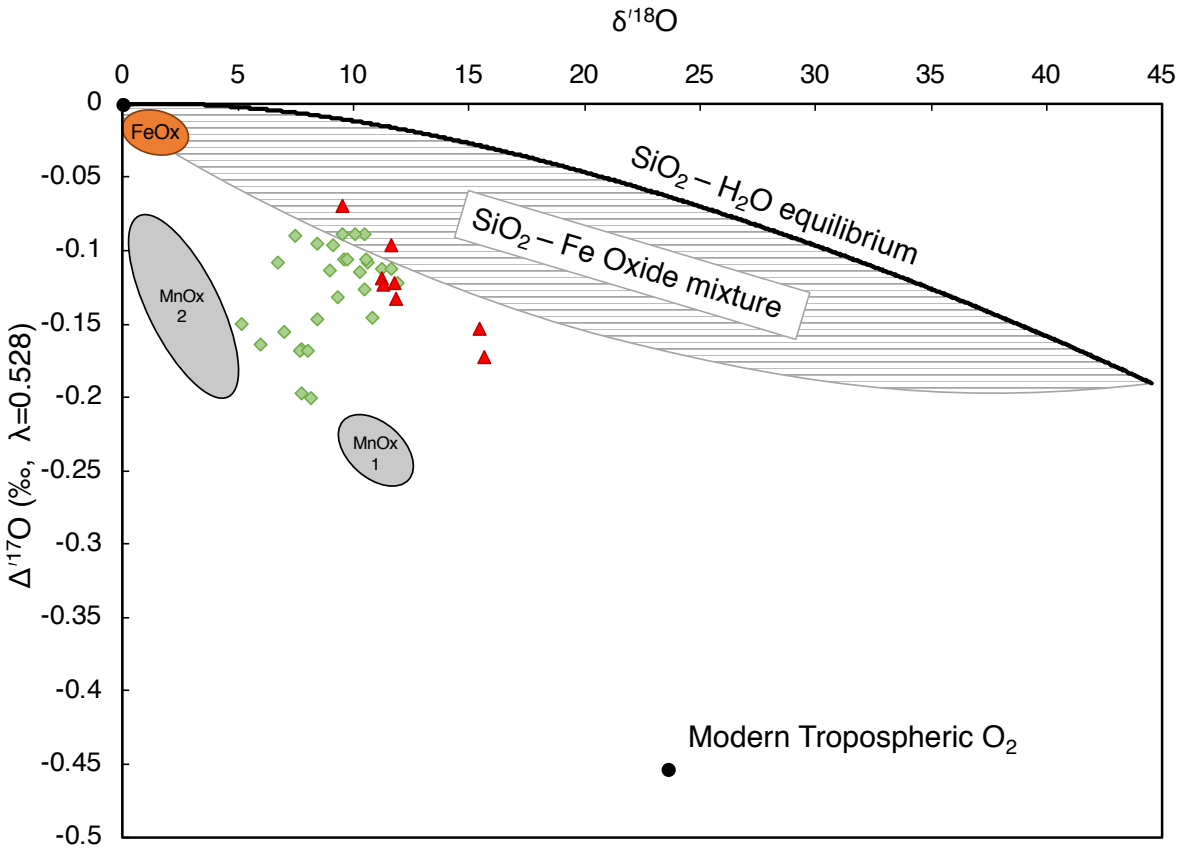

Figure 3- Triple oxygen isotope values of marine ferromanganese crusts from this study (green) and a ferromanganese nodule from near Hawaii (Sharp et al., 2018) (red). The triple oxygen isotope composition of seawater ($\delta'^{18}O=0$ and $\Delta'^{17}O=0$) and tropospheric oxygen ($\delta'^{18}O=+23.6‰$ and $\Delta'^{17}O=-0.452$ ‰) are plotted. The theoretic triple oxygen isotope range of low-temperature Fe oxides (Hayles et al., 2018) (orange circle), detrital and authigenic silicates (SiO_2-H_2O equilibrium line (Sharp et al., 2016), solid black curve), and the range of mixtures between these two components (gray lined area) is unable to explain the distribution of $\delta'^{18}O$ and $\Delta'^{17}O$ of ferromanganese crusts. The Mn oxide endmember requires a lower $\Delta'^{17}O$ to satisfy the three-component mass balance. We include two candidate Mn-oxide endmembers. MnOx1 represents a theoretical Mn-oxide endmember with 40-60% mixture of dissolved oxygen and seawater oxygen without significant fractionation (Mandernack et al., 1995). MnOx2 is the theoretical Mn oxide endmember assuming a 40 to 60% mixture of dissolved oxygen and seawater oxygen (Sutherland et al., 2018), a large oxygen isotope effect (-17 to -23‰ (Sutherland et al., 2018)), and a typical kinetic mass relationship of $\theta_{KIE}=0.515$-0.520.

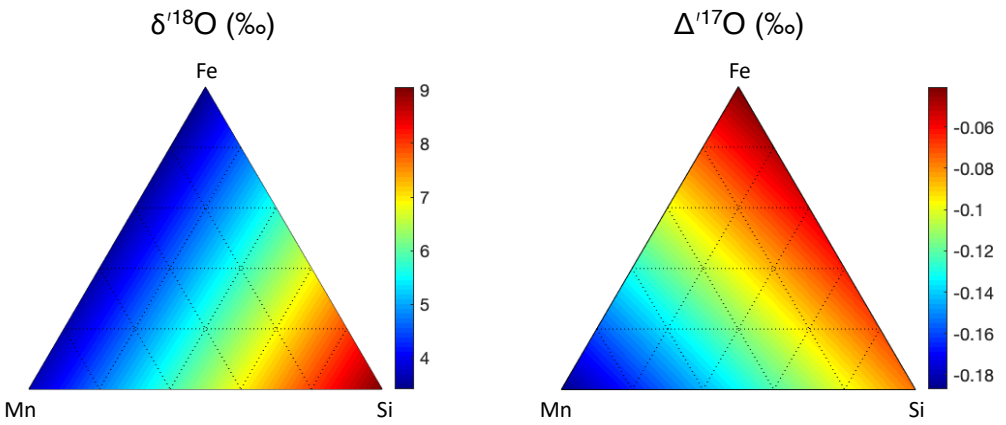

Figure 4- Oxygen isotope ternary diagram for mixture of primary components of ferromanganese crust as MnO_2, Fe_2O_3, and SiO_2. The Mn oxide endmember is one of many possible values from MnOx2. We use hematite-water low-temperature equilibrium to estimate the oxygen isotope composition of the Fe endmember (Hayles et al., 2018). SiO_2 is calculated as a 80:20 oxygen isotopic mixture of detrital (high temperature) and authigenic (near 0ºC) SiO_2, respectively (Sharp et al., 2016). We note that the choice of endmembers in this example are non-unique, these parameters are chosen primarily to illustrate the utility of ferromanganese crust triple oxygen measurements.

Tables

Table 1- Ferromanganese Crust Sample Location

Fig. 1 ID	Cruise ID	Sample No.	Water depth (m)	Latitude	Longitude
1	Antipode (ANTP)	109D-E-L0-12	5698-5778	-27.980	60.803
2	Antipode (ANTP)	145D-D3	2748-2094	-7.333	57.938
3	DODO	232D-B-L0-11	4119-3558	-5.383	97.483
4	F10-89-CP	D11-1K	1870-1690	11.648	161.675
5	HLY1202	DR3-035	1605	78.700	-160.050
6	HLY1202	DR3-036	1605	78.700	-160.050
7	MW-8801	D18-1F	3993	-50.040	126.742
8	PLUME 02	D3-1B	2035-1885	-1.010	-85.658
9	S6-79-NP	D4-13A	2100	53.543	-144.373
10	MBARI 2004	T667-R41A	1033.7	32.394	-120.084
11	TN037	D4-1B	4000	39.838	163.913
12	VULCAN 5 (VULC)	D34-39A	3983-3684	-57.782	-7.672
13	F7-86-HW	CD29-2B	2390-1970	16.707	-168.237

Table 2-Triple oxygen isotope values of ferromanganese crusts

Crust Top	$\delta^{17}O$	$\delta^{18}O$	$\delta'^{17}O$	$\delta'^{18}O$	$\Delta'^{17}O$ (λ=0.528)	$\Delta'^{17}O$ (λ=0.5305)	$\theta_{EQ\text{-}inferred}$
ANTP 109D-E-L0-12	5.450	10.516	5.435	10.461	-0.088	-0.114	0.520
ANTP 109D-E-L0-12 (2)	4.944	9.554	4.932	9.509	-0.089	-0.113	0.519
ANTP 145D-D3	3.837	7.451	3.830	7.423	-0.089	-0.108	0.516
DODO 232D-B-L0-11	4.639	9.021	4.628	8.981	-0.114	-0.136	0.515
F10-89-CPD11-1K	4.792	9.347	4.781	9.304	-0.132	-0.155	0.514
F10-89-CPD11-1K (2)	5.296	10.273	5.282	10.221	-0.115	-0.140	0.517
HLY1202DR3-035	5.488	10.627	5.473	10.571	-0.108	-0.135	0.518
HLY1202DR3-036	5.825	11.277	5.808	11.214	-0.113	-0.141	0.518
MW-8801 D18-1F	5.456	10.562	5.441	10.507	-0.107	-0.133	0.518
MW-8801 D18-1F (2)	4.948	9.594	4.936	9.548	-0.105	-0.130	0.517
PLUME 02 D3-1B	5.415	10.523	5.400	10.468	-0.127	-0.153	0.516
PLUME 02 D3-1B (2)	4.705	9.113	4.694	9.072	-0.096	-0.119	0.517
PLUME 02 D3-1B (3)	5.564	10.843	5.549	10.785	-0.145	-0.173	0.514
S6-79-NP D4-13A	6.049	11.702	6.031	11.634	-0.112	-0.141	0.518
S6-79-NP D4-13A (2)	4.348	8.432	4.339	8.397	-0.095	-0.116	0.517
MBARI 2004T667-R41A	3.427	6.707	3.421	6.685	-0.109	-0.125	0.512
TN037D4-1B	6.167	11.945	6.148	11.874	-0.121	-0.151	0.518
VULC D34-39A	5.225	10.089	5.211	10.038	-0.089	-0.114	0.519
VULC D34-39A (2)	5.047	9.782	5.034	9.734	-0.106	-0.130	0.517
Down Crust							
F7-86-HW CD29 0-2.5mm	4.113	8.186	4.105	8.153	-0.200	-0.220	0.503
F7-86-HW CD29 7-9.5mm	3.891	7.703	3.883	7.673	-0.168	-0.187	0.506
F7-86-HW CD29 14-16.5mm	4.286	8.413	4.277	8.378	-0.147	-0.168	0.510
F7-86-HW CD29 14-16.5mm (2)	4.070	8.043	4.062	8.011	-0.168	-0.188	0.507
F7-86-HW CD29 21-23.5mm	3.535	7.002	3.529	6.978	-0.155	-0.173	0.506
F7-86-HW CD29 21-23.5mm (2)	2.547	5.115	2.544	5.102	-0.150	-0.163	0.499
F7-86-HW CD29 28-30.5mm	2.995	5.993	2.991	5.975	-0.164	-0.179	0.500
F7-86-HW CD29 35-37.5mm	3.900	7.776	3.892	7.746	-0.198	-0.217	0.503
F7-86-HW CD29 35-37.5mm (2)	3.932	7.779	3.924	7.749	-0.167	-0.187	0.506

(2) And (3) indicate duplicate and triplicate analyses, respectively

References

Adkins, J. F., K. McIntyre, and D. P. Schrag. 2002. The salinity, temperature, and δ18O of the glacial deep ocean. Science (80-.). **298**: 1769–1773.

Bao, H., X. Cao, and J. A. Hayles. 2015. The confines of triple oxygen isotope exponents in elemental and complex mass-dependent processes. **170**: 39–50. doi:10.1016/j.gca.2015.07.038

Bao, H., X. Cao, and J. A. Hayles. 2016. Triple Oxygen Isotopes: Fundamental Relationships and Applications. Annu. Rev. Earth Planet. Sci. **44**: 463–492. doi:10.1146/annurev-earth-060115-012340

Bar-Matthews, M., and A. Matthews. 1990. Chemical and stable isotope fractionation in manganese oxide-phosphorite mineralization, Timna Valley, Israel. Geol. Mag. **127**: 1–12.

Barkan, E., and B. Luz. 2005. High precision measurements of O-17/O-16 and O-18/O-16 ratios in H2O. Rapid Commun. Mass Spectrom. **19**: 3737–3742. doi:10.1002/rcm.2250

Basu, S., F. M. Stuart, V. Klemm, G. Korschinek, K. Knie, and J. R. Hein. 2006. Helium isotopes in ferromanganese crusts from the central Pacific Ocean. Geochim. Cosmochim. Acta **70**: 3996–4006.

Bender, M., T. Sowers, and L. Labeyrie. 1994. The Dole Effect and its Variations During the Last 130,000 Years as Measured in the Vostok Ice Core. Global Biogeochem. Cycles **8**: 363–376. doi:10.1029/94gb00724

Blunier, T., B. Barnett, M. L. Bender, and M. B. Hendricks. 2002. Biological oxygen productivity during the last 60 , 000 years from triple oxygen isotope measurements. **16**.

Cao, X., and H. Bao. 2013. Dynamic model constraints on oxygen-17 depletion in atmospheric O 2 after a snowball Earth. **110**. doi:10.1073/pnas.1302972110

Cao, X., and Y. Liu. 2011. Equilibrium mass-dependent fractionation relationships for triple oxygen isotopes. Geochim. Cosmochim. Acta **75**: 7435–7445. doi:10.1016/j.gca.2011.09.048

Chyi, M. S., D. A. Crerar, R. W. Carlson, and R. F. Stallard. 1984. Hydrothermal Mn-deposits of the Franciscan Assemblage , II . Isotope and trace element geochemistry , and implications for hydrothermal convection at spreading centers. **71**: 31–45.

Clayton, R. N., and T. K. Mayeda. 1996. Oxygen isotope studies of achondrites. Geochim. Cosmochim. Acta **60**: 1999–2017.

Clayton, R. N., T. K. Mayeda, E. J. Olsen, and M. Prinz. 1983. Oxygen isotope relationships in iron meteorites. Earth Planet. Sci. Lett. **65**: 229–232.

Crockford, P. W., J. A. Hayles, H. Bao, and others. 2018. Triple oxygen isotope evidence for limited mid-Proterozoic primary productivity. Nature **559**: 613–616. doi:10.1038/s41586-018-0349-y

Dymond, J., J. B. Corliss, G. R. Heath, C. W. Field, E. J. Dasch, and H. H. Veeh. 1973. Origin of Metalliferous Sediments from the Pacific Ocean.

Flanagan, F. J., and D. Gottfried. 1980. USGS rock standards; III, Manganese-nodule reference samples USGS-Nod-A-1 and USGS-Nod-P-1.

Frank, M., R. K. O'Nions, J. R. Hein, and V. K. Banakar. 1999. 60 Myr records of major elements and Pb-Nd isotopes from hydrogenous ferromanganese crusts: Reconstruction of seawater paleochemistry. Geochim. Cosmochim. Acta **63**: 1689–1708. doi:10.1016/s0016-7037(99)00079-4

Garcia, H. E., K. Weathers, C. R. Paver, and others. 2018. World ocean atlas 2018. Volume 3, Dissolved oxygen, apparent oxygen utilization, and oxygen saturation.

Gehler, A., T. Tütken, and A. Pack. 2011. Triple oxygen isotope analysis of bioapatite as tracer for diagenetic alteration of bones and teeth. Palaeogeogr. Palaeoclimatol. Palaeoecol. **310**: 84–91. doi:10.1002/cctc.201300971

Halbach, P., C. Kriete, B. Prause, and D. Puteanus. 1989. Mechanisms to explain the platinum concentration in ferromanganese seamount crusts. Chem. Geol. **76**: 95–106.

Hayles, J., C. Gao, X. Cao, Y. Liu, and H. Bao. 2018. Theoretical calibration of the triple oxygen isotope thermometer. Geochim. Cosmochim. Acta **235**: 237–245. doi:10.1016/j.gca.2018.05.032

Hein, J. R., and A. Koschinsky. 2014. Deep-ocean ferromanganese crusts and nodules. The Treatise on Geochemistry 273–291.

Helman, Y. 2005. Fractionation of the Three Stable Oxygen Isotopes by Oxygen-Producing and Oxygen-Consuming Reactions in Photosynthetic Organisms. Plant Physiol. **138**: 2292–2298. doi:10.1104/pp.105.063768

Hoffmann, G., M. Cuntz, C. Weber, and others. 2004. A model of the Earth ' s Dole effect. **18**: 1–15. doi:10.1029/2003GB002059

Hulston, J. R., and H. G. Thode. 1965. Variations in the S33, S34, and S36 contents of meteorites and their relation to chemical and nuclear effects. J. Geophys. Res. **70**: 3475–3484.

Koschinsky, A., and P. Halbach. 1995. Sequential leaching of marine ferromanganese precipitates : Genetic implications. **59**: 5113–5132.

Koschinsky, A., and J. R. Hein. 2003. Uptake of elements from seawater by ferromanganese crusts: solid-phase associations and seawater speciation. Mar. Geol. **198**: 331–351. doi:10.1016/s0025-3227(03)00122-1

Kroopnick, P. 1980. Isotopic Fractionations During Oxygen Consumption and Carbonate Dissolution within the North-Atlantic Deep-Water. Earth Planet. Sci. Lett. **49**: 485–498. doi:10.1016/0012-821x(80)90089-8

Learman, D. R., B. M. Voelker, A. I. Vazquez-Rodriguez, and C. M. Hansel. 2011. Formation of manganese oxides by bacterially generated superoxide. Nat. Geosci. **4**: 95–98. doi:10.1038/ngeo1055

Levin, N. E., T. D. Raub, N. Dauphas, and J. M. Eiler. 2014. ScienceDirect Triple oxygen isotope variations in sedimentary rocks. Geochim. Cosmochim. Acta **139**: 173–189. doi:10.1016/j.gca.2014.04.034

Levine, N. M., M. L. Bender, and S. C. Doney. 2009. The d 18 O of dissolved O 2 as a tracer of mixing and respiration in the mesopelagic ocean. **23**: 1–12. doi:10.1029/2007GB003162

Luther, G. W. 2010. The Role of One- and Two-Electron Transfer Reactions in Forming

Thermodynamically Unstable Intermediates as Barriers in Multi-Electron Redox Reactions. Aquat. Geochemistry **16**: 395–420. doi:10.1007/s10498-009-9082-3

Luz, B., E. Barkan, M. L. Bender, M. H. Thiemens, and K. A. Boering. 1999. Triple-isotope composition of atmospheric oxygen as a tracer of biosphere productivity. Nature 547–550. doi:10.1038/22987

Mandernack, K. W., M. L. Fogel, B. M. Tebo, and A. Usui. 1995. Oxygen Isotope Analyses of Chemically and Microbially Produced Manganese Oxides and Manganates. Geochim. Cosmochim. Acta **59**: 4409–4425. doi:10.1016/0016-7037(95)00299-f

Menicucci, A. J., J. A. Matthews, and H. J. Spero. 2013. Oxygen isotope analyses of biogenic opal and quartz using a novel microfluorination technique. Rapid Commun. Mass Spectrom. **27**: 1873–1881. doi:10.1002/rcm.6642

Miller, M. F. 2002. Isotopic fractionation and the quantification of O-17 anomalies in the oxygen three-isotope system: an appraisal and geochemical significance. Geochim. Cosmochim. Acta **66**: 1881–1889. doi:10.1016/s0016-7037(02)00832-3

Oldham, E., A. Mucci, B. M. Tebo, and G. W. Luther. 2017. ScienceDirect Soluble Mn (III)– L complexes are abundant in oxygenated waters and stabilized by humic ligands. Geochim. Cosmochim. Acta **199**: 238–246. doi:10.1016/j.gca.2016.11.043

Pack, A., A. Höweling, D. C. Hezel, and others. 2017. Tracing the oxygen isotope composition of the upper Earth's atmosphere using cosmic spherules. Nat. Commun. **8**: 1–7. doi:10.1038/ncomms15702

Sengupta, S. 2016. Triple Oxygen Isotopes of Cherts : Implications for the δ 18 O and Temperatures of Early Oceans.

Sharp, Z. D. 1990. A laser-based microanalytical method for the in situ determination of oxygen isotope ratios of silicates and oxides. Geochim. Cosmochim. Acta **54**: 1353–1357.

Sharp, Z. D. 2017. Principles of stable isotope geochemistry.

Sharp, Z. D., J. A. Gibbons, O. Maltsev, V. Atudorei, A. Pack, S. Sengupta, E. L. Shock, and L. P. Knauth. 2016. ScienceDirect A calibration of the triple oxygen isotope fractionation in the SiO 2 – H 2 O system and applications to natural samples. **186**: 105–119. doi:10.1016/j.gca.2016.04.047

Sharp, Z. D., J. A. G. Wostbrock, and A. Pack. 2018a. Mass-dependent triple oxygen isotope variations in terrestrial materials. Geochemical Perspect. Lett. 27–31. doi:10.7185/geochemlet.1815

Sharp, Z. D., J. A. G. Wostbrock, and A. Pack. 2018b. Mass-dependent triple oxygen isotope variations in terrestrial materials. 27–31. doi:10.7185/geochemlet.1815

Stolper, D. A., W. W. Fischer, and M. L. Bender. 2018. Effects of temperature and carbon source on the isotopic fractionations associated with O2 respiration for 17O/16O and 18O/16O ratios in E. coli. Geochim. Cosmochim. Acta **240**: 152–172. doi:10.1016/j.gca.2018.07.039

Sutherland, K. M., S. D. Wankel, and C. M. Hansel. 2018. Oxygen isotope analysis of bacterial and fungal manganese oxidation. Geobiology. doi:10.1111/gbi.12288

Tebo, B. M., H. A. Johnson, J. K. McCarthy, and A. S. Templeton. 2005. Geomicrobiology of

manganese(II) oxidation. Trends Microbiol. **13**: 421–428. doi:10.1016/j.tim.2005.07.009

Thiemens, M. H. 2006. History and Applications of Mass-Independent Isotope Effects.doi:10.1146/annurev.earth.34.031405.125026

Thiemens, M. H., and J. E. Heidenreich. 1983. The Mass-Independent Fractionation of Oxygen : A Novel Isotope Effect and its Possible Cosmochemical Implications. **219**: 1073–1075.

Uramoto, G. I., Y. Morono, N. Tomioka, and others. 2019. Significant contribution of subseafloor microparticles to the global manganese budget. Nat. Commun. **10**: 1–10. doi:10.1038/s41467-019-08347-2

Wostbrock, J. A. G., E. Cano, and Z. D. Sharp. An internally consistent triple oxygen isotope calibration of standards for silicates, carbonates and air relative to VSMOW2 and SLAP2. Press.

Yeh, H.-W., J. R. Hein, and R. A. Koski. 1985. Stable-Isotope Study of Volcanogenic- and Sedimentary-Manganese Deposits. UNITED STATES Dep. Inter. Geol. Surv. Open File Rep. 85-662.

Zachos, J., M. Pagani, L. Sloan, E. Thomas, and K. Billups. 2001. Trends, rhythms, and aberrations in global climate 65 Ma to present. Science (80-.). **292**: 686–693.

Supplemental Material: Statistical Analysis of Concentration and Isotope Values

Linear Regression between dissolved oxygen and measured parameters:

The following table contains the observed values (or averages for duplicate and triplicate samples) for crust surface scrapes analyzes in this study. We also include an estimate of dissolved oxygen concentration using the WOA2018 data set discussed in the main text.

Table S1

Sample	O_2 (μmol/kg)*	Fe (wt %)	Mn (wt %)	Si (wt %)	$\delta'^{18}O$ (‰)	$\Delta'^{17}O$ (‰)
Antipode (ANTP) 109D-E-L0-12	209.2	20.0	17.8	4.9	10.0	-0.089
Antipode (ANTP) 145D-D3	160.6	18.4	23.3	4.2	7.5	-0.089
DODO 232D-B-L0-11	184.4	22.0	19.2	5.7	9.0	-0.114
F10-89-CP D11-1K	97.6	17.0	27.3	3.1	9.8	-0.124
HLY1202 DR3-035	296.0	22.6	14.4	4.3	10.6	-0.108
HLY1202 DR3-036	296.0	22.3	15.1	3.2	11.3	-0.113
MW-8801 D18-1F	213.5	22.0	10.7	12.0	10.1	-0.106
PLUME 02 D3-1B	99.4	26.6	29.6	6.2	10.2	-0.123
S6-79-NP D4-13A	64.8	21.0	22.9	3.3	10.1	-0.104
MBARI 2004 T667-R41A	35.1	24.6	32.5	5.0	6.7	-0.109
TN037 D4-1B	148.4	27.8	24.7	9.0	11.9	-0.121
VULCAN 5 (VULC) D34-39A	239.7	26.6	8.4	11.8	9.9	-0.098
F7-86-HW CD29-2B	114.2	23.5	26.9	5.9	7.3	-0.169
Linear regression fits (O_2 vs. each parameter)						
slope		0.21	-9.56	5.64	26.80	1198.16
intercept		161.3	366.8	132.0	-90.4	301.0
R^2		0.00007	0.72	0.04	0.25	0.09

*Estimated from WOA2018 database

Principle component analysis of measured and estimated crust parameters:

Using the "pca" function in MATLAB, we conducted a principle component analysis of the z-scores of each of the parameters in the table above. The six principle components explain the following fraction of the total variance of the system: PC1: 43.5%, PC2: 26.0%, PC3: 13.6%, PC4: 10.6%, PC5: 5.3%, PC6: 1.0%.

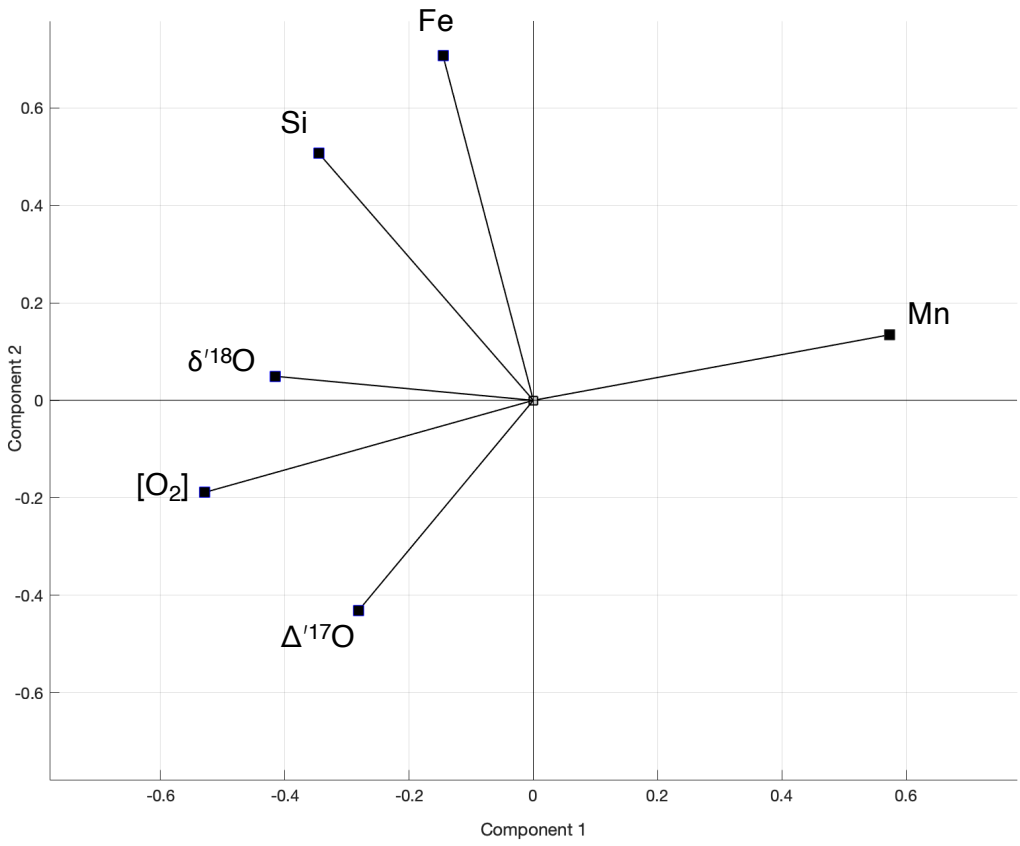

Figure S1-Loadings of component 1 vs. component 2 for the six measured parameters in Table S1.

The following table provides the complete set of principal component coefficients:

Table S2-PCA Principal Component Coefficients

Parameters	PC1	PC2	PC3	PC4	PC5	PC6
[O2]	-0.529	-0.189	0.230	-0.380	0.448	0.536
Fe	-0.145	0.707	0.022	0.272	0.599	-0.212
Mn	0.573	0.135	0.123	0.328	0.083	0.724
Si	-0.345	0.507	-0.491	-0.115	-0.481	0.370
$\delta'^{18}O$	-0.415	0.049	0.639	0.505	-0.402	0.027
$\Delta'^{17}O$	-0.282	-0.432	-0.531	0.637	0.200	0.082

Supplemental Material: SIMS Analysis of a Ferromanganese Crust

Chapters 2-4 demonstrate the promise for using the oxygen isotope signature of ferromanganese crust as a proxy for the oxygen isotope signature for marine dissolved oxygen. A clear challenge to reading this record in its full detail is the small spatial scales on which the record of oxygen is recorded. Typical ferromanganese crusts in central regions of ocean basins grow at ~1mm per million years (Hein and Koschinsky 2014). Typical oxygen isotope techniques, including the triple oxygen isotope analyses that we conducted in Chapter 4 can require up to several milligrams of sample material, which when milled out from a crust sample will integrate a significant amount of time and yield overall poor temporal resolution. To address the problem of poor spatial and temporal resolution in oxygen isotope measurements of ferromanganese crusts, we conducted isotope analysis of multiple sections of CD-29 using secondary ion mass spectrometry (SIMS, Cameca IMS 7f-Geo SIMS at Washington University in St. Louis). Using a step size on the order of ~50 micron, we can drastically improve the temporal record of analysis (20 points per Ma vs. ~0.5 points per Ma). The data and details presented in this supplement are very much incomplete, are primarily meant to outline the status of method development and present preliminary data.

Standards:

As we showed in Chapter 3, ferromanganese crusts are extremely heterogeneous with respect to elemental composition, mineralogy, growth texture, and diagenetic features. This complex medium makes choosing an isotope standard particularly challenging. At first, we tried using a small, visually homogeneous layer of a ferromanganese nodule from the North Atlantic acquired from the WHOI Seafloor Samples Laboratory. This sample was characterized for bulk $\delta^{18}O$ using the micro-fluorination technique described in Chapter 4 (Menicucci et al. 2013), the assumption being that raw $\delta^{18}O$ measured on the SIMS would be correctable based on the measured bulk value in the lab. This assumption turned out to be incorrect. The measurements produced raw $\delta^{18}O$ that varied significant from spot to spot for samples that were collected in a close grid (spaced approximately 50 microns apart). Fifteen individual spot analyses produced a raw $\delta^{18}O$ range of ~26 permil and a standard deviation of 7 permil, which is unacceptable for our purposes.

We chose next to steer away from natural samples, which, although visually homogeneous, did not produce homogeneous result using SIMS. We prepared pure MnO_2 (Sigma Aldrich) grains in epoxy on 1-inch glass round for SIMS analysis. We conducted the same series of analyses on these grains, and observed a similar range in raw $\delta^{18}O$, 28.5 permil (n=20). We found that this variability was drastically improved by increasing the size of the ion beam during pre-sputtering and increasing the duration of pre-sputtering. This improved results of the MnO_2 grain to a standard deviation of 3 permil (n=80). The final parameters used for analysis were 28 micron beam for pre-sputtering, 120 seconds of pre-sputtering, and an 18 micron beam for analysis. The results of the optimized standard analysis are shown in Figure S2.

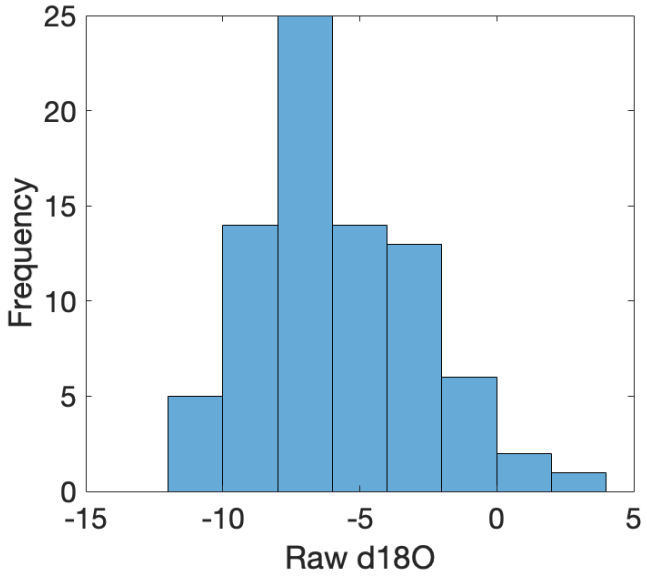

Figure S2- Histogram of raw $\delta^{18}O$ of standard MnO_2 grains (Sigma), n=80.

Samples:

Using the beam conditions that yielded the optimum standard reproducibility, we collected several spot analyses of sections of ferromanganese crust in gridded regions as to produce two-dimensional isotope maps of regions of interest. Analyses were performed in regions in the interior of individual growth structures so that silicates would not represent a significant contribution to the oxygen mass balance (see Chapter 3). We have chosen two representative regions to demonstrate typical results: one analysis region near the crust surface (A) and one region in the

crust interior (B) (Figure S3). Results of SIMS analysis as well as Mn and Fe concentrations (collected via XRF, Chapter 3) are shown in Figure S3 and Figure S4.

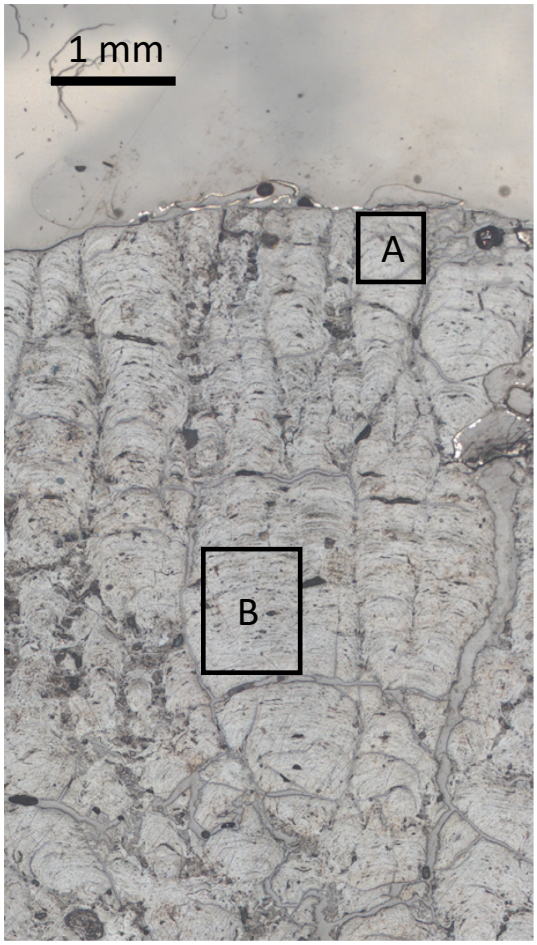

Figure S3- Light microscope image of the topmost section of CD-29. Regions A and B, denoted above, are the two regions of interest for which SIMS and XRF analysis were conducted and presented in Figures S4 and S5.

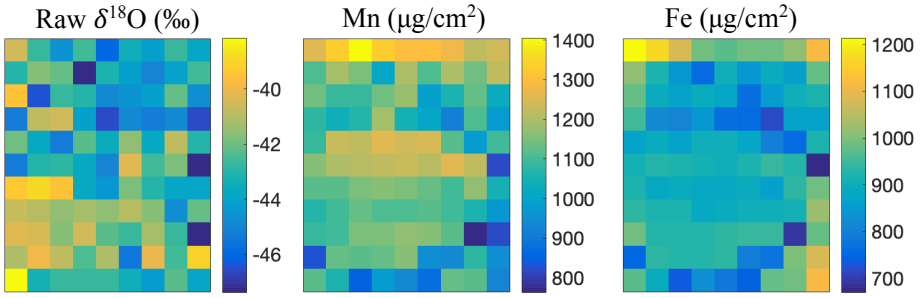

Figure S4- Raw SIMS δ^{18}O values (left), Mn concentration (middle), and Fe concentration (right) for section A

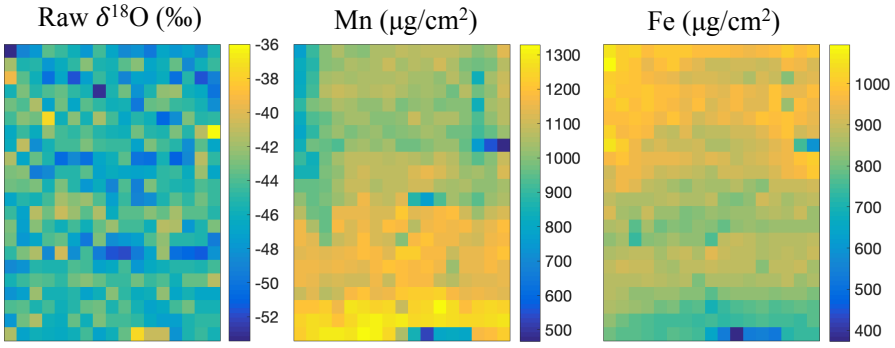

Figure S5- Raw SIMS δ^{18}O values (left), Mn concentration (middle), and Fe concentration (right) for section B

The range of $\delta^{18}O$ raw values is similar in both section A and section B, approximately 15 permil. While it is unclear if this isotope range is real or confounded by a combination of matrix effects and true variation, the lack of robust correlation with either Mn or Fe ($R^2<0.1$) in both A and B suggest that isotope variation observed in the SIMS data is not entirely linked to chemistry. We presented in Chapter 4 the hypothesis that changes in dissolved oxygen would be the primary source of $\delta^{18}O$ variation for a given bulk composition. In this model, we would expect to de-trend $\delta^{18}O$ with Fe concentration, and any remaining variation would result changes in the manganese oxide $\delta^{18}O$ value (which in turn relates to that of O_2). These SIMS results, if taken at face value, would suggest that there is some other source of variability that cannot be corrected for by bulk Mn and Fe concentration alone. These results show that our model of $\delta^{18}O$ of ferromanganese crust needs to be further refined or, the SIMS methods we use here need to be further improved to be able to resolve these differences.

Figure S2 revealed an approximately normal distribution of raw isotope values around a central value for several spot analyses on a standard that we assumed to be homogenous. Region A is not different from a normal distribution (P=0.968, Kolmogorov-Smirnov test), Region B as a whole is different from a normal distribution, but the removal of a single low outlier changes this result at a 5 percent significance level (P=0.08). The mean of Regions A and B are -42.8 permil and -45.4 permil, respectively (Figure S6).

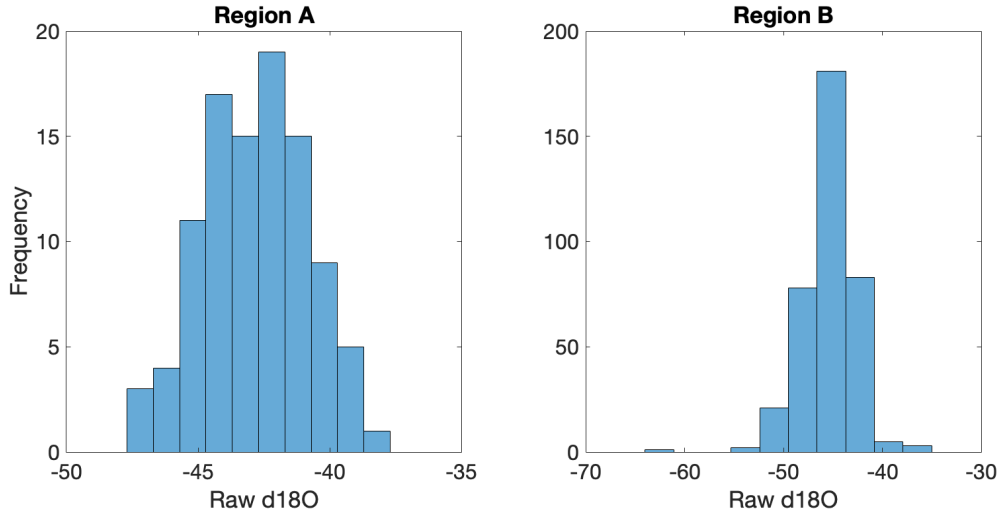

Figure S6- Histogram of raw $\delta^{18}O$ values from Regions A (n=99) and Region B (n=374)

The standard deviations of Regions A and B are 2.0 and 2.6 permil, respectively, which is less than the variably we observed for our standard grains. The lack of a clear bimodal distribution of data suggests that either the sample is isotopically homogenous within the resolution of the SIMS, or that analytical artifacts are preventing us from discerning distinct endmembers. Given the substantial compositional variability in the sample and the fact that we observe a several permil range in the bulk sample (Chapter 4), we have good reason to suspect that analytical artifacts are the underlying root of the lack of clearer signal.

Despite these unclear results in the case of CD-29, there are a few steps that could be taken to determine if SIMS will ultimately be amenable to ferromanganese crust analysis. Identification of more homogeneous standard and sample material will help isolate sources of uncertainty. Ferromanganese deposits that form more rapidly may offer more homogeneity. Examples of these are hydrothermal or lake ferromanganese deposits where rates may be several orders of magnitude higher than those of CD-29 (Hein and Koschinsky 2014). Pressing synthetic or natural standards into pellets or implanting them into foils is another possible path forward. I was cautioned at the outset of this work against using pressed or implanted standards as they would not be directly comparable to more crystalline samples, however, such steps may help define the analytical limits of SIMS analysis on ferromanganese material.

References

Hein, J. R., and A. Koschinsky. 2014. Deep-ocean ferromanganese crusts and nodules. The Treatise on Geochemistry 273–291.

Menicucci, A. J., J. A. Matthews, and H. J. Spero. 2013. Oxygen isotope analyses of biogenic opal and quartz using a novel microfluorination technique. Rapid Commun. Mass Spectrom. **27**: 1873–1881. doi:10.1002/rcm.6642

5. Extracellular Superoxide Production by Key Microbes in the Global Ocean

This chapter was originally published as:

Sutherland, Kevin M., et al. "Extracellular superoxide production by key microbes in the global ocean." *Limnology and Oceanography* (2019).

Abstract

Bacteria and eukaryotes produce the reactive oxygen species superoxide both within and outside the cell. While superoxide is typically associated with the detrimental and sometimes fatal effects of oxidative stress, superoxide has also been shown to be involved in a range of essential biochemical processes, including cell signaling, growth, differentiation, and defense. Light-independent extracellular superoxide production has been shown to be widespread among many marine heterotrophs and phytoplankton, but the extent to which this trait is relevant to marine microbial physiology and ecology throughout the global ocean is unknown. Here, we investigate the dark extracellular superoxide production of five groups of organisms that are geographically widespread, and represent some of the most abundant organisms in the global ocean. These include *Prochlorococcus, Synechococcus, Pelagibacter*, *Phaeocystis*, and *Geminigera.* Cell-normalized net extracellular superoxide production rates ranged seven orders of magnitude, from undetectable to 14,830 amol cell^{-1} hr^{-1}, with the cyanobacterium *Prochlorococcus* being the lowest producer and the cryptophyte *Geminigera* being the most prolific producer. Extracellular superoxide production exhibited a strong inverse relationship with cell number, pointing to a potential role in cell signaling. We demonstrate that rapid, cell number dependent changes in the net superoxide production rate by *Synechococcus* and *Pelagibacter* arose primarily from changes in gross production of extracellular superoxide, not decay. These results expand the relevance of dark extracellular superoxide production to key marine microbes of the global ocean, suggesting that superoxide production in marine waters is regulated by a diverse suite of marine organisms in both dark and sunlit waters.

5.1 Introduction

Reactive oxygen species (ROS) are oxygen-containing radicals and compounds present at low concentrations, with half-lives ranging from nanoseconds to hours in aquatic systems. The most common forms of ROS in marine systems are hydrogen peroxide (H_2O_2), superoxide ($O_2^{\bullet-}$/HO_2), hydroxyl radical ($HO^{\bullet}$), singlet oxygen ($^1O_2$), and carbonate radical ($CO_3^{\bullet-}$). The formation of many ROS within aqueous systems occurs via sequential one-electron transfer reactions (Fridovich 1998). For instance, the ROS $O_2^{\bullet-}$, H_2O_2, and $HO^{\bullet}$ are the intermediates of the sequential one-electron reduction of molecular oxygen to water. ROS play a key role in the remineralization of carbon and the cycling of numerous metals within the ocean (Heller and Croot 2010; Rose 2012; Wuttig et al. 2013a).

The ROS superoxide is ubiquitous in marine environments (Rose et al. 2008b; Hansard et al. 2010; Rusak et al. 2011; Diaz et al. 2016; Roe et al. 2016). Concentrations of superoxide in marine environments range from picomolar to hundreds of nanomolar, with higher concentrations typically observed in high productivity waters and shallow coastal environments (Rose et al. 2008b; Hansard et al. 2010; Rusak et al. 2011; Diaz et al. 2016; Roe et al. 2016). In sunlit surface waters, superoxide forms as a photochemical product from the photolysis of colored dissolved organic matter (Heller et al. 2016). Historically, photochemical processes have been viewed as the primary source of superoxide to the ocean, but recent work demonstrates that microbes are a significant source of superoxide to marine environments (Diaz et al. 2013). In sunlit and dark waters alike, microbes appear to be prolific producers of extracellular superoxide (Rose et al. 2008b; Diaz et al. 2013; Hansel et al. 2016; Schneider et al. 2016). The diversity of microorganisms contributing to the oceanic superoxide flux is just beginning to come to light with a broad taxonomic representation already evident (Kustka et al. 2005; Marshall et al. 2005; Rose et al. 2008b; Learman et al. 2011; Diaz et al. 2013, 2016; Hansel et al. 2016; Zhang et al. 2016b; Diaz and Plummer 2018).

Within microbial systems, superoxide is produced intracellularly as a byproduct of photosynthesis and respiration and extracellularly by transmembrane or secreted enzymes belonging generally to NAD(P)H oxidases and peroxidases (Fridovich 1983; Asada 2006; Dickinson and Chang 2011; Diaz et al. 2013; Andeer et al. 2015; Diaz and Plummer 2018). Intracellular and extracellular superoxide production has both detrimental and beneficial impacts on life. As a radical with a half-life on the order of minutes (Heller and Croot, 2011), superoxide

reacts with biomolecules and redox active metals such as iron within the cell (Fridovich 1998). Thus, high concentrations of superoxide within cells can be toxic, leading to oxidative stress and apoptosis (Buetler et al. 2004). To eliminate oxidative stress caused by excess intracellular superoxide, cells produce antioxidants such as superoxide dismutase (SOD) to keep superoxide at healthy physiological levels (Korshunov and Imlay 2002). As a singly charged anion under physiological pH, superoxide diffusion across the cell membrane is limited (Korshunov and Imlay 2002). Indeed, permeability of superoxide across lipid bilayer membranes is entirely insufficient to explain extracellular superoxide fluxes from microbes (Gus' kova et al. 1984; Diaz et al. 2013). There is an increasing recognition that superoxide is an essential molecule required for basic cellular physiology and growth of other plant, animal, and microbial cells (Saran 2003; Buetler et al. 2004). For instance, extracellular superoxide has been shown to play an important role in cell signaling and growth stimulation in eukaryotes, and cell differentiation in fungi (Buetler et al. 2004; Dickinson and Chang 2011). In higher plants, oxidative bursts play a beneficial role in multiple physiological responses, including antimicrobial defense, oxidative cross-linking of cell walls preceding transcription-dependent defenses in wound repair, and gene activation of various stress responses (Lamb and Dixon 1997).

The trade-offs of extracellular superoxide production between the harmful effects of oxidative damage by ROS and the potential benefits of signaling and growth promotion (or other helpful effects) is still very much an active area of study. While the reasons and mechanisms of extracellular superoxide production within marine microbes have only been minimally explored and remain unclear, a wide diversity of photoautotrophic and heterotrophic microbes have been shown to produce superoxide outside their cells under both light and dark conditions in natural waters (Rose et al. 2008b; Diaz et al. 2013; Hansel et al. 2016). Nevertheless, many key marine organisms have not been previously explored. In this study, we set out to better understand the role of extracellular superoxide within the ocean by examining its production by some of the ocean's most abundant organisms. We examine the extracellular production by cyanobacteria *Synechococcus* and *Prochlorococcus*, the two most abundant photosynthesizing organisms in the global ocean. We also measured extracellular superoxide production by SAR11, the most abundant group of marine heterotrophic bacterioplankton, and two marine phytoplankton abundant in coastal Antarctica, *Phaeocystis antarctica* and *Geminigera cryophila*. We test the influence of cell density on extracellular superoxide production, and demonstrate a strong inverse relationship

between cell number and the cell normalized superoxide production rate. We show that the cell-normalized extracellular superoxide rate responds to changes in cell number on the order of seconds to hours. This dependence of extracellular superoxide rate to cell number is apparent regardless of whether cells are concentrated or diluted. These data build upon previous studies highlighting the widespread nature of extracellular superoxide production across microbial life and provide essential rates for improved modeling of superoxide distributions within the global ocean.

5.2 Methods

5.2.1 Measurement of extracellular superoxide

Extracellular $O_2^{\bullet-}$ production was measured with an FeLume (Waterville Analytical, Waterville, ME) using a previously described method (Diaz et al. 2013). The FeLume system is a flow-cell reactor designed to measure chemiluminescence, which in this case, results from the mixture of a superoxide-containing sample and the superoxide-specific chemiluminescent probe methyl *Cypridina* luciferin analog (MCLA, TCI America) (Rose et al. 2008a). The FeLume system is composed of two separate fluid lines, one being dedicated to the analyte solution and the other to the MCLA reagent. Both solutions are independently flushed through the system at an identical flow rate using a peristaltic pump until they converge in a spiral flow cell immediately adjacent to a photomultiplier tube. The spiral flow cell and photomultiplier tube are housed within an opaque box to eliminate any incidental ambient light. Extracellular superoxide production rates by cells were measured by placing the cells in-line with the FeLume system using either 0.22 μm or 0.1 μm syringe filters (the latter being used for *Prochlorococcus* and *Pelagibacter* cells). Extracellular superoxide was measured by running artificial seawater (ASW, recipe below) past the filter-supported cells directly into the instrument where it was mixed with MCLA. Samples of *Phaeocystis* and *Geminigera* were kept on ice to prevent stress to the cells and lysis. All measurements, including calibrations, were collected under dark conditions, which were maintained by covering sample tubing and filter with aluminum foil. Similar systems have been used to generate high sensitivity measurements of natural superoxide concentrations and decay rates (Rose et al. 2008a; Hansard et al. 2010), as well as extracellular superoxide production by bacteria (Diaz et al. 2013), phytoplankton isolates (Kustka et al. 2005; Rose et al. 2008b), and natural *Trichodesmium* colonies (Hansel et al. 2016).

For calibration, primary standard solutions of potassium dioxide (KO_2, ACROS Organics, superoxide content > 215cc/g) were prepared in NaOH (pH = 12.5) amended with 90 μM diethylene-triaminepentaacetic acid (DTPA, Sigma >99%) in order to sequester trace contaminants that would otherwise significantly reduce the lifetime of superoxide. Superoxide concentrations in primary standards were quantified by measuring the difference in absorbance at 240 nm before and after the addition of 2 U mL^{-1} superoxide dismutase (SOD; Superoxide Dismutase from bovine erythrocytes ≥ 3,000 U mg^{-1}, Sigma, stock prepared in DI water to 4,000 U mL^{-1}) and then converting to molar units based on the molar absorptivity of superoxide corrected for the absorption of hydrogen peroxide formed during decay at the same wavelength (Bielski et al. 1985). In order to create secondary standards for analysis on the FeLume, these solutions were further diluted in TAPS buffered ASW (481 mM NaCl, 27 mM $MgCl_2$•$6H_2O$, 10 mM $CaCl_2$•$2H_2O$, 9 mM KCl, 6 mM $NaHCO_3$, $MgSO_4$•$7H_2O$, 3.75 mM N-[Tris(hydroxymethyl)methyl]-3-aminopropanesulfonic acid, pH=8.0, 75 μM DTPA, all major salts are Sigma BioXtra grade, TAPS is ARCOS Organics 99+% for biochemistry). Superoxide standards were run with an in-line filter without cells to provide consistency with biological experiments and account for any possible artifacts of filtration. The carrier solution was allowed to pass across the filter and react with the MCLA reagent (4.0 μM MCLA, 50 μM DTPA, 0.10 M MES, pH=6.0, reagent grades same as listed above, MES hydrate is Alfa Aesar 99+%) until a stable baseline (<5% coefficient of variation) was achieved for ~1 minute. Then the secondary standards were pumped directly through the analyte line across the in-line filter. The analyte and reagent were typically pumped at a flow rate of 3.0-4.0 mL min^{-1}, which was confirmed gravimetrically. Because superoxide is unstable, both primary and secondary standards were prepared immediately before each measurement.

To prepare calibration curves, the chemiluminescence signal generated from the secondary standards was baseline-corrected for chemiluminescence signal arising from the autooxidation of the MCLA reagent. Baseline correction was achieved by subtracting the average background signal generated from the carrier solution passing over the in-line filter (without KO_2) and reacting with the MCLA reagent for at least one minute. Baseline-corrected chemiluminescence data collected over several minutes of superoxide decay in standard solutions were log-linear with respect to time, and therefore modeled using pseudo-first order decay kinetics. The half-life of superoxide in most calibrations was typically 2.5 minutes or less.

Daily calibration curves were generated from three paired observations of time-zero superoxide concentration (dependent variable) and extrapolated chemiluminescence (independent variable) using linear regression. Because chemiluminescence values were baseline-corrected, regression lines were forced through the origin. Calibrations yielded highly linear curves (typically $R^2 > 0.9$), with a typical sensitivity of 1 chemiluminescence unit per pM superoxide.

As in calibration experiments, each biological experiment began with the placement of a clean syringe filter downstream of the peristaltic pump and upstream of the flow cell in the analyte line. Stable baseline signals (<5% coefficient of variation) were generated in biological experiments from carrier solution passing through the in-line filter and reacting with MCLA for at least one minute prior to the addition of cells. The pump was temporarily stopped and cells were added by syringe to the in-line filter to achieve the desired cell number. The presence of cells did not alter flow rates during the experiment. Extracellular superoxide produced by the organisms supported on the in-line filter and released into the carrier solution was detected downstream upon mixing with the MCLA reagent in the flow cell. These signals were corrected for background chemiluminescence by subtracting the average baseline obtained immediately before the addition of cells and converted to steady state concentration measurements using the calibration function determined on that day. The detection limit for these measurements, calculated assuming that the minimum detectable baseline-corrected signal was three times the standard deviation of the baseline, typically ranged from 25 to 50 pM. Net superoxide production rates were then calculated as the product of the steady state superoxide concentration and flow rate (pmol hr^{-1}). Production rates of superoxide by each culture sample were normalized to the total number of cells added to provide cell-normalized rates (in units of amol $cell^{-1}$ hr^{-1}).

Superoxide decay rates were determined by standard additions of superoxide to cell cultures of a subset of organisms in this study. After stable chemiluminescence signals were achieved using the carrier solution, secondary standards ranging from 3 to 60 nM were prepared in an aliquot of identical carrier solution, as described above, and pumped across the cells deposited onto the in-line filter. Standard additions were prepared at concentrations chosen to represent a significant (but not excessive) addition to the cell signal. As in calibration experiments, baseline-corrected chemiluminescence data collected over at least one minute of decay were log-linear. However, in this case, the stable, cell-derived signal measured immediately before the standard addition was used as the baseline. Time-zero chemiluminescence values were then

determined by modeling the log-transformed decay data with pseudo-first order kinetics. The extrapolated chemiluminescence values thus represent the difference in signal due to the added superoxide standard. These were converted to a concentration using the daily calibration factor. These "recovered" concentrations were finally expressed as a percentage of the actual added superoxide concentration. Net superoxide production rates were divided by these standard recoveries to generate gross production rates.

To verify that the signal produced by the cells was due to superoxide, SOD was added to the buffer at the end of each individual run to produce a final SOD concentration of 0.8 U mL^{-1}. SOD always caused a rapid drop in signal, to a final baseline that was typically below the initial baseline measured before cells were loaded. The difference in the initial and final baselines (~200 chemiluminescence units) was of the same magnitude as the drop in baseline observed when the same amount of SOD was added to the carrier solution in the absence of cells. The baseline drop reflects either a small, yet non-zero concentration of superoxide in the carrier solutions and/or (more likely) an effect of SOD on the background chemiluminescence produced by the autooxidation of MCLA (Hansard et al. 2010). To provide the most conservative value for the superoxide production rates, the higher baseline (without SOD) was used in biological superoxide production calculations.

5.2.2 Culturing and cell counts

Cultures of each organism were grown to mid- to late exponential phase for extracellular superoxide production measurement. Axenic cultures of *Synechococcus* WH8102 were grown in 0.2 μm filtered sterile Vineyard Sound water amended with SN nutrients (Waterbury et al. 1986) at 18˚C in 14:10 hour light:dark cycles (35 μmol photons m^{-2} s^{-1}). Growth was monitored via optical density at 750 nm (Molecular Devices SpectraMax M3 microplate spectrophotometer). Cultures of two strains of *Pelagibacter* isolated from contrasting oceanic environments (HTCC1062, Oregon Coast; HTCC7211, Sargasso Sea) were grown at 16˚C (HTCC1062) or 20˚C (HTCC7211) in 12 hour light:dark cycles using sterile artificial seawater (ASW) amended with 100 μM pyruvate, 50 μM glycine, 10 μM methionine, and 1x vitamin mix (Carini et al. 2013). Four strains of *Prochlorococcus*, each representing a different ecotype, *Synechococcus* WH8102, and *Synechococcus* WH7803 cells were grown in 0.2 μm filtered sterile Sargasso Sea water amended with Pro99 nutrients prepared as previously described (Moore et al. 2007). Since

Synechococcus was cultured in both SN and Pro99 media as part of this study, we will refer to the media conditions when referring to *Synechococcus* throughout the study (SN or Pro99). Cells were grown in a 13:11 light:dark cycle with simulated dawn and dusk (Zinser et al. 2009) at 24°C. Near optimal peak light levels for maximizing growth rate were used for all *Prochlorococcus* strains involved and included the following combinations: MED4 (74 µmol photons m^{-2} s^{-1}), MIT9312 (80 µmol photons m^{-2} s^{-1}), NATL2A (39 µmol photons m^{-2} s^{-1}), and MIT9313 (26 µmol photons m^{-2} s^{-1}). *Synechococcus* WH8102 and *Synechococcus* WH7803 grown in Pro99 media were both grown at peak light levels of 70 µmol photons m^{-2} s^{-1}. To monitor cell growth, cells were monitored via bulk chlorophyll fluorescence (10AU model, Turner Designs, Sunnyvale, CA). Cultures used in all experiments were axenic and were tested for purity using three broths ProAC, ProMM, and MPTB (Saito et al. 2002; Morris et al. 2008; Berube et al. 2015), as well as by flow cytometry. *Phaeocystis antarctica* and *Geminigera cryophila* were grown in f/2 + Si media and maintained at 2–4ºC in a 14:10 light:dark cycle (Guillard 1975).

Cultures were harvested and measured for extracellular superoxide concentration and production while cells were actively growing in their respective growth media. *Synechococcus, Prochlorococcus,* and *Pelagibacter* were harvested when the log of cell density (as measured by fluorescence, optical density, and/or flow cytometry) versus time was linear, indicating exponential growth phase. *Geminigera* and *Phaeocystis* are both relatively slow-growing Antarctic strains that take approximately 1 month to complete a growth cycle. *Geminigera* was harvested when cell counts reached approximately half of the maximum cell count observed at stationary phase (max is ~$6.5x10^5$ under the growth conditions described). Quantifying *Phaeocystis* cell counts can be challenging in the late stages of cell growth due to a mixture of individual and colonial organisms. Therefore, cells were harvested two weeks after inoculation, and the absence of colonial cells was confirmed with flow cytometry. The range of growth media requirements, organism size, and organism physiology meant that cells were harvested at different cell densities. Although culture density varied, organisms were measured at similar cell number by varying the volume of culture that was passed over through the filter prior to analysis. Cell densities at the time of analysis were as follows: *Synechococcus* WH8102 (Vineyard Sound SN media): $9.0x10^5$ cells/mL, *Synechococcus* WH8102 (Pro99): $6.3\text{-}9.8x10^5$ cells/mL, *Synechococcus* WH7803 (Pro99): $6.1\text{-}6.3x10^5$ cells/mL, *Prochlorococcus* MED4: $1.0\text{-}2.2x10^8$ cells/mL, *Prochlorococcus* MIT9312: $1.9\text{-}2.3x10^8$ cells/mL, *Prochlorococcus* NATL2A: $6.9x10^7\text{-}1.2x10^8$ cells/mL,

Prochlorococcus MIT9313: $2.3x10^7$-$4.1x10^7$ cells/mL, *Pelagibacter* HTCC1062: 4.9-5.0x10^7, *Pelagibacter* HTCC7211: 4.8-5.1x10^7, *P. Antarctica*: $2.7x10^5$ cells/mL, and *G. Cryophila* $3.2x10^5$ cells/mL.

Cell counts of each organism were collected by using flow cytometry. Concentrations of *Synechococcus* sp. (cells mL^{-1}) were found by processing 200 µL aliquots of sample as well as 0.01 µm filtered seawater blanks on a Guava easyCyte flow cytometer (Millipore Sigma) at a low flow rate (0.24 µL s^{-1}) for 3 min. Data analyses were performed using Guava InCyte 3.1 software. Populations of *Synechococcus* spp. were identifiable on plots of orange fluorescence versus forward scatter. Particle concentrations of seawater blanks were subtracted from *Synechococcus* spp. concentrations. The Guava easyCyte flow cytometer was calibrated with instrument-specific beads. Growth of *Pelagibacter* cells was measured by enumerating cells every 48 hours. Cell counts were conducted by staining with SYBR Green I (Molecular Probes, Inc.), and counting with a Guava Technologies flow cytometer as described elsewhere (Carini et al. 2013). *Prochlorococcus* cell abundance measurements were run on a Guava easyCyte flow cytometer. Cells were excited with a blue 488nm laser analyzed for chlorophyll fluorescence (692/40nm) and size (forward scatter). *P. antarctica* and *G. cryophila* were counted on an Accuri C6 flow cytometer (BD Biosciences) using the chlorophyll (excitation 640:670/LP) and forward scatter channels. Counts were made using the fast setting (66 µl min^{-1}) with a 2 minute run time.

The target cell counts in sequential loading experiments were meant to approach that of a typical milliliter of surface ocean water (10^5–10^6 cells), however, in the case of *Prochlorococcus* and *Pelagibacter*, lower net superoxide production rates necessitated higher cell counts to produce a signal above the detection limit of the method. Since population dynamics were not readily determined for four strains of *Prochlorococcus*, the extracellular superoxide concentration and net production are determined from two replicates.

5.3 Results and Discussion

5.3.1 Extracellular Superoxide by Key Marine Microbes

Extracellular superoxide production has long been established as a characteristic of fungi and higher plants, yet it is only recently that this phenomenon has been recognized as a widespread phenomenon in heterotrophic bacteria (Lamb and Dixon 1997; Buetler et al. 2004; Diaz et al. 2013) and phytoplankton (Marshall et al. 2002, 2005; Rose et al. 2008b; Schneider et al. 2016;

Diaz and Plummer 2018). Here we show that this phenomenon is also widespread among some of the most abundant and ecologically important microorganisms of the global ocean. Extracellular superoxide production was detected and quantified by all nine microbes explored here, including *Synechococcus* (WH8102 and WH7803), *Phaeocystis* (*P. antarctica*), and *Geminigera* (*G. cryophila*), two *Pelagibacter* ecotypes (HTCC1062 and HTCC7211), and four *Prochlorococcus marinus* strains including high-light and low-light ecotype representatives (MIT9312, MED4, NATL2A, and MIT9313) (Table 1). Overall, these mid- to late exponential phase cultures showed a large range in dark extracellular superoxide production, with steady-state superoxide concentrations ranging from <35 pM to 21,768 pM and cell normalized superoxide production rates spanning from undetectable levels to 14,830 amol cell^{-1} hr^{-1}.

The two Southern Ocean algal representatives were prolific superoxide producers, with *G. cryophila* producing far more superoxide than the other organisms studied here under these laboratory conditions. Average steady-state superoxide concentrations and corresponding cell normalized superoxide production rates were 15,170 pM and 6,088 amol cell^{-1} hr^{-1} for *Geminigera* and 5,332 pM and 3,019 amol cell^{-1} hr^{-1} for *P. antarctica* (Table 1). *G. cryophila* is a cryptophyte widespread within surface waters of the Southern Ocean (Gast et al. 2014), while its distribution outside of the Southern Ocean is not well characterized. *G. cryophila* is a mixotrophic protist capable of carbon acquisition by oxygenic phototrophy and bacterial ingestion (McKie-Krisberg et al. 2015). *Phaeocystis* spp., a marine haptophyte genus, is typically found at high latitudes (>50º) in both the Northern and Southern hemisphere (Vogt et al. 2012). *Phaeocystis* spp. play a particularly important role in the Southern Ocean biological pump, where it is responsible for >10% of primary productivity and >30% of the sinking particle flux in some regions (Alvain et al. 2008; Wang and Moore 2011). *Phaeocystis* forms large seasonal blooms in the Southern Ocean that rapidly draw down nutrients in the surface water and can have deleterious effects on other marine organisms (Schoemann et al. 2005; Vogt et al. 2012). Despite their ecological relevance in the biogeochemistry of the Southern Ocean, these are the first measurements of ROS production by *Phaeocystis* and *Geminigera,* or haptophytes and cryptophytes in general.

The extracellular superoxide production rates of these two organisms are well within the range of values previously measured for eukaryotic algae, which spans ~60 to >10^7 amol cell^{-1} hr^{-1} (Marshall et al. 2002, 2005; Diaz and Plummer 2018). With respect to eukaryotic phytoplankton, *G. cryophila* and *P. antarctica* extracellular superoxide production rates are intermediate to those

of Raphidophytes involved in harmful algal blooms and diatoms (Diaz and Plummer 2018). Elevated ROS production is a common feature among species that produce harmful algal blooms, which typically occupy the higher end of this range (Diaz and Plummer 2018). Raphidophytes belonging to the genus *Chattonella* produce extracellular superoxide at rates between $6.6x10^6$ and 1.6×10^7 amol cell^{-1} hr^{-1} (Marshall et al. 2002). Diatoms occupy the lower part of this range, with net extracellular superoxide production rates between 60 and ~1300 amol cell^{-1} hr^{-1} (Rose et al. 2008b; Schneider et al. 2016). The high extracellular superoxide production rates that appear common among many eukaryotic algae point to their potential importance in regulating superoxide levels within marine surface waters, particularly in regions where eukaryotic algae contribute significantly to primary production (e.g. Southern Ocean).

The three globally representative picoplankton explored here produced extracellular superoxide at a wide range of rates, with *Synechococcus* producing the greatest and *Prochlorococcus* the least extracellular superoxide (Table 1). Average steady-state superoxide concentrations and corresponding cell normalized superoxide production rates were 5,838 pM and 337 amol cell^{-1} hr^{-1} for *Synechococcus* grown in Vineyard Sound SN media, 87 pM and 23 amol cell^{-1} hr^{-1} for *Synechococcus* WH8102 and WH7803 grown in Sargasso Sea Pro99 media, 289 pM and 0.16 amol cell^{-1} hr^{-1} for two ecotypes of *Pelagibacter*, and 380 pM and 0.026 amol cell^{-1} hr^{-1} for four strains of *Prochlorococcus* (Table 1). The concentrations of extracellular superoxide measured from the *Prochlorococcus* strains were below the method detection limit until the number of cells analyzed on the filter was greater than 10^8 (Table 1).

The superoxide production rates from the current study represent the first measurements of superoxide by *Prochlorococcus*. All four *Prochlorococcus* strains measured in this study exhibit extremely low extracellular superoxide production rates relative to the other organisms in this study. The four strains of *Prochlorococcus* represent both high-light (HL) and low-light (LL) adapted ecotypes. HL adapted Prochlorococcus strains MED4 (HLI) and MIT9312 (HLII) are more abundant in surface waters and the LL adapted strains NATL2A (LLI) and MIT9313 (LLIV) are more abundant at the mixed layer or deeper (Kettler et al. 2007, Johnson et al. 2006), Regardless of light adaptation, the strains did not exhibit any monotonic trend in net or gross superoxide production (Table 2). *Prochlorococcus* MED4 was the lowest superoxide producer among these *Prochlorococcus* strains. In fact, the net extracellular superoxide production by *Prochlorococcus* MED4 is among the lowest values measured of any marine microbe to date (Diaz

et al. 2013; Diaz and Plummer 2018). Net extracellular superoxide production rates among the HLII, LLI, and LLIV ecotypes are not dissimilar, but determining whether light tolerance adaptations and extracellular ROS production are related is not readily tractable without knowledge of a superoxide production mechanism. One possibility for the significantly lower rates seen in *Prochlorococcus* may be related to a lack of genes encoding superoxide-producing proteins due to genomic streamlining (Giovannoni et al. 2005). It is interesting to note that the lowest producer of extracellular superoxide also contains the smallest genome among these *Prochlorococcus* strains (Hess et al. 2001). Further mechanistic study is needed adequately address these observations.

Previous measurements of extracellular superoxide production by *Synechococcus* have demonstrated overlapping rates ranging from ~10 amol cell^{-1} hr^{-1} to in excess of 100 amol cell^{-1} hr^{-1} (Rose et al. 2008b). The rates we measure for *Synechococcus* also overlap with the range in extracellular superoxide production rates of another cyanobacterium. *Trichodesmium*, a nitrogen-fixing cyanobacterium present in oligotrophic surface waters, produces extracellular superoxide at rates that range from 5-20 pM colony^{-1} hr^{-1}, which, corresponds to approximately 250–1000 amol cell^{-1} hr^{-1} (assuming ~200 trichoms per colony and ~100 cells per trichome (Carpenter et al. 2004)). *Lyngbya majuscula*, a coastal marine cyanobacterium, also demonstrates extracellular superoxide production, although the cell specific rate was not quantified (Rose et al. 2005). These measurements suggest extracellular superoxide production is indeed a common trait among marine cyanobacteria. *Synechococcus* is second only to *Prochlorococcus* in cyanobacterium abundance in the ocean, and is similarly globally distributed (Flombaum et al. 2013). Its widespread nature and relatively high extracellular superoxide production point toward *Synechococcus* as perhaps the most significant producer and biological regulator of extracellular ROS in the surface ocean.

As with *Prochlorococcus*, these are the first superoxide measurements of organisms belonging to the ubiquitous SAR11 clade. The average superoxide production rate of strains of HTCC1062 and HTCC7211 (0.16 amol cell^{-1} hr^{-1}) falls within previous measurements of marine heterotrophic bacteria. One previous survey of heterotrophic bacteria demonstrated that nearly all heterotrophic bacteria produce extracellular superoxide, with net production rates ranging from 0.003 to 13.1 amol cell^{-1} hr^{-1} (Diaz et al. 2013). When we consider only previous measurements of marine bacteria in exponential phase belonging to the same phylum as *Pelagibacter*, *Alphaproteobacteria*, this range narrows to 0.04 to 1.7 amol cell^{-1} hr^{-1}. *Roseobacter* spp., which

can account for over 20% of marine bacteria in coastal waters (Brinkhoff et al. 2008), exhibits net extracellular superoxide at a rate of 0.09 to 0.3 amol cell^{-1} hr^{-1}. The net extracellular superoxide production exhibited by *Pelagibacterales* is remarkably similar to previously characterized *Alphaproteobacteria* despite quite significant differences in metabolic lifestyles (i.e. oligotroph vs. copiotroph). The two *Pelagibacterales* ecotypes we examined in this study are found in contrasting regions of the surface ocean; HTCC1062 is a member of group Ia.1 which are found in colder high latitude regions, whereas HTCC7211 is a member of group Ia.3 which are found in warm stratified oceans (Giovannoni 2017). SAR11 cells are present and abundant throughout the dark ocean as well, providing a source of superoxide below the photic zone (Giovannoni 2017). *Pelagibacterales*, which contains the most highly conserved genome of any free-living bacteria, is thought to represent approximately 25% of cells in the global ocean (Morris et al. 2002; Grote et al. 2012; Giovannoni 2017). While it has been shown that dark, extracellular superoxide production among marine heterotrophic bacteria is widespread, the confirmed production of superoxide by *Pelagibacterales,* the most abundant marine, heterotrophic bacterial group, suggests that superoxide production is ubiquitous across a diverse array of oceanic ecosystems (Diaz et al. 2013).

Given the wide range in cell size and hence surface area explored here, trends in extracellular superoxide production were also compared by normalizing rates to cell surface area (Table 1). Surface area estimates are derived from various sources as follows: *Synechococcus* (Olson et al. 1990), *Phaeocystis* (Moisan and Mitchell 1999), *Prochlorococcus* (Partensky et al. 1999), *Geminigera* (Johnson et al. 2009), and *Pelagibacter* (Zhao et al. 2017). The order of magnitude difference in net extracellular superoxide production between *Synechococcus* and the two algae, *Phaeocystis* and *Geminigera*, collapses to a much narrower range when normalized to cell surface area (Table 1). *Synechococcus* (SN media) surface area normalized rates ranged from 36 to 176 amol μm^{-2} hr^{-1}, that of *Synechococcus* (Pro99 media) ranged from 1.4 to 21.2 amol μm^{-2} hr^{-1}, *Phaeocystis* produced between 33 and 83 amol μm^{-2} hr^{-1}, and *Geminigera* produced between 3.1 and 28 amol μm^{-2} hr^{-1}. Extracellular superoxide production rates by *Prochlorococcus*, however, are not reconciled with those of other organisms when normalized to surface area. The typical *Synechococcus* cell has about three times the surface area of the typical *Prochlorococcus* cell, but the measured extracellular superoxide production rates differ by more than two orders of magnitude (Olson et al. 1990; Partensky et al. 1999). The net extracellular superoxide production

rate by *Pelagibacter* falls toward the low end of that of previously observed in marine heterotrophs (Diaz et al. 2013) when normalized to cell number, but when normalized to cell surface area, *Pelagibacter* exhibits a net superoxide production rates that are well within the range of other marine heterotrophs (between 0.38 and 0.79 amol μm^{-2} hr^{-1}). *G. cryophila*, the organism in this study that is capable of phototrophy and heterotrophy, produced extracellular superoxide at rates in a range that falls in between the phototrophs and heterotrophs in this study. The differences between phototrophs and heterotrophs with respect to extracellular superoxide production, and the similarity of surface area normalized extracellular superoxide production rates among many phototrophs and heterotrophs suggests that extracellular superoxide production may be fundamentally related to carbon acquisition metabolism. However, more information about the pathways of extracellular superoxide production is needed to make such a determination.

Overall, these findings highlight significant potential sources of ROS to the surface and deep ocean. Although these measurements were collected under laboratory conditions with nutrient amended artificial or natural seawater, the maintenance of extracellular superoxide concentrations ranging from ~100 pM to >10 nM is consistent with observations of dark extracellular superoxide production in natural waters (Rose et al. 2008b; Hansard et al. 2010; Rusak et al. 2011; Diaz et al. 2016; Roe et al. 2016). The similarity between extracellular superoxide concentrations observed in culture studies and natural waters is consistent with the ability of marine microbes to regulate extracellular ROS in aquatic systems.

5.3.2 Cell Number Effects on Superoxide Production

Steady-state net extracellular superoxide production rates varied as a function of cell number (Figure 1). Generally speaking, as cell number increased, the cell-normalized net extracellular superoxide production decreased. The effects of decreasing per-cell net production rate were apparent in the measured steady-state superoxide concentrations (Figure 2; representative FeLume and corresponding concentration data for *Phaeocystis*). As cell number increased, the steady-state superoxide concentration also increased. However, this increase was not proportional to the number of cells; the marginal increase in extracellular superoxide production diminished with increasing cell numbers. In some cases, this trend reached a maximum steady state superoxide concentration, and subsequent cell additions led to a small decrease in superoxide concentration. These cell-number dependent trends were observed for all organisms

investigated in this study with the exception of *Prochlorococcus*. Due to the high cell numbers required to obtain a detectable superoxide signal for *Prochlorococcus* using this methodology, sequential loading experiments did not allow us to determine what, if any, population effects may be at work in *Prochlorococcus* cultures.

To test whether the same trend was observed when cells were diluted prior to analysis, as opposed to sequential addition during analysis, superoxide production was measured for serially diluted cultures of *Synechococcus* WH8102 (Figure 3). Exponential phase cells of *Synechococcus* were diluted 10- and 100-fold into sterile seawater, and extracellular superoxide production was analyzed by loading a single aliquot after 3 hours and 7.5 hours following dilution. We found similar cell density trends for dilution series and sequentially loaded *Synechococcus* cells. While the per-cell superoxide production rates did not change significantly between the undiluted and the 10-fold dilution ($p=0.11$ and $p=0.30$ for 3 hour and 7.5 hour time point, respectively, using two-sample t-test), the 100-fold dilution demonstrated a significantly higher cell-normalized superoxide production rate at both time points ($p=0.02$ and $p=0.004$ for the 3 hour and 7.5 hour time point, respectively). Additionally, the 100x dilution at the 7.5 hour time point yielded nearly twice the cell-normalized superoxide production rate than the 3 hour time point.

The low cell-normalized net superoxide production rate by *Prochlorococcus* under the conditions of this study made it difficult to draw any direct comparisons between *Synechococcus* and *Prochlorococcus* at the same cell number. To account for differences in extracellular superoxide production that may arise from growth conditions, we measured extracellular superoxide production rates by *Synechococcus* and *Prochlorococcus* controlling for growth media. Figure 4 shows the net extracellular superoxide production rate of *Synechococcus* and *Prochlorococcus* grown in Sargasso Sea Pro99 media at similar cell numbers ranging from ~10^5 to ~10^7 cells. *Synechococcus* grown under these conditions produced net superoxide ranging from 4.3 amol cell^{-1} hr^{-1} at 6.1 x 10^6 cells to 67 amol cell^{-1} hr^{-1} at 1.5 x 10^5 cells, while *Prochlorococcus* produced net extracellular superoxide at undetectable levels. The cell number trend seen for *Synechococcus* grown in Vineyard Sound SN media is still quite apparent for *Synechococcus* grown in Sargasso Sea Pro99 media. Net extracellular superoxide production rates were similar between *Synechococcus* WH8102 and *Synechococcus* WH7803, which we discuss below. Although both strains of *Synechococcus* produce significantly more extracellular superoxide than *Prochlorococcus*, the more nutrient-poor Pro99 media influenced the net extracellular superoxide

produced by *Synechococcus*. At the same cell density, *Synechococcus* WH8102 grown in Sargasso Sea Pro99 media produced extracellular superoxide at a rate 1 to 2 orders of magnitude less that observed in Vineyard Sound SN media. Such a difference suggests that nutrient replete coastal waters may be greater sources of extracellular superoxide to the ocean than their nutrient deprived counterparts. Additionally, this suggests that growth rate may be factor in determining extracellular superoxide production rate.

The cell-number trends that we see across this suite of disparate organisms have been previously recorded for several HAB-forming algae, and the cyanobacterium *Trichodesmium* (Marshall et al. 2005; Hansel et al. 2016; Diaz et al. 2018). Our work and these previous works establish cell abundance control on ROS as a common trait among extremely diverse groups of marine microorganisms. This cell number response is consistent with cell signaling behavior and may point to extracellular superoxide production as a key physiological process within these microbes. Although a more general response to changing environmental conditions cannot be ruled out, the only systematic change between measurements of a given microbe was the number of cells loaded on the filter. Therefore, any change in environmental conditions is most likely cell density dependent. At the very least, we can rule out a systematic effect of cell biomass and growth stage since cells were added from the same culture. The extracellular concentration of ROS is likely set by a consortium of microbial members that produce and degrade extracellular superoxide, whereby superoxide levels likely evolve toward some community optimum.

5.3.3 Superoxide Decay and Gross Superoxide Production

To determine the role of superoxide decay on measured net superoxide production rates, a subset of measurements was conducted on *Synechococcus, Pelagibacter, and Prochlorococcus* using standard superoxide additions (Table 2, Figure 5). The recovery of standard KO_2 spikes provides insight as to the general mechanisms by which organisms modulate extracellular superoxide concentration, specifically via production or decay. The pseudo first order decay rate constants among these three picoplankton ranged from 0.0059 to 0.0207 s^{-1}, with *Pelagibacter* exhibiting the lowest rate and *Synechococcus* exhibiting the highest (Table 2). These decay rate constants of extracellular superoxide are similar to rates observed in culture and in natural seawater (Rose et al. 2008b; Diaz et al. 2013; Roe et al. 2016). For *Synechococcus*, the average recovery for a superoxide standard addition (i.e. the fraction of added superoxide that was not degraded by

cells) was 13.1% (SEM = 5.5%) and did not correlate with the number of cells used in the measurement ($R^2 = 0.03$, cell number range: $1.5x10^5$ to $3.6x10^6$ cells). Both strains of *Pelagibacter* produced an average yield of 78.9% (SEM = 11.1%), and similarly did not correlate with cell number ($R^2 = 0.002$, cell number range: $2.5x10^8$ to $7.5x10^8$ cells). The four *Prochlorococcus* strains had standard recoveries ranging from 27.5 to 54.2%. The HL strain MIT9312, which represents the most abundant *Prochlorcoccus* ecotype,, exhibited the highest superoxide decay rate constant and lowest recovery of exogenous superoxide among other *Prochlorococcus* strains, 27.5% (Table 2). This elevated superoxide decay rate constant may be related to an inherent capacity to degrade photochemically generated superoxide in the uppermost surface waters (Powers and Miller 2014). These values highlight the elevated ability for *Synechococcus* and to a lesser extent *Prochlorococcus* to eliminate extracellular superoxide. The relative insensitivity of extracellular superoxide degradation to cell number also suggests that variation in the extracellular superoxide concentrations observed here is primarily a function of rapid changes in production.

Gross extracellular superoxide production, much like net extracellular superoxide production, exhibited a wide range among the picoplankton analyzed in this study (Table 2). Average gross extracellular superoxide production rates were 786 amol $cell^{-1}$ hr^{-1} for *Synechococcus*, 0.057 amol $cell^{-1}$ hr^{-1} for four *Prochlorococcus* strains, and 0.20 amol $cell^{-1}$ hr^{-1} for two ecotypes of *Pelagibacter*. The relatively high cell normalized superoxide production rate by *Synechococcus* has been previously reported, but its elevated capacity to degrade exogenous superoxide indicates that its gross production is nearly 10 times higher than measurements of net superoxide production would suggest (Rose et al. 2008b). Its ability to degrade nearly 90 percent of the exogenous superoxide also suggests that *Synechococcus* may play an important role in controlling superoxide levels within the surface ocean via antioxidant pathways.

5.3.4 Insights into Marine ROS Formation

Despite a widespread ability of marine microbes to produce extracellular superoxide, the reasons for this process and underlying mechanisms remain unclear. Extracellular superoxide production rates are dependent upon physiological and environmental factors, such as cell growth stage, cell density, light intensity, iron availability, and overall nutrient availability (Rose et al. 2008b; Diaz et al. 2013, 2018; Hansel et al. 2016; Schneider et al. 2016; Hansel et al. 2019). The data we present in this study expand the number of organisms known to display cell density

dependent superoxide production to include additional eukaryotic algae, picocyanobacteria, and picobacteria. While we cannot make broad claims about the functionality of extracellular superoxide in these organisms based on these observations, the apparent upregulation of biological superoxide production at low cell densities is certainly consistent with a role for extracellular superoxide in cell signaling and/or cell growth (Buetler et al. 2004). In fact, recent studies found that extracellular superoxide within the widespread *Roseobacter* clade is tightly regulated via both production and decay processes over the course of a life cycle (Hansel et al., 2019). Removal of this extracellular superoxide greatly inhibited cell growth, pointing to an essential role for superoxide in growth by this ubiquitous bacterial group. For the eukaryotic microbes explored here (*Geminigera* and *Phaeocystis*), extracellular superoxide may be produced by NAD(P)H oxidases, the widespread eukaryotic enzyme that is involved in fungal and plant extracellular superoxide production (Lara-Ortíz et al. 2003). Similar enzymes have also been implicated in superoxide production by the coral algal symbiont *Symbiodinium* (Saragosti et al. 2010), the toxic raphidophyte *Chattonella* (Kim et al. 2000), and the diatoms *Thalassiosira weissflogii* and *Thalassiosira pseudonana* (Kustka et al. 2005). The enzymes responsible for extracellular superoxide production have not been established in *Synechococcus* or *Prochlorococcus*, hindering predictions of the mechanisms at play in these microorganisms. Within heterotrophic bacteria, heme peroxidases are responsible for formation of extracellular superoxide production by a bacterium within the common marine *Roseobacter* clade (Andeer et al. 2015). Similar heme peroxidases are not annotated within current *Pelagibacter* genomes. Considering that the heme peroxidase in *Roseobacter* sp. is large (~3500 amino acids) (Andeer et al. 2015) and the fact that *Pelagibacter* possesses a streamlined genome, alternative enzymes are most likely responsible for extracellular superoxide production in this organism. In addition to enzymes responsible for superoxide production, the superoxide scavenger SOD is responsible for regulation of extracellular superoxide levels in some organisms, including the bacteria *Escherichia coli* and *Salmonella typhimurium* (Carlioz and Touati 1986; Storz et al. 1987) and is likely responsible at least in part for the superoxide decay observed here. Clearly, further insight into the processes at play in these superoxide dynamics is needed, and future investigations will specifically target the biochemical process(es) responsible for superoxide production within these key marine microbes.

Prochlorococcus appears to be an outlier among both picoplankton and marine oxygenic phototrophs with respect to extracellular superoxide production. One study observed the

expression of genes related to ROS protection and detoxification through a diel cycle for *Synechococcus* and *Prochlorococcus* and found oxidative stress from both external sources and internal sources (such as the Mehler reaction) can arise from excess visible and UV light (Mella-Flores et al. 2012). *Synechococcus* exhibited strongly upregulated SOD production during the most intense sunlight hours, whereas *Prochlorococcus* exhibited weakly downregulated SOD production during the most intense sunlight hours, and slightly upregulated SOD production in the dark (Mella-Flores et al. 2012). Although *Synechococcus* and *Prochlorococcus* contain different SOD genes (*sodB* and *sodC* in *Synechococcus* vs. *sodN* in *Prochlorococcus*), the divergent behavior with respect to the elimination of superoxide cannot be readily explained. If extracellular superoxide production is involved in cell growth promotion, this divergent behavior could arise from the inability of *Prochlorococcus* to produce optimal extracellular superoxide for its own growth, thus relying on exogenous sources. However, such a conclusion cannot be drawn from this study. The mechanisms of extracellular superoxide production are not well known, so the low relative extracellular ROS production by *Prochlorococcus* cannot be readily explored with genomic or transcriptomic tools at this time. It would be consistent with the genomic streamlining in *Prochlorococcus* to lose much of the ability to produce extracellular superoxide in the presence of abundant sources in the water column (Biller et al. 2015). *Prochlorococcus* is known to take advantage of the ROS degradation capacity of other organisms in the water column to compensate its own ROS degradation deficiencies (Morris et al. 2008, 2011). Itself lacking the ability to produce catalase, *Prochlorococcus* relies on passive diffusion of hydrogen peroxide across the cell membrane where other organisms can degrade it (Morris et al. 2011). Superoxide production and degradation via a reductive pathway or dismutation will lead to hydrogen peroxide formation (Wuttig et al. 2013b). Thus, extracellular superoxide production may ultimately be a disadvantage for *Prochlorococcus* if it adds additional oxidative stress in the form of intracellular hydrogen peroxide. It is also important to note that the *Prochlorococcus* cell numbers added to the filters during superoxide analysis in this study far exceed those of natural waters because of its low extracellular superoxide production rate; extracellular superoxide dynamics may differ at lower cell densities. We also must consider the possibility that *Prochlorococcus* in axenic culture may produce less extracellular superoxide to manage hydrogen peroxide concentrations, which may not be representative of the natural environment, where ROS-degrading microbial associates are likely present. The notion that *Prochlorococcus* produces less extracellular superoxide for the sole

purpose of managing hydrogen peroxide stress becomes less tractable, however, when comparing the net extracellular superoxide production rates by *Synechococcus* WH8102 and *Synechococcus* WH7803 (Figure 4), which are catalase-negative and catalase-positive, respectively (Scanlan et al. 2009). These two strains produce net extracellular superoxide at similar rates, suggesting that upstream regulation of hydrogen peroxide levels via modulation of extracellular superoxide production does not occur. More studies are needed to detail the mix of extracellular and intracellular superoxide production and the spatial allocation of SOD within cells to better understand the economy of ROS in and around cells. Co-culture studies and culture studies with an artificial superoxide source are potential ways to address the potential role of extracellular superoxide in *Prochlorococcus* physiology.

5.4 Summary and Conclusions

Here, we report dark, extracellular superoxide production by five widespread marine microbe groups: *Synechococcus, Prochlorococcus, Pelagibacter, Phaeocystis,* and *Geminigera*. All organisms produced measurable dark extracellular superoxide, exhibiting a large range in steady-state superoxide concentrations and cell normalized production rates. *Synechococcus, Pelagibacter, Phaeocystis,* and *Geminigera* decreased their per-cell net superoxide production rate with increasing cell number. Recovery of standard superoxide additions in the form of KO_2 did not vary significantly with cell number, suggesting that changes in the net generation of superoxide as a function of cell number are driven by changes in gross production.

Extracellular superoxide production was markedly lower for all four strains of *Prochlorococcus* compared to other organisms assessed in this study. The data presented here and previous studies interrogating ROS degradation by *Prochlorococcus* suggest that *Prochlorococcus* has a different relationship altogether with extracellular superoxide (Mella-Flores et al. 2012). Should *Prochlorococcus* indeed have a physiological need for extracellular superoxide, as appears to be the case for some microbes that utilize it as an autocrine growth promotor or as a means to influence iron bioavailability (Buetler et al. 2004; Rose 2012), it is possible that it relies upon extracellular superoxide produced by other organisms and/or abiotic processes to meet this need.

The data we collected in this study highlight the dynamic nature of ROS cycling in representative microorganisms that are present throughout the global ocean. The suite of globally significant marine organisms in this study demonstrate a significant flux of superoxide that is

similarly globally distributed. Four of the five organisms in this study are oxygenic phototrophs or mixotrophs that live in the surface ocean. Previous work has shown that these photosynthetic organisms may produce significant internal ROS from light-dependent processes, but we show here that these organisms are also prolific producers of superoxide in the dark. Further, light has been shown to increase extracellular superoxide levels by some phytoplankton (Hansel et al. 2016; Schneider et al. 2016; Zhang et al. 2016a; Diaz et al. 2018), suggesting that these organisms may be even greater sources of marine superoxide, depending on prevailing light conditions. The significant superoxide flux suggested by our measurements has further implications on trace nutrient cycling within the ocean. Superoxide has been suggested to play a role in nutrient acquisition, particularly in the case of metals that are mobilized via reaction with superoxide (Kustka et al. 2005). Iron is one such metal; superoxide reduces Fe^{3+} to Fe^{2+} under surface ocean conditions (Kustka et al. 2005; Rose et al. 2008a). In addition to Fe, organic carbon, copper (Cu), and manganese (Mn) have been shown to be primary sinks of superoxide in the surface ocean (Wuttig et al. 2013a; b). Superoxide production in the ocean and its reactivity with these biologically significant nutrients, electron donors, and electron acceptors suggests that superoxide, and ROS in general, provides an abiotic shunt in the cycling of redox active element cycles, the scope of which has yet to be realized.

With this study, we continue to expand the measurements of cell specific dark extracellular superoxide production rates. Here we focused on organisms belonging to globally widespread groups to demonstrate the significant potential of superoxide flux in the global ocean. Extracellular superoxide production appears to be widespread throughout the surface and deep ocean. Whether such significant production is largely for physiological benefit or a byproduct of cellular metabolisms remains unclear, but regardless, extracellular superoxide production certainly has consequences for elemental cycling and marine microbial ecology throughout the global ocean.

Figures

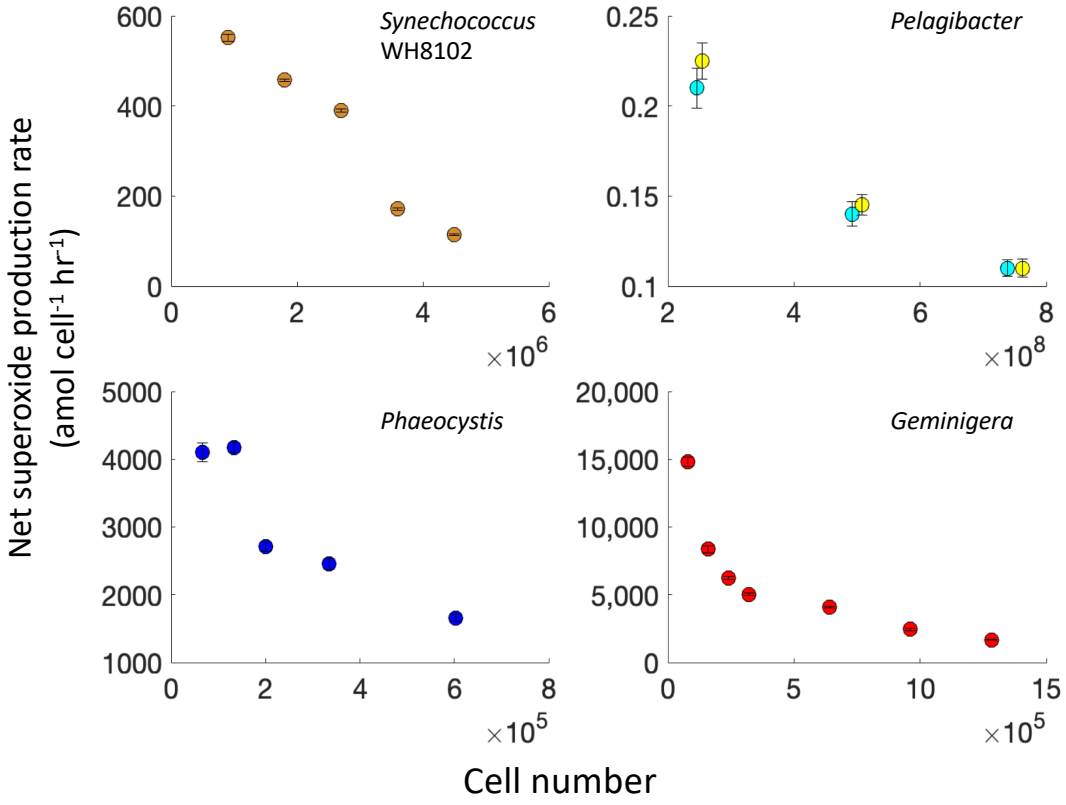

Figure 1- Net extracellular superoxide production rates (amol cell^{-1} hr^{-1}) of *Synechococcus* sp. WH8102 grown in SN media (top left, orange), *Pelagibacter* strain HTCC1062 (top right, cyan) and strain HTCC7211 (top right, yellow), *Phaeocystis antarctica* (bottom left, blue), and *Geminigera cryophila* (bottom right, red). Production rates are shown as a function of different number of cells added to the filter during analysis (added as sequential aliquots of a cell culture with cell densities provided in the methods section). Error bars represent one standard error of the mean superoxide production rate of a single biological sample of the duration of the measurement.

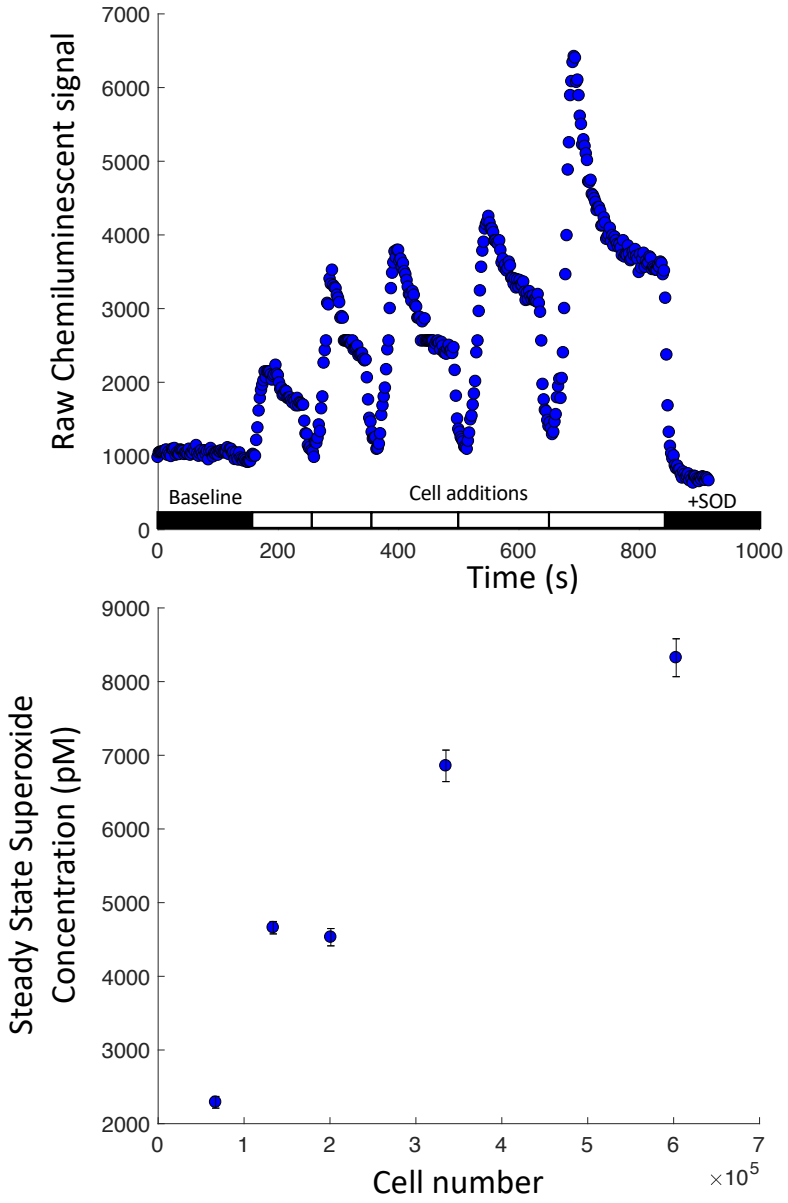

Figure 2- (Top) FeLume trace collected from *Phaeocystis antarctica* cells. Baseline, sequential cell additions, and superoxide dismutase additions are indicated in the black and white boxes below the trace. (Bottom) Steady state superoxide concentration (pM) produced by cells of *Phaeocystis antarctica* harvested at exponential growth phase. Data shown from one bio replicate; error bars represent one standard error of FeLume signal stability.

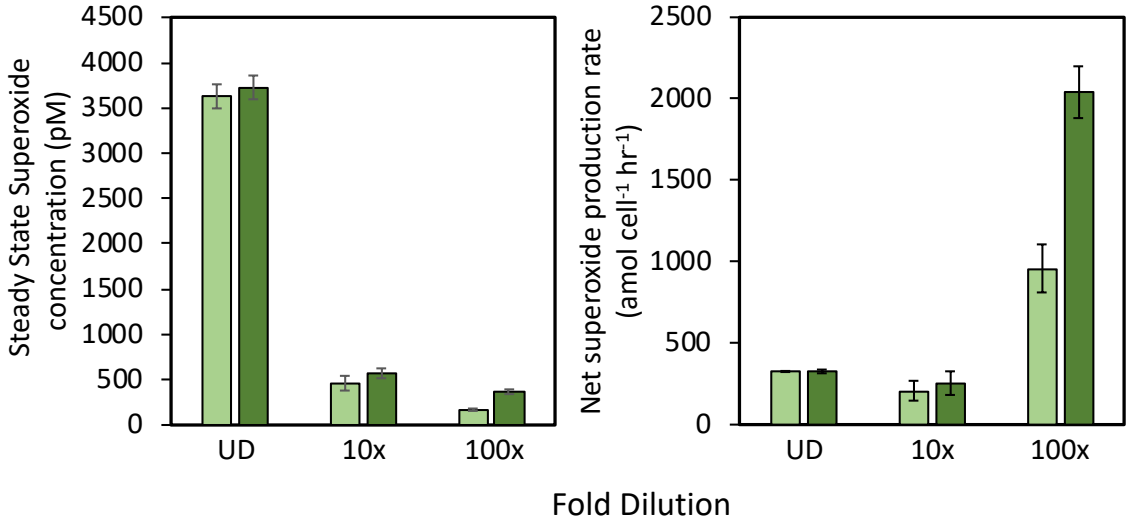

Figure 3- Steady state extracellular superoxide concentration (left) and cell-normalized net superoxide production rate (right). Cell numbers range from $1.3x10^6$ cells in the undiluted cultures to $2.2x10^4$ cells in the 100x dilution at the end of the 7.5 hour time point. Error bars represent one standard error of two biological replicates.

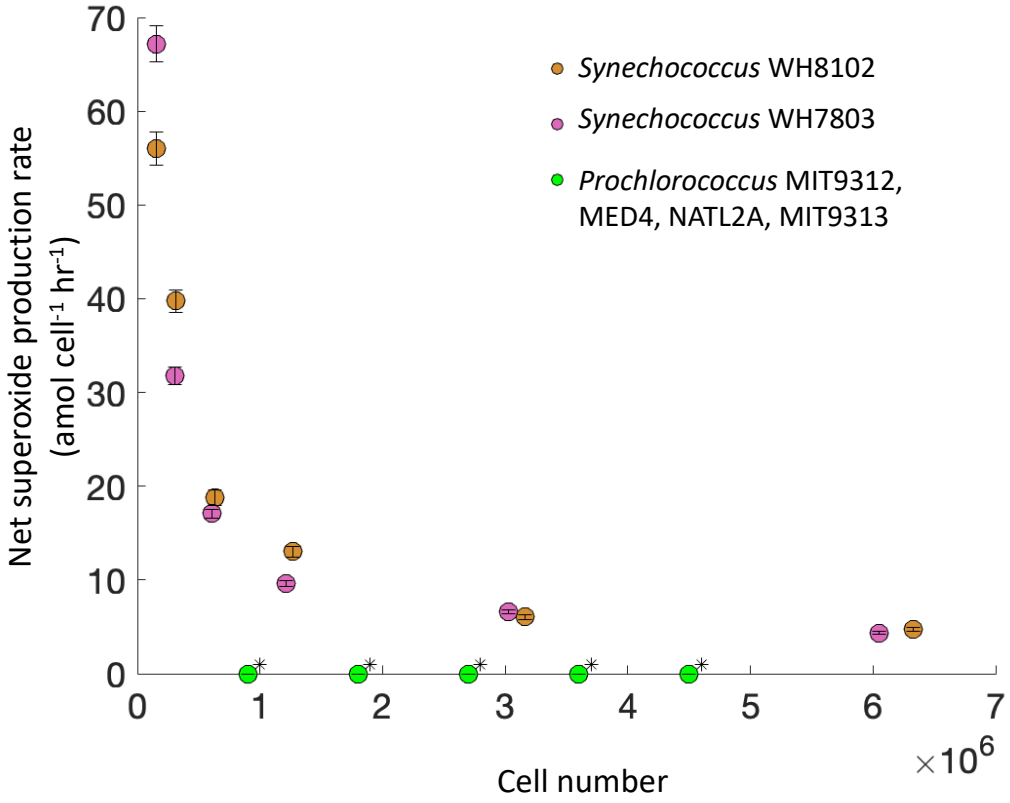

Figure 4- Direct comparison of net extracellular superoxide production rates as a function of cell number by *Synechococcus* WH8102 (orange), *Synechococcus* WH7803 (pink), *Prochlorococcus* MIT9312 (green), *Prochlorococcus* MED4 (green), *Prochlorococcus* NATL2A (green), and *Prochlorococcus* MIT9313 (green) all grown in Sargasso Sea Pro99 media (see methods). All *Prochlorococcus* strains were measured at the same cell numbers and produced net extracellular superoxide below the detection limit (indicated with *), thus each green circle represents four independent measurements.

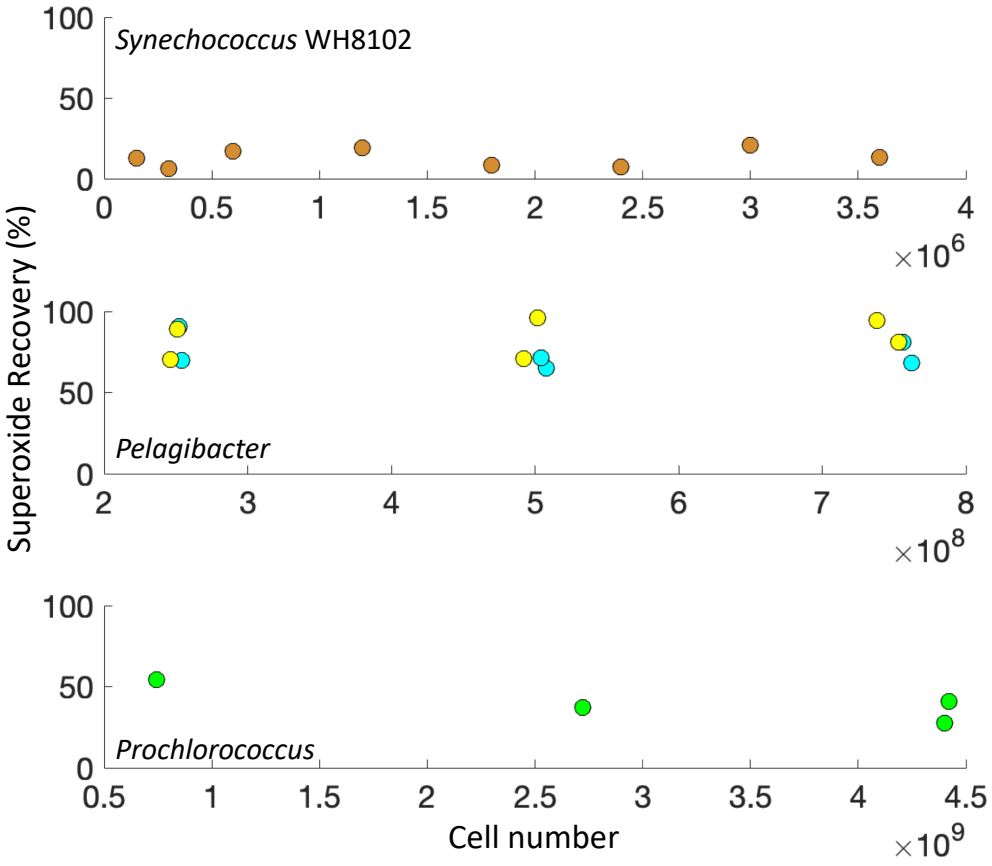

Figure 5- Recovery of standard superoxide spikes (as KO_2) through filter supported cells. Average superoxide recovery for *Synechococcus* sp. WH8102 (orange) is 13.1 ± 5.5% (R^2 = 0.03). Average recovery for *Pelagibacter* strain HTCC1062 (cyan) and strain HTCC7211 (yellow) is 78.9 ± 11.1% (R^2 = 0.002). Average recovery for four *Prochlorococcus* strains (light green) is 39.9 ± 11.0% (R^2 = 0.68).

Tables

Table 1- Summary of extracellular superoxide concentrations and production rates from cell addition experiments

Organism	Cell number	Steady State [$O_2^{\bullet-}$] (pM) Average (range)*	Net $O_2^{\bullet-}$ Production (amol cell^{-1} hr^{-1}) Average (range)*	Surface area normalized Net $O_2^{\bullet-}$ Production (amol μm^{-2} hr^{-1})
Prochlorococcus MIT9312	$9.0x10^5 – 4.5x10^9$	920 (ND-1,368)	0.041 (ND–0.064)	0.017–0.057
Prochlorococcus MED4	$9.0x10^5 – 4.4x10^9$	100 (ND-131)	0.005 (ND–0.007)	0.003–0.006
Prochlorococcus NATL2A	$9.0x10^5 – 2.7x10^9$	382 (ND-417)	0.030 (ND–0.037)	0.021–0.033
Prochlorococcus MIT9313	$9.0x10^5 – 8.2x10^8$	120 (ND-205)	0.029 (ND–0.050)	0.007–0.045
Synechococcus sp. WH8102 (Vineyard Sound SN media)	$9.0x10^5 – 4.5x10^6$	5,838 (4,135–8,777)	337 (114–551)	36–176
Synechococcus sp. WH8102 (Sargasso Sea Pro99 media)	$1.6x10^5 – 6.3x10^6$	92 (49–466)	23.1 (4.8–56.0)	1.4–17.7
Synechococcus sp. WH7803 (Sargasso Sea Pro99 media)	$1.5x10^5 – 6.1x10^6$	82 (56–146)	22.8 (4.3–67.2)	1.4–21.2
Pelagibacter HTCC1062	$2.5x10^8 – 7.5x10^8$	281 (217–339)	0.15 (0.11–0.21)	0.38–0.73
Pelagibacter HTCC7211	$2.5x10^8 – 7.6x10^8$	297 (238–349)	0.16 (0.11–0.23)	0.38–0.79
Phaeocystis antarctica	$6.7x10^4 – 6.0x10^5$	5,332 (2,290–8,324)	3,019 (1,657–4,173)	33–83
Geminigera cryophila	$8.0x10^4 – 1.3x10^6$	15,170 (9,907–21,768)	6,088 (1,673–14,830)	3.1–28

*ND: Non-detect; values not included in averages

Table 2- Summary of extracellular superoxide decay among picoplankton.

Organism	Average Net $O_2^{\bullet-}$ Production (amol cell^{-1} hr^{-1})	Pseudo first order decay rate constant (x10^{-3} s^{-1})	Average Standard Recovery (%)	Average Gross $O_2^{\bullet-}$ Production (amol cell^{-1} hr^{-1})
Prochlorococcus MIT9312	0.019	13.9	27.5	0.070
Prochlorococcus MED4	0.003	8.5	40.8	0.007
Prochlorococcus NATL2A	0.023	8.8	37.2	0.061
Prochlorococcus MIT9313	0.050	9.6	54.2	0.091
Synechococcus sp. WH8102 (SN media)	103	20.7	13.1	786
Pelagibacter HTCC1062	0.15	7.6	83.5	0.18
Pelagibacter HTCC7211	0.16	5.9	74.4	0.22

References

Alvain, S., C. Moulin, Y. Dandonneau, and H. Loisel. 2008. Seasonal distribution and succession of dominant phytoplankton groups in the global ocean : A satellite view. **22**: 1–15. doi:10.1029/2007GB003154

Andeer, P. F., D. R. Learman, M. McIlvin, J. A. Dunn, and C. M. Hansel. 2015. Extracellular haem peroxidases mediate Mn(II) oxidation in a marine R oseobacter bacterium via superoxide production. Environ. Microbiol. **17**: 3925–3936. doi:10.1111/1462-2920.12893

Asada, K. 2006. Production and scavenging of reactive oxygen species in chloroplasts and their functions. Plant Physiol. **141**: 391–396. doi:10.1104/pp.106.082040

Berube, P. M., S. J. Biller, A. G. Kent, and others. 2015. Physiology and evolution of nitrate acquisition in Prochlorococcus. ISME J. **9**: 1195–1207. doi:10.1038/ismej.2014.211

Bielski, B. H. J., D. E. Cabelli, R. L. Arudi, and A. B. Ross. 1985. Reactivity of HO2/O−2Radicals in Aqueous Solution. J. Phys. Chem. Ref. Data **14**: 1041–1100. doi:10.1063/1.555739

Biller, S. J., P. M. Berube, D. Lindell, and S. W. Chisholm. 2015. Prochlorococcus: the structure and function of collective diversity. Nat. Rev. Microbiol. **13**: 13.

Brinkhoff, T., H. A. Giebel, and M. Simon. 2008. Diversity, ecology, and genomics of the Roseobacter clade: A short overview. Arch. Microbiol. **189**: 531–539. doi:10.1007/s00203-008-0353-y

Buetler, T. M., A. Krauskopf, and U. T. Ruegg. 2004. Role of superoxide as a signaling molecule. Physiology **19**: 120–123.

Carini, P., L. Steindler, S. Beszteri, and S. J. Giovannoni. 2013. Nutrient requirements for growth of the extreme oligotroph "Candidatus Pelagibacter ubique" HTCC1062 on a defined medium. Isme J. **7**: 592–602. doi:10.1038/ismej.2012.122

Carlioz, A., and D. Touati. 1986. Isolation of superoxide dismutase mutants in Escherichia coli: is superoxide dismutase necessary for aerobic life? EMBO J. **5**: 623–630. doi:10.1002/j.1460-2075.1986.tb04256.x

Carpenter, E. J., A. Subramaniam, and D. G. Capone. 2004. Biomass and primary productivity of the cyanobacterium Trichodesmium spp . in the tropical N Atlantic ocean. **51**: 173–203. doi:10.1016/j.dsr.2003.10.006

Diaz, J. M., C. M. Hansel, A. Apprill, C. Brighi, T. Zhang, L. Weber, S. McNally, and L. P. Xun. 2016. Species-specific control of external superoxide levels by the coral holobiont during a natural bleaching event. Nat. Commun. **7**. doi:10.1038/ncomms13801

Diaz, J. M., C. M. Hansel, B. M. Voelker, C. M. Mendes, P. F. Andeer, and T. Zhang. 2013. Widespread Production of Extracellular Superoxide by Heterotrophic Bacteria. Science (80-.). **340**: 1223–1226. doi:10.1126/science.1237331

Diaz, J. M., and S. Plummer. 2018. Production of extracellular reactive oxygen species by phytoplankton: past and future directions. J. Plankton Res.

Diaz, J. M., S. Plummer, C. Tomas, and C. Alves-de-souza. 2018. Production of extracellular superoxide and hydrogen peroxide by five marine species of harmful bloom-forming algae. J. Plankton Res. **00**: 1–11. doi:10.11821/dlxb201802008

Dickinson, B. C., and C. J. Chang. 2011. Chemistry and biology of reactive oxygen species in signaling or stress responses. Nat. Chem. Biol. **7**: 504.

Flombaum, P., J. L. Gallegos, R. A. Gordillo, and others. 2013. Present and future global distributions of the marine Cyanobacteria Prochlorococcus and Synechococcus. Proc. Natl. Acad. Sci. U. S. A. **110**: 9824–9829. doi:10.1073/pnas.1307701110

Fridovich, I. 1983. SUPEROXIDE RADICAL - AN ENDOGENOUS TOXICANT. Annu. Rev. Pharmacol. Toxicol. **23**: 239–257. doi:10.1146/annurev.pa.23.040183.001323

Fridovich, I. 1998. Oxygen toxicity: a radical explanation. J. Exp. Biol. **201**: 1203–1209.

Gast, R. J., Z. M. Mckie-krisberg, S. A. Fay, J. M. Rose, and R. W. Sanders. 2014. Antarctic mixotrophic protist abundances by microscopy and molecular methods. Fems Microbiol. Ecol. doi:10.1111/1574-6941.12334

Giovannoni, S. J. 2017. SAR11 Bacteria: The Most Abundant Plankton in the Oceans, p. 231–255. *In* Annual Review of Marine Science, Vol 9. Annual Reviews.

Giovannoni, S. J., H. J. Tripp, S. Givan, and others. 2005. Genome streamlining in a cosmopolitan oceanic bacterium. Science (80-.). **309**: 1242–1245.

Grote, J., J. C. Thrash, M. J. Huggett, Z. C. Landry, P. Carini, S. J. Giovannoni, and M. S. Rappé. 2012. Streamlining and Core Genome Conservation among Highly Divergent Members of the SAR11 Clade. MBio **3**. doi:10.1128/mBio.00252-12

Guillard, R. R. L. 1975. Culture of phytoplankton for feeding marine invertebrates, p. 29–60. *In* Culture of marine invertebrate animals. Springer.

Gus' kova, R. A., I. I. Ivanov, V. K. Kol'tover, V. V Akhobadze, and A. B. Rubin. 1984. Permeability of bilayer lipid membranes for superoxide (O2−) radicals. Biochim. Biophys. Acta (BBA)-Biomembranes **778**: 579–585.

Hansard, S. P., A. W. Vermilyea, and B. M. Voelker. 2010. Deep-Sea Research I Measurements of superoxide radical concentration and decay kinetics in the Gulf of Alaska. Deep. Res. Part I **57**: 1111–1119. doi:10.1016/j.dsr.2010.05.007

Hansel, C. M., C. Buchwald, J. M. Diaz, J. E. Ossolinski, S. T. Dyhrman, B. A. S. Van Mooy, and D. Polyviou. 2016. Dynamics of extracellular superoxide production by Trichodesmium colonies from the Sargasso Sea. Limnol. Oceanogr. **61**: 1188–1200. doi:10.1002/lno.10266

Hansel, C. M., J. M. Diaz, and S. Plummer. 2019. Tight Regulation of Extracellular Superoxide Points to Its Vital Role in the Physiology of the Globally Relevant Roseobacter Clade. **10**: 1–13.

Heller, M. I., and P. L. Croot. 2010. Kinetics of superoxide reactions with dissolved organic matter in tropical Atlantic surface waters near Cape Verde (TENATSO). J. Geophys. Res. **115**. doi:10.1029/2009jc006021

Heller, M. I., and P. L. Croot. 2011. Superoxide decay as a probe for speciation changes during dust dissolution in Tropical Atlantic surface waters near Cape Verde. Mar. Chem. **126**: 37–55.

Heller, M. I., K. Wuttig, and P. L. Croot. 2016. Identifying the Sources and Sinks of CDOM/FDOM across the Mauritanian Shelf and Their Potential Role in the Decomposition

of Superoxide (O2-). Front. Mar. Sci. **3**. doi:10.3389/fmars.2016.00132

Hess, W. R., G. Rocap, C. S. Ting, F. Larimer, S. Stilwagen, J. Lamerdin, and S. W. Chisholm. 2001. The photosynthetic apparatus of Prochlorococcus: insights through comparative genomics. Photosynth. Res. **70**: 53–71.

Johnson, M. D., J. Volker, H. V. Moeller, E. Laws, K. J. Breslauer, and P. G. Falkowski. 2009. Universal constant for heat production in protists. Proc. Natl. Acad. Sci. **106**: 6696–6699. doi:10.1073/pnas.0902005106

Johnson, Z. I., E. R. Zinser, A. Coe, N. P. McNulty, E. M. S. Woodward, and S. W. Chisholm. 2006. Niche partitioning among Prochlorococcus ecotypes along ocean-scale environmental gradients. Science (80-.). **311**: 1737–1740.

Kettler, G. C., A. C. Martiny, K. Huang, and others. 2007. Patterns and implications of gene gain and loss in the evolution of Prochlorococcus. PLoS Genet. **3**: 2515–2528. doi:10.1371/journal.pgen.0030231

Kim, D., A. Nakamura, T. Okamoto, N. Komatsu, T. Oda, T. Iida, A. Ishimatsu, and T. Muramatsu. 2000. Mechanism of superoxide anion generation in the toxic red tide phytoplankton Chattonella marina: Possible involvement of NAD(P)H oxidase. Biochim. Biophys. Acta - Gen. Subj. **1524**: 220–227. doi:10.1016/S0304-4165(00)00161-6

Korshunov, S. S., and J. A. Imlay. 2002. A potential role for periplasmic superoxide dismutase in blocking the penetration of external superoxide into the cytosol of Gram-negative bacteria. Mol. Microbiol. **43**: 95–106.

Kustka, A. B., Y. Shaked, A. J. Milligan, D. W. King, and F. M. M. Morel. 2005. Extracellular production of superoxide by marine diatoms: Contrasting effects on iron redox chemistry and bioavailability. Limnol. Oceanogr. **50**: 1172–1180. doi:10.4319/lo.2005.50.4.1172

Lamb, C., and R. A. Dixon. 1997. The oxidative burst in plant disease resistance. Annu. Rev. Plant Biol. **48**: 251–275.

Lara-Ortíz, T., H. Riveros-Rosas, and J. Aguirre. 2003. Reactive oxygen species generated by microbial NADPH oxidase NoxA regulate sexual development in Aspergillus nidulans. Mol. Microbiol. **50**: 1241–1255. doi:10.1046/j.1365-2958.2003.03800.x

Learman, D. R., B. M. Voelker, A. I. Vazquez-Rodriguez, and C. M. Hansel. 2011. Formation of manganese oxides by bacterially generated superoxide. Nat. Geosci. **4**: 95–98. doi:10.1038/ngeo1055

Marshall, J.-A., M. Hovenden, T. Oda, and G. M. Hallegraeff. 2002. Photosynthesis does influence superoxide production in the ichthyotoxic alga Chattonella marina (Raphidophyceae). J. Plankton Res. **24**: 1231–1236. doi:10.1093/plankt/24.11.1231

Marshall, J.-A., T. Ross, S. Pyecroft, and G. Hallegraeff. 2005. Superoxide production by marine microalgae II . Towards understanding ecological consequences and possible functions. 541–549. doi:10.1007/s00227-005-1597-6

McKie-Krisberg, Z. M., R. J. Gast, and R. W. Sanders. 2015. Physiological responses of three species of Antarctic mixotrophic phytoflagellates to changes in light and dissolved nutrients. Microb. Ecol. **70**: 21–29.

Mella-Flores, D., C. Six, M. Ratin, and others. 2012. Prochlorococcus and Synechococcus have Evolved Different Adaptive Mechanisms to Cope with Light and UV Stress. Front. Microbiol. **3**. doi:10.3389/fmicb.2012.00285

Moisan, T. A., and B. G. Mitchell. 1999. Photophysiological acclimation of Phaeocystis antarctica Karsten under light limitation. Limnol. Oceanogr. **44**: 247–258. doi:10.4319/lo.1999.44.2.0247

Moore, L. R., A. Coe, E. R. Zinser, and others. 2007. Culturing the marine cyanobacterium Prochlorococcus. Limnol. Oceanogr. Methods **5**: 353–362. doi:10.4319/lom.2007.5.353

Morris, J. J., Z. I. Johnson, M. J. Szul, M. Keller, and E. R. Zinser. 2011. Dependence of the cyanobacterium Prochlorococcus on hydrogen peroxide scavenging microbes for growth at the ocean's surface. PLoS One **6**: e16805.

Morris, J. J., R. Kirkegaard, M. J. Szul, Z. I. Johnson, and E. R. Zinser. 2008. Facilitation of robust growth of Prochlorococcus colonies and dilute liquid cultures by "helper" heterotrophic bacteria. Appl. Environ. Microbiol. **74**: 4530–4534. doi:10.1128/AEM.02479-07

Morris, R. M., M. S. Rappé, S. A. Connon, K. L. Vergin, W. A. Siebold, C. A. Carlson, and S. J. Giovannoni. 2002. SAR11 clade dominates ocean surface bacterioplankton communities. Nature **420**: 806.

Olson, R. J., S. W. Chisholm, E. R. Zettler, and E. V Armbrust. 1990. PIGMENTS, SIZE, AND DISTRIBUTION OF SYNECHOCOCCUS IN THE NORTH-ATLANTIC AND PACIFIC OCEANS. Limnol. Oceanogr. **35**: 45–58. doi:10.4319/lo.1990.35.1.0045

Partensky, F., W. R. Hess, and D. Vaulot. 1999. Prochlorococcus, a marine photosynthetic prokaryote of global significance. Microbiol. Mol. Biol. Rev. **63**: 106–+.

Powers, L. C., and W. L. Miller. 2014. Blending remote sensing data products to estimate photochemical production of hydrogen peroxide and superoxide in the surface ocean. Environ. Sci. Impacts **16**: 792–806. doi:10.1039/c3em00617d

Roe, K. L., R. J. Schneider, C. M. Hansel, and B. M. Voelker. 2016. Measurement of dark, particle-generated superoxide and hydrogen peroxide production and decay in the subtropical and temperate North Pacific Ocean. Deep. Res. Part I-Oceanographic Res. Pap. **107**: 59–69. doi:10.1016/j.dsr.2015.10.012

Rose, A. L. 2012. The influence of extracellular superoxide on iron redox chemistry and bioavailability to aquatic microorganisms. Front. Microbiol. **3**: 1–21. doi:10.3389/fmicb.2012.00124

Rose, A. L., J. W. Moffett, and T. D. Waite. 2008a. Determination of superoxide in seawater using 2-methyl-6-(4-methoxyphenyl)- 3,7-dihydroimidazo[1,2-a]pyrazin-3(7H)-one chemiluminescence. Anal. Chem. **80**: 1215–1227. doi:10.1021/ac7018975

Rose, A. L., T. P. Salmon, T. Lukondeh, B. A. Neilan, and T. D. Waite. 2005. Use of superoxide as an electron shuttle for iron acquasition by the marine cyanobacterium Lyngbya majuscula. Environ. Sci. Technol. **39**: 3708–3715. doi:10.1021/es048766c

Rose, A. L., E. A. Webb, T. D. Waite, and J. W. Moffett. 2008b. Measurement and implications of nonphotochemically generated superoxide in the equatorial Pacific Ocean. Environ. Sci. Technol. **42**: 2387–2393. doi:10.1021/es7024609

Rusak, S. A., B. M. Peake, L. E. Richard, S. D. Nodder, and W. J. Cooper. 2011. Distributions of hydrogen peroxide and superoxide in seawater east of New Zealand. Mar. Chem. **127**: 155–169. doi:10.1016/j.marchem.2011.08.005

Saito, M. A., J. W. Moffett, S. W. Chisholm, and J. B. Waterbury. 2002. Cobalt limitation and uptake in Prochlorococcus. Limnol. Oceanogr. **47**: 1629–1636. doi:10.4319/lo.2002.47.6.1629

Saragosti, E., D. Tchernov, A. Katsir, and Y. Shaked. 2010. Extracellular production and degradation of superoxide in the coral stylophora pistillata and cultured symbiodinium. PLoS One **5**: 1–10. doi:10.1371/journal.pone.0012508

Saran, M. 2003. To what end does nature produce superoxide? NADPH oxidase as an autocrine modifier of membrane phospholipids generating paracrine lipid messengers. Free Radic. Res. **37**: 1045–1059. doi:10.1080/10715760310001594631

Scanlan, D. J., M. Ostrowski, S. Mazard, and others. 2009. Ecological Genomics of Marine Picocyanobacteria. Microbiol. Mol. Biol. Rev. **73**: 249–299. doi:10.1128/MMBR.00035-08

Schneider, R. J., K. L. Roe, C. M. Hansel, and B. M. Voelker. 2016. Species-Level Variability in Extracellular Production Rates of Reactive Oxygen Species by Diatoms. Front. Chem. **4**. doi:10.3389/fchem.2016.00005

Schoemann, V., S. Becquevort, J. Stefels, W. Rousseau, C. Lancelot, V. Rousseau, and C. Lancelot. 2005. Phaeocystis blooms in the global ocean and their controlling mechanisms: a review. J. Sea Res. **53**: 43–66. doi:10.1016/j.seares.2004.01.008

Storz, G., M. F. Christman, H. Siest, and B. N. Ames. 1987. Spontaneous mutagenesis and oxidative damage to DNA in Salmonella typhimurium. Biochemistry **84**: 8917–8921. doi:10.1073/pnas.84.24.8917

Vogt, M., C. O'Brien, J. Peloquin, and others. 2012. Global marine plankton functional type biomass distributions: *Phaeocystis* spp. Earth Syst. Sci. Data **4**: 107–120. doi:10.5194/essd-4-107-2012

Wang, S. L., and J. K. Moore. 2011. Incorporating Phaeocystis into a Southern Ocean ecosystem model. J. Geophys. Res. **116**: 18. doi:10.1029/2009jc005817

Waterbury, J. B., S. W. Watson, F. W. Valois, and D. G. Franks. 1986. Biological and ecological characterization of the marine unicellular cyanobacterium Synechococcus., T. Platt and W.W.K. Li [eds.]. Canadian Bulletin of Fisheries and Aquatic Sciences 214.

Wuttig, K., M. I. Heller, and P. L. Croot. 2013a. Reactivity of Inorganic Mn and Mn Desferrioxamine B with O-2, O-2(-), and H2O2 in Seawater. Environ. Sci. Technol. **47**: 10257–10265. doi:10.1021/es4016603

Wuttig, K., M. I. Heller, and P. L. Croot. 2013b. Pathways of Superoxide (O-2(-)) Decay in the Eastern Tropical North Atlantic. Environ. Sci. Technol. **47**: 10249–10256. doi:10.1021/es401658t

Zhang, T., J. M. Diaz, C. Brighi, R. J. Parsons, S. McNally, A. Apprill, and C. M. Hansel. 2016a. Dark Production of Extracellular Superoxide by the Coral Porites astreoides and Representative Symbionts. Front. Mar. Sci. **3**: 1–16. doi:10.3389/fmars.2016.00232

Zhang, T., C. M. Hansel, B. M. Voelker, and C. H. Lamborg. 2016b. Extensive Dark Biological Production of Reactive Oxygen Species in Brackish and Freshwater Ponds. Environ. Sci. Technol. **50**: 2983–2993. doi:10.1021/acs.est.5b03906

Zhao, X. W., C. L. Schwartz, J. Pierson, S. J. Giovannoni, J. R. McIntosh, and D. Nicastroa. 2017. Three-Dimensional Structure of the Ultraoligotrophic Marine Bacterium "Candidatus Pelagibacter ubique." Appl. Environ. Microbiol. **83**. doi:10.1128/aem.02807-16

Zinser, E. R., D. Lindell, Z. I. Johnson, and others. 2009. Choreography of the transcriptome, photophysiology, and cell cycle of a minimal photoautotroph, Prochlorococcus. PLoS One **4**. doi:10.1371/journal.pone.0005135

6. Dark Biological Superoxide Production as a Significant Flux and Sink of Marine Dissolved Oxygen

This chapter is in review at *PNAS*.

Abstract

The balance between sources and sinks of molecular oxygen in the oceans has greatly impacted the composition of Earth's atmosphere since the evolution of oxygenic photosynthesis, thereby exerting key influence on Earth's climate and the redox state of the (sub)surface Earth. The canonical source and sink terms of the marine oxygen budget include photosynthesis, respiration, photorespiration, the Mehler reaction, and other smaller terms. However, recent advances in understanding cryptic oxygen cycling, namely the ubiquitous one-electron reduction of O_2 to superoxide by microorganisms outside the cell, remains unexplored as a potential player in global oxygen dynamics. Here we show that dark extracellular superoxide production by marine microbes represents a previously unconsidered global oxygen flux and sink comparable in magnitude to other key terms. We estimate that extracellular superoxide production represents a gross oxygen sink comprising about a third of marine gross oxygen production, and a net oxygen sink amounting to 15-50 percent of that. We further demonstrate that this total marine dark extracellular superoxide flux is consistent with concentrations of superoxide in marine environments. These findings underscore prolific marine sources of reactive oxygen species and a complex and dynamic oxygen cycle in which oxygen consumption and corresponding carbon oxidation are not necessarily confined to cell membranes nor exclusively related to respiration. This revised model of the marine oxygen cycle will ultimately allow for greater reconciliation among estimates of primary production and respiration, the O_2:C ratio of oxygen utilization in the water column, and the net metabolic state of the global ocean.

6.1 Introduction

Carbon fixation by oxygenic phototrophs produces O_2 in marine and terrestrial environments. On short timescales, the concentration of O_2 in the atmosphere and dissolved in the global ocean is maintained by an equal and opposite series of oxygen-consuming reactions. The preeminent of these O_2 loss terms is cellular respiration, although multiple additional loss processes are operative in oxygenic phototrophs (Badger et al. 2000; Asada 2006; Eisenhut et al. 2008). These include photorespiration, which occurs when the enzyme RuBisCO (Ribulose-1,5-bisphosphate carboxylase/oxygenase) uses O_2 as a substrate instead of CO_2 in the reaction with ribulose 1,5-bisphosphate (RuBP) as part of the normal functioning of the Calvin-Benson-Bassham Cycle. Loss of O_2 through photorespiration may be as high as 30% of gross oxygen production (Guy et al. 1993; Bender et al. 1994). The Mehler reaction is another significant oxygen loss term in oxygenic phototrophs, occurring when O_2 is reduced to superoxide ($O_2^{\bullet-}$) by electrons evolved from reduced ferredoxin in photosystem I in the presence of light (Asada 2006). The fraction of O_2 evolved from photosystem II that is subsequently lost to reduction via the Mehler reaction is estimated at 10% of photosynthetically evolved O_2 in higher plants (Guy et al. 1993). These estimates of photosynthetic oxygen loss are based on model organisms of varying environmental relevance, and a great deal of uncertainty remains in how oxygen reduction in the environment is distributed among these many sinks. Cyanobacteria and algae, for example, exhibit decreased or unchanged photosynthetic oxygen loss under low CO_2 conditions relative to that observed at high CO_2 conditions (Badger et al. 2000). In other words, photosynthetic oxygen loss in cyanobacteria and algae is not enhanced under conditions that would otherwise enhance RuBisCO oxygenase activity, suggesting the proportion of Mehler-related oxygen loss in cyanobacteria and algae is much greater than in higher plants.

The role of intracellular superoxide production as a significant sink of oxygen has been recognized since the 1950's for its place in the Mehler reaction (Mehler 1951), however, the role of extracellular superoxide production as an oxygen sink in both the presence and absence of light has not been assessed. Yet, dark (light-independent), particle associated superoxide production accounts for a significant fraction of superoxide measured in natural waters within both the photic and aphotic zone (Diaz et al. 2013; Zhang et al. 2016). Dark, extracellular superoxide production is in fact prolific among marine heterotrophic bacteria, cyanobacteria, and eukaryotes (Lamb and Dixon 1997; Kim et al. 2000; Kustka et al. 2005; Learman et al. 2011; Hansel et al. 2012, 2016;

Diaz et al. 2013; Plummer et al. 2019; Sutherland et al. 2019). Production of extracellular superoxide proceeds via a one-electron transfer initiated by transmembrane, outer membrane bound, or soluble extracellular enzymes thought to belong generally to NAD(P)H oxidoreductases (Aguirre et al. 2005), and more recently to heme peroxidases, and glutathione reductases (Diaz et al. 2013, 2019; Andeer et al. 2015). At circumneutral pH, the superoxide anion ($O_2^{\bullet-}$) dominates over the conjugate acid $HO_2^{\bullet}$ (pKa = 4.8) (Bielski et al. 1985). This short-lived, reactive anion is highly impermeable to cell membranes (Cordeiro 2014). Thus, limited transmembrane diffusion and proportionally low levels of intracellular superoxide are insufficient to account for observed extracellular fluxes (Gus' kova et al. 1984; Diaz et al. 2013; Cordeiro 2014). Superoxide has a half-life on the order of a few minutes or less (Takahashi and Asada 1983; Diaz et al. 2013), with its fate highly dependent on seawater chemistry; superoxide may be re-oxidized to O_2 or reduced to H_2O_2, other peroxides, and ultimately water by reactions with redox active metals including copper, iron, and manganese, organic matter, or via (un)catalyzed dismutation (Heller and Croot 2010a; Wuttig et al. 2013a).

Extracellular superoxide plays a diverse suite of roles in cell physiology, including cell signaling, growth, defense, and redox homeostasis. In microbial eukaryotes, enzymatic extracellular superoxide production is involved in cell differentiation (Aguirre et al. 2005). In plants, superoxide serves as a pre-transcription defense in wound repair (Lamb and Dixon 1997). Recently, extracellular superoxide within marine bacteria was shown to be tightly regulated through the growth cycle with superoxide eliminated upon entering stationary phase (Hansel et al. 2019). Addition of superoxide dismutase (SOD), an enzyme that eliminates superoxide, inhibited growth suggesting that superoxide is involved in growth and proliferation as previously suggested for pathogenic strains of *Escherichia coli* and *Chattonella marina* (Carlioz and Touati 1986; Oda et al. 1995; Saran 2003; Buetler et al. 2004). Further, recent evidence indicates that extracellular superoxide production by the diatom *Thalassiosira oceanica* may play a critical role in maintaining the internal redox conditions in photosynthesizing cells (Diaz et al. 2019). This suite of beneficial physiological processes all result from or result in the reduction of molecular oxygen that is not otherwise considered in biogeochemical cycles of oxygen and related elements.

Our aim in this study is to leverage recent assessments of dark extracellular superoxide production rates by globally important groups of marine microbes to determine the resulting oxygen sink. Our approach consists of two parts: (1) constrain the gross oxygen reduction that

results from dark, extracellular superoxide production and (2) estimate the fraction of gross superoxide produced that is ultimately reduced to water. Generally speaking, the most abundant group of organisms in the global ocean is heterotrophic bacteria. *Alphaproteobacteria* and *Gammaproteobacteria* comprise >70% of heterotrophic bacteria in the water column, and a subset of *Alphaproteobacteria*, *Pelagibacterales* (SAR11 clade), makes up nearly 25% of cells in the ocean (Zinger et al. 2011; Giovannoni 2017). Here we compile measured extracellular superoxide production rates of several marine *Alphaproteobacteria* and *Gammaproteobacteria,* including SAR11 clade organisms (Figure 1). Although far outnumbered by marine heterotrophs in the global ocean, oxygenic phototrophs have been shown to produce both light-dependent and -independent extracellular superoxide up to several orders of magnitude higher than average marine heterotrophs on a per cell basis, meaning a representative accounting of the superoxide flux from phototrophs is necessary to adequately constrain superoxide production (Rose et al. 2008; Diaz et al. 2013; Hansel et al. 2016). In this study we include superoxide production rates of the following organisms: *Prochlorococcus* and *Synechococcus*, the two most abundant photosynthetic organisms in the global ocean; *Trichodesmium*, a dominant N_2-fixing cyanobacterium in oligotrophic waters; coccolithophores, the most abundant group of calcifying micro-algae present throughout the global ocean; several species of diatoms, a diverse group of silicifying algae found in nutrient rich waters; and *Phaeocystis*, an alga predominately found in the Southern Ocean. In constructing this estimate of superoxide production, we assign measured dark superoxide production rates to organisms that fall within these groups of organisms, and conservatively consider all others to be non-producing.

The dark superoxide production rates compiled in this study (with the exception of coccolithophores) were measured from cells grown to mid-exponential phase under ideal growth conditions using a flow-injection chemiluminescent approach (Diaz et al. 2013). The study investigating the cell-specific superoxide production rate of coccolithophores measured their production rate throughout their growth curve, which we converted to a time-weighted average using trapezoidal integration of the cell superoxide production rate as a function of time (Plummer et al. 2019). Cell-normalized superoxide production rates presented in the scientific literature are either presented as net or gross superoxide production rates, the latter requiring an exogenous spike of superoxide to determine the proportion of extracellular ROS that is enzymatically degraded by the organisms. Gross superoxide production rates were used here when available, otherwise, net superoxide production rates were used. Marine heterotrophs belonging to *Alphaproteobacteria* and

Gammaproteobacteria, including two *Pelagibacterales* members, produce gross extracellular superoxide within a fairly narrow range of 0.1-3.7 amol cell^{-1} hr^{-1} (Figure 1). Oxygenic phototrophs, with the exception of *Prochlorococcus*, far exceed heterotrophic cell normalized superoxide production, with net production rates ranging from 4.3 to 13,400 amol cell^{-1} hr^{-1} (Sutherland et al. 2019). *Prochlorococcus* produces significantly less extracellular superoxide across four ecotypes, with average gross rates ranging from 0.007 to 0.091 amol cell^{-1} hr^{-1} (Sutherland et al. 2019).

Also shown in Figure 1 is an estimate for the average marine cell O_2 utilization rate assuming a balanced marine oxygen budget (see SI for calculation), or in other words, the total amount of oxygen produced in the global ocean, divided by the number of cells. This estimate demonstrates that dark extracellular superoxide production of several groups of marine organisms exceeds the average oxygen utilization rate. Here we use the more general term oxygen utilization instead of respiration because other oxygen-consuming biological reactions (e.g. photorespiration, Mehler reaction) are each responsible for >10% of the marine oxygen sink. To extrapolate these superoxide production values to the global ocean, we provide estimates of total cell numbers in the water column of each organismal group included in this study (Table 1). We assigned cells from each group the mean and standard error determined from our bootstrapping approach, and use a Monte Carlo approach to determine the mean and probability distribution for the whole ocean superoxide flux. A slightly different approach was used for diatoms; production rate was normalized to cell surface area and average diatom surface area was determined from a database containing >90,000 geo-referenced diatom observations (see Table S1). Using these total cell number estimates and modeled dark extracellular superoxide production rates for each organismal group, we calculate that gross dark extracellular superoxide production represents a flux of 3.9 (± 0.5) x10^{15} mol O_2 per year. For comparison, a central estimate for gross oxygen production (GOP) in all marine environments derived from estimates of marine productivity is 1.09 x 10^{16} mol O_2 year^{-1} (see SI) (Field et al. 1998). Thus, gross light-independent extracellular superoxide production by microorganisms represents an O_2 loss flux approximately 36 (±5) percent of marine GOP. This gross superoxide production estimate is illustrative for demonstrating the size of this reductive flux, however, it is the net reduction of superoxide that ultimately determines the weight of this reductive flux on the global oxygen cycle. We provide constraints on the net reduction of extracellular superoxide below.

While we show that model estimates based on lab-based rates yield a dark superoxide flux that is a substantial and previously unrecognized part of the global oxygen budget, a claim that represents such a significant shift in the model of marine oxygen utilization requires some ground-truthing with environmental data. In particular, we used a bootstrapping approach to estimate the mean and standard error of all extracellular superoxide production rates available in the literature for each group discussed here (see SI). The available data on extracellular superoxide production within axenic cultures does not contain the ideal richness for relying on this numerical approach alone. Thus, we tested our culture-based estimate by calculating expected marine superoxide concentrations based on our estimate of global superoxide production, and compare these values to available marine superoxide concentration data. If our estimate for average marine superoxide concentration falls within observations, this provides an independent line of evidence that extracellular superoxide production comprises a significant global oxygen flux, with our reasoning as follows. The mean pseudo first-order decay rate of superoxide in marine environments has been previously characterized at 0.0106 s^{-1}, with a 1σ confidence interval from 0.0050 s^{-1} to 0.0226 s^{-1} (see Figure S3) (Rose et al. 2008; Hansard et al. 2010; Rusak et al. 2011; Roe et al. 2016). Using these observed decay rates we estimate steady-state superoxide concentrations from biological production to be 152 pM (1σ confidence interval: 71-322 pM) in the surface ocean, and 0.6 pM (1σ confidence interval: 0.3-1.3 pM) below 200m (Table S2). All available superoxide concentration measurements from the marine water column are shown in Figure 2 along with the calculated expected concentration range based on our model of global superoxide production (gray bar). As indicated, the expected range of superoxide concentrations is largely consistent with measurements collected in the surface ocean, and, in fact, underestimates measured concentrations in all deep ocean measurements. Although not shown in Figure 2, superoxide concentrations in some coastal systems have been reported as high as 120 nM, four orders of magnitude higher than our estimate, underscoring the conservative nature of our estimate (Diaz et al. 2016).

6.2 Additional Sources of Superoxide

This accounting of the marine superoxide flux only considers extracellular dark superoxide production by dominant organisms with known production rates. In fact, the total O_2 flux via all superoxide production pathways in marine environments undoubtedly exceeds our estimates here by a sizable margin and would lead an even greater contribution of superoxide production on O_2

loss. In particular, light-dependent (a)biotic superoxide production is not included in our present estimate. Within sunlit waters, there is significant abiotic photochemical production of superoxide, and extracellular superoxide production rates by marine phototrophs are significantly higher in the light (Powers and Miller 2014; Hansel et al. 2016; Schneider et al. 2016). Indeed, the extracellular superoxide production exhibited by multiple species of diatoms more than doubled in the presence of light (Schneider et al. 2016). The same behavior was observed for the coccolithophore *E. Huxleyi* (Plummer et al. 2019) and certain *Trichodesmium* ecotypes (Hansel et al. 2016), where light-dependent increases in extracellular superoxide could not be accounted for by abiotic factors. Since phototrophs as a group are responsible for most of the dark extracellular superoxide production, even modest modulation in extracellular superoxide production in the light could produce a substantial increase in our estimate of the gross superoxide flux and the net oxygen sink that results, which we discuss in the next section.

Possibly the most well-characterized abiotic source of superoxide in the oceans is the photochemical excitation of chromophoric dissolved organic matter (CDOM) and subsequent reduction of O_2 to superoxide in the surface ocean (Goldstone and Voelker 2000). One model using a remote sensing approach to estimate photochemical ROS production in the surface ocean estimated that midday superoxide concentrations resulting from photochemical production and a range of superoxide sinks ranged from near 10 pM at high latitudes to near 200 pM at low latitudes (Powers and Miller 2014). These results demonstrate that photochemical production of superoxide can exceed dark biological production in sunlit surface waters. Notably, contribution of this photochemical superoxide will vary temporally and decrease with depth upon the attenuation of photo-active wavelengths (290-490 nm), with local variations in productivity and the compositional nature of surface ocean CDOM also impacting its reactivity.

6.3 The Fate of Superoxide

Both lab- and field-based measurements converge on the similar conclusion that dark extracellular superoxide flux is a substantial component of oxygen turnover in the global ocean. To further place this process into the context of the global O_2 budget, it is important to distinguish gross dark superoxide production from the net loss of dissolved O_2. Superoxide in aqueous systems may decay by oxidation back to O_2, with no net effect on marine dissolved oxygen, or via reduction, which may lead to a net loss of oxygen. Superoxide decay is considered the primary

source of hydrogen peroxide (H_2O_2), and thus much of what we know and assume about the fate of superoxide is inferred from studies of hydrogen peroxide concentration and rate measurements. Nevertheless, other secondary and direct sources of hydrogen peroxide have also been identified within microbial cultures (Palenik et al. 1987; Palenik and Morel 1991; Schneider et al. 2016) and natural waters (Zhang et al. 2016). For the purposes of this estimate, we accept the general premise that superoxide decay is the primary source of hydrogen peroxide and ignore other sources, while recognizing that the foundation of this premise needs further evaluation. It is also often assumed that the primary reduction or disproportionation product of superoxide production is H_2O_2, however, superoxide decay may also occur through bond-forming redox reactions with dissolved organic carbon, metals, or through unknown sinks (Lee-Ruff 1977; Petasne and Zika 1987; Andrews et al. 2000; Kettler et al. 2007; Burns et al. 2012). Such reactions will not produce a H_2O_2 intermediate. In fact, it has been shown that hydrogen peroxide formation can only account for 45 percent of net oxygen loss in photochemical oxidation of marine waters (Andrews et al. 2000). While photochemical superoxide production is not a perfect analogy for dark biological superoxide production, the large body of work investigating the fate of photochemically derived superoxide offers the most transferable insight into the likely fate of biologically derived superoxide in seawater. What follows is our attempt to constrain the net reduction of marine dissolved oxygen from the estimate of gross extracellular superoxide production using a combination of measurements from photochemical and biogeochemical literature.

Ultimately, the fate of superoxide and hydrogen peroxide is highly dependent on the availability of dissolved organic matter (and its reactivity), the abundance of redox active metals (and their redox states), and the expression of enzymes that eliminate reactive oxygen species such as superoxide dismutase, catalase, and peroxidases (Petasne and Zika 1987; Heller and Croot 2010b; Wuttig et al. 2013b). Superoxide can be both oxidized (Eq. 1) or reduced (Eq. 2) leading to the net consumption of 0 or 1 mole O_2 per mole superoxide, respectively (Figure 3). Superoxide can also undergo uncatalyzed dismutation, a process that results in 50% oxidation to O_2 and 50% reduction to H_2O_2 (Eq. 3). Hydrogen peroxide is more stable than superoxide in natural waters, with pseudo-first order decay rate constants approximately three orders of magnitude lower than that of superoxide. Consequently, H_2O_2 has a lifetime of approximately 1-2 days, and typical concentrations are ~10^3 higher for H_2O_2 than for superoxide (from <1nM in the deep ocean to ~100 nM in sunlight surface water (Moffett and Zafiriou 1990; Hopwood et al. 2017)). Typical

production and decay rates range from 0.8-2.4 nM hr^{-1} for dark seawater (Moffett and Zafiriou 1990) and 0.9-8.3 nM hr^{-1} in sunlit seawater(Powers et al. 2015). As for the fate of H_2O_2, previous work has shown that light-independent, biological processes are primarily responsible for its degradation in marine systems, with 65-80% of H_2O_2 degradation resulting from catalase activity (Eq. 4), and the remainder resulting from peroxidase activity (Eq. 5) (Moffett and Zafiriou 1990).

$$O_2^{\cdot-} \longrightarrow O_2 + e^- \qquad \text{(Eq. 1; } O_2^{\bullet-} \text{ oxidation)}$$

$$O_2^{\cdot-} + 2H^+ + e^- \longrightarrow H_2O_2 \qquad \text{(Eq. 2; } O_2^{\bullet-} \text{ reduction)}$$

$$2O_2^{\cdot-} + 2H^+ \longrightarrow H_2O_2 + O_2 \qquad \text{(Eq. 3; SOD or uncatalyzed dismutation)}$$

$$2H_2O_2 \longrightarrow 2H_2O + O_2 \qquad \text{(Eq. 4; catalase-based } H_2O_2 \text{ decay)}$$

$$H_2O_2 + AH_2 \longrightarrow 2H_2O + A \qquad \text{(Eq. 5; peroxidase-based } H_2O_2 \text{ decay)}$$

Assuming this range of catalase and peroxidase activity holds throughout the water column, between 60 and 67.5 percent of H_2O_2 is ultimately reduced to water. Thus, the theoretical net loss of oxygen through the superoxide production pathway can range from 0 (e.g., all superoxide is oxidized back to O_2, Eq. 1) to 67.5% (e.g., superoxide reduction to H_2O_2 (Eq. 2) followed by catalase and peroxidase mediated degradation of H_2O_2 (Eq. 4,5)) (see Figure 3).

There are two ways we can use previous data to estimate the net sink of oxygen that results from the dark biological superoxide flux in the ocean. The first, and more conservative approach is to multiply the global superoxide production flux by the ratio of hydrogen peroxide production to superoxide production observed in natural waters, P_{H2O2}/P_{O2-}, followed by the oxidation-reduction ratio observed for hydrogen peroxide. This yields the total O_2 reduced to water via an H_2O_2 intermediate and accounts for dismutation (Eq. 3), univalent oxidation (Eq. 1), and univalent reduction (Eq. 2). This method will produce a more conservative estimate of net oxygen loss because it implicitly assumes that all superoxide not reduced to hydrogen peroxide is re-oxidized to O_2, when in reality a large fraction of the superoxide sink may yield products other than hydrogen peroxide (e.g. organic peroxides, other ROS) (Petasne and Zika 1987; Andrews et al.

2000). The second approach uses the same P_{H2O2}/P_{O2-} ratio to determine the hydrogen peroxide flux that results from the superoxide flux, followed by multiplying by the observed ratio of net oxygen loss to hydrogen peroxide formation in a marine photochemical system where superoxide is implicated as the primary oxidant. This approach may slightly overestimate the net oxygen sink because it ignores the possibility that some oxygen reduction may occur through multi-electron transfers (Andrews et al. 2000).

For both of these approaches, we need a reasonable estimate of the production ratio of hydrogen peroxide to that of superoxide (P_{H2O2}/P_{O2-}). In experiments investigating production of superoxide and hydrogen peroxide during DOM irradiation, P_{H2O2}/P_{O2-} ranged from 0.10 to 0.67, with an average value of 0.24 (Powers et al. 2015). Another similar study on waters collected from the transition between terrestrial and marine environment found that P_{H2O2}/P_{O2-} ranged from ~0.5 in riverine waters to ~0.30 in Gulf Stream waters (Powers and Miller 2016). Slightly lower values (0.08-0.17) have been observed in photochemical systems with terrestrial organic matter (Zhang and Blough 2016), possibly due to the differing nature of terrestrial DOM (aromatic vs. aliphatic). In a brackish and a freshwater pond, P_{H2O2}/P_{O2-} sometimes exceeded the stoichiometry of 0.5 expected for dismutation, suggesting there may be other sources of hydrogen peroxide (Zhang et al. 2016). We use the average value presented by Powers et al. (2015) of 0.24 as the most relevant to the marine environment and the best choice at this time for a global marine estimate. Using our first approach and P_{H2O2}/P_{O2} of 0.24, we estimate a lower bound for the net oxygen reduction resulting from superoxide production at 14.4% of the marine superoxide flux (or 5% of the marine oxygen budget). A significant fraction of this superoxide (52% of the marine superoxide flux) is unaccounted for because it does not produce hydrogen peroxide, meaning the fate of as much as 19 percent of the marine oxygen budget that cycles through superoxide remains unknown.

Using the second approach, we assume hydrogen peroxide formation and net oxygen loss that result from superoxide formation occur with a fixed ratio in seawater (0.45:1 H_2O_2:-O_2 (Andrews et al. 2000)). We find that superoxide production will result in a net oxygen loss of 53.3 percent of the global superoxide flux (or 19 percent of the marine oxygen budget).

These two estimation methods suggest dark, biological production of extracellular superoxide is a sink between 5 and 19 percent in the marine oxygen budget, indicating that the oxygen sink from dark extracellular superoxide production is similar in magnitude to the Mehler reaction and photorespiration. Notably, total superoxide production in photochemical systems has

been shown to correlate with CO_2 production from DOM (Powers and Miller 2015), suggesting that a significant fraction of the superoxide sink is ultimately through reduction tied to organic carbon oxidation, favoring the higher end of this estimate. Shipboard incubations show that marine superoxide decay is primarily correlated with dissolved organic matter and dissolved manganese, both of which allow for a significant reductive sink of superoxide (Heller and Croot 2010a; Wuttig et al. 2013b) and subsequent higher O_2 loss. Oxygen loss in marine environments has previously been attributed primarily to a combination of respiration, photorespiration, and the Mehler reaction in the surface ocean and respiration alone in the deep ocean. We propose that dark extracellular superoxide production and its net oxygen sink has likely been overlooked and unintentionally incorporated into other sinks because separation of this secondary physiological process presents a methodological challenge. The sinks of marine oxygen resulting from respiration, photorespiration, and the Mehler reaction should therefore be revised downward to accommodate for the reductive sink from extracellular superoxide production.

6.4 Further Implications

We anticipate that the identification of an appreciable cryptic sink of oxygen, and consequently, organic carbon, may help reconcile spatiotemporal and methodological discrepancies among measurements of marine primary productivity arising as variable contributions of superoxide production to net O_2 loss. Adding another layer of complexity, the resulting H_2O_2 produced in excess during times of increased metabolic activity (e.g. photosynthetic organisms under full light) may store oxidizing equivalents that persist in the environment for hours to days. These processes may lead to variable O:C reaction stoichiometry as well as possible complexity in corresponding stable isotope dynamics. As measurements of primary productivity collected using multiple methods concurrently can produce primary productivity estimates that vary more than an order of magnitude (Regaudie-de-Gioux et al. 2014), we propose that cryptic ROS cycling and ROS-related oxygen loss may explain some of these discrepancies (e.g. ^{14}C vs triple oxygen isotopes). Studies of respiration, respiration stoichiometries ($-O_2$:C), and respiration isotope effects will also be impacted if organism level extracellular superoxide production rate is an appreciable fraction of respiration rate. Production of superoxide and subsequent oxidation of organic carbon in the surface ocean can, depending on the source of electrons, require more oxidant to fully oxidize carbon than respiring organic carbon with O_2; consistent with this, the $-O_2$:C ratio

of oxygen utilization in the ocean has been observed to vary by up to 30 percent (Redfield 1963; Martin et al. 1987; Anderson and Sarmiento 1994). The exact utility of extracellular superoxide for cells and the magnitude of influence superoxide has on the global carbon budget (today and throughout Earth history) both remain important and open questions. Nevertheless, this newly identified gross flux of superoxide in the global ocean underscores the critical role reactive oxygen species play in the global cycling of O_2, carbon, and redox active elements essential to life.

Figures

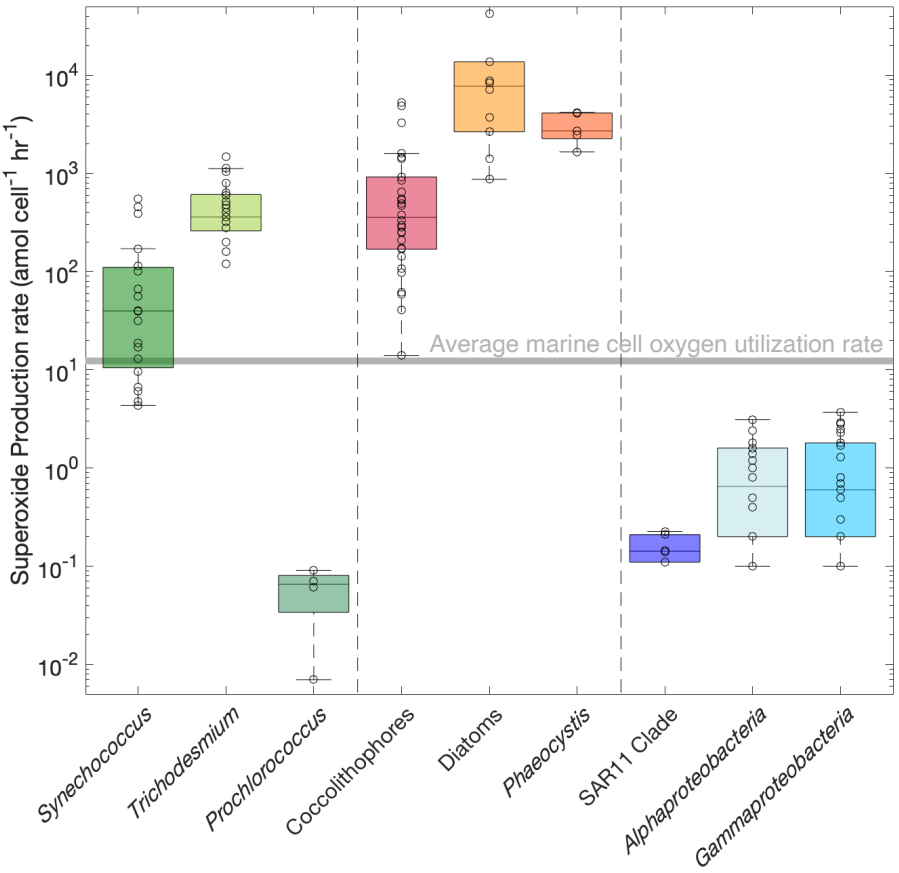

Figure 1- Extracellular superoxide production rates Cyanobacteria (green) include *Synechococcus*, *Trichodesmium*, and *Prochlorococcus*, eukaryotic algae (orange) include coccolithophores, diatoms, and *Phaeocystis*, and heterotrophic bacteria (blue) include *Pelagibater*, other *Alphaproteobacteria*, and *Gammaproteobacteria* (see Table S1 for data, sources, and organism details). Average marine cell respiration rate is shown in gray (see SI for calculation).

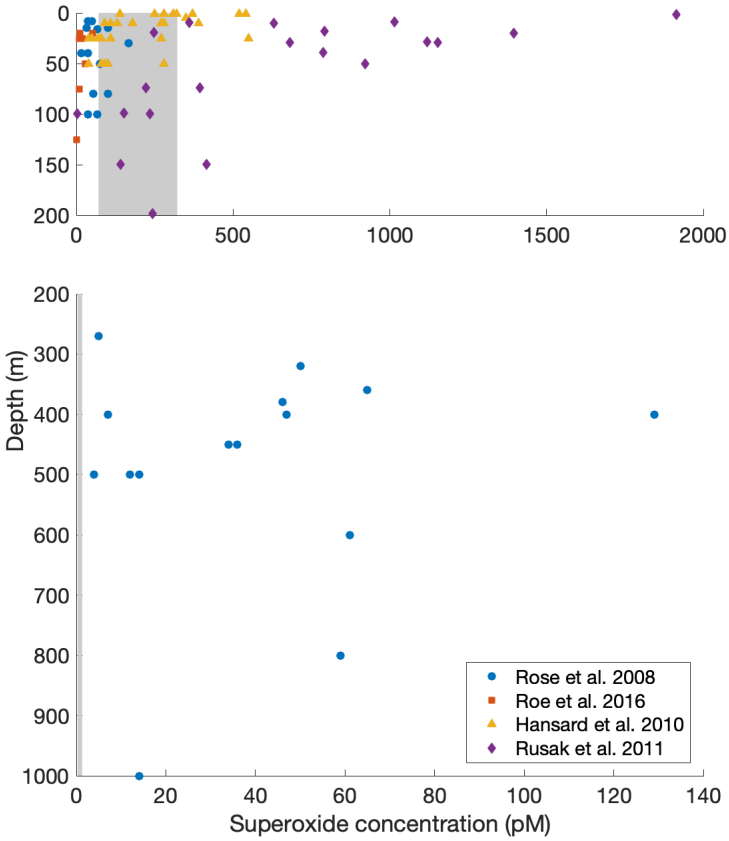

Figure 2- Measured and expected marine superoxide concentration Complied marine superoxide measurements from Rose et al. (2008) (Rose et al. 2008) (green diamond), Hansard et al. (2010) (Hansard et al. 2010) (yellow triangle), Rusak et al. (2011) (Rusak et al. 2011) (red square), and Roe et al. (2016) (Roe et al. 2016) (blue circle). The gray bars indicate the 68% confidence interval for the expected superoxide concentration based on our total superoxide flux estimate. The 68% confidence intervals for the expected superoxide concentrations in the surface (<200m) and deep (>200m) ocean are 71-332 pM and 0.3-1.3 pM, respectively.

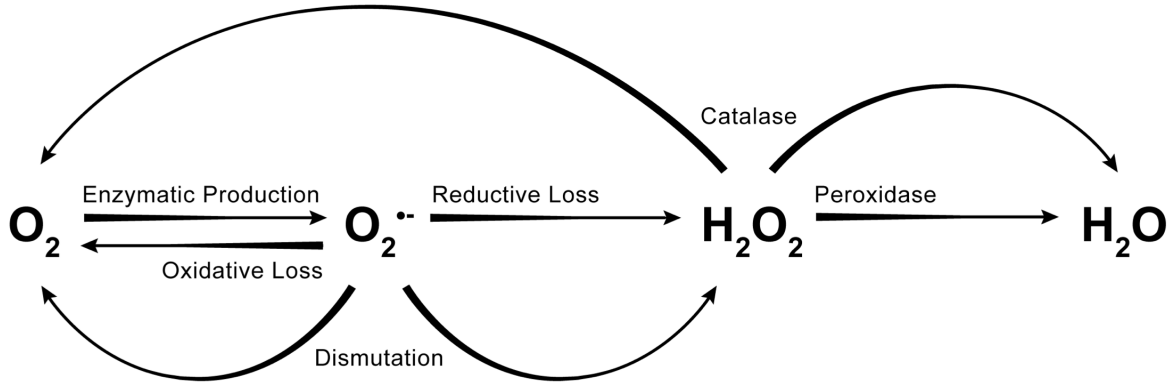

Figure 3- Decay pathways of superoxide in biogeochemical systems Summary of superoxide decay pathways in marine environments. Superoxide, once produced, may be oxidized to O_2 and/or reduced to H_2O_2 (or other peroxides). Peroxides may be oxidized to O_2 and/or reduced to H_2O. The net dissolved oxygen sink that results from extracellular superoxide production is the product of gross production times that fraction of O that is ultimately reduced to water.

Tables

Table 1- Estimate of global superoxide flux Summary of cell number estimates, cell specific superoxide production rates, and contribution of each marine clade towards the marine superoxide flux.

Group	Cell estimate*	Range superoxide production (amol cell^{-1} hr^{-1})	Mean model value* (amol cell^{-1} hr^{-1})	Superoxide production (mol year^{-1})
Synechococcus	7.0×10^{26}	4.3–550	106	6.49×10^{14}
Trichodesmium	4.6×10^{23}	ND-1,500	465	1.87×10^{12}
Prochlorococcus	2.9×10^{27}	0.007–0.091	0.06	1.40×10^{12}
Coccolithophores	2.6×10^{26}	ND-5,300	342	7.78×10^{14}
Diatoms	2.6×10^{24}	75–13,000	47,560**	1.07×10^{15}
Phaeocystis	3.9×10^{25}	1,700-4,200	2,925	9.99×10^{14}
Pelagibacterales (SAR11)	2.4×10^{28}	0.11–0.23	0.15	3.20×10^{13}
Alphaproteobacteria (without SAR11)	1.9×10^{28}	0.1–3.1	0.9	1.51×10^{14}
Gammaproteobacteria	2.7×10^{28}	0.1–3.7	1.1	2.57×10^{14}
			Total	**3.94×10^{15}**

*See SI for sources, derivations of cell number estimates, and model value assignment
**Calculated using cell surface area normalized rates, see SI
ND=Measurement reported below method detection limit

References

Aguirre, J., M. Rios-Momberg, D. Hewitt, and W. Hansberg. 2005. Reactive oxygen species and development in microbial eukaryotes. Trends Microbiol. **13**: 111–118. doi:10.1016/j.tim.2005.01.007

Andeer, P. F., D. R. Learman, M. McIlvin, J. A. Dunn, and C. M. Hansel. 2015. Extracellular haem peroxidases mediate Mn(II) oxidation in a marine R oseobacter bacterium via superoxide production. Environ. Microbiol. **17**: 3925–3936. doi:10.1111/1462-2920.12893

Anderson, L. A., and J. L. Sarmiento. 1994. REDFIELD RATIOS OF REMINERALIZATION DETERMINED BY NUTRIENT DATA-ANALYSIS. Global Biogeochem. Cycles **8**: 65–80. doi:10.1029/93gb03318

Andrews, S. S., S. Caron, and O. C. Zafiriou. 2000. Photochemical oxygen consumption in marine waters : A major sink for colored dissolved organic matter ? **45**: 267–277.

Asada, K. 2006. Production and scavenging of reactive oxygen species in chloroplasts and their functions. Plant Physiol. **141**: 391–396. doi:10.1104/pp.106.082040

Badger, M. R., S. von Caemmerer, S. Ruuska, and H. Nakano. 2000. Electron flow to oxygen in higher plants and algae: rates and control of direct photoreduction (Mehler reaction) and rubisco oxygenase. Philos. Trans. R. Soc. B-Biological Sci. **355**: 1433–1445.

Bender, M., T. Sowers, and L. Labeyrie. 1994. The Dole Effect and its Variations During the Last 130,000 Years as Measured in the Vostok Ice Core. Global Biogeochem. Cycles **8**: 363–376. doi:10.1029/94gb00724

Bielski, B. H. J., D. E. Cabelli, R. L. Arudi, and A. B. Ross. 1985. Reactivity of HO2/O−2Radicals in Aqueous Solution. J. Phys. Chem. Ref. Data **14**: 1041–1100. doi:10.1063/1.555739

Buetler, T. M., A. Krauskopf, and U. T. Ruegg. 2004. Role of superoxide as a signaling molecule. Physiology **19**: 120–123.

Burns, J. M., W. J. Cooper, J. L. Ferry, and others. 2012. Methods for reactive oxygen species (ROS) detection in aqueous environments. 683–734. doi:10.1007/s00027-012-0251-x

Carlioz, A., and D. Touati. 1986. Isolation of superoxide dismutase mutants in Escherichia coli: is superoxide dismutase necessary for aerobic life? EMBO J. **5**: 623–630.

Cordeiro, R. M. 2014. Reactive oxygen species at phospholipid bilayers: distribution, mobility and permeation. Biochim. Biophys. Acta (BBA)-Biomembranes **1838**: 438–444.

Diaz, J. M., C. M. Hansel, A. Apprill, C. Brighi, T. Zhang, L. Weber, S. McNally, and L. P. Xun. 2016. Species-specific control of external superoxide levels by the coral holobiont during a natural bleaching event. Nat. Commun. **7**. doi:10.1038/ncomms13801

Diaz, J. M., C. M. Hansel, B. M. Voelker, C. M. Mendes, P. F. Andeer, and T. Zhang. 2013. Widespread Production of Extracellular Superoxide by Heterotrophic Bacteria. Science (80-.). **340**: 1223–1226. doi:10.1126/science.1237331

Diaz, J. M., S. Plummer, C. M. Hansel, P. F. Andeer, M. A. Saito, and M. R. Mcilvin. 2019. NADPH-dependent extracellular superoxide production is vital to photophysiology in the marine diatom Thalassiosira oceanica. **116**. doi:10.1073/pnas.1821233116

Eisenhut, M., W. Ruth, M. Haimovich, H. Bauwe, A. Kaplan, and M. Hagemann. 2008. The photorespiratory glycolate metabolism is essential for cyanobacteria and might have been conveyed endosymbiontically to plants. Proc. Natl. Acad. Sci. U. S. A. **105**: 17199–17204. doi:10.1073/pnas.0807043105

Field, C. B., M. J. Behrenfeld, J. T. Randerson, and P. Falkowski. 1998. Primary production of the biosphere: Integrating terrestrial and oceanic components. Science (80-.). **281**: 237–240. doi:10.1126/science.281.5374.237

Giovannoni, S. J. 2017. SAR11 Bacteria: The Most Abundant Plankton in the Oceans, p. 231–255. *In* Annual Review of Marine Science, Vol 9. Annual Reviews.

Goldstone, J. V, and B. M. Voelker. 2000. Chemistry of Superoxide Radical in Seawater : CDOM Associated Sink of Superoxide in Coastal Waters. **34**: 1043–1048. doi:10.1021/es9905445

Gus' kova, R. A., I. I. Ivanov, V. K. Kol'tover, V. V Akhobadze, and A. B. Rubin. 1984. Permeability of bilayer lipid membranes for superoxide (O2−) radicals. Biochim. Biophys. Acta (BBA)-Biomembranes **778**: 579–585.

Guy, R. D., M. L. Fogel, and J. A. Berry. 1993. Photosynthetic Fractionation of the Stable Isotopes of Oxygen and Carbon. Plant Physiol. **101**: 37–47. doi:10.1104/pp.101.1.37

Hansard, S. P., A. W. Vermilyea, and B. M. Voelker. 2010. Deep-Sea Research I Measurements of superoxide radical concentration and decay kinetics in the Gulf of Alaska. Deep. Res. Part I **57**: 1111–1119. doi:10.1016/j.dsr.2010.05.007

Hansel, C. M., C. Buchwald, J. M. Diaz, J. E. Ossolinski, S. T. Dyhrman, B. A. S. Van Mooy, and D. Polyviou. 2016. Dynamics of extracellular superoxide production by Trichodesmium colonies from the Sargasso Sea. Limnol. Oceanogr. **61**: 1188–1200. doi:10.1002/lno.10266

Hansel, C. M., J. M. Diaz, and S. Plummer. 2019. Tight Regulation of Extracellular Superoxide Points to Its Vital Role in the Physiology of the Globally Relevant Roseobacter Clade. **10**: 1–13.

Hansel, C. M., C. A. Zeiner, C. M. Santelli, and S. M. Webb. 2012. Mn(II) oxidation by an ascomycete fungus is linked to superoxide production during asexual reproduction. Proc. Natl. Acad. Sci. U. S. A. **109**: 12621–12625. doi:10.1073/pnas.1203885109

Heller, M. I., and P. L. Croot. 2010a. Kinetics of superoxide reactions with dissolved organic matter in tropical Atlantic surface waters near Cape Verde (TENATSO). J. Geophys. Res. **115**. doi:10.1029/2009jc006021

Heller, M. I., and P. L. Croot. 2010b. Superoxide Decay Kinetics in the Southern Ocean. Environ. Sci. Technol. **44**: 191–196. doi:10.1021/es901766r

Hopwood, M. J., I. Rapp, C. Schlosser, and E. P. Achterberg. 2017. Hydrogen peroxide in deep waters from the Mediterranean Sea, South Atlantic and South Pacific Oceans. Sci. Rep. **7**: 43436.

Kettler, G. C., A. C. Martiny, K. Huang, and others. 2007. Patterns and implications of gene gain and loss in the evolution of Prochlorococcus. PLoS Genet. **3**: 2515–2528. doi:10.1371/journal.pgen.0030231

Kim, D., A. Nakamura, T. Okamoto, N. Komatsu, T. Oda, T. Iida, A. Ishimatsu, and T. Muramatsu.

2000. Mechanism of superoxide anion generation in the toxic red tide phytoplankton Chattonella marina: Possible involvement of NAD(P)H oxidase. Biochim. Biophys. Acta - Gen. Subj. **1524**: 220–227. doi:10.1016/S0304-4165(00)00161-6

Kustka, A. B., Y. Shaked, A. J. Milligan, D. W. King, and F. M. M. Morel. 2005. Extracellular production of superoxide by marine diatoms: Contrasting effects on iron redox chemistry and bioavailability. Limnol. Oceanogr. **50**: 1172–1180. doi:10.4319/lo.2005.50.4.1172

Lamb, C., and R. A. Dixon. 1997. The oxidative burst in plant disease resistance. Annu. Rev. Plant Biol. **48**: 251–275.

Learman, D. R., B. M. Voelker, A. I. Vazquez-Rodriguez, and C. M. Hansel. 2011. Formation of manganese oxides by bacterially generated superoxide. Nat. Geosci. **4**: 95–98. doi:10.1038/ngeo1055

Lee-Ruff, E. 1977. The organic chemistry of superoxide. Chem. Soc. Rev. **6**: 195–214.

Martin, J. H., G. A. Knauer, D. M. Karl, and W. W. Broenkow. 1987. VERTEX - CARBON CYCLING IN THE NORTHEAST PACIFIC. Deep. Res. Part a-Oceanographic Res. Pap. **34**: 267–285. doi:10.1016/0198-0149(87)90086-0

Mehler, A. H. 1951. Studies on reactions of illuminated chloroplasts: I. Mechanism of the reduction of oxygen and other hill reagents. Arch. Biochem. Biophys. **33**: 65–77.

Moffett, J. W., and O. C. Zafiriou. 1990. An investigation ofhydrogen peroxide chemistry in surface waters of Vineyard Sound with H218O2 and 18O2. Limnol. Oceanogr. **35**: 1221–1229.

Oda, T., J. Moritomi, I. Kawano, S. Hamaguchi, A. Ishimatsu, and T. Muramatsu. 1995. Catalase- and superoxide dismutase-induced morphological changes and growth inhibition in the red tide phytoplankton Chattonella marina. Biosci. Biotechnol. Biochem. **59**: 2044–2048.

Palenik, B., and F. M. M. Morel. 1991. Amine oxidases of marine phytoplankton. Appl. Environ. Microbiol. **57**: 2440–2443.

Palenik, B., O. C. Zafiriou, and F. M. M. Morel. 1987. Hydrogen peroxide production by a marine phytoplankter1. Limnol. Oceanogr. **32**: 1365–1369.

Petasne, R. G., and R. G. Zika. 1987. Fate of superoxide in coastal sea water. Nature **325**: 516–518. doi:10.1038/325516a0

Plummer, S., A. E. Taylor, E. L. Harvey, C. M. Hansel, and J. M. Diaz. 2019. Dynamic regulation of extracellular superoxide production by the coccolithophore Emiliania huxleyi (CCMP 374). Front. Microbiol. **10**: 1546.

Powers, L. C., L. C. Babcock-adams, J. K. Enright, and W. L. Miller. 2015. Probing the photochemical reactivity of deep ocean refractory carbon (DORC): Lessons from hydrogen peroxide and superoxide kinetics. Mar. Chem. **177**: 306–317. doi:10.1016/j.marchem.2015.06.005

Powers, L. C., and W. L. Miller. 2014. Blending remote sensing data products to estimate photochemical production of hydrogen peroxide and superoxide in the surface ocean. Environ. Sci. Impacts **16**: 792–806. doi:10.1039/c3em00617d

Powers, L. C., and W. L. Miller. 2015. Hydrogen peroxide and superoxide photoproduction in

diverse marine waters: A simple proxy for estimating direct CO2 photochemical fluxes. 7696–7704. doi:10.1002/2015GL065669.Received

Powers, L. C., and W. L. Miller. 2016. Apparent Quantum Efficiency Spectra for Superoxide Photoproduction and Its Formation of Hydrogen Peroxide in Natural Waters. **3**: 1–9. doi:10.3389/fmars.2016.00235

Redfield, A. C. %J T. sea. 1963. The influence of organisms on the composition of seawater. **2**: 26–77.

Regaudie-de-Gioux, A., S. Lasternas, S. Agustí, and C. M. Duarte. 2014. Comparing marine primary production estimates through different methods and development of conversion equations. Front. Mar. Sci. **1**. doi:10.3389/fmars.2014.00019

Roe, K. L., R. J. Schneider, C. M. Hansel, and B. M. Voelker. 2016. Measurement of dark, particle-generated superoxide and hydrogen peroxide production and decay in the subtropical and temperate North Pacific Ocean. Deep. Res. Part I-Oceanographic Res. Pap. **107**: 59–69. doi:10.1016/j.dsr.2015.10.012

Rose, A. L., E. A. Webb, T. D. Waite, and J. W. Moffett. 2008. Measurement and implications of nonphotochemically generated superoxide in the equatorial Pacific Ocean. Environ. Sci. Technol. **42**: 2387–2393. doi:10.1021/es7024609

Rusak, S. A., B. M. Peake, L. E. Richard, S. D. Nodder, and W. J. Cooper. 2011. Distributions of hydrogen peroxide and superoxide in seawater east of New Zealand. Mar. Chem. **127**: 155–169. doi:10.1016/j.marchem.2011.08.005

Saran, M. 2003. To what end does nature produce superoxide? NADPH oxidase as an autocrine modifier of membrane phospholipids generating paracrine lipid messengers. Free Radic. Res. **37**: 1045–1059. doi:10.1080/10715760310001594631

Schneider, R. J., K. L. Roe, C. M. Hansel, and B. M. Voelker. 2016. Species-Level Variability in Extracellular Production Rates of Reactive Oxygen Species by Diatoms. Front. Chem. **4**. doi:10.3389/fchem.2016.00005

Sutherland, K. M., A. Coe, R. J. Gast, and others. 2019. Extracellular superoxide production by key microbes in the global ocean. Limnol. Oceanogr.

Takahashi, M. A., and K. Asada. 1983. SUPEROXIDE ANION PERMEABILITY OF PHOSPHOLIPID-MEMBRANES AND CHLOROPLAST THYLAKOIDS. Arch. Biochem. Biophys. **226**: 558–566. doi:10.1016/0003-9861(83)90325-9

Wuttig, K., M. I. Heller, and P. L. Croot. 2013a. Reactivity of Inorganic Mn and Mn Desferrioxamine B with O-2, O-2(-), and H2O2 in Seawater. Environ. Sci. Technol. **47**: 10257–10265. doi:10.1021/es4016603

Wuttig, K., M. I. Heller, and P. L. Croot. 2013b. Pathways of Superoxide (O-2(-)) Decay in the Eastern Tropical North Atlantic. Environ. Sci. Technol. **47**: 10249–10256. doi:10.1021/es401658t

Zhang, T., C. M. Hansel, B. M. Voelker, and C. H. Lamborg. 2016. Extensive Dark Biological Production of Reactive Oxygen Species in Brackish and Freshwater Ponds. Environ. Sci. Technol. **50**: 2983–2993. doi:10.1021/acs.est.5b03906

Zhang, Y., and N. V Blough. 2016. Photoproduction of One-Electron Reducing Intermediates by Chromophoric Dissolved Organic Matter (CDOM): Relation to O 2 − and H 2 O 2 Photoproduction and CDOM Photooxidation.doi:10.1021/acs.est.6b02919

Zinger, L., L. A. Amaral-Zettler, J. A. Fuhrman, and others. 2011. Global Patterns of Bacterial Beta-Diversity in Seafloor and Seawater Ecosystems. PLoS One **6**. doi:10.1371/journal.pone.0024570

Supplemental Material: Parameters and Calculations

Cell Specific Superoxide Production Rates:

Cell specific superoxide production rates were compiled from the scientific literature (Kustka et al. 2005; Rose et al. 2008; Diaz et al. 2013; Hansel et al. 2016; Schneider et al. 2016; Zhang et al. 2016; Plummer et al. 2019; Sutherland et al. 2019). Figure S1 displays estimates for the mean and standard error (bootstrapping, N=10,000) of each microbial extracellular superoxide production rate, with the exception of diatoms. Diatoms were calculated using the cell surface area as discussed below. The (*) in the figure below indicates alternate units of amol/μm^2/hr. While some microbial groups data sets contain non-ideal data richness for bootstrapping, we do not rely on these estimated sample parameters alone to support our conclusion. We present these estimates as one of two lines of evidence for our superoxide flux estimate, the second being field depth profiles.

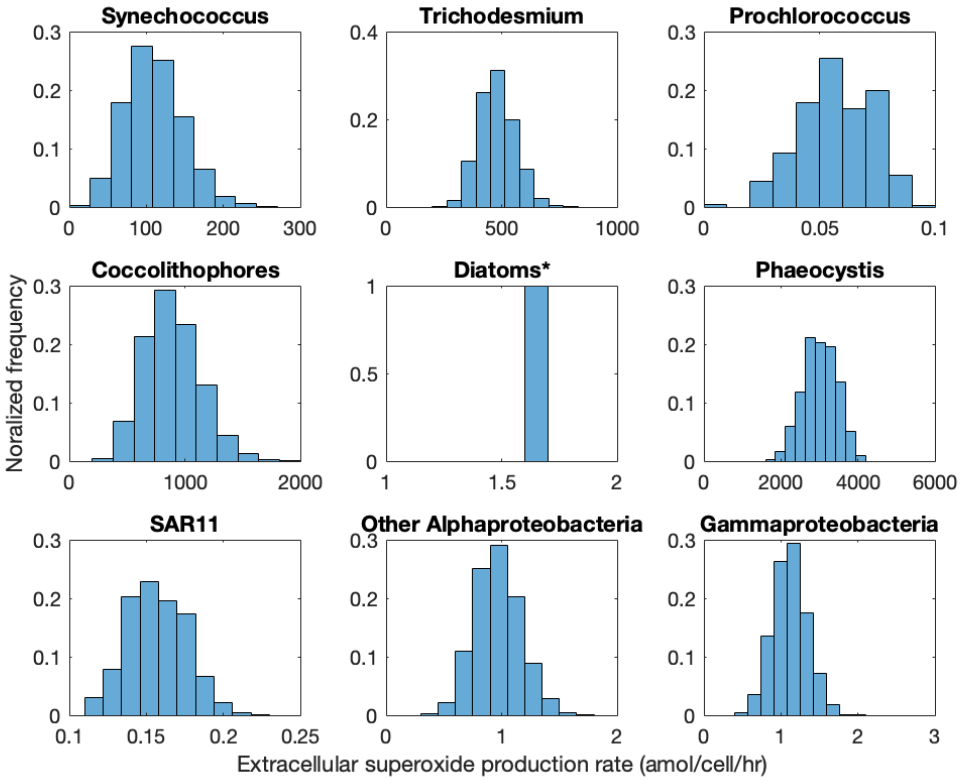

Figure S1- Distribution of mean extracellular superoxide production rates based on bootstrap estimation. The units of the mean diatom rate are amol/um^2/hr, and a more detailed treatment of diatom extracellular superoxide production estimate is provided below.

Average cell oxygen utilization rate in the global ocean:

This estimate was made using a central estimate for marine net primary productivity (NPP) in Field et al. (1998) of 48.5 Pg C year^{-1}, gross oxygen production to carbon assimilation (GOP:NPP) value of 2.7 from Marra (2002), an estimate for the total number of prokaryotic cells in the water column from Whitman et al. (1998) (Field et al. 1998; Whitman et al. 1998; Marra 2002).

$$\frac{48.5\ Pg\ C}{year} \times \frac{1\ x\ 10^{15}\ g}{1\ Pg} \times \frac{1 mol}{12.01 g} \times \frac{2.7\ mol\ GOP\ (O_2)}{1\ mol\ NPP\ (C)} \times \frac{1}{1.01\ x\ 10^{29} cells} \times \frac{1\ year}{8760\ hr}$$

$$= 1.23\ x\ 10^{-17} \frac{mol}{cell\ hr} = 12.3\ \frac{amol}{cell\ hr}$$

Note that the product of the first four terms in the above equation gives marine gross oxygen production of 1.09x10^{16} mol O_2 year^{-1}.

Cell Number Estimates:

The estimates of cell count, net primary production, and cell size have an unknown degree of uncertainty and likely contain bias toward well-studied regions and microbial groups. To account for this uncertainty in our estimation of the mean extracellular superoxide flux in the ocean, we let the cell counts for each biological grouping vary ±30% (uniform distribution) about the cell count estimates that we describe below.

Cell number estimates for each marine group were either obtained directly from previous estimates or calculated from parameters in relevant scientific literature. Estimates of *Alphaproteobacteria* and *Gammaproteobacteria* were made by multiplying estimates of total bacteria in the water column (1.01 x 10^{29} cells) (Whitman et al. 1998) by relative abundances of each group in the water column (43% and 27%, respectively) (Zinger et al. 2011). The *Pelagibacterales* cell number was taken directly from a previous estimate (Giovannoni 2017): 2.4 x 10^{28} cells. Cell numbers for *Prochlorococcus* and *Synechococcus* were taken from annual mean global abundance estimates: 2.9 x 10^{27} cells and 7.0 x 10^{26}, respectively (Flombaum et al. 2013). The data used to estimate diatom abundance was taken from a global diatom database (Leblanc et al. 2012); a cell estimate of 2.6x10^{24} diatoms was made using the annual diatom biomass (as carbon) production and the mean carbon content of each diatom cell (see diatom section below).

The biomass of *Trichodesmium* in the global ocean is estimated using biomass distributions available in the Community Earth Systems Model (CESM) Large Ensemble Project using the following file (Kay et al. 2015): b.e11.B20TRC5CNBDRD.f09_g16.001.pop.h.diazC.185001-200512. This contains the distribution of carbon from diazotrophs. For simplicity, we assigned each spatial cell in the model the average carbon content over the ten-year period from January 1995 to December 2005. *Trichodesmium* cell numbers were derived using the annual average diazotroph biomass from CESM and *Trichodesmium* cell carbon content (Goebel et al. 2008) (42 pg C $cell^{-1}$), producing a total of 4.6 x 10^{23} cells. Similarly, *Phaeocystis* cell numbers were calculated using net *Phaeocystis* primary production (*Phaeocystis* represents 13% of Southern ocean net primary production, 4.5 PgC, which yields 0.58 PgC for *Phaeocystis* NPP) (Arrigo et al. 2008; Wang and Moore 2011; Rousseaux and Gregg 2014) and a mean *Phaeocystis* cell size (15 pg C $cell^{-1}$) (Schoemann et al. 2005; Vogt et al. 2012), producing an annual *Phaeocystis* cell count of 3.9x10^{25} cells. *Coccolithophore* cell counts were determined using the fraction of primary production attributed to the clade (21%) (Rousseaux and Gregg 2014) times global marine NPP (48.5 Pg C $year^{-1}$) (Field et al. 1998) and the mean *Coccolithophore* cell biomass (weighted average of each species from O'brien et al. 2013, 39.3 pg C/cell) (O'Brien et al. 2013) producing a total cell count of 2.6 x 10^{26} cells.

Diatom extracellular superoxide production:

The diatom cell normalized extracellular $O_2^{\bullet-}$ is much less straightforward to estimate than other phytoplankton groups, as the classification division of diatoms is coarser than for the other clades discussed in this study. The biovolume of diatoms span up to 9 orders of magnitude, requiring discrete accounting for cell size in assigning this group a cell specific superoxide production rate (Leblanc et al. 2012). Table S2 shows the surface area normalized extracellular superoxide production rates for the diatoms included in this study.

Table S1

Organism	Superoxide production rate (amol cell^{-1} hr^{-1})	Source of rate	Surface area normalized rate (amol cell^{-1} μm^{-2} hr^{-1})	Source of surface area estimate
Coscinodiscus	900-13,400	(Hansel et al. 2016)	0.18, 0.29	(Hansel et al. 2016)
Thalassiosira oceananica	60	(Schneider et al. 2016)	0.77	(Maldonado and Price 2001)
Thalassiosira pseudonana	75	(Schneider et al. 2016)	1.47	(Rose et al. 2008)
Thalassiosira pseudonana (Low Fe)	830	(Rose et al. 2008)	16.27	(Rose et al. 2008)
Thalassiosira pseudonana (High Fe)	450	(Rose et al. 2008)	8.82	(Rose et al. 2008)
Thalassiosira weissflogii	840	(Kustka et al. 2005)	1.83	(Rose et al. 2008)
Thalassiosira weissflogii	252	(Schneider et al. 2016)	0.55	(Rose et al. 2008)
Thalassiosira weissflogii (Low Fe)	1,300	(Rose et al. 2008)	2.83	(Rose et al. 2008)
Thalassiosira weissflogii (High Fe)	800	(Rose et al. 2008)	1.74	(Rose et al. 2008)

The range of extracellular superoxide production rates falls within a much narrower range when normalized to cell surface area, as shown in the table. For this reason, we estimated the total extracellular superoxide production from diatoms using the median surface area normalized production rate listed above (1.6 amol cell^{-1} μm^{-2} hr^{-1}). To determine the cell abundances and their relative contribution to the marine superoxide flux, we turned to a diatom database containing >200,000 georeferenced diatom observations that include estimates of biomass, biovolume, and surface area (Leblanc et al. 2012). None of these cell parameters can be approximated as a normal distribution. The cell surface area and biomass all have considerable skew (e.g. mean surface area =2.9x10^4 μm^2 vs median surface area = 4825 μm^2). Using the median cell biomass as an estimator for calculating diatom abundance will overestimate small cells, which have a higher surface area to volume ratio, and will therefore contribute more significantly to the superoxide flux. Using the mean biomass to calculate diatom abundance places significant weight on exceptionally large diatoms, but will produce a more conservative estimate of global cell count and cell surface area to volume ratio. We calculate the annual diatom cell count using the fraction of NPP contributed by diatoms (52%), a central estimate of annual NPP (48.5 PgC), the mean diatom biomass (9,794 pgC/cell), mean diatom surface area 29,632 um^2/cell. This estimate produces a mean annual diatom cell count of 2.6x10^{24} cells in the top 200 meters of the marine water column.

Estimation of global superoxide flux:

Using MATLAB, we simulated the cumulative superoxide flux, or the sum of the 9 major microbial groups reviewed in this work. Each major group's contribution to the global superoxide flux was determined by randomly assigning a cell count from a uniform distribution ranging from the -30% to +30% of the cell estimates calculated above. This cell number was then randomly assigned a superoxide production rate, with a probability distribution shown in Figure S1. The total superoxide production flux of all 9 microbial groups was summed, and the simulation repeated a total of 1 million times. The histogram of results is shown in figure S2.

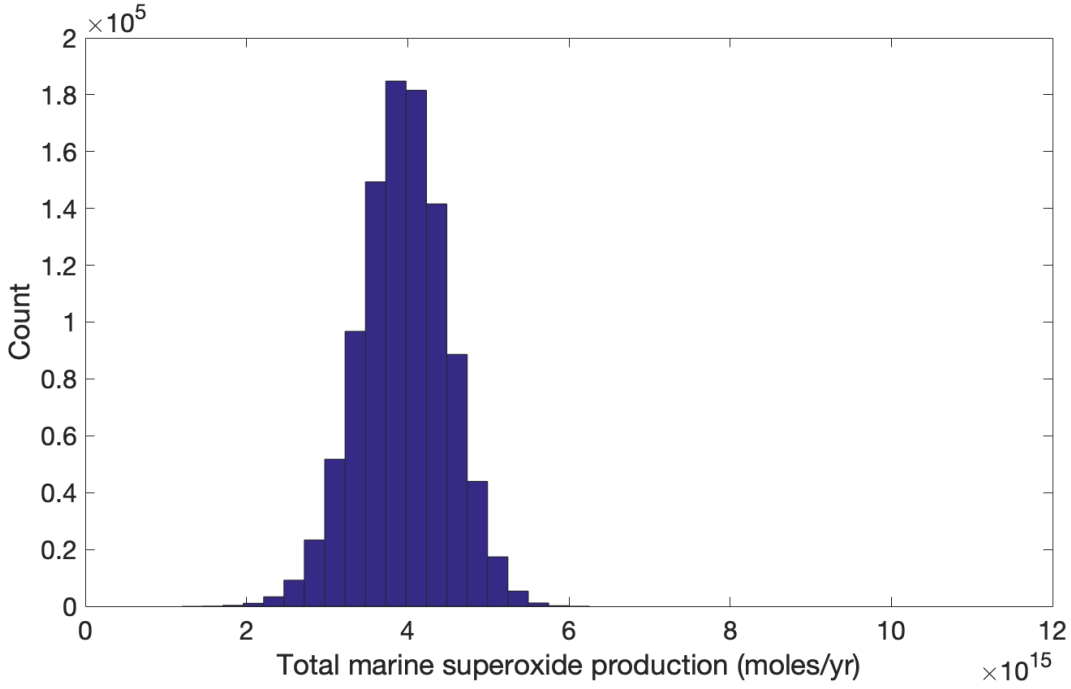

Figure S2-Histogram of the sum of extracellular superoxide production of 9 major marine microbial groups.

The 5th percentile estimate is 3.1x10^{15}, and the 95th percentile estimate is 4.8x10^{15}. The 9 microbial groups each had the following fractional contributions: diatoms: 27.2%, *Phaeocystis*: 25.3%, Coccolithophores: 19.8%, *Synechococcus*: 16.4%, *Gammaproteobacteria*: 6.5%, *Alphaproteobacter* (excluding SAR11): 3.8%, SAR11: 0.8%, *Trichodesmium*: 0.05%, *Prochlorococcus*: 0.04%.

Calculation of expected marine superoxide concentration:

To test the robustness of our estimate of the global oxygen loss from extracellular superoxide production, we compare the expected superoxide concentration in the water column (based on our estimate of global production) against measurements of (dark) superoxide concentration in the water column. In order to calculate the expected superoxide concentration based on dark superoxide production, superoxide decay rates in natural water are required, which are well documented. We compiled superoxide decay rates from several studies on natural waters and present them in Figure S3 (Rose et al. 2008; Hansard et al. 2010; Heller and Croot 2010a; b; Heller et al. 2016; Roe et al. 2016).

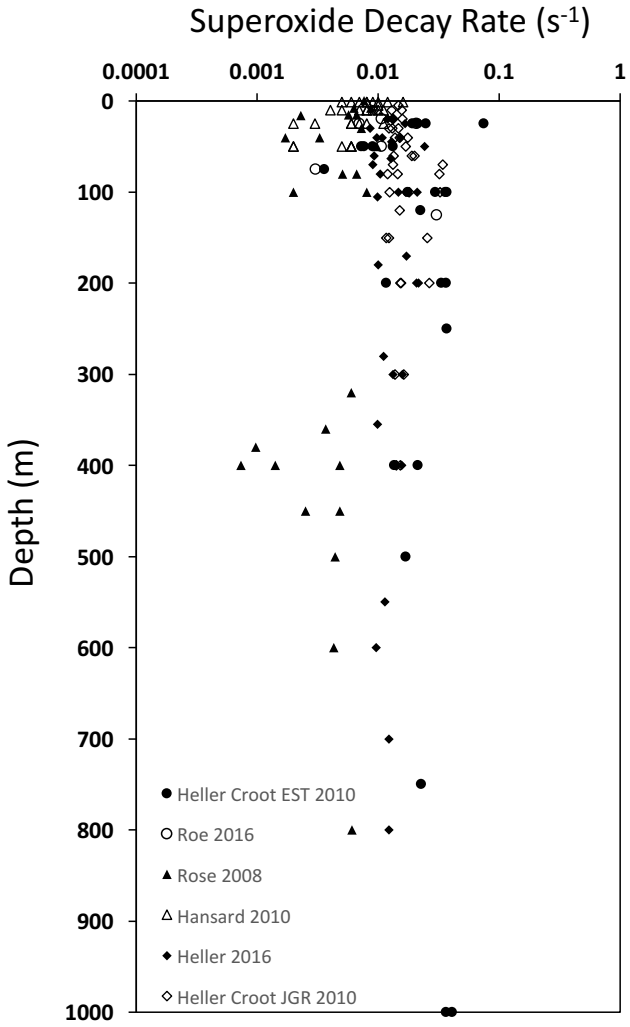

Figure S3- Compilation of superoxide decay rates in seawater versus seawater depth.

The complete set of decay rate constants has an approximately log-normal distribution, which was determined using one-sample Kolmogorov-Smirnov test (n=157). The mean of the natural log of all compiled superoxide decay rate constants is -4.5484 ± 0.7598 (ln(rate) ± 1 standard deviation, rate units are s^{-1}). This corresponds to a mean rate of 0.0106 s^{-1} with a 68% confidence interval ranging from 0.0050 s^{-1} to 0.0226 s^{-1}.

To calculate the expected superoxide concentration in seawater we began with an annual estimate for global superoxide flux. The total global superoxide flux was divided between the surface and the deep ocean based on estimates from Whitman et al. (1998) for the proportion of non-phototroph organisms above and below 200 meters (Whitman et al. 1998). The annual gross superoxide production was divided by the volume of water in the surface and deep ocean, respectively, yielding volume normalized annual superoxide production rates (mol L^{-1} yr^{-1}). Annual production rates were divided by the superoxide decay rate to determine the steady-state concentration. Given that the half-life superoxide is on the order of 1 minute or less, steady-state concentrations are achieved quickly. The following table summarizes the calculations:

Table S2

	Above 200 m	**Below 200 m**
Surface area of ocean (m^2)	$3.62x10^{14}$	$3.62x10^{14}$
Volume (m^3)	$7.24x10^{16}$	$1.34x10^{18}$
Fraction of phototroph dark superoxide production (%)	100	0
Fraction of heterotroph dark superoxide production (%)	39.5	60.5
Total superoxide produced (mol yr^{-1})	$3.68x10^{15}$	$2.67x10^{14}$
Total superoxide production rate per volume (mol yr^{-1} m^{-3})	$5.08x10^{-2}$	$1.99x10^{-4}$
Total superoxide production rate per volume (mol L^{-1} s^{-1})	$1.61x10^{-12}$	$6.31x10^{-15}$
Average concentration using k=0.0106 s-1 (pM)	152	0.6
Concentration using 1sd rate below average mean (pM)	322	1.3
Concentration using 1sd rate above average mean (pM)	71	0.3

Our estimates for global dark superoxide production predict the surface ocean will have an average concentration of 152 pM (68% confidence interval 71 to 322 pM) and the dark ocean a concentration of 0.6 pM (68% confidence interval 0.3 to 1.3 pM).

References

Arrigo, K. R., G. L. van Dijken, and S. Bushinsky. 2008. Primary production in the Southern Ocean, 1997-2006. J. Geophys. Res. **113**: 27. doi:10.1029/2007jc004551

Diaz, J. M., C. M. Hansel, B. M. Voelker, C. M. Mendes, P. F. Andeer, and T. Zhang. 2013. Widespread Production of Extracellular Superoxide by Heterotrophic Bacteria. Science (80-.). **340**: 1223–1226. doi:10.1126/science.1237331

Field, C. B., M. J. Behrenfeld, J. T. Randerson, and P. Falkowski. 1998. Primary production of the biosphere: Integrating terrestrial and oceanic components. Science (80-.). **281**: 237–240. doi:10.1126/science.281.5374.237

Flombaum, P., J. L. Gallegos, R. A. Gordillo, and others. 2013. Present and future global distributions of the marine Cyanobacteria Prochlorococcus and Synechococcus. Proc. Natl. Acad. Sci. U. S. A. **110**: 9824–9829. doi:10.1073/pnas.1307701110

Giovannoni, S. J. 2017. SAR11 Bacteria: The Most Abundant Plankton in the Oceans, p. 231–255. *In* Annual Review of Marine Science, Vol 9. Annual Reviews.

Goebel, N. L., C. A. Edwards, B. J. Carter, K. M. Achilles, and J. P. Zehr. 2008. Growth and carbon content of three different-sized diazotrophic cyanobacteria observed in the subtropical North Pacific. J. Phycol. **44**: 1212–1220. doi:10.1111/j.1529-8817.2008.00581.x

Hansard, S. P., A. W. Vermilyea, and B. M. Voelker. 2010. Deep-Sea Research I Measurements of superoxide radical concentration and decay kinetics in the Gulf of Alaska. Deep. Res. Part I **57**: 1111–1119. doi:10.1016/j.dsr.2010.05.007

Hansel, C. M., C. Buchwald, J. M. Diaz, J. E. Ossolinski, S. T. Dyhrman, B. A. S. Van Mooy, and D. Polyviou. 2016. Dynamics of extracellular superoxide production by Trichodesmium colonies from the Sargasso Sea. Limnol. Oceanogr. **61**: 1188–1200. doi:10.1002/lno.10266

Heller, M. I., and P. L. Croot. 2010a. Superoxide Decay Kinetics in the Southern Ocean. Environ. Sci. Technol. **44**: 191–196. doi:10.1021/es901766r

Heller, M. I., and P. L. Croot. 2010b. Kinetics of superoxide reactions with dissolved organic matter in tropical Atlantic surface waters near Cape Verde (TENATSO). J. Geophys. Res. **115**. doi:10.1029/2009jc006021

Heller, M. I., K. Wuttig, and P. L. Croot. 2016. Identifying the Sources and Sinks of CDOM/FDOM across the Mauritanian Shelf and Their Potential Role in the Decomposition of Superoxide (O2-). Front. Mar. Sci. **3**. doi:10.3389/fmars.2016.00132

Kay, J. E., C. Deser, A. Phillips, and others. 2015. THE COMMUNITY EARTH SYSTEM MODEL (CESM) LARGE ENSEMBLE PROJECT A Community Resource for Studying Climate Change in the Presence of Internal Climate Variability. Bull. Am. Meteorol. Soc. **96**: 1333–1349. doi:10.1175/bams-d-13-00255.1

Kustka, A. B., Y. Shaked, A. J. Milligan, D. W. King, and F. M. M. Morel. 2005. Extracellular production of superoxide by marine diatoms: Contrasting effects on iron redox chemistry and bioavailability. Limnol. Oceanogr. **50**: 1172–1180. doi:10.4319/lo.2005.50.4.1172

Leblanc, K., J. Aristegui, L. Armand, and others. 2012. A global diatom database - abundance, biovolume and biomass in the world ocean. Earth Syst. Sci. Data **4**: 149–165. doi:10.5194/essd-4-149-2012

Maldonado, M. T., and N. M. Price. 2001. Reduction and transport of organically bound iron by Thalassiosira oceanica (Bacillariophyceae). J. Phycol. **37**: 298–309. doi:10.1046/j.1529-8817.2001.037002298.x

Marra, J. 2002. Approaches to the measurement of plankton production. Phytoplankt. Product. Carbon Assim. Mar. Freshw. Ecosyst. 78–108.

O'Brien, C. J., J. A. Peloquin, M. Vogt, and others. 2013. Global marine plankton functional type biomass distributions: coccolithophores. Earth Syst. Sci. Data **5**: 259–276.

Plummer, S., A. E. Taylor, E. L. Harvey, C. M. Hansel, and J. M. Diaz. 2019. Dynamic regulation of extracellular superoxide production by the coccolithophore Emiliania huxleyi (CCMP 374). Front. Microbiol. **10**: 1546.

Roe, K. L., R. J. Schneider, C. M. Hansel, and B. M. Voelker. 2016. Measurement of dark, particle-generated superoxide and hydrogen peroxide production and decay in the subtropical and temperate North Pacific Ocean. Deep. Res. Part I-Oceanographic Res. Pap. **107**: 59–69. doi:10.1016/j.dsr.2015.10.012

Rose, A. L., E. A. Webb, T. D. Waite, and J. W. Moffett. 2008. Measurement and implications of nonphotochemically generated superoxide in the equatorial Pacific Ocean. Environ. Sci. Technol. **42**: 2387–2393. doi:10.1021/es7024609

Rousseaux, C., and W. Gregg. 2014. Interannual variation in phytoplankton primary production at a global scale. Remote Sens. **6**: 1–19.

Schneider, R. J., K. L. Roe, C. M. Hansel, and B. M. Voelker. 2016. Species-Level Variability in Extracellular Production Rates of Reactive Oxygen Species by Diatoms. Front. Chem. **4**. doi:10.3389/fchem.2016.00005

Schoemann, V., S. Becquevort, J. Stefels, W. Rousseau, C. Lancelot, V. Rousseau, and C. Lancelot. 2005. Phaeocystis blooms in the global ocean and their controlling mechanisms: a review. J. Sea Res. **53**: 43–66. doi:10.1016/j.seares.2004.01.008

Sutherland, K. M., A. Coe, R. J. Gast, and others. 2019. Extracellular superoxide production by key microbes in the global ocean. Limnol. Oceanogr.

Vogt, M., C. O'Brien, J. Peloquin, and others. 2012. Global marine plankton functional type biomass distributions: *Phaeocystis* spp. Earth Syst. Sci. Data **4**: 107–120. doi:10.5194/essd-4-107-2012

Wang, S. L., and J. K. Moore. 2011. Incorporating Phaeocystis into a Southern Ocean ecosystem model. J. Geophys. Res. **116**: 18. doi:10.1029/2009jc005817

Whitman, W. B., D. C. Coleman, and W. J. Wiebe. 1998. Prokaryotes: The unseen majority. Proc. Natl. Acad. Sci. U. S. A. **95**: 6578–6583. doi:10.1073/pnas.95.12.6578

Zhang, T., C. M. Hansel, B. M. Voelker, and C. H. Lamborg. 2016. Extensive Dark Biological Production of Reactive Oxygen Species in Brackish and Freshwater Ponds. Environ. Sci. Technol. **50**: 2983–2993. doi:10.1021/acs.est.5b03906

Zinger, L., L. A. Amaral-Zettler, J. A. Fuhrman, and others. 2011. Global Patterns of Bacterial Beta-Diversity in Seafloor and Seawater Ecosystems. PLoS One **6**. doi:10.1371/journal.pone.0024570

Supplemental Material: Measurement of Dark Superoxide Concentrations at the Bermuda Atlantic Time-series Study and Hydrostation S Monitoring Stations

The primary conclusion of Chapter 6, that superoxide production and decay represent a significant flux and sink of oxygen in the marine oxygen cycle, has profound implications for how we understand and measure biogeochemical fluxes of oxygen in the ocean. There still remains, however, an important need to validate and refine the primary model results, which at its core are no more than a careful back-of-the-envelope calculation. In this section, we outline our attempt to contribute to the body of work that we compiled in this preceding chapter through additional collection of environmental superoxide concentration data.

In Figure 2 of Chapter 6, we compared the expected superoxide concentrations based on our global superoxide production estimate to those measured in four studies (Rose et al. 2008; Hansard et al. 2010; Rusak et al. 2011; Roe et al. 2016). These measurements were primarily targeted at the surface ocean, with only one study collecting superoxide concentration measurements below 200 meters depth. To address what we see as the shortcomings of this collective data set, we conducted a series of superoxide concentration measurements at or near the Bermuda Atlantic Time Series (BATS) long term monitoring station. This location is desirable for addressing the set of questions that arise in our preceding study because it is situated in the oligotrophic Sargasso Sea, and therefore serves as a better indicator of processes that occur in the open ocean. BATS also offers a location with considerable ocean depth (>4000 meters), which will better illuminate the behavior of superoxide in the deep ocean.

Samples were collected during the monthly BATS and Hydrostation S monitoring expedition in September, 2018, from the *R/V Atlantic Explorer* (AE1825). Water was collected using 12 L Ocean Test Equipment bottles on a 24 position Sea-Bird CTD rosette. Samples were transferred into dark, acid washed bottles and measured between 30 mins and 6 hours of the collection time. Thirty minutes was chosen as a sample delay period because it is greater than 10 half-lives of superoxide in typical marine waters, meaning that any superoxide remaining is the result of dark bio(geo)chemical superoxide production by microbial communities in the bottles (Roe et al. 2016). Samples collected above the thermocline were incubated on deck with continuously flowing surface water, samples collected below the thermocline were incubated in a refrigerator at 4 degrees C.

Superoxide concentrations were measured using an FeLume Mini (Waterville Analytical) and the superoxide-specific chemiluminescent probe MCLA (see section 5.2.1 in Chapter 5 for a more detailed methods description of the FeLume system). Recent work using these methods has demonstrated that filtration of natural seawater can produce additional superoxide (Roe et al. 2016). To avoid introducing this bias into sample measurements, we adopted the following procedure from (Roe et al. 2016):

$$[O_2^{\cdot-}]_{sample} = [O_2^{\cdot-}]_{USW} - [O_2^{\cdot-}]_{AFSW}$$

where $[O_2^{\cdot-}]_{USW}$ represents the measured concentration of superoxide in unfiltered seawater (USW) and $[O_2^{\cdot-}]_{AFSW}$ represents the measured concentration of superoxide in aged (>24 hours) filtered (0.22 μm Sterivex filter) seawater amended with 75 μM diethylene-triaminepentaacetic acid (DTPA) to complex any metals present in the sample.

Each measurement consisted of running a 25 mL USW sample through the FeLume system (3mL/min) for several minutes until a steady signal was recorded. In most cases, a known amount of KO_2 was added to the sample to observe the decay rate of superoxide in the sample. Following this addition, 2μL superoxide dismutase (SOD; Superoxide Dismutase from bovine erythrocytes ≥ 3,000 U mg-1, Sigma, stock prepared in DI water to 4,000 U mL-1) was added to the sample to quench all superoxide in the sample. The same procedure was followed for the AFSW samples. The reported superoxide concentrations represent the difference between the USW and the AFSW concentrations, the latter allowing us to eliminate the portion of the measured signal due to MCLA auto-oxidation in each particular sample matrix. Calibration curves were generated daily from three or more paired observations of time-zero superoxide concentration (dependent variable) and extrapolated chemiluminescence (independent variable) using linear regression. Because chemiluminescence values were baseline-corrected, regression lines were forced through the origin. Calibrations yielded highly linear curves (typically R2 > 0.9), with a typical sensitivity of 1 chemiluminescence unit per pM superoxide.

BATS

The following table includes the results of a 21-point depth profile of superoxide concentration at BATS. Each reported value is the average and standard deviation of two replicates.

Table S3-Superoxide concentrations measured at BATS

Depth (m)	Average conc. (USW-AFSW)	Stdev (pM), n=2
1	ND*	-
20	150	50
40	170	80
60	90	30
80	210	12
100	8	13
120	40	50
140	250	40
200	220	70
300	370	70
400	66	13
500	700	20
600	110	50
1000	340	50
1400	105	12
2200	31	7
2600	18	9
3000	83	12
3400	140	30
4000	4	6
4553	130	80

*Below method detection limit

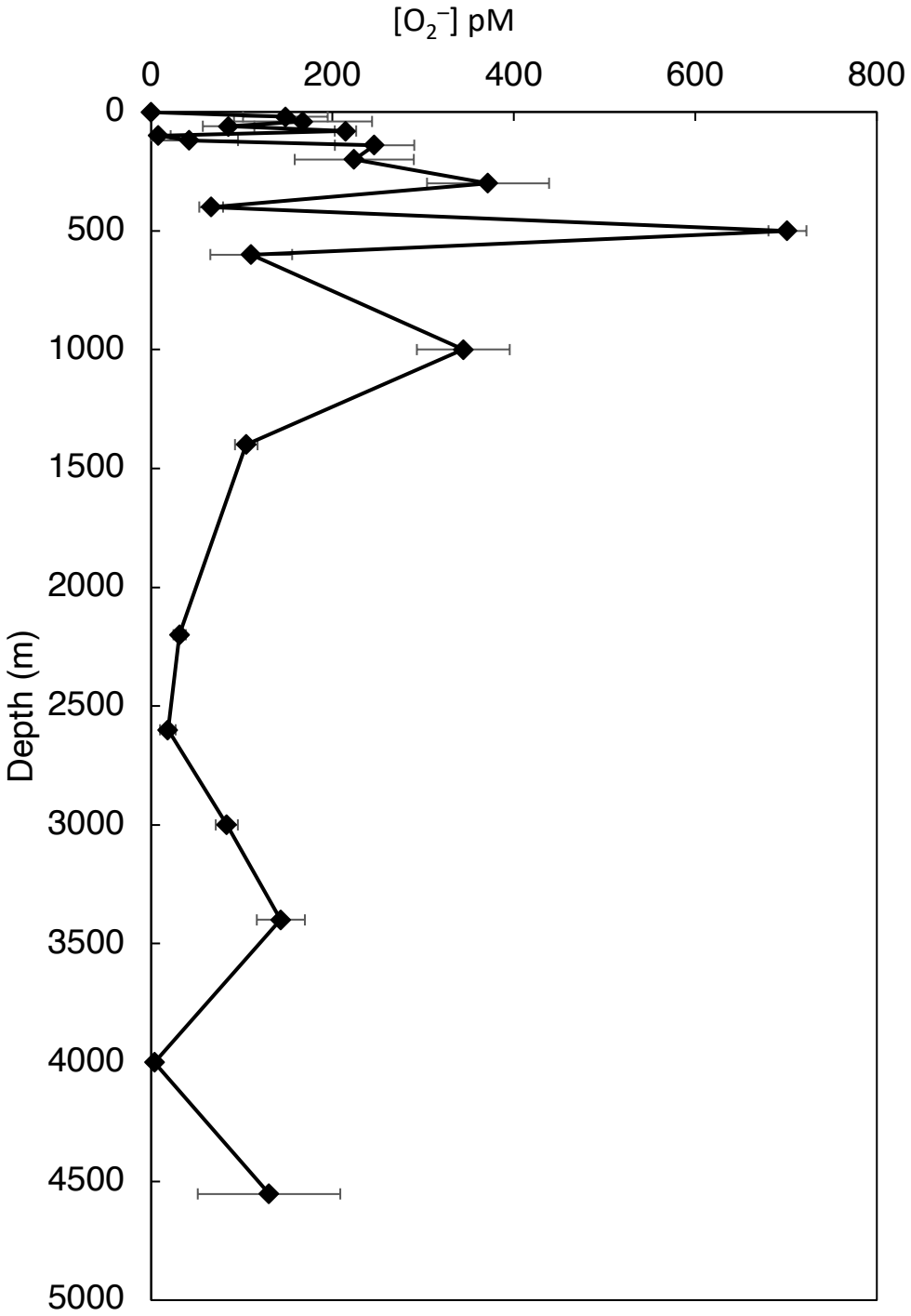

Figure S4- Superoxide concentration measured at BATS in September, 2018.

Hydrostation S:

The following table includes the results of a 10-point surface profile of superoxide concentration at Hydrostation S. Each reported value is the average and standard deviation of two replicates.

Table S4-Superoxide concentrations measured at Hydrostation S

Depth (m)	Average conc. (USW-AFSW)	Stdev (pM), n=2
1	10	20
25	71	2
60	146	3
100	130	11
130	720	60
200	70	20
240	200	100
300	556	5
400	270	100
500	600	50

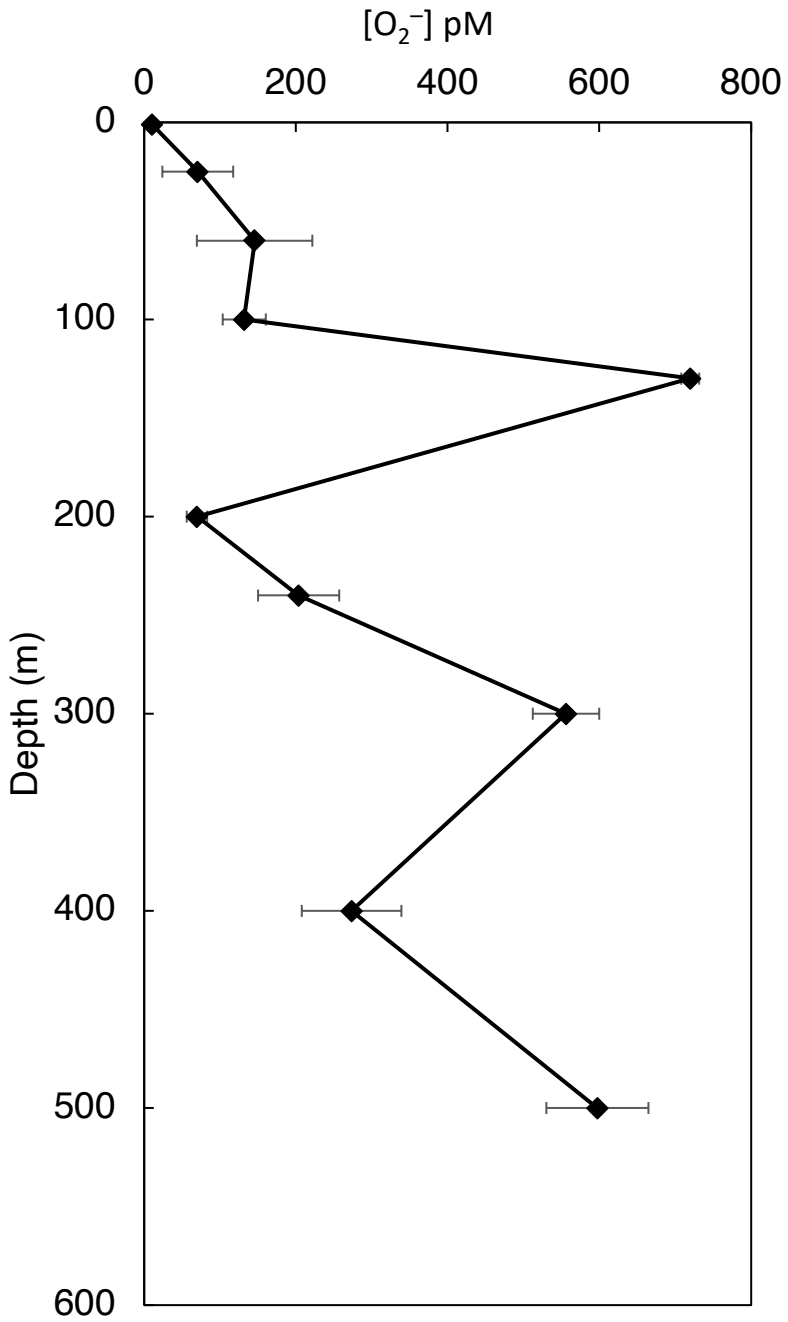

Figure S5- Superoxide concentration measured at Hydrostation S in September, 2018.

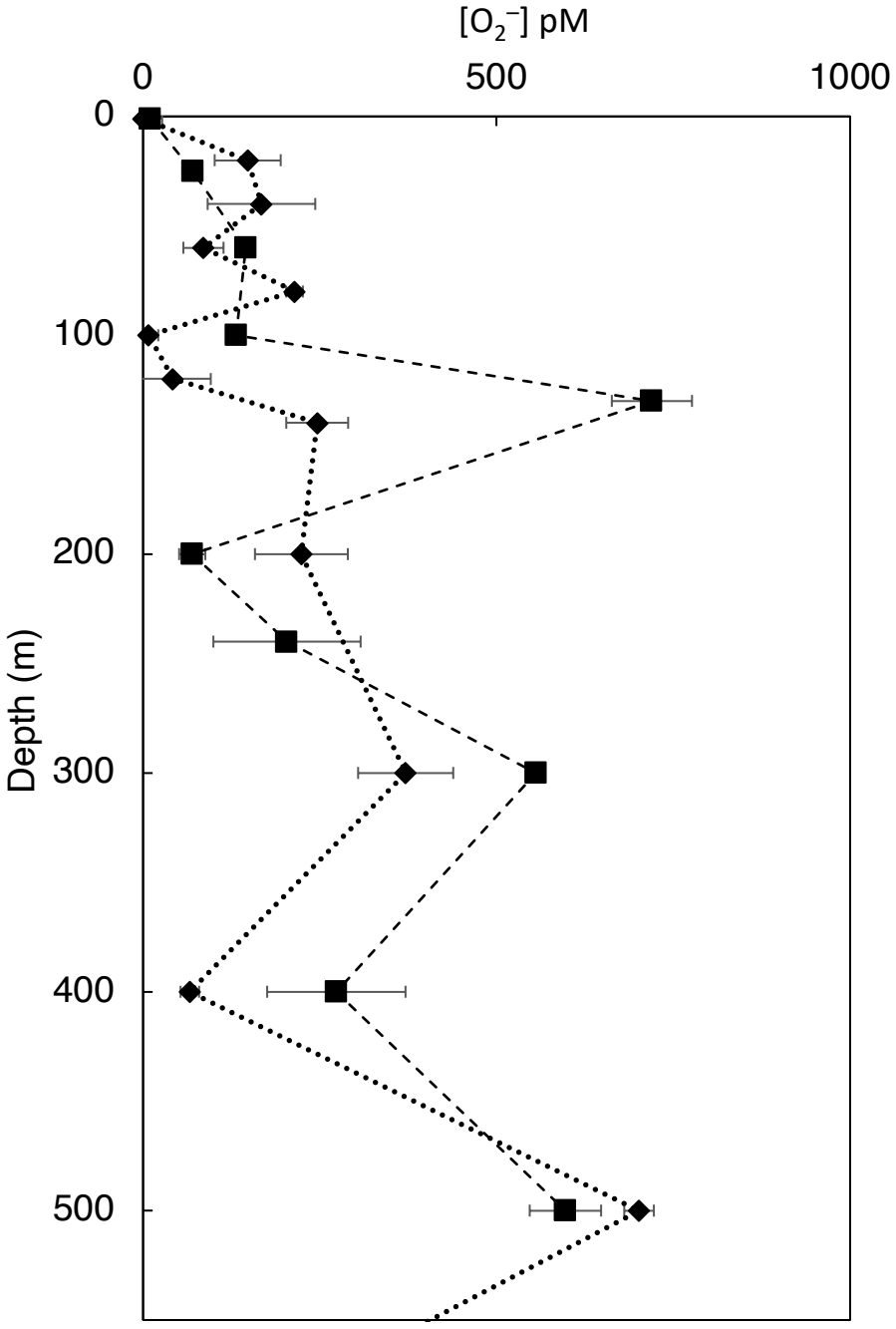

Figure S6-Overlay of the superoxide concentrations profiles collected at BATS (diamond with dotted line) and Hydrostation S (square with dashed line).

Figures S6 demonstrate an important result that has not before been investigated in great detail: two locations near one another have very similar superoxide concentrations and exhibit very similar depth trends with depth. Regional influences (e.g. microbial sources, microbial and abiotic sinks, depth in the water column) as opposed to small-scale microenvironments appear to exercise significant influence on the water column superoxide concentrations. The spatial extent to which regional influences is not clear from this study, however, regional similarity implicates common source and sink terms, which would allow for a more in-depth model of superoxide production in the ocean. Development of more high throughput techniques would allow for a more thorough confirmation of this result.

How do thesis values compare to those reported in other studies? And, more importantly, how do fit into this chapter's conclusion that superoxide comprises a significant portion of the global oxygen flux and sink? Figure S7 (replotting of Figure 2 from Chapter 6 with new data included) shows how our measurements compare to those reported in other studies. Overall, these data fall within a very similar range to those previously reported. In the surface ocean, most of the measured superoxide concentrations also fall within the 68% confidence interval of expected superoxide concentration based on the global superoxide flux estimate from Chapter 6. The close agreement between the expected concentration range and the observed concentration in the oligotrophic ocean provides further support to the notion that superoxide is an important global sink of oxygen.

One striking feature in Figure S7 is that superoxide concentrations in the deep ocean far exceed the 68% confidence interval based on the global superoxide production estimate in this chapter. In fact, superoxide concentrations below 200 meters sometimes exceed that observed above 200 meters. These values suggest that the global superoxide flux estimated from cell type, abundance, and distribution may be insufficient to model microbial superoxide production behavior. We observed in Chapter 5 that cell cultures of several marine microbes modulated their extracellular superoxide production rate based on the cell concentration. We propose that this same phenomenon, an increased extracellular superoxide production rate at low cell densities, may explain why our estimates for the deep ocean are so much lower than the observed concentrations. Future studies aimed at the mechanistic underpinnings of extracellular superoxide production by marine microbes may allow for an improved understanding of these higher-than-estimated

concentrations and allow for more refined estimates of global superoxide production in the deep ocean.

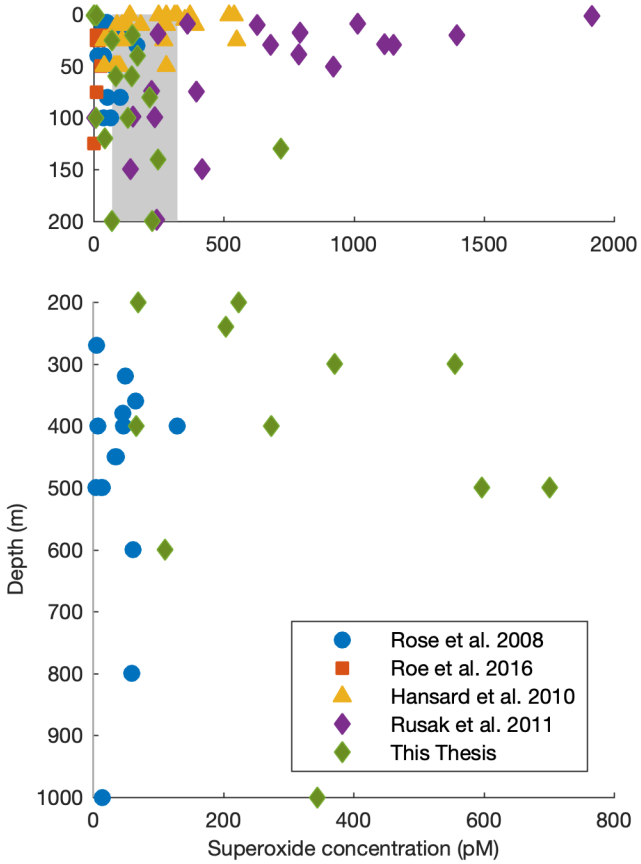

Figure S7- Replotting of Figure 2, Chapter 6 with additional BATS and Hydrostation S values also reported. The gray bars indicate the 68% confidence interval for the expected superoxide concentration based on our total superoxide flux estimate. The 68% confidence intervals for the expected superoxide concentrations in the surface (<200m) and deep (>200m) ocean are 71-332 pM and 0.3-1.3 pM (cannot be seen on this scale), respectively.

References

Hansard, S. P., A. W. Vermilyea, and B. M. Voelker. 2010. Deep-Sea Research I Measurements of superoxide radical concentration and decay kinetics in the Gulf of Alaska. Deep. Res. Part I **57**: 1111–1119. doi:10.1016/j.dsr.2010.05.007

Roe, K. L., R. J. Schneider, C. M. Hansel, and B. M. Voelker. 2016. Measurement of dark, particle-generated superoxide and hydrogen peroxide production and decay in the subtropical and temperate North Pacific Ocean. Deep. Res. Part I-Oceanographic Res. Pap. **107**: 59–69. doi:10.1016/j.dsr.2015.10.012

Rose, A. L., E. A. Webb, T. D. Waite, and J. W. Moffett. 2008. Measurement and implications of nonphotochemically generated superoxide in the equatorial Pacific Ocean. Environ. Sci. Technol. **42**: 2387–2393. doi:10.1021/es7024609

Rusak, S. A., B. M. Peake, L. E. Richard, S. D. Nodder, and W. J. Cooper. 2011. Distributions of hydrogen peroxide and superoxide in seawater east of New Zealand. Mar. Chem. **127**: 155–169. doi:10.1016/j.marchem.2011.08.005

7. The Production and Fate of Superoxide and Hydrogen Peroxide in a Brackish, Meromictic Pond

Abstract

The reactive oxygen species superoxide and hydrogen peroxide are widespread environmental compounds produced from one- and two-electron reduction of molecular oxygen, respectively, resulting from a diverse array of biologically-mediated and abiotic reactions. The production of ROS can be a net sink of dissolved oxygen in natural waters when they are degraded by a consortium of microbially mediated pathways, namely enzymatic elimination by superoxide dismutases, catalases, and peroxidases. The relative activity of these enzyme groups ultimately determines the magnitude of the dissolved oxygen sink that results from ROS production. In this study, we focus on two major aspects that determine the fate of ROS in the surface waters of a stratified pond: the contribution of dark superoxide production to total hydrogen peroxide production and the fate of hydrogen peroxide. We determine that hydrogen peroxide production resulting from light and dark processes in surface waters exceeds dark superoxide production by 14-fold. This ratio increases to ~300-fold at aphotic depths. Hydrogen peroxide degradation occurs via a combination of catalase- and peroxidase- like stoichiometries, with 39-46 percent of hydrogen peroxide being oxidized back to O_2, and 56-61 percent ultimately being reduced. This relatively narrow range of hydrogen peroxide decay pathways occurs across a range of light and oxygen conditions. These results highlight the decoupled nature of superoxide and hydrogen peroxide in this stratified system, and suggest dark hydrogen peroxide production and subsequent reduction may be a significant sink of dissolved oxygen in natural waters.

7.1 Introduction

The reactive oxygen species (ROS) superoxide and hydrogen peroxide are pervasive, reactive compounds that mediate a wide range of redox reactions in the surface Earth. These redox transformations include the remineralization of simple and complex organic compounds, and oxidation and reduction of transition metals used by organisms as enzyme cofactors or electron donors and acceptors (Rose et al. 2008b; Wuttig et al. 2013). The origin of these two reactive oxygen species is complex. For example, light absorption by colored dissolved organic matter (CDOM) in sunlit surface waters will induce an electron transfer to dissolved oxygen, producing the superoxide radical (Zhang et al. 2012). Under typical surface conditions, it is favorable for superoxide to act as an oxidant or a reductant depending on the nature of the species it is reacting with (Powers and Miller 2015). The net result is that superoxide is either oxidized back to O_2, or reduced to hydrogen peroxide. Superoxide will often undergo catalyzed or uncatalyzed dismutation, in which both O_2 and H_2O_2 result as products. Superoxide reduction is thought to be the primary pathway through which hydrogen peroxide is formed (Zhang et al. 2012), although in some systems hydrogen peroxide production can exceed superoxide production (Zhang et al. 2016), suggesting a more complex series of formation pathways, and a potential decoupling of these two ROS.

The view that photochemical processes are the primary source ROS in the environment has come into question more recently as dark microbial processes have been identified as widespread sources of ROS (Diaz et al. 2013; Zhang et al. 2016; Sutherland et al. 2019). In some cases, dark ROS production rivals that of photochemical production (Roe et al. 2016). Marine microbes in the photoic and aphotic zone alike are significant sources of the ROS superoxide, and therefore hydrogen peroxide. Dark, particle associated superoxide and hydrogen peroxide have been observed in both freshwater and seawater, and have been found to result directly from the presence of living cells (Roe et al. 2016; Zhang et al. 2016). Extracellular superoxide production can also persist after cell death in some cases (Schneider et al. 2016; Diaz et al. 2019).

The presence of ROS in sunlit and dark natural waters has far-reaching implications for dissolved oxygen in the environment. Intracellular ROS have been recognized for decades for their role as a significant global sink of oxygen (Mehler 1951; Guy et al. 1993; Bender et al. 1994). Mehler photoreduction of O_2 can exceed 40% of total electron flows in some cyanobacteria (Kana 1993; Helman 2005). The notion that extracellular ROS may also be an important sink in the global

oxygen cycle has recently been proposed, suggesting that ROS may mediate between 5 and 20 percent of net oxygen consumption in the marine biosphere (see Chapter 6). While these findings are consistent with available data, further review of the underlying assumptions of the production and fate of ROS is critical to better constraining the role of ROS in the global oxygen and carbon budgets.

In this study, we examine the production, fate, and abundance of dark superoxide and light and dark hydrogen peroxide in Sider's Pond, a meromictic brackish pond in Falmouth, MA (Vallino and Huber 2018). The pond transitions form oxic to sulfidic within several meters of the surface. This microcosm allows us to investigate how these ROS behave across both the photic to aphotic transition and a range of oxygen concentrations. While the internal dynamics of a single pond may not be directly transferable to ROS (photo)biogeochemistry in the global ocean, the insights gained from this study help to better constrain ROS dynamics in natural waters and the major environmental controls thereof.

7.2 Methods

Water samples were collected from Siders Pond in Falmouth, MA on September 23 and 25, 2019 using a peristaltic pump with black Norprene tubing (Cole-Palmer). Temperature, salinity, dissolved oxygen, and pH were measured using a YSI field sampling devise, which was calibrated immediately prior to both field sampling days. Photosynthetically active radiation (PAR) was also measured. At each sample depth, water was pumped through the tubing for several minutes (and several volumes of tubing) prior to collection. Following characterization of the vertical hydrography, four sample depths were chosen for in-depth ROS characterization from 1 to 4 meters depth. This includes two depths in the photic and aphotic zones, and oxygen concentrations ranging from 30 to 160 percent oxygen saturation.

Hydrogen peroxide concentrations were measured using the POHPPA (4-hydroxyphenylacetic acid) technique, as previously described elsewhere (Miller et al. 2005; Shaked and Armoza-Zvuloni 2013). In summary, horseradish peroxidase catalyzes the reaction between POHPPA reagent and hydrogen peroxide to form a fluorescent dimer. The POHPPA reagent was prepared with 0.25mM POHPPA reagent, 70 units mL^{-1} of horseradish peroxidase, and 0.25 M Tris buffer (pH 8.8). The reagent was added to water samples in a ratio of 1:50 (reagent:sample), and incubated in the dark amber vials for a minimum of 10 minutes before its

fluorescence spectrum was collected. Fluorescence was measured using a Molecular Devices SpectraMax M3 with excitation at 315 nm and emission at 408 nm. Standard curves were prepared each day by adding hydrogen peroxide (3% H_2O_2 w/w, Sigma) to filtered Sider's Pond water, and separate standard curves were prepared for photic and aphotic depths. Hydrogen peroxide stock solutions were quantified each day from UV absorbance at 240 nm before preparing standard curve solutions, typically ranging from 10 nM to 1 μM H_2O_2 (Shaked and Armoza-Zvuloni 2013). The blank was determined by measuring the fluorescence of Sider's Pond water with catalase (Sigma, 25 units mL^{-1}). It is important to note that this method cannot distinguish between hydrogen peroxide and organic peroxide present in the water column (Shaked and Armoza-Zvuloni 2013). In situ concentrations were measured by transferring sample water into amber vials containing pre-aliquoted POHPPA method reagents within minutes of sample collection. Samples were collected and measured in triplicate. The hydrogen peroxide concentrations collected in situ represent the combined influence of both dark and light production processes.

Hydrogen peroxide decay rates and decay branching ratio (i.e. fraction oxidized vs. fraction reduced) were determined by adding a 1 μM spike of ^{17}O labeled hydrogen peroxide. A concentration of 1 μM was chosen because it is close to the mid-day high concentration that was observed in this system (see Results). In short, we monitored the change in labeled peroxide over time and the evolution of isotope label into the dissolved oxygen pool, and used mass balance to constrain the total oxidative and reductive sinks of peroxide. The methods were used were very similar to those in Moffett and Zafiriou (1990), but with some modifications (Moffett and Zafiriou 1990). A solution of $H_2{}^{17}O_2$ (>90% ^{17}O, ICON Isotopes/Berry and Associates) was diluted with 3% H_2O_2 (Sigma) and ultrapure water. The spike was added to several liters of sample, homogenized, and aliquoted into many 125mL Wheaton serum vials, which were capped and crimped with no headspace and incubated in the dark for approximately 10 hours. Over the incubation period, duplicate bottles were sacrificed and sampled for the oxygen isotope composition of dissolved O_2. Dissolved oxygen was collected from the sample by adding a 5 mL headspace of ultra-high purity helium gas, and equilibrating by rapidly shaking the sample on an orbital shaker for at least 30 minutes. We found no significant difference in O_2 isotope composition or O_2:Ar ratio when samples were equilibrated for longer. The headspace gas was collected from the serum vial using a Hamilton Sample Lock syringe, and transferred to a He-flushed 2 mL serum vial. This over-pressurized mixture of He and sample gas was found to have high fidelity against

atmospheric contamination as no measurable change was observed in a labeled standard over the period of collection and analysis. The amount of label H_2O_2 remaining in solution at each timepoint was determined by adding 1 mL of $KMnO_4$ slurry (40 mg per mL) and acidifying the sample with 100 uL 6N HCl to oxidize all remaining H_2O_2 to O_2 gas (Moffett and Zafiriou 1990; Savarino and Thiemens 1999). The oxygen collected from permanganate treatment contains the combined label (now as O_2) from natural H_2O_2 oxidation and the unreacted H_2O_2. The amount of peroxide that was reduced to water (or other reductive pathways) was calculated by difference. No significant difference was observed between net and gross hydrogen peroxide decay, suggesting hydrogen peroxide production was negligible following sample collection.

The oxygen isotope composition and O_2:Ar were measured on an Isoprime100 isotope ratio mass spectrometer modified with a manual injection port as previously described (Sutherland et al. 2018). O_2:Ar ratios were used to determine the extent to which O_2 was consumed by dark cellular processes over the course of the incubation. $H_2{}^{17}O_2$ was chosen instead of $H_2{}^{18}O_2$ because hydrogen peroxide oxidation to O_2 does not break the oxygen-oxygen bond in peroxide. The resulting ^{17}O-^{17}O molecule can be analyzed in the same manner that traditional ^{18}O measurements are collected (as mass 34). The 1 μM spike of $H_2{}^{17}O_2$ was prepared such that the mass 34 contribution to the O_2 pool would be sufficiently high to resolve peroxide decay on the percent level. Specifically, the $^{34}O_2$:$^{32}O_2$ of the spike was ~0.15, which, when completely oxidized to the O_2 pool (~1 in 300 dilution for water in equilibrium with atmosphere) produced a $\delta^{18}O$ equivalent of >100 permil. The isotope label was quantified by adding 1 μM of $H_2{}^{17}O_2$ to 18.2 MΩ cm water that had equilibrated with atmosphere for several days at a known temperature in duplicate. Duplicate bottles containing 1 μM of $H_2{}^{17}O_2$ and ultrapure water were treated in the same manner as incubation samples (i.e. one set analyzed for natural decay, one set treated with permanganate to determine the remaining label). No peroxide decay was observed in the ultra-pure water, and duplicate bottles of permanganate-treated labeled reproduced to within 1 percent of the magnitude of the label. Typical reproducibility of $\delta^{18}O$ of standard lab air was <0.1 permil, and typical reproducibility of bio-replicates in this study (reported as $\delta^{18}O$ equivalent) was <0.3 permil. All references to isotopically labeled hydrogen peroxide and its decay products will henceforth be denoted with an asterisk (e.g. H_2O_2*, O_2*). We report H_2O_2* oxidation and reduction as a fraction of the total spike since the dissolved oxygen reservoir, and therefore the magnitude of the label, varies at each sample depth.

Superoxide concentrations were collected using a chemiluminescent flow reactor (FeLume, Waterville Analytical) as previously described with some slight modification (Diaz et al. 2013; Roe et al. 2016; Sutherland et al. 2019). The FeLume system is designed to measure chemiluminescence which results from the mixture of a superoxide-containing sample and the superoxide-specific chemiluminescent probe methyl *Cypridina* luciferin analog (MCLA, TCI America) (Rose et al. 2008a). This instrument uses two fluid lines (sample and MCLA), which are flushed through the system at an identical flow rate using a peristaltic pump until they converge in a spiral flow cell immediately adjacent to a photomultiplier tube. The spiral flow cell and photomultiplier tube are housed within an opaque box to eliminate any incidental ambient light. The samples were pumped into the FeLume for several minutes until a stable signal was observed. After the signal stabilized, 2 U mL^{-1} superoxide dismutase (SOD; Superoxide Dismutase from bovine erythrocytes ≥ 3,000 U mg^{-1}, Sigma, stock prepared in DI water to 4,000 U mL^{-1}) was added to the sample, which typically caused a significant drop in the baseline. The same sample was then filtered with a sterile 0.22 μm membrane filter to remove cells and particles and aged for 24 hours with 75 μM diethylene-triaminepentaacetic acid (DTPA, Sigma >99%) to complex any metals in the sample. The aged, filtered sample was then run in the same manner above to determine the blank for MCLA in each sample matrix. This signal was subtracted from the unfiltered sample signal. Superoxide concentrations were measured more than 30 minutes after sample collection. The typical half-life of superoxide in natural water is 1-2 minutes, meaning the concentrations that were measured are the result of dark superoxide production processes.

Superoxide decay rate constants were determined by observing the change in chemiluminescent signal over time of a superoxide addition in the form of potassium dioxide (KO_2, ACROS Organics, superoxide content > 215cc/g). Potassium dioxide solutions were prepared in NaOH (pH = 12.5) amended with 90 μM DTPA in order to sequester trace contaminants that would otherwise significantly reduce the lifetime of superoxide. Superoxide concentrations in primary standards were quantified by measuring the difference in absorbance at 240 nm before and after the addition of 2 U mL^{-1} superoxide dismutase and then converting to molar units based on the molar absorptivity of superoxide corrected for the absorption of hydrogen peroxide formed during decay at the same wavelength (Bielski et al. 1985). Daily calibration curves were generated from three paired observations of time-zero superoxide concentration (dependent variable) and extrapolated chemiluminescence (independent variable) using linear regression. Because

chemiluminescence values were baseline-corrected, regression lines were forced through the origin. Calibrations yielded highly linear curves (typically $R^2 > 0.9$), with a typical sensitivity of 1 chemiluminescence unit per pM superoxide. The detection limit for superoxide concentration was taken as three times the standard deviation of a stabile signal measured in aged, filtered water was from Sider's pond, which was determined to be approximately 100 pM.

7.3 Results

Temperature, pH, salinity, and dissolved oxygen profiles are presented in Figure 1. Temperature ranged from 21 ºC at the surface to 15 ºC at 10 meters. The pH maximum was 7.3 at 2 meters depth, and the pH minimum was 6.5 at 5.5 meters depth. Salinity increased with depth, ranging from 3.6 ppt in the surface to 15.0 ppt at depth. The photic zone extended from the surface to approximately 2.8 meters, where PAR reached one percent of the surface level. Dissolved oxygen concentrations varied from 395 μM in the surface, 434 μM at the oxygen maximum, and below detection (<15 μM) below 6.5 meters.

Hydrogen peroxide concentrations in the water column ranged from 900 nM in the surface to 110 nM at 10 meters depth (Figure 2). Hydrogen peroxide concentrations decreased with increasing depth in the photic zone, and ranged between 100 and 400 nM in the aphotic zone. Dark superoxide concentrations range from 450 pM in water collected from surface waters to below detection (<100 pM) in both aphotic zone samples. Superoxide pseudo first order decay constants were highest in the surface (0.021 s^{-1}) and lowest just beneath the photic zone transition (0.0055 s^{-1}). There was no difference between net and gross hydrogen peroxide decay within the precision of the POHPPA method, we therefore report and discuss hydrogen peroxide decay rate constants measured using H_2O_2*. Additions of H_2O_2* revealed that dark peroxide decay was highest in the surface waters (k = 1.53 hr^{-1}) and slowest at 4 meters (k = 0.34 hr^{-1}). The 1 μM of H_2O_2* was completely consumed over the 10-hour at all depths except 4 meters (of which only 3% H_2O_2* remained). The fraction of H_2O_2* that decayed through oxidative pathways (relative to total decay) was highest at 2 m (46 percent oxidized) and lowest at 4 meters (39 percent oxidized) (Figure 3). In some cases, the fraction of H_2O_2* that decayed through oxidation was more or less consistent at each time step (e.g. 3 meters), in other cases, oxidation appeared to occur more quickly than reduction (e.g. 4 meters).

7.4 Discussion

Hydrogen peroxide is present at concentrations between 100 to 900 nM in the top 10 meters of Sider's pond, with the highest concentrations present in the sunlit surface waters, and the lowest concentrations found in the oxygen poor, sulfidic bottom waters. While light dependent processes likely account for most ROS production in the sunlit surface waters (Petasne and Zika 1987; Cooper et al. 1988; Zhang et al. 2012), dark, microbially-mediated processes may also contribute to ROS in natural waters. The persistence of ROS beneath the oxic surface waters suggests abundant light-independent production of ROS. Dark, particle associated hydrogen peroxide and superoxide production have been observed in a wide variety of settings, including the oligotrophic ocean, a brackish pond, and a freshwater pond (Palenik and Morel 1988; Roe et al. 2016; Zhang et al. 2016). In some cases of oligotrophic waters dark, particle associated ROS production matches that of photoproduction (Roe et al. 2016). The notable difference in this case is that Sider's pond can exceed 2.5 mM dissolved sulfide (Vallino and Huber 2018). One potential pathway of ROS production under these conditions is through sulfide oxidation (Tapley et al. 1999; Murphy et al. 2016).

Hydrogen peroxide decay is exceptionally rapid in Sider's pond. If we assume that dark hydrogen peroxide decay rates are representative of decay rates in the sunlight, the steady state hydrogen peroxide production rates range from 82 nM hr^{-1} in the aphotic zone to 1130 nM hr^{-1} in the photic zone. Light can inhibit biological degradation of hydrogen peroxide (Zepp et al. 1987), so the calculated production rates in the photic zone should be considered an upper bound rather than an exact figure in the two photic sampling depths. In comparison, hydrogen peroxide production and decay rates in seawater range from <1 nM hr^{-1} in the dark to >10 nM hr^{-1} in sunlit waters (Moffett and Zafiriou 1990; Avery Jr et al. 2005; Powers et al. 2015). The rates observed in Sider's pond are much more similar to production rates observed in irradiation experiments in the presence of humic substances (Zhang et al. 2012), which is not surprising considering the terrestrial organic carbon inputs likely present at this particular pond.

Dark superoxide production yielded superoxide concentrations ranging from below detection (<100 pM in this case) to approximately 450 pM. Given that we analyzed samples for superoxide concentrations after >10 half-lives of superoxide under these conditions, we can approximate production by assuming dark extracellular superoxide concentrations have reached steady state. Steady state superoxide production rates range from <0.5 pM s^{-1} to 9.3 pM s^{-1}. Dark

superoxide production therefore accounts 2-7 percent of total hydrogen peroxide (light and dark processes) generated in the photic zone, and <1 percent of hydrogen peroxide generated in the aphotic zones. While we cannot rule out some physiological change occurring in the hours between sample collection and analysis, the >2 order of magnitude difference in the steady state production of hydrogen peroxide relative to superoxide hint at abundant dark hydrogen peroxide production that is independent of a superoxide pathway. Such a pathway would be an even greater oxygen sink in aqueous environments than superoxide-dependent peroxide production because superoxide is commonly degraded through dismutation pathways that yields half a mole of oxygen per mole of superoxide.

In sunlit seawater, superoxide production has been observed to exceed hydrogen peroxide production by a factor of 2-10 (Petasne and Zika 1987; Goldstone and Voelker 2000; Powers and Miller 2015; Powers et al. 2015). When the production ratio of superoxide relative to that of hydrogen peroxide (P_{O2-}:P_{H2O2}) is ~2, superoxide dismutation is implicated. However, when P_{O2-}:P_{H2O2} exceeds 2, alternative sinks of superoxide must be invoked. Some studies have assumed that such a production ratio implies an oxidative sink of superoxide (back to O_2) (Petasne and Zika 1987; Powers and Miller 2015; Powers et al. 2015), however one study that measured hydrogen peroxide production and dissolved oxygen loss during DOM irradiation experiments showed that hydrogen peroxide production only accounts for about half of dissolved oxygen loss (Andrews et al. 2000). The bounds of P_{O2-}:P_{H2O2} appear to be different entirely for dark, microbially-mediated processes. Incubations of water from a brackish pond, a freshwater pond, and an oligotrophic monitoring station, demonstrating that P_{O2-}:P_{H2O2} can be much greater than 1 or much less than 1 (Roe et al. 2016; Zhang et al. 2016). In these studies, there is no apparent correlation between superoxide and hydrogen peroxide production. Addition of superoxide dismutase did not significantly alter hydrogen peroxide production (Zhang et al. 2016), suggesting that dismutation was already the dominant superoxide decay pathway. Indeed, it appears that hydrogen peroxide production independent of superoxide production is present in dark natural waters.

Hydrogen peroxide decay in natural waters is primary mediated by microbial processes (Zepp et al. 1987; Cooper and Zepp 1990; Moffett and Zafiriou 1990). There are two primary pathways by which microbes degrade hydrogen peroxide: catalases and peroxidases.

$$2H_2O_2 \longrightarrow 2H_2O + O_2 \qquad \text{(Eq. 1; catalase } H_2O_2 \text{ decay)}$$

$$H_2O_2 + AH_2 \longrightarrow 2H_2O + A$$ (Eq. 2; peroxidase H_2O_2 decay)

While both processes yield a net loss of hydrogen peroxide, the relative activities of catalase and peroxidase will determine the net loss of dissolved oxygen in an environment. Using the reaction stoichiometries in equations 1 and 2, we determine that catalase-like decay accounts for 78-92% of peroxide decay, and the remaining 8-22% resulting from peroxidases and peroxidase-like stoichiometry. The two sample depths in the photic zone saw more peroxide degrade through oxidative loss (catalase-like) than the two sample depths in the aphotic zones (88-92 percent in the photic zone vs. 78-80 in the aphotic zone). In comparison, hydrogen peroxide decay in productive surface ocean water has been shown to degrade through 65-80% catalase activity and 20-35% peroxidase activity (Moffett and Zafiriou 1990). In Sider's Pond, one mole of H_2O_2 produced yields a net loss of ~0.55 moles of O_2 in the photic zone and ~0.6 moles of O_2 in the aphotic zone.

One notable feature of Figure 3 is that that the relative proportions of oxidative and reductive loss of hydrogen peroxide appears to be somewhat temporally variable over of the course of this incubation. At 4 meters depth, the amount of H_2O_2 oxidation between T0 and T1 appears to exceed the theoretical stoichiometry of catalase-mediated peroxide decay (Ox:Red of ~4:1 observed versus 2:1 from Eq.1). In subsequent time points, there is a significant increase in H_2O_2* reduction without much increase in O_2* in the dissolved oxygen pool. Purely oxidative elimination of hydrogen peroxide is not among biologically mediated pathways, suggesting that abiotic factors may contribute to peroxide oxidation. Oxidative loss of hydrogen peroxide is observed in the presence of light, but photooxidation of hydrogen peroxide is much slower than biological degradation (Moffett and Zafiriou 1990). Dissolved Mn(III) and particulate Mn(III/IV) oxide are possible oxidants of peroxide (Learman et al. 2013). Reaction kinetics of hydrogen peroxide and the mineral pyrolusite would suggest that H_2O_2* oxidization by Mn oxides would be rapid, potentially exhausting the supply oxidant in the first time interval (Do et al. 2009). Mn-redox cycling may be heavily influenced by photo-reduction in the surface waters followed by (a)biotic oxidation elsewhere in the oxic surface waters (Marafatto et al. 2015).

Altogether, these results highlight the complex nature of ROS production and decay across the range of environmental conditions observed in the top several meters of a stratified pond. While these results are important for understanding ROS in marine environments, the elevated levels of

dissolved organic carbon, the more aromatic nature of organic carbon in waters with terrestrial influence, and the elevated metal content all influence ROS cycling in ways that are fundamentally different from the marine environment. The high levels of hydrogen peroxide observed in the aphotic zone were not sustained in the lab, suggesting dark hydrogen peroxide production may still result from dynamic links between the surface or deep waters such as particle flux sustained redox gradients resulting from photochemistry.

7.5 Summary and Conclusion

Superoxide and hydrogen peroxide concentrations and decay kinetics reveal rapid ROS cycling across the photic-aphotic transition and along a steep oxygen gradient of a stratified pond. We found that dark superoxide production accounts for just a small percentage of combined light and dark hydrogen peroxide production in sunlit and aphotic depths. The fate of hydrogen peroxide was divided between oxidation and reduction, with 44-46 percent decomposing through oxidative pathways in waters from photic zone, and 39 percent decomposing through oxidative pathways in aphotic waters. The remaining majority of hydrogen peroxide was degraded through reduction, and is therefore a net sink of dissolved oxygen. Although the setting of this study may not have broad implications for the marine environment, this study highlights some important areas of ROS cycling that require further attention to better constrain the flux and impact of ROS on dissolved oxygen and other redox-active species in the environment. There are some instances in which superoxide and hydrogen peroxide appear to be tightly coupled and others where they appear to be decoupled entirely. Future work should investigate whether the apparent decoupling of superoxide and hydrogen peroxide is a result of environmental factors (i.e. factors that affect the relative amount of superoxide oxidation and reduction), or if a significant fraction of hydrogen peroxide production may result from superoxide-independent pathways.

Figures

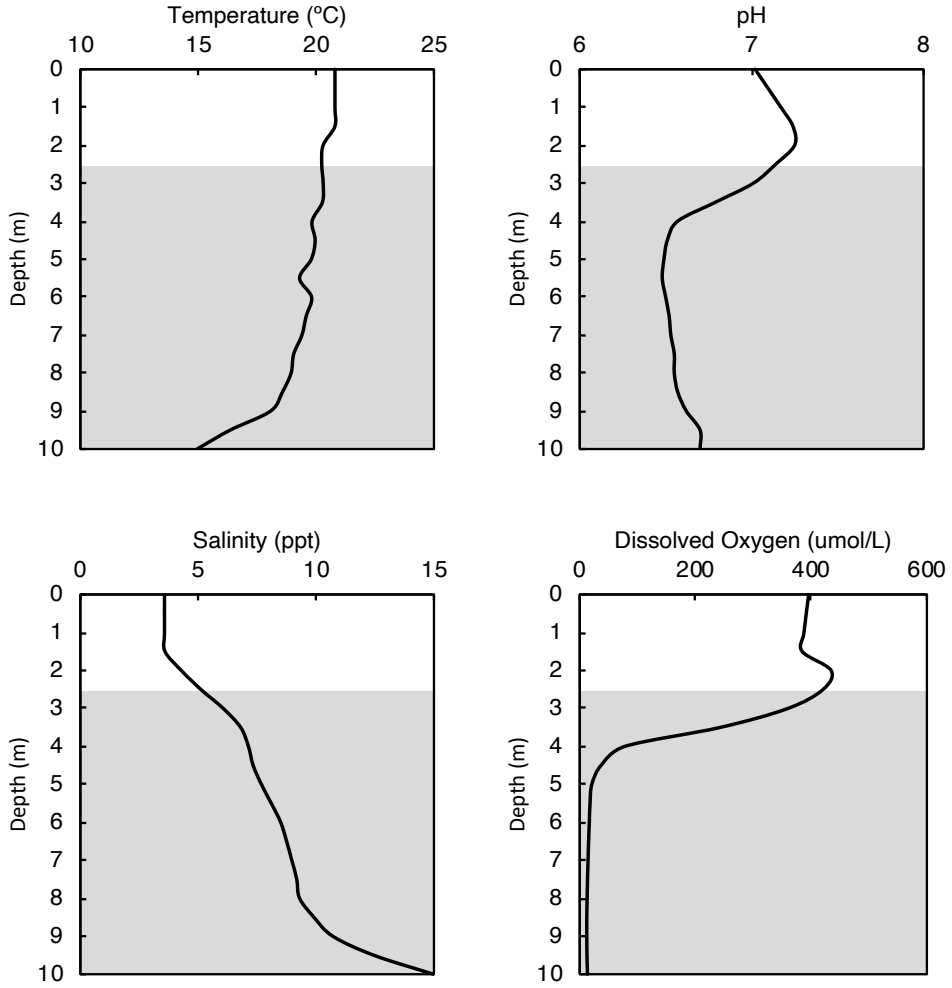

Figure 1- Temperature, pH, salinity, and dissolved oxygen of Sider's Pond at the time of sampling. Gray shaded region represents the aphotic zone (<1% surface PAR).

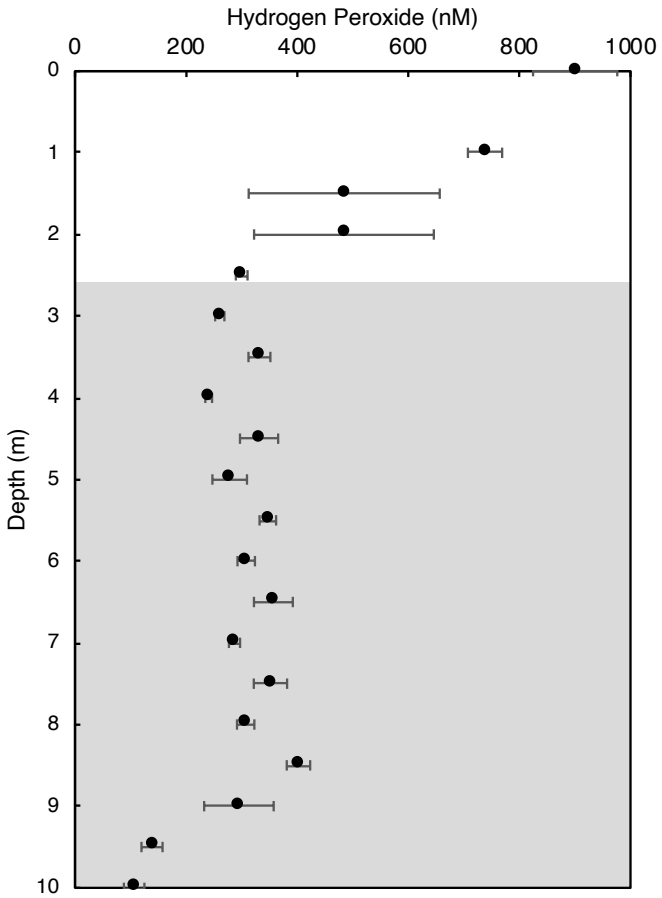

Figure 2- Hydrogen peroxide depth profile measured at Sider's Pond during midday light.

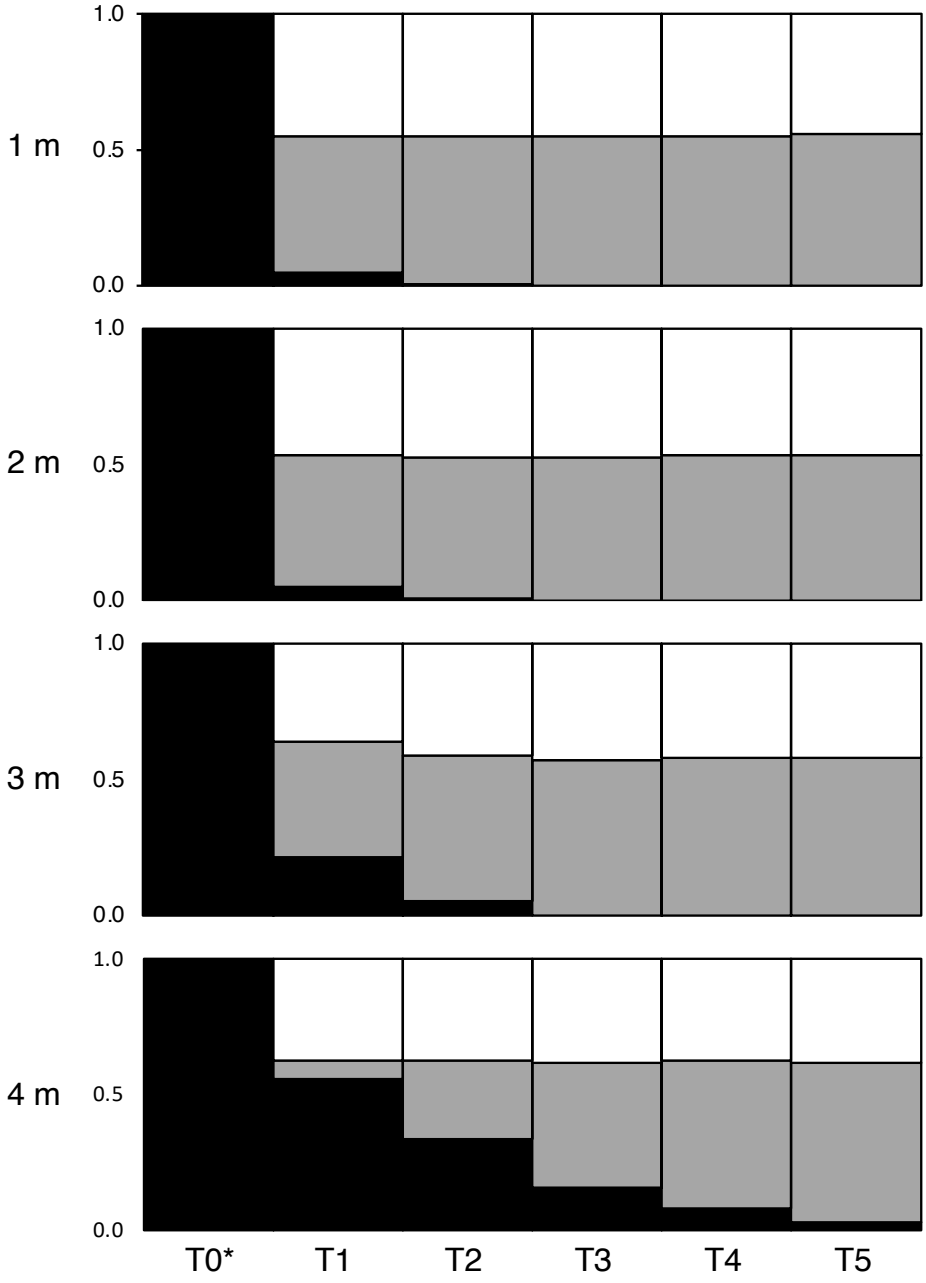

Figure 3- Fate of H_2O_2* in 10 hour dark incubations of Sider's Pond water from four depths from 1 to 4 meters. Black area represents fraction of unreacted H_2O_2* remaining, white area represents H_2O_2* that was oxidized to O_2*, gray area represents H_2O_2* that is reduced (see Methods). T0-T5 are approximately 2-hour intervals throughout the 10-hour incubation. T0* is inferred from amount of H_2O_2* added because decay was too rapid to explicitly measure starting H_2O_2*.

Tables

Table 1-Summary of measured Superoxide and Hydrogen peroxide

Sample Depth (m)	1	2	3	4
Superoxide concentration (pM)	450 ± 130	140 ± 70	<100	<100
Superoxide pseudo first order decay rate constant (s^{-1})	0.021 ± 0.006	0.015 ± 0.006	0.005 ± 0.004	0.007 ± 0.003
Superoxide dark steady state production rate (pM s^{-1})	9.3	2.0	<0.5	<0.7
Hydrogen peroxide concentration in sunlight (nM)	740 ± 90	480 ± 60	260 ± 210	240 ± 100
Hydrogen peroxide decay rate constant (hr^{-1})	-1.53	-1.52	-1.00	-0.34
Hydrogen peroxide sead state production rate (nM hr^{-1})	1130	740	260	80

References

Andrews, S. S., S. Caron, and O. C. Zafiriou. 2000. Photochemical oxygen consumption in marine waters : A major sink for colored dissolved organic matter ? **45**: 267–277.

Avery Jr, G. B., W. J. Cooper, R. J. Kieber, and J. D. Willey. 2005. Hydrogen peroxide at the Bermuda Atlantic Time Series Station: temporal variability of seawater hydrogen peroxide. Mar. Chem. **97**: 236–244.

Bender, M., T. Sowers, and L. Labeyrie. 1994. The Dole Effect and its Variations During the Last 130,000 Years as Measured in the Vostok Ice Core. Global Biogeochem. Cycles **8**: 363–376. doi:10.1029/94gb00724

Bielski, B. H. J., D. E. Cabelli, R. L. Arudi, and A. B. Ross. 1985. Reactivity of HO2/O−2Radicals in Aqueous Solution. J. Phys. Chem. Ref. Data **14**: 1041–1100. doi:10.1063/1.555739

Cooper, W. J., and R. G. Zepp. 1990. Hydrogen peroxide decay in waters with suspended soils: evidence for biologically mediated processes. Can. J. Fish. Aquat. Sci. **47**: 888–893.

Cooper, W. J., R. G. Zika, R. G. Petasne, and J. M. C. Plane. 1988. Photochemical formation of hydrogen peroxide in natural waters exposed to sunlight. Environ. Sci. Technol. **22**: 1156–1160.

Diaz, J. M., C. M. Hansel, B. M. Voelker, C. M. Mendes, P. F. Andeer, and T. Zhang. 2013. Widespread Production of Extracellular Superoxide by Heterotrophic Bacteria. Science (80-.). **340**: 1223–1226. doi:10.1126/science.1237331

Diaz, J. M., S. Plummer, C. M. Hansel, P. F. Andeer, M. A. Saito, and M. R. Mcilvin. 2019. NADPH-dependent extracellular superoxide production is vital to photophysiology in the marine diatom Thalassiosira oceanica. **116**. doi:10.1073/pnas.1821233116

Do, S.-H., B. Batchelor, H.-K. Lee, and S.-H. Kong. 2009. Hydrogen peroxide decomposition on manganese oxide (pyrolusite): kinetics, intermediates, and mechanism. Chemosphere **75**: 8–12.

Goldstone, J. V, and B. M. Voelker. 2000. Chemistry of Superoxide Radical in Seawater : CDOM Associated Sink of Superoxide in Coastal Waters. **34**: 1043–1048. doi:10.1021/es9905445

Guy, R. D., M. L. Fogel, and J. A. Berry. 1993. Photosynthetic Fractionation of the Stable Isotopes of Oxygen and Carbon. Plant Physiol. **101**: 37–47. doi:10.1104/pp.101.1.37

Helman, Y. 2005. Fractionation of the Three Stable Oxygen Isotopes by Oxygen-Producing and Oxygen-Consuming Reactions in Photosynthetic Organisms. Plant Physiol. **138**: 2292–2298. doi:10.1104/pp.105.063768

Kana, T. M. 1993. Rapid oxygen cycling in Trichodesmium thiebautii. Limnol. Oceanogr. **38**: 18–24.

Learman, D. R., B. M. Voelker, A. S. Madden, and C. M. Hansel. 2013. Constraints on superoxide mediated formation of manganese oxides. Front. Microbiol. **4**: 11. doi:10.3389/fmicb.2013.00262

Marafatto, F. F., M. L. Strader, J. Gonzalez-Holguera, A. Schwartzberg, B. Gilbert, and J. Peña. 2015. Rate and mechanism of the photoreduction of birnessite (MnO2) nanosheets. Proc. Natl. Acad. Sci. **112**: 4600–4605.

Mehler, A. H. 1951. Studies on reactions of illuminated chloroplasts: I. Mechanism of the reduction of oxygen and other hill reagents. Arch. Biochem. Biophys. **33**: 65–77.

Miller, G. W., C. A. Morgan, D. J. Kieber, D. W. King, J. A. Snow, B. G. Heikes, K. Mopper, and J. J. Kiddle. 2005. Hydrogen peroxide method intercomparision study in seawater. Mar. Chem. **97**: 4–13.

Moffett, J. W., and O. C. Zafiriou. 1990. An investigation ofhydrogen peroxide chemistry in surface waters of Vineyard Sound with H218O2 and 18O2. Limnol. Oceanogr. **35**: 1221–1229.

Murphy, S. A., S. Meng, B. M. Solomon, D. Dias, T. J. Shaw, and J. L. Ferry. 2016. Hydrous ferric oxides in sediment catalyze formation of reactive oxygen species during sulfide oxidation. Front. Mar. Sci. **3**: 227.

Palenik, B., and F. M. M. Morel. 1988. Dark production of H2O2 in the Sargasso Sea. Limnol. Oceanogr. **33**: 1606–1611.

Petasne, R. G., and R. G. Zika. 1987. Fate of superoxide in coastal sea water. Nature **325**: 516–518. doi:10.1038/325516a0

Powers, L. C., L. C. Babcock-adams, J. K. Enright, and W. L. Miller. 2015. Probing the photochemical reactivity of deep ocean refractory carbon (DORC): Lessons from hydrogen peroxide and superoxide kinetics. Mar. Chem. **177**: 306–317. doi:10.1016/j.marchem.2015.06.005

Powers, L. C., and W. L. Miller. 2015. Hydrogen peroxide and superoxide photoproduction in diverse marine waters: A simple proxy for estimating direct CO2 photochemical fluxes. 7696–7704. doi:10.1002/2015GL065669.Received

Roe, K. L., R. J. Schneider, C. M. Hansel, and B. M. Voelker. 2016. Measurement of dark, particle-generated superoxide and hydrogen peroxide production and decay in the subtropical and temperate North Pacific Ocean. Deep. Res. Part I-Oceanographic Res. Pap. **107**: 59–69. doi:10.1016/j.dsr.2015.10.012

Rose, A. L., J. W. Moffett, and T. D. Waite. 2008a. Determination of superoxide in seawater using 2-methyl-6-(4-methoxyphenyl)- 3,7-dihydroimidazo[1,2-a]pyrazin-3(7H)-one chemiluminescence. Anal. Chem. **80**: 1215–1227. doi:10.1021/ac7018975

Rose, A. L., E. A. Webb, T. D. Waite, and J. W. Moffett. 2008b. Measurement and implications of nonphotochemically generated superoxide in the equatorial Pacific Ocean. Environ. Sci. Technol. **42**: 2387–2393. doi:10.1021/es7024609

Savarino, J., and M. H. Thiemens. 1999. Analytical procedure to determine both $δ$18O and $δ$17O of H2O2 in natural water and first measurements. Atmos. Environ. **33**: 3683–3690.

Schneider, R. J., K. L. Roe, C. M. Hansel, and B. M. Voelker. 2016. Species-Level Variability in Extracellular Production Rates of Reactive Oxygen Species by Diatoms. Front. Chem. **4**. doi:10.3389/fchem.2016.00005

Shaked, Y., and R. Armoza-Zvuloni. 2013. Dynamics of hydrogen peroxide in a coral reef: sources and sinks. J. Geophys. Res. Biogeosciences **118**: 1793–1801.

Sutherland, K. M., A. Coe, R. J. Gast, and others. 2019. Extracellular superoxide production by

key microbes in the global ocean. Limnol. Oceanogr.

Sutherland, K. M., S. D. Wankel, and C. M. Hansel. 2018. Oxygen isotope analysis of bacterial and fungal manganese oxidation. Geobiology. doi:10.1111/gbi.12288

Tapley, D. W., G. R. Buettner, and J. M. Shick. 1999. Free radicals and chemiluminescence as products of the spontaneous oxidation of sulfide in seawater, and their biological implications. Biol. Bull. **196**: 52–56.

Vallino, J. J., and J. A. Huber. 2018. Using Maximum Entropy Production to Describe Microbial Biogeochemistry Over Time and Space in a Meromictic Pond. Front. Environ. Sci. **6**: 100. doi:10.3389/fenvs.2018.00100

Wuttig, K., M. I. Heller, and P. L. Croot. 2013. Pathways of Superoxide (O-2(-)) Decay in the Eastern Tropical North Atlantic. Environ. Sci. Technol. **47**: 10249–10256. doi:10.1021/es401658t

Zepp, R. G., Y. I. Skurlatov, and J. T. Pierce. 1987. Algal-induced decay and formation of hydrogen peroxide in water: its possible role in oxidation of anilines by algae, p. 215–224. *In* Photochemistry of environmental aquatic systems. ACS Publications.

Zhang, T., C. M. Hansel, B. M. Voelker, and C. H. Lamborg. 2016. Extensive Dark Biological Production of Reactive Oxygen Species in Brackish and Freshwater Ponds. Environ. Sci. Technol. **50**: 2983–2993. doi:10.1021/acs.est.5b03906

Zhang, Y., R. Del Vecchio, and N. V Blough. 2012. Investigating the mechanism of hydrogen peroxide photoproduction by humic substances. Environ. Sci. Technol. **46**: 11836–11843.

8. Conclusion

This thesis outlines our investigation of two major facets of the oxygen cycle: the isotopic record of dioxygen in marine ferromanganese crusts and significant reductive flux of oxygen that results from extracellular superoxide production. While the experiments conducted and the results described in the preceding chapters shed light on these two major topics in the marine oxygen cycle, they also underscore the complexity and significant challenges that still exist in understanding the nature and fate of oxygen in the global ocean. From here we will highlight major findings of the preceding chapters, followed by a discussion of the research avenues that could address many of the outstanding questions that remain following this work.

In Chapter 2, we demonstrated that manganese oxide minerals produced by bacteria, fungi, and abiotic oxidation pathways derive approximately half of their oxygen atoms from O_2. This means that information stored within the isotopic signature of O_2 molecules (e.g. the Dole Effect, combined effect of atmospheric chemistry and biological fluxes on the triple oxygen isotope signature, oxygen saturation state in ocean water mass) is retained by manganese oxide minerals provided no significant exchange or diagenesis has occurred. Since about ~50 percent of the oxygen atoms in synthetic oxides are derived from O_2, we expect that the magnitude of this signal in pure Mn oxides would be muted by the same proportion. This signal would be more muted still for instances where Mn oxides form alongside other oxide minerals. Since the scope of this study is limited to lab-based synthesis methods, we turned next to natural Mn oxide deposits to determine if our findings are consistent with the natural environment.

In Chapter 3, we conducted an in-depth chemical, mineralogical, and redox analysis of one of Earth's most abundant and widespread deposits of Mn oxide minerals: ferromanganese crusts. Ferromanganese crusts cover vast regions of the world's major ocean basins. Since crusts, as opposed to nodules, form as layered deposits in direct contact with the water column, they offer a controlled view of oxygen in the oceans. Our study revealed a great deal of geochemical complexity in ferromanganese crusts, including complex two-dimensional element distributions, changes in Mn mineralogy with increasing depth in the crust, and an increase in Mn oxidation state with depth in the crust.

The convergence of multiple complex processes that influence the properties of ferromanganese crusts over time no doubt presents a challenge to accessing the oxygen isotope record contained within its Mn oxides. We still need a tool, however, to determine if the signal

housed within the Mn-endmember of ferromanganese crusts does capture the signature of O_2. In Chapter 4, we measured the triple oxygen isotope signature of ferromanganese crusts from throughout the global ocean. Guided by the findings from Chapter 3, we chose sections of these ferromanganese crusts that are likely unaltered, and we demonstrate that ferromanganese crust oxygen isotope signatures are consistent with incorporation of dissolved oxygen. We also demonstrate that this signal is present several centimeters into the crust, demonstrating that the dissolved oxygen signal present in the crust persists as long as approximately 30 million years old.

In the latter half of this thesis, we zoom in on one aspect of the oxygen cycle that has not been considered in global biogeochemical cycling of oxygen: extracellular superoxide production. In Chapter 5, we survey some of the ocean's most abundant and ecologically significant phototrophs and heterotrophs for extracellular superoxide production. We found that all of these organisms produce extracellular superoxide in measurable quantities, with phototrophs producing the most extracellular superoxide. Additionally, we found that local cell abundances play an important role in determining cell-specific extracellular superoxide production rates.

In Chapter 6, we compile extracellular superoxide production rates from Chapter 5 and published literature to determine what weight this system has on the global oxygen cycle. We estimate that the gross global superoxide flux is an oxygen sink approximately one third the size of gross oxygen production. We determine as much as half of extracellular superoxide may ultimately be reduced to water, thus playing a substantial role in the global O_2 cycle. We validate our estimate by demonstrating close agreement between expected superoxide concentrations and measured superoxide concentrations presented in the scientific literature. Further, we measured a depth profile of dark, steady state superoxide concentration at an oligotrophic monitoring station that is similarly consistent with our estimate.

Lastly, we take a look at one of the underlying assumptions we used in Chapter 6: the fate of hydrogen peroxide. In Chapter 7, we used isotope-labeling techniques to trace the fate of hydrogen peroxide in a stratified pond and compared the fate of hydrogen peroxide across a photic-aphotic transition, and down to <30% dissolved oxygen saturation. We found that this range of environmental conditions exhibited significant influence on the rate of hydrogen peroxide degradation, but only a minor influence on the ultimate fate of hydrogen peroxide. The amount of hydrogen peroxide that was oxidized back to O_2 range from 39-46 percent across a photic to aphotic transition, and across a significant oxygen concentration gradient.

The isotope systematics of Mn oxides that we demonstrate in the first half of this thesis outline the necessary tools for a more detailed view of oxygen during the Cenozoic than is currently accessible through other means. Indeed, Mn oxides show considerable promise for their ability to retain local oxygen isotope composition, but Mn oxides are rarely found in pure phases under surface earth conditions. While our original goal in embarking on this project was to be able to access and interpret this record, we found the compositional complexity of ferromanganese crust a tremendous challenge in doing so. Future work investigating the oxygen isotope systematics of Mn-bearing oxide co-precipitates (e.g. Fe- and Mn-oxide mixtures) could prove valuable in potentially unlocking the isotopic record of ferromanganese crusts. Similarly, we highlighted the mineralogical variability contained within a single ferromanganese crust. Future work should also focus on mineralogy as a source of oxygen isotope fractionation during Mn oxidation.

One finding that came out of our analysis of the results in Chapter 4 was that bulk Mn concentration in ferromanganese crust tops has a negative correlation with modern dissolved oxygen concentration ($R^2>0.7$). The observation that high Mn concentration tends to be found in waters with low O_2 is not a new one (Hein and Koschinsky 2014), however, the relatively tight correlation across extreme changes in dissolved oxygen suggests that this simple tool may be able to reconstruct dissolved oxygen concentration. This could provide extremely valuable context to the ferromanganese crust oxygen isotope signal and serve as an internal calibration/validation of that signal. Clearly a more rigorous treatment of this finding is warranted. Similarly, development of a mechanistic understanding of the underlying processes is needed to determine when and how such a tool may be applied.

Our measurements and observations of the magnitude of superoxide production in the global ocean raise many questions that point to important next steps in validating and accommodating these new findings in global cycles of oxygen and carbon. Firstly, our understanding of electron flows in photosynthetic microorganisms that fix carbon in the Earth's oceans is lacking. Previous studies have shown that >40% of electron flows result in non-respiratory O_2 reduction in cyanobacteria (Kana 1993; Helman 2005). While most studies have attributed this photosynthetic oxygen loss to Mehler processes, one recent study investigating extracellular superoxide production in a diatom could implicate extracellular superoxide production as one of several tools, along with the Mehler reaction, for managing intracellular redox conditions (Diaz et al. 2019). In this study, visible light enhanced extracellular superoxide

production several-fold in a diatom culture. Light dependent extracellular superoxide production and Mehler photoreduction will likely be indistinguishable in a range of experimental designs. Future experiments investigating either of these pathways should be mindful of their impact on one another. Another obstacle to collecting these measurements is that only a small number of operative enzymes that produce extracellular superoxide have been isolated or identified. Identification of trans-membrane, outer membrane, and extracellular superoxide-producing enzymes would provide valuable insight into the underlying environmental or physiological conditions under which cells produce extracellular superoxide (and how much).

Although extracellular superoxide production and degradation will certainty have a significant impact on organic carbon oxidation, primary production techniques that use carbon tracers (e.g. ^{14}C) will not be able to distinguish between these various non-respiratory pathways. Triple oxygen isotope measurements of superoxide producing and consuming reactions are a clear next step in determining the impact and scale of superoxide production on the environment and our measurement of primary productivity. Gross and net primary productivity measurements rely on an endmember mixing model in which deviation from a canonical respiration line is interpreted as photosynthetic input (Nicholson et al. 2012). An issue here is that this model assumes all oxygen loss terms behave isotopically similar to respiration. One study has shown that Mehler-realted losses have a triple oxygen isotope relationship that is entirely distinct from aerobic respiration (Helman 2005). Even small uncertainty in the modeled triple-oxygen relationship of oxygen loss terms yields tremendous uncertainty in corresponding GPP estimates (Ash et al. 2019). Targeted triple oxygen measurements of O_2 under the influence of extracellular superoxide production would be extremely valuable for determining how much this reaction occurs in nature, where in the water column it is most impactful on oxygen cycling, and what weight it might have of our understanding of gross and net primary productivity.

Taking this idea one step further, triple oxygen isotope signatures of oxygen producing and consuming reactions may not be unique. In other words, the oxygen isotope signature may be the result of a single reaction, or a combination of two or more reactions. Thus, a more thorough fingerprinting of these various oxygen consuming reactions may still be insufficient for modeling dissolved oxygen. Indeed, many oxygen consuming reactions have similar mass relationships and can produce a non-unique interpretation of environmental processes (Angert et al. 2003). Improvements in mass spectrometer technology and now allowing sufficient mass resolution to

measure not only three-oxygen isotopes, but oxygen isotopologues including mass-35 and mass-36 (Yeung et al. 2015). The specific bond-ordering of oxygen atoms in molecular oxygen, particularly in closed systems like the ocean water column, may offer further insight into the leverage each oxygen-consuming reaction has in the natural environment. In addition to potentially fingerprinting each of the biogeochemical sources and sinks of O_2, clumped O_2 measurements offer a way to distinguish between biological processes and physical process (e.g. diffusion) (Ash et al. 2019), thus allowing more rigorous determination of multi-step reaction mechanism that may be expressed by microorganisms.

Our focus and attention in this thesis has been on microbial processes that influence dissolved oxygen. It is these cellular processes that underpin the cycling of oxygen on Earth, determine the rate and amount of organic carbon oxidation, and control the makeup of the atmosphere and the habitability of the planet. Our contribution to the body of work has been to highlight the complexity of oxygen loss and demonstrate the multifold ways in which oxygen may be utilized by microorganisms, even outside the cell membrane. It is our hope that future work will challenge, refine, and incorporate these results in to a more nuanced model of the marine oxygen cycle.

References

Angert, A., S. Rachmilevitch, E. Barkan, and B. Luz. 2003. Effects of photorespiration, the cytochrome pathway, and the alternative pathway on the triple isotopic composition of atmospheric O2. Global Biogeochem. Cycles **17**. doi:10.1029/2002GB001933

Ash, J., H. Hu, and L. Yeung. 2019. What Fractionates Oxygen Isotopes During Respiration? Insights from Multiple Isotopologues and Theory.

Diaz, J. M., S. Plummer, C. M. Hansel, P. F. Andeer, M. A. Saito, and M. R. Mcilvin. 2019. NADPH-dependent extracellular superoxide production is vital to photophysiology in the marine diatom Thalassiosira oceanica. **116**. doi:10.1073/pnas.1821233116

Hein, J. R., and A. Koschinsky. 2014. Deep-ocean ferromanganese crusts and nodules. The Treatise on Geochemistry 273–291.

Helman, Y. 2005. Fractionation of the Three Stable Oxygen Isotopes by Oxygen-Producing and Oxygen-Consuming Reactions in Photosynthetic Organisms. Plant Physiol. **138**: 2292–2298. doi:10.1104/pp.105.063768

Kana, T. M. 1993. Rapid oxygen cycling in Trichodesmium thiebautii. Limnol. Oceanogr. **38**: 18–24.

Nicholson, D. P., R. H. R. Stanley, E. Barkan, D. M. Karl, B. Luz, P. D. Quay, and S. C. Doney. 2012. Evaluating triple oxygen isotope estimates of gross primary production at the Hawaii Ocean Time-series and Bermuda Atlantic Time-series Study sites. **117**: 1–18. doi:10.1029/2010JC006856

Yeung, L. Y., J. L. Ash, and E. D. Young. 2015. Biological signatures in clumped isotopes of O2. Science (80-.). **348**: 431–434. doi:10.1126/science.aaa6284